

DESIGN AND DEVELOPMENT OF SCANNING EDDY CURRENT FORCE
MICROSCOPY FOR CHARACTERIZATION OF ELECTRICAL, MAGNETIC
AND FERROELECTRIC PROPERTIES WITH NANOMETER RESOLUTION

Dissertation

Submitted to

The School of Engineering of the
UNIVERSITY OF DAYTON

In Partial Fulfillment of the Requirements for

The Degree

Doctor of Philosophy in Mechanical Engineering

By

Vijayaraghava Nalladega, M.S.

Dayton, Ohio

August, 2009



DESIGN AND DEVELOPMENT OF SCANNING EDDY CURRENT FORCE
MICROSCOPY FOR CHARACTERIZATION OF ELECTRICAL, MAGNETIC
AND FERROELECTRIC PROPERTIES WITH NANOMETER RESOLUTION

APPROVED BY:

Shamachary Sathish, Ph.D.
Advisory Committee Chairman
Professor, Materials Engineering
Department

P.Terrence Murray, Ph.D.
Committee Member
Professor, Materials Engineering
Department

Donald Klosterman, Ph.D.
Committee Member
Assistant Professor, Chemical and
Materials Engineering Department

Chakrapani Varanasi, Ph.D.
Committee Member
Sr. Research Engineer
University of Dayton Research
Institute

Mark P. Blodgett, Ph.D.
Materials Research Engineer
Wright-Patterson Air Force Base
Dayton, Ohio

Joseph E. Saliba, Ph.D., P.E.
Dean, School of Engineering

Malcolm W. Daniels, Ph.D.
Interim Dean, School of Engineering

© Copyright by
Vijayaraghava Nalladega
All rights reserved
2009

ABSTRACT

DESIGN AND DEVELOPMENT OF SCANNING EDDY CURRENT FORCE MICROSCOPY FOR CHARACTERIZATION OF ELECTRICAL, MAGNETIC AND FERROELECTRIC PROPERTIES WITH NANOMETER RESOLUTION

Name: Nalladega, Vijayaraghava
University of Dayton

Advisor: Dr. Shamachary Sathish

This dissertation describes the design and development of a new high-resolution electrical conductivity imaging technique combining the basic principles of eddy currents and atomic force microscopy (AFM). An electromagnetic coil is used to generate eddy currents in an electrically conducting material. The eddy currents induced in the sample are detected and measured with a magnetic tip attached to the AFM cantilever. The interaction of eddy currents with the magnetic tip-cantilever is theoretically modeled. The model is then used to estimate the eddy current forces generated in a typical metallic material placed in induced current field. The magnitude of the eddy current force is directly proportional to the electrical conductivity of the sample. The theoretical eddy current forces are used to design a magnetic tip-cantilever system with appropriate magnetic field and spring constant to facilitate the

development of a high-resolution, high sensitivity electrical conductivity imaging technique.

The technique is used to experimentally measure eddy current forces in metals of different conductivities and compared with theoretical and finite element models. The experimental results show that the technique is capable of measuring pN range eddy current forces. The experimental eddy current forces are used to determine the electrical resistivity of a thin copper wire and the experimental value agrees with the bulk resistivity of copper reported in literature. The imaging capabilities of the new technique are demonstrated by imaging the electrical conductivity variations in a composite sample and a dual-phase titanium alloy in lift mode AFM. The results indicate that this technique can be used to detect very small variations in electrical conductivity. The spatial resolution of the technique is determined to be about 25 nm by imaging carbon nanofibers reinforced in polymer matrix. Since AFM is extensively used to characterize nanomaterials, the newly developed technique is used to characterize metallic nanoparticles. The results showed for the first time that it is possible to image helicons in nanometallic particles at low electromagnetic frequencies using an AFM. The theoretical analysis of the helicons in nanostructured materials is presented using the concept of effective mass of electrons.

The primary objective of the research work reported in this dissertation is to develop a high-resolution electrical conductivity imaging system. However, the interaction of induced currents with different materials gives rise to different

interaction forces. If an appropriate probe and an imaging mode are used, different material properties can be characterized using the same experimental setup. Therefore, in this study, magneto-acoustic, magnetic and dielectric properties of materials placed in induced current fields are studied. The modifications necessary to image these properties are discussed in detail. The advantages, limitations and applications of the new methodology are discussed.

Dedicated to my parents and my wife

ACKNOWLEDGEMENTS

This dissertation could not have been completed without the help and support of many people. Finishing my doctoral studies is definitely a high point in my career. Here, I would like to express my thanks and gratitude to all those people who helped me throughout my research and contributed to the successful completion of this dissertation.

First, I would like to thank my research advisor Dr. Sathish for his encouragement, help and support throughout the course of this research work. He has been a great mentor from my Master's research days and I have always learnt something new from our technical discussions. I am grateful for his guidance, insightful comments and his patience in answering my questions at all times. I truly value his advice in both personal and professional matters. I am lucky to have him as my teacher, friend and mentor.

I would like to thank the members of doctoral advisory committee, Dr. Terry Murray, Dr. Don Klosterman, Dr. Mark Blodgett and Dr. Pani Varanasi for their willingness to serve on my thesis committee. I greatly appreciate their time, discussions and helpful suggestions throughout the research work and in preparation of the dissertation.

I am exceptionally grateful to the financial support provided by Dayton Area Graduate Studies Institute (DAGSI), University of Dayton Research Institute, and Wright-Patterson Air Force Base for the successful completion of my doctoral research work.

Samples used in this study came from different people. I would like to thank Dr. Terry Murray for providing the platinum nanoparticles sample, Dr. Klosterman for the carbon nanofiber composite sample, Dr. Blodgett for the titanium alloy sample. I am grateful to Dr. Michael Gigliotti and Dr. P. R. Subramanian, GE Global Research, for providing amorphous and nanocrystalline magnetic ribbon samples. I thank Dr. Dave Zelmon, Wright-Patterson Air Force Base for providing the ferroelectric KTP samples.

I take this opportunity to personally thank Mr. Mike Bouchard, Division Head, Structural Integrity Division, UDRI, for providing me with an opportunity to work in the division and carry out my research. I am grateful for his constant support and encouragement throughout the research work. I am sincerely grateful to Dr. Allan Crasto, Associate Director, UDRI, for the encouragement and the financial support for my research. I would like to thank Dr. Kumar Jata, Wright-Patterson AFB for technical discussions. I would also like to express my sincere thanks to Mr. Brian Frock, UDRI, for his help, discussions, and encouragement over the last six years. He patiently taught me the basics of image processing which helped me to understand images and contrast in a better way for which I am always grateful to him. I would like to thank Tim Campbell for helping me with sample preparation whenever I needed and Ed

Klosterman for his help in the lab. I would like to specially thank Richard Reibel for his extensive help with the instrumentation through out the project. I would like to thank Marla McCleskey, Administrative Assistant, Structural Integrity Division, for her gracious administrative assistance.

I would like to thank all my friends who have directly or indirectly helped me throughout my graduate studies in University of Dayton. I am grateful for their support and encouragement. I truly cherish all the memories of last seven years spent at UD.

I would like to thank, from the bottom of my heart, my parents and brothers for their love, support and encouragement. I am especially grateful to my father who taught me the importance of higher education and gaining knowledge. Finally, I thank my wife Pushyami for her constant encouragement, motivation, support and love throughout my research work. Without her patience and support, this work would not have been possible.

TABLE OF CONTENTS

ABSTRACT.....	iv	
DEDICATION.....	vii	
ACKNOWLEDGEMENTS.....	viii	
LIST OF ILLUSTRATIONS.....	xvi	
LIST OF PRINCIPAL SYMBOLS.....	xxii	
CHAPTER		
1. INTRODUCTION.....	1	
1.1. Motivation.....	1	
1.2. Dissertation Overview.....	13	
2. MEASUREMENT OF ELECTRICAL AND MAGNETIC PROPERTIES AT MULTIPLE LENGTH SCALES.....		15
2.1. Introduction.....	15	
2.2. Electrical Conductivity.....	16	
2.3. Macroscale Measurement of Electrical and Magnetic Properties.....	19	
2.3.1. Two-point Probe Technique.....	20	
2.3.2. Four-point Probe Technique.....	22	
2.3.3. Electromagnetic Induction Methods.....	25	
2.3.3.1. Eddy currents.....	26	
2.3.3.2. Measurement of electrical properties using eddy currents.....	30	
2.3.3.3. Measurement of magnetic properties using eddy currents.....	35	
2.3.3.4. Eddy current NDE.....	36	

2.3.3.5. Eddy current imaging.....	42
2.4. Microscale Electrical and Magnetic Property Measurement Techniques.....	45
2.4.1. Eddy Current Microscopy.....	45
2.4.2. Scanning Tunneling Microscopy.....	47
2.4.3. Atomic Force Microscopy.....	50
2.4.3.1. Characterization of electric and dielectric properties using AFM.....	53
2.4.3.2. Characterization of magnetic properties using AFM.....	61
2.5. Summary.....	63
 3. SCANNING PROBE MICROSCOPY.....	 65
3.1. Introduction.....	65
3.2. Principle of Scanning Tunneling Microscopy.....	66
3.3. Atomic Force Microscopy.....	70
3.3.1. Principle of AFM.....	71
3.3.2. Design and Instrumentation of AFM.....	74
3.3.2.1. Force sensor.....	74
3.3.2.2. Cantilever deflection measurement.....	77
3.3.2.3. Scanner.....	79
3.3.2.4. Feedback mechanism.....	80
3.4. Probe-Sample Interactions in AFM.....	81
3.4.1. Macroscopic Forces.....	82
3.4.1.1. Van der Waals force.....	82
3.4.1.2. Capillary forces.....	83
3.4.2. Microscopic Forces.....	84
3.5. Modes of Operation in AFM.....	86
3.5.1. Static Mode: Contact AFM.....	87
3.5.2. Dynamic Mode: Non-contact AFM.....	90
3.5.3. Tapping Mode AFM.....	91

3.6. Force-Distance Curves in AFM.....	94
3.7. Electrostatic and Magnetostatic Interactions in AFM.....	97
3.7.1. Electrostatic Interactions.....	97
3.7.2. Magnetostatic Interactions.....	99
3.8. MFM Based Eddy Current Microscopy.....	101
3.8.1. Improving Spatial Resolution and Sensitivity in Eddy Current Microscopy.....	105
4. DEVELOPMENT OF SCANNING EDDY CURRENT FORCE MICROSCOPY (SECFM).....	108
4.1. Introduction.....	108
4.2. Maxwell's Equations.....	110
4.2.1. Maxwell's Equations in Matter.....	114
4.3. Electromagnetic Field Equations.....	118
4.3.1. Boundary Conditions.....	122
4.4. Classification of Fields.....	124
4.5. Eddy Current Problem.....	125
4.5.1. Eddy Current Field Equations.....	126
4.5.2. Boundary Conditions.....	129
4.6. Theoretical Modeling of Eddy Current Forces.....	130
4.6.1. Eddy Current Forces.....	131
4.6.2. Magnetic Field Due to Eddy Currents in the Sample.....	133
4.6.3. Magnetic Field of the Tip.....	137
4.7. Selection of Cantilever and Tip.....	140
4.8. Scanning Eddy Current Force Microscope.....	141
5. CHARACTERIZATION OF ELECTRICAL CONDUCTIVITY OF BULK CONDUCTORS.....	147
5.1. Introduction.....	147
5.2. Materials.....	148

5.3. Experimental Setup.....	149
5.4. Results and Discussion.....	151
5.4.1. Experimental Eddy Current Force Measurement.....	151
5.4.2. Finite Element Modeling of Eddy Current Forces.....	160
5.4.3. Quantitative Measurement of Electrical Resistivity.....	165
5.4.4. Imaging Local Electrical Conductivity Variations.....	169
5.4.4.1. Carbon fiber reinforced composite material.....	171
5.4.4.2. Ti-6Al-4V alloy.....	175
5.4.5. Spatial Resolution.....	188
5.5. Conclusions.....	190
6. CHARACTERIZATION OF ELECTRICAL AND ELECTROMAGNETIC PROPERTIES OF NANOSTRUCTURED MATERIALS.....	193
6.1. Introduction.....	193
6.2. Materials and Experiment.....	196
6.3. Results and Discussion.....	198
6.3.1. Carbon Nanofiber Polymer Composite.....	198
6.3.2. Metallic Nanoparticles.....	203
6.4. Conclusions.....	218
7. GENERATION, DETECTION AND IMAGING OF ELECTROMAGNETIC ACOUSTIC FIELDS.....	220
7.1. Introduction.....	220
7.2. Materials and Experiment.....	222
7.3. Results and Discussion.....	223
7.3.1. Detection of Acoustic Amplitudes in Single Crystal Metallic Samples.....	223
7.3.2. Imaging Acoustic Fields Generated by Electromagnetic Fields.....	226
7.4. Conclusions.....	228

8. CHARACTERIZATION OF MAGNETIC PROPERTIES.....	230
8.1. Introduction.....	230
8.2. Materials and Experiment.....	233
8.3. Results and Discussion.....	234
8.3.1. Iron and Carbon Nanoparticles.....	234
8.3.2. Amorphous and Nanocrystalline Magnetic Ribbons.....	236
8.4. Conclusions.....	240
9. CHARACTERIZATION OF FERROELECTRIC PROPERTIES.....	242
9.1. Introduction.....	242
9.2. Materials and Experiment.....	245
9.3. Results and Discussion.....	245
9.3.1. Detection of Electrostrictive and Piezoelectric Interactions in KTP crystals.....	246
9.3.2. Imaging Ferroelectric Interactions in KTP crystals.....	248
9.4. Conclusions.....	252
10. SUMMARY AND CONCLUSIONS.....	253
11. FUTURE WORK.....	263
REFERENCES.....	266

LIST OF ILLUSTRATIONS

2.1.	Schematic of a two-point probe method.....	21
2.2.	Schematic of a four-point probe technique.....	23
2.3.	Generation of eddy currents in a conductor.....	27
2.4.	Skin effect in a conductor due to eddy currents.....	29
2.5.	Schematic of eddy current inspection by a surface coil.....	38
3.1.	Schematic of a scanning tunneling microscope.....	68
3.2.	A schematic diagram illustrating the working principle of AFM.....	73
3.3.	Optical beam deflection detection in AFM.....	79
3.4.	A schematic view of an AFM tip in close proximity to sample surface....	84
3.5.	Interaction potential between the AFM probe and sample surface.....	86
3.6.	Typical experimental force-distance curve and the points along a force curve.....	96
4.1.	A non-magnetic electrical conductor placed in time varying external magnetic field. The eddy current density decreases exponentially as a function of increasing thickness of the conductor.....	134
4.2.	Schematic of a cone shaped AFM magnetic tip along with its dimensions.....	137
4.3.	Schematic of AFM-based eddy current imaging system.....	143
4.4.	V-shaped cantilever used in the experiments. The tip is attached at the end of the cantilever.....	143

5.1.	Comparison of cantilever vibration amplitudes over copper and insulator at a frequency of 82 kHz. The waveform on copper has been slightly shifted in time to show the waveforms separately.....	153
5.2.	A schematic of the AFM cantilever used in the experiments showing dimensions. The tip is shown as a solid rectangle at the end of the cantilever.....	155
5.3.	Eddy current force in the copper sample as a function of separation distance between the magnetic tip and the sample.....	157
5.4.	Amplitude of oscillation of the AFM cantilever on different metallic samples. The waveforms on the metals have been slightly shifted in time to show the waveforms separately.....	158
5.5.	Variation of eddy current force as a function of electrical resistivity in different metals.....	160
5.6.	Maxwell 3D model showing (a) coil, sample, and (b) tip and cantilever.	164
5.7.	Eddy current density (J) in the copper sample.....	164
5.8.	Magnetic field strength vector (H) in the copper sample.....	165
5.9.	Forces on the cantilever due to eddy currents measured as a function of the input current to the coil. Line corresponds to linear fit of the data...	169
5.10.	Vibration spectra of the AFM cantilever positioned on titanium alloy showing multiple resonance peaks.....	171
5.11.	(a) Surface topography and (b) electrical conductivity images of carbon fibers reinforced in PEEK matrix. The conductive fiber and insulating matrix are shown by arrows in the eddy current image.....	172
5.12.	A section analysis of the eddy current image of fibers and matrix showing the variations in eddy current force.....	174
5.13.	Section analysis of a high magnification eddy current image showing the variations in eddy current force at the interface of matrix and fiber.....	175
5.14.	(a) Surface topography and (b) electrical conductivity image of Ti-6Al-4V alloy. The excitation frequency of the coil was 92 kHz.....	177

- 5.15. (a) Surface topography and (b) electrical conductivity images of Ti-6Al-4V. The coil was excited at a frequency of 92 kHz..... 179
- 5.16. (a) Surface topography and the corresponding line scan across the line shown in the topography. (b) Electrical conductivity image and the corresponding line scan across the line shown in the eddy current image of Ti-6Al-4V sample. The excitation frequency of the coil was 92 kHz...182
- 5.17. (a) Surface topography and (b) electrical conductivity image obtained very near the crack initiation region of the fatigue fractured titanium sample. The electrical conductivity image shows lamellar structure with dark contrast within α grain and also very fine cracks with bright contrast as indicated by arrows. The frequency of the excitation was 92 kHz..... 184
- 5.18. (a) A high magnification electrical conductivity image showing fine cracks in fatigue fractured titanium sample (b) Line scan across the crack showing the size of the crack. The coil was operated at a frequency of 92 kHz..... 184
- 5.19. (a) Surface topography and (b) relative electrical conductivity images of $\alpha + \beta$ platelets in Ti-6Al-4V sample. The scale bar for electrical conductivity image is provided in terms of eddy current force. Excitation frequency 92 kHz..... 187
- 5.20. Images and single-scan-line response signals from carbon nanofibers in an epoxy matrix. (a) Surface topography and (b) eddy current (relative electrical conductivity). Frequency 85 kHz..... 190
- 6.1. High resolution SEM images of raw Pyrograf III carbon nanofibers, a) 500X magnification, showing agglomerated nature of raw materials, and b) 10kX magnification showing individual nanofibers within agglomerate.. 197
- 6.2. SEM micrograph of platinum nanoparticles synthesized by through thin film ablation..... 198
- 6.3. (a) Surface topography and (b) electrical conductivity images of a carbon nanofiber composite thin film. Arrows on the eddy current image indicate some of the nanofibers. Frequency of the excitation 85 kHz..... 200
- 6.4. (a) Surface topography and (b) electrical conductivity images of carbon nanofibers. The images show a uniform size distribution and better dispersion of nanofibers in the polymer matrix. Excitation frequency 85 kHz..... 201

- 6.5. (a) Surface topography and (b) electrical conductivity images obtained at another region of nanocomposite thin film. The arrow indicates the fiber pull-out from the matrix. The frequency of excitation was 85 kHz..... 202
- 6.6. (a) Magnified image of the carbon nanofiber showing the separation of fiber from the matrix. (b) Single line section analysis of the fiber showing the variation in the conductivity near the interface..... 202
- 6.7. (a) Surface topography and (b) eddy current images of an individual nanoparticle of platinum. Frequency of excitation 85 kHz..... 203
- 6.8. (a) Surface topography and (b) eddy current images of a 500 nm platinum nanoparticle. The surface topography looks similar to the previous image, but the eddy current force image shows the particle is split into bright and dark regions. Frequency 85 kHz..... 204
- 6.9. (a) Surface topography and (b) eddy current images of platinum nanoparticles. While two smaller particles are split into half showing two different contrasts, the bigger particle is split into three parts showing bright-dark-bright contrast within the particle. Frequency 85 kHz..... 205
- 6.10. (a) Eddy current image of the platinum nanoparticle and (b) line scan across the nanoparticle showing the magnetic field variation across the nanoparticle. The size of the nanoparticle is about 250 nm..... 213
- 6.11. (a) Eddy current image of the individual platinum nanoparticle showing the second resonance mode of helicon wave. (b) Section analysis showing the variation of magnetic field across the line. The size of the nanoparticle is about 500 nm..... 214
- 6.12. (a) Eddy current image of an individual nanoparticle showing the third resonance mode of helicon wave (b) corresponding section analysis of the nanoparticle showing the variation of magnetic field across the line. The size of the nanoparticle is about 800 nm..... 215
- 6.13. (a) Magnetic lines of force for the first, second, and third resonance modes in spherical particles. (b) Magnetic field images of platinum nanoparticles..... 216
- 6.14. (a) Surface topography and (b) eddy current images showing the distribution of platinum nanoparticles. Frequency 85 kHz..... 218
- 7.1. Amplitude of the AFM cantilever plotted as a function of the input voltage to the coil for copper, aluminum and cadmium single crystal samples...224

7.2.	(a) Surface topography and (b) acoustic amplitude images obtained on a dual-phase polycrystalline Ti-6Al-4V sample. Excitation frequency: 85 kHz.....	227
7.3.	A higher magnification (a) surface topography and (b) acoustic field images of Ti-6Al-4V showing the contrast difference in the grains. Frequency of excitation: 85 kHz.....	228
8.1.	(a) Surface topography and (b) magneto-elastic images of the sample containing Fe and C nanoparticles. Excitation frequency: 91 kHz.....	235
8.2.	(a) Surface topography and (b) magneto-elastic images of Fe and C nanoparticles showing more number of iron nanoparticles than the carbon nanoparticles. Excitation frequency: 91 kHz.....	236
8.3.	(a) Surface topography and (b) magneto-elastic images of amorphous FINEMET magnetic ribbon sample. Magnetic domains can be observed in the magneto-elastic image and are indicated by arrows. Frequency of excitation: 58 kHz.....	237
8.4.	(a) Surface topography and (b) magneto-elastic image of amorphous magnetic ribbon sample. The magneto-elastic image shows relatively large circular magnetic domains. Some of the domains are indicated by arrows. Frequency of excitation: 58 kHz.....	238
8.5.	(a) Surface topography and (b) magneto-elastic images of nanocrystalline magnetic ribbon sample. Frequency of excitation: 58 kHz. Nanocrystalline phase can be observed in the images.....	239
8.6.	A high magnification (a) surface topography and (b) magneto-elastic images of the nanocrystalline FINEMET alloy magnetic ribbon. A domain wall with a width of 40 nm is shown by arrow. Frequency of excitation: 58 kHz.....	240
9.1.	Amplitude of the AFM cantilever plotted as a function of the input voltage applied to the coil for the different KTP crystal samples.....	246
9.2.	Amplitude of AFM cantilever vibration plotted as a function of separation distance between magnetic tip and sample surface for different KTP crystal samples.....	248
9.3.	(a) Surface topography and (b) eddy current images of KTP6 sample. Frequency of excitation: 90 kHz.....	249

9.4.	(a) Surface topography and (b) eddy current images of KTP4 sample. Frequency of excitation: 90 kHz.....	250
9.5.	(a) Surface topography and (b) eddy current images of HGTR KTP sample. Frequency of excitation: 90 kHz.....	251
9.6.	(a) Surface topography and (b) eddy current images of K0557 sample. Frequency of excitation: 90 kHz.....	251

LIST OF PRINCIPAL SYMBOLS

ρ	Electrical resistivity
σ	Electrical conductivity
τ	Relaxation time of electrons
μ_0	Magnetic permeability of free space
μ_r	Relative magnetic permeability
ω	Angular frequency
f	Frequency of electromagnetic wave
δ	Electromagnetic skin depth
ϵ_0	Electric permittivity of space
ϵ_r	Relative electric permittivity
χ_m	Magnetic susceptibility
B	Magnetic Induction
H	Magnetic field
E	Electric field
J	Eddy current density
P	Electric Polarization
D	Electric Displacement
k	Spring constant of AFM cantilever

e	Charge of electron
m	Mass of electron
m^*	Effective mass of electron
ω_p	Plasmon frequency
ω_c	Cyclotron frequency
M	Magnetization
λ	Wavelength (m)
Q	Quality factor of cantilever
l	Mean free path of electron
v_{ph}^H	Helicon phase velocity
c	Speed of light

CHAPTER 1

INTRODUCTION

1.1. Motivation

Electrical conductivity is one of the fundamental physical properties of materials. Electrical conductivity provides information about the composition, microstructure, and heat treatment of metals and alloys. Therefore, measurement of electrical conductivity is important in many fields of engineering and science. Various techniques are available to measure the electrical conductivity.

Two-point probe [1] and four-point probe techniques [2,3] are the most popular and commonly used techniques to measure electrical resistivity. The general principle of these techniques is to pass known voltage or current between the probes, which are in contact with the specimen, and measuring the resistance across the probes. If the dimensions of the specimen are known, the resistance can be used to determine the electrical resistivity of the specimen. This simple methodology is extensively used for measuring electrical resistivity of conductors. They provide a direct and absolute measurement of the electrical conductivity. The four-point probe methods have been extensively used to characterize electrical conductivity of semi-conductors, thin films, conducting

polymer composites etc. The point probe methods are useful when the electrical conductivity of the sample is homogeneous in a volume that is large compared to the spacing of the probes. In two-point probe method, contact resistance between the probe and the sample leads to measurement errors. In the four-point probe method the contact resistance is avoided. In general, for accurate measurements of the electrical resistivity, the probe methods require good ohmic contact of the probe with the specimen surface. This requirement can sometimes involve costly sample preparation methods, especially in semiconductor materials. Usually, resistivity measurements on a contaminated surface lead to erroneous results. Therefore, the point probe methods require samples free of contamination. Also, if the electrical conductivity is not homogeneous within the volume between the electrode spacing, these methods will not be able to detect the inhomogeneity. Finally, these techniques provide an average value of the resistivity over the sample surface.

If a conducting material is placed in an AC magnetic field, currents will be generated inside the material by the principle of electromagnetic induction. Therefore, direct physical electrical contact is not required to generate electrical currents in conductors. The electromagnetic induction mechanism is one of the most frequently used non-contact methods to measure electrical properties [4]. Since the currents are induced in the material, there is no need of contact between the probe and the specimen. Therefore, problems associated with contact in the point-probe methods can be avoided. The induced currents are also known as eddy currents. Hence these methods are also known as eddy

current methods. Generally, in eddy current methods of conductivity measurements, the sample is placed in a time-varying magnetic field generated by an inductive coil. Currents are generated in the sample due to induction. The density of the generated eddy currents is dependent on different factors including the electrical conductivity of the sample. Therefore by analyzing the flow of eddy currents, one can measure the resistivity of the material.

It is well known that the presence of a defect in a material modifies the electrical conductivity around the defect. Consequently, the flow of induced currents also gets modified. This fact has been exploited to develop nondestructive evaluation (NDE) method based on eddy currents [5]. By monitoring the changes in the flow of eddy currents, it is possible to detect defects in the materials. The presence of a defect changes the characteristic loading conditions of the coil. Thus by monitoring the changes in the coil characteristics the material can be evaluate for the presence of any flaws. This simple methodology is extensively used in the NDE of materials in different industries, most notably, in the NDE of aircraft structures. Various configurations of probe coils can be used in the eddy current testing. By attaching the coil probe to a XY scanner, the eddy current method can be converted into an imaging system. The coil probe is raster-scanned across the sample surface and the changes in the flow of eddy currents are used to construct an image of the electrical conductivity.

Eddy current methods have considerable advantages over the point probe methods. The primary advantage is that these methods are completely non-

contact in nature. Hence surface contamination is not a problem. The second advantage is that these methods are sensitive to small variations in electrical conductivity. Since the currents generated by the coil are confined to a region defined by the size of the coil, they can be used to characterize local changes in the electrical conductivity within that small region. The consequence of this is that small cracks and defects can be detected. However if the defects are smaller than the size of the coil, they are difficult to detect using this method. Therefore, the resolution in eddy current methods is limited by the size of the coil used.

The point-probe methods and the eddy current methods are sufficient for the measurement of electrical conductivity of bulk materials on macroscale. However, there has been an enormous growth of nanoscience and nanotechnology in the last decade, primarily due to the availability of new methods for synthesizing nanomaterials, as well as tools for characterization and manipulation. The physical properties of materials become size-dependent in the nanometer regime [6]. It is well known that nanostructured materials exhibit dramatically different physical and material properties when compared to bulk states [7-10]. Considerable research work is focused on the development of low-dimension nanostructured materials, due to their potential application as building blocks for nanocircuits, nanodevices etc. One of the key technologies is microelectronics where as a consequence of the decreasing scale of many devices, high resolution characterization methods have become a fundamental importance for further development in this area. Another discipline, where progress is directly related to the availability of powerful microscopy methods, is

the development of new and functional materials. The latter strongly relies on the characterization of materials at various and increasing levels of resolution. Structure, microstructure, and defect geometry as well as chemical composition and spatial distribution are important parameters that determine the behavior of materials and practical applications. Moreover, with the continuous reduction in the size of the devices, the defects in these devices are also approaching the size of the devices themselves. Therefore it is important to characterize the properties of nanostructured materials at the scales which they operate, i.e. at micro- and nanoscales. The development of atomic force microscopy (AFM) [11] has provided a path to the possibility of imaging materials with unprecedented spatial resolution and led to the further development of many techniques based on atomic force microscopy to image material properties on local scales.

The AFM measures very small forces (less than 1 nN) present between the tip and a sample surface. These small forces are measured by measuring the motion of a very flexible cantilever while the tip is scanned across the sample surface. In addition to the topography imaging, AFM has been modified to image the elastic, thermal, magnetic, and electrical properties of materials. Various techniques are available to characterize electrical properties of materials with nanometer scale resolution. Electrostatic force microscopy [12], conducting atomic force microscopy [13], tunneling AFM [14], scanning capacitance microscopy [15], surface potential imaging [16] are some of the widely used AFM based techniques to image electrical properties of materials. The general working principle of these techniques is similar to that of point probe techniques. In these

techniques, a bias voltage is applied between a conductive tip and the sample. The tip is brought into contact with the sample and scanned across the sample surface. The resulting electric interactions are measured. Based on the type of interaction measured, different electrical properties can be imaged. To obtain an image, measurements are performed at each location by moving the tip from one discrete location to the next across the sample. Hence, these techniques are quite time consuming. Since a bias voltage needs to be applied, the tips need to be conductive. Therefore, special conducting tips have to be used.

The ability to detect and measure nanonewton forces by using microfabricated sensors with scanning probe methods has enabled the development of eddy current microscopy with resolution superior to that of conventional eddy current techniques. Hoffmann *et al.* [17] developed an AFM based eddy current microscopy with improvement in spatial resolution. They used the eddy currents generated by the oscillating magnetic probes to image the local electrical conductivity variations. Although high resolution images were acquired, the eddy current forces generated by a typical magnetic tip used in the AFM are very weak and hence the technique is not expected to be very sensitive to small variations in electrical conductivity. An improvement in the sensitivity was achieved by using a permanent magnetic particle with a diameter of 650 nm as a tip attached to a silicon cantilever of AFM [18]. With a huge increase in the magnetic stray field of the tip, an increased sensitivity to local variations in conductivity was observed. However, the spatial resolution was limited by the increased diameter of the probe. In both the cases, stiffer cantilevers with a

spring constant of about 2 N/m were used. Therefore small variations in electrical conductivity would be difficult to detect using the stiffer cantilevers.

This dissertation describes the development and demonstration of a new scanning probe method to characterize electrical properties of materials. This new technique is called Scanning Eddy Current Force Microscopy (SECFM). It combines the principles of eddy currents and atomic force microscopy to achieve high spatial resolution and high sensitivity to local variations in electrical conductivity. To achieve the goal of high sensitivity and high spatial resolution, the eddy current forces are first theoretically analyzed for a typical metallic material and the sensitivity of the cantilever needed for the measurement of those forces is determined. Using these analyses, an appropriate cantilever with suitable spring constant is designed. A small electromagnetic coil is placed under the sample and excited with an oscillating AC signal. By using a coil to generate the eddy currents, the eddy current fields in the sample can be independently adjusted. The time-varying magnetic field generated by the excitation of the coil induces electric currents in the sample. The induced currents generate a secondary magnetic field opposing the primary field. The magnetic interactions due to the secondary magnetic field deflect the magnetic tip-cantilever, which is positioned at a distance of few nm from the sample surface. The resulting eddy current forces are calculated using Hooke's law, $F = k\Delta z$, where k is the spring constant of the cantilever and Δz is the deflection of the cantilever. The amount of deflection of the cantilever is directly proportional to the eddy current forces, which in turn depend on the conductivity of the material. The deflection of the

cantilever due to eddy current forces is analyzed by electronic instrumentation and the surface topography and electrical conductivity images of the sample are obtained simultaneously.

The new methodology is similar to that of a conventional eddy current testing technique. In a conventional eddy current testing, a driver coil generates eddy currents in the material and a pickup coil detects them. In the new methodology, a coil generates the eddy currents in the material but a *magnetic probe* is used to detect the eddy currents. The magnetic probe in this case performs the function of the pick up coil. While in conventional method, the impedance changes in the coil are measured, in the new method, changes in the eddy current forces are measured. One big difference, though, is in the spatial resolution. In the conventional method, the spatial resolution is determined by the size of the coil, since a coil is being used to detect the currents. However, in this case, the detection of the eddy currents is performed by a sharp tip attached to a flexible cantilever. Therefore, the resolution (spatial and force) in this case would be dictated by the size of the tip and the flexibility of the cantilever. The coil is used only for the generation of the induced currents in the sample.

The eddy currents were experimentally measured for different metals and are compared with the results calculated from theoretical model. A finite element model of the interactions between the magnetic tip and the eddy currents in the sample was developed and the eddy current forces are computed. The results from the finite element model are compared with both theoretical and experimental results. The forces between the magnetic tip and the sample are

measured as a function of the separation distance between the tip and the sample. The eddy current forces are also used to quantitatively measure the electrical resistivity of thin metallic wires.

To demonstrate the imaging capabilities of the new methodology, the technique was first applied to characterize the electrical conductivity bulk conducting materials. A 7 μ m diameter carbon fiber reinforced in polymer matrix was used to image the electrical conductivity of the composite. The contrast in the images is explained based on large electrical conductivity difference between the conducting carbon fiber and the insulating polymer matrix. The technique is then applied to characterize electrical conductivity variations in polycrystalline, dual-phase titanium alloy. The experimental eddy current forces are also used to calibrate the electrical conductivity imaging of different metals.

The technique was then applied to characterize the electrical conductivity of nanostructured materials. The images of nanofibers of carbon reinforced in polymer thin film were obtained. The contrast in this case is also the electrical conductivity variations between conducting carbon fibers and the insulating polymer. The images were used to study the distribution and dispersion of the nanofibers in the polymer matrix. The technique was then used to image metallic nanoparticles. The images showed individual nanoparticles with quite different contrast within a single nanoparticle. Whereas the contrast observed in bulk conducting materials and nanocomposite thin film can be attributed to the variations in the electrical conductivity between two different phases, the same explanation does not hold good in the case of nanoparticles. It is well known that

the electron mean free path lengths in nanoparticles approaches the actual dimensions of the nanoparticles. In this case, the electromagnetic properties of the nanoparticles are quite different from those in the bulk states. Moreover, the periodic arrangement of nanoparticles is thought to exhibit different properties and finds many novel applications. Therefore, the results obtained on nanoparticles are analyzed in view of the different properties exhibited by nanoparticles.

Even though the primary objective of this study is to develop a technique to characterize electrical properties, the same technique can also be used to study the local variations in magnetic and ferroelectric properties of materials. Generally, in AFM, in order to image magnetic properties, a ferromagnetic probe is attached to a stiff cantilever and is oscillated few nanometers above the magnetic sample [19]. The resulting magneto-static interactions between the tip and the sample are measured along with surface topography. However, if the stray field of the magnetic tip is too high, then the magnetization of sample will be changed during scanning [20]. This will be a problem for soft magnetic materials. Therefore, in this study, the magnetic properties are studied using a *non-magnetic* probe. Thus, problems relating to the stray field of the magnetic tip will be avoided. Moreover, by using a flexible cantilever, it is possible to detect small changes in local magnetic properties with high sensitivity.

Similarly, to study ferroelectric properties using AFM, a bias voltage is applied between a conducting tip and the ferroelectric sample and the resulting interactions are used to obtain the information about ferroelectric domains,

piezoelectric properties, and dielectric behavior [21]. However, in this study, eddy currents are used to characterize the ferroelectric samples. Instead of using a conductive tip, a magnetic tip is used. In this configuration, bias voltage between the sample and the tip is not required. Again, since a flexible cantilever is used, small variations in local ferroelectric properties can be imaged with high sensitivity.

The new technique combines the localized nature and high sensitivity of eddy currents and high spatial resolution and the versatility of AFM. This technique has many advantages over the conventional AFM based electrical and magnetic property imaging techniques or conventional eddy current methods. Since induced currents are used in this method, no bias voltage is required to be applied between the sample and the tip and the instrument can be operated in a non-contact mode. Since bias voltage is not applied in this technique, conductive tips are not required for imaging the electrical properties. Regular magnetic tip-cantilevers can be used. Unlike conventional AFM methods, where a stiffer cantilever is used, this methodology, instead, uses flexible cantilevers. By employing softer cantilevers, the cantilever's ability to detect small variations in the forces due to eddy currents is greatly enhanced, thus allowing the detection small variations in electrical conductivity. By using a separate electromagnetic coil to generate eddy currents in the samples, eddy current amplitudes can be independently adjusted for different materials based on electrical conductivity of the sample. Since conventional eddy current techniques can be operated at multiple frequencies, the newly developed technique can also be used at multiple

frequencies. Thus, the dependence of frequency on the contrast observed in eddy current images can be studied. Since the detection of the eddy currents is accomplished by a magnetic probe, the spatial resolution of the technique is dependent on the size of the probe. The technique is shown to have a spatial resolution of about 20-30 nm. The technique can be used on both bulk conducting materials as well as nanostructured materials. Moreover, the same technique can also be used to characterize properties of ferromagnetic and ferroelectric materials with minimum modifications. Quantitative characterization of electrical resistivity is possible. Since an AFM is capable of measuring twisting of the cantilever due to horizontal forces exerted on it, this technique can also be used to measure the torsional effects of the eddy current forces. The torsional eddy current forces are expected to be sensitive to the presence of a flaw parallel to the probe coil or to the probe scan direction and also to grain boundaries. One major advantage of the scanning eddy current force microscope is that the same instrument can be used to image electrical, magnetic, electromagnetic acoustic and ferroelectric properties. The only difference is that different probes need to be used for a particular property in different imaging modes. Therefore, the new instrument offers ease of use and versatility in a single instrument.

The unifying theme in this dissertation is the application of atomic force microscopy to detect and measure various probe-sample interactions to image different material properties using a single instrumental setup. The possible applications of the new technique are discussed in detail. In particular the application to nano NDE is discussed in view of extensive applications of eddy

current NDE. Also, the possibility of the using this technique for sensing applications is also explored. The applicability of the technique for the characterization of electric, magnetic and dielectric properties of materials on micro- and nanoscales is discussed. Finally, suggestions for the future research work are presented.

1.2. Dissertation Overview

The rest of the dissertation is organized as follows. In chapter 2, a review of the methods to characterize electrical and magnetic properties on multiple length scales is presented. A brief review of the DC two-point and four-point probe methods is presented. It is followed then by the description of electromagnetic induction principles. Measurement of electrical resistivity based on induction methods is discussed. The point-probe and induction methods are compared and the advantages and limitations of each are discussed. The microscale measurements of electrical properties by AFM and its related techniques are described in detail. The advantages and limitations of these techniques are discussed. In chapter 3, the principle of scanning probe microscopy is presented. A detailed description of the design and instrumentation of the AFM along with different imaging modes relevant to the present research work is presented. The importance of probe-sample interactions and how they can be exploited to image material properties is explained in the context of the

development of the new methodology. In chapter 4, the theory of eddy currents is presented. The electromagnetic field equations relevant to the present work are provided. The field equations are used to develop a theoretical model to determine the eddy current forces between the magnetic probe and the magnetic fields generated by eddy currents. Based on the theoretical calculations, the design and selection of the cantilever-tip system and coil is discussed. The chapter ends with a detailed description of the external modifications made to the conventional AFM to develop electrical conductivity imaging system. The next four chapters describe the application of the new methodology to characterize different materials on both bulk and nano scales. Chapter 5 discusses the characterization of electrical properties of bulk metals. Eddy current forces on different metallic materials are measured experimentally and compared with theoretical and finite element simulation results. The eddy current forces are then used to quantitatively determine electrical resistivity of selected metals. The qualitative imaging of electrical conductivity is also presented. In Chapter 6, the applications of the technique to nanomaterials are presented. Chapter 7 discusses the generation and detection of acoustic waves using electromagnetic waves using the newly developed technique. Chapters 8 and 9 discuss respectively the characterization of magnetic and ferroelectric properties. The summary and conclusions of the work is presented in Chapter 10. Suggestions for future work are discussed in chapter 11.

CHAPTER 2

MEASUREMENT OF ELECTRICAL AND MAGNETIC PROPERTIES AT MULTIPLE LENGTH SCALES

2.1. Introduction

This chapter reviews some of the methods for measuring electrical and magnetic properties on macro- and microscales. DC measurement techniques like two-probe and four-probe methods are described along with the advantages and limitations of these techniques. A brief theory of the induced currents is then introduced. The non-contact measurement of electrical and magnetic properties of materials using eddy current methods is described. Microscale characterization of electrical and magnetic properties using scanning probe methods is discussed. Finally, high-resolution eddy current microscopy techniques are discussed.

2.2. Electrical Conductivity

In simple monovalent metals, such as sodium, potassium, silver etc., the valence electrons of the constituent atoms are able to move through the crystal almost freely. These valence electrons are termed conduction electrons to distinguish them from electrons in the filled shells of the ion cores. If the conduction electrons moved through the crystal as perfectly free agents, without hindrance, under an applied electric field E , they would flow through the solid with infinite velocity. The electrical resistivity would then be zero. Actually, however, the motion of conduction electrons is not completely free. The collision of the conduction electrons with the ion cores (or atoms) of the metallic atoms cannot be disregarded. If there were to be no disturbing influences inside a metal lattice, infinite conductivity would result. However, such disturbances are invariably present and they can be very diverse and numerous. They impede the flow of electrons, scattering them and giving rise to a resistance called electrical resistance.

The conducting electrons are scattered by collision with the ion cores-the motion of the electrons is like that of the molecules of a gas, which are well known to exhibit Brownian motion. In the absence of an applied field, the average velocity of the conduction electrons moving at random across any plane is zero. With an electric field E applied to the system, the electrons have an acceleration eE/m during the time between collisions, where m is the mass of electron, and e , its charge. If the mean time of flight between collisions, that is, the mean free

time, is denoted by 2τ , the mean velocity under the influence of the field, $\langle v_E \rangle$, is given by

$$\langle v_E \rangle = \left(\frac{eE}{m} \times 2\tau \right) / 2 \quad (2.1)$$

where e and m are the charge and mass of the electron respectively. The order of magnitude for τ for ordinary metals is about 10^{-14} sec. The average velocity of conduction electrons moving with thermal velocities is zero. Therefore the average velocity of electrons in the electric field $\langle v \rangle$ is

$$\langle v \rangle = \langle v_{thermal} \rangle + \langle v_E \rangle = (0 + 2\tau eE / m) / 2 = \tau eE / m \quad (2.2)$$

When the number of electrons per unit volume is N , the electric current density J is given by

$$J = Ne\langle v \rangle = Ne^2\tau E / m \quad (2.3)$$

Usually, τ is independent of E . On the basis of above equation, therefore, the current is directly proportional to the electric field. The electrical conductivity σ is then defined by the following relation

$$J = \sigma E \quad (2.4)$$

The above equation is the well-known Ohm's law.

Therefore,

$$\sigma = \frac{Ne^2\tau}{m} = Ne\mu \quad (2.5)$$

where $\mu = e\tau/m$ is called the electron mobility which is an indication of the frequency of the scattering events and is also the drift velocity per unit electric field. Ohm's law can also be expressed as

$$V = IR \quad (2.6)$$

where V is the applied voltage and I is the current and R is known as electrical resistance. The reciprocal of electrical conductivity is called electrical resistivity. Resistivity, ρ is independent of specimen geometry and is given by the expression

$$r = \frac{RA}{l} \quad (2.7)$$

where A is the cross sectional area perpendicular to the direction of current, and l is the distance between two points at which the voltage is measured.

Electrical conductivity is one of the fundamental physical properties of the materials. The ability to conduct electricity is the basis of classification of materials into conductors and insulators. Electrical conductivity not only informs about how well a metal conducts electrical currents but also provides information about its composition, microstructure, mechanical properties, heat treatment of metals and alloys etc. Measurements of electrical conductivity are useful in metal sorting, alloy identification, detection of flaws, thermal damage in aircraft structures, and quality assurance in the manufacture, maintenance or repair of airplanes. Electrical conductivity plays an important role in technical applications. Knowledge of the resistivity of the material can have many immediate theoretical and practical consequences. For example, it controls the flow of melts under the influence of electromagnetic force in the process of refining or growing semiconductor crystals, and it is a sensitive measure of concentration fluctuation in a critically mixed liquid alloy near the critical point in the homogeneous liquid phase. Another application of the electrical resistivity would be to detect the

purity of the metal. Electrical resistivity can also be used in the detection of the presence or absence of ordered lattice structure in alloys.

2.3. Macroscale Measurement of Electrical and Magnetic Properties

In general, the electrical conductivity measurement methods can be divided into two groups: direct current (DC) and alternating current (AC) methods. In DC methods, conductivity is determined by measuring the resistance of the conductor and dimensions. Once the resistance and dimensions are known, resistivity can be measured by using Eq. (2.7). The resistance is usually determined by a voltage-current method. A known current is sent into the sample and voltage is measured by electrode contacts. The resistance is then calculated using Ohm's law. DC methods can only be applied to materials of particular shape like rods or bars. DC methods require good contact between the material and electrode. In general, the surface of a metal is covered by a thin oxide layer. For a correct DC measurement this thin layer has to be penetrated. This problem can be eliminated by utilizing AC measurement technique. Eddy current method is the most commonly used AC technique to measure electrical conductivity. One advantage of the eddy current methods is that they can be used to measure magnetic properties also in addition to the electrical properties. In the following sections, a brief description of the DC and AC methods is presented.

2.3.1. Two-point Probe Technique

The simplest DC method to measure electrical conductivity is the two-point probe method. In the two-point probe method [1], a voltage source applies a voltage V across the bar of a material causing a current I to flow through the bar. Alternatively, a current source could force current through the sample bar, while a voltmeter in parallel with the current source measures the voltage induced across the bar. A schematic of the two-point probe technique is shown in Figure 1. The resistivity can be obtained by measuring the resistance and physical dimensions of the sample bar. This method is called two-point technique, since wires are attached to the material at two points. The amount of current I that flows through the bar is measured by the ammeter, which is connected in series with the sample bar and voltage source. The voltage drop across the ammeter should be negligible. The resistance R of the bar is measured using Ohm's law. The two-point resistivity of the material is then given by

$$\rho = \frac{Rwh}{l} \quad (2.8)$$

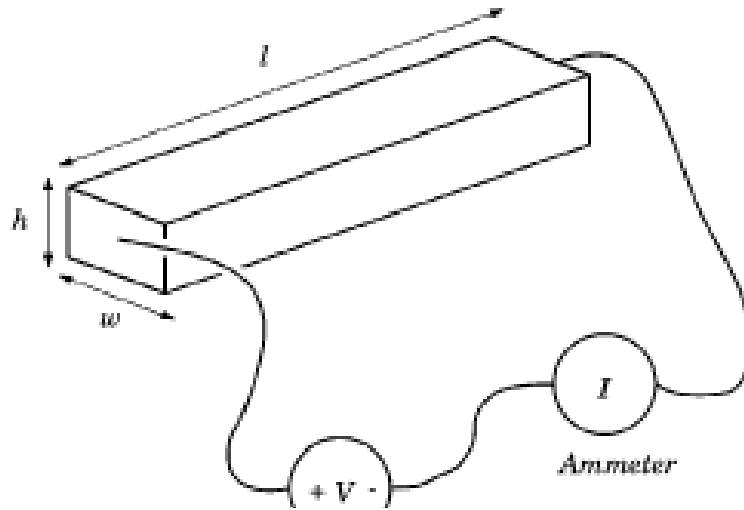


Figure 2.1. Schematic of a two-point probe method [1]

The attainable accuracy using two-point probe method depends on the accuracy of the deflecting instruments, ammeter and voltmeter. The measurement of resistivity using two-point method is not always reliable. Two-point probe methods are easier to implement, because only two probes are needed for the measurement, but the interpretation of the measured data is more difficult. In the two-point probe method, each contact serves as a current and voltage probe. The total resistance then consists of the probe resistance, contact resistance and the resistance of the sample. Therefore, it is impossible to accurately determine the resistance of the sample with this arrangement. Another problem is modulation of the sample resistivity due to the applied current. This is often a possibility for semi-conducting materials. The two-point probe method requires a good ohmic contact between the probe and the sample for accurate measurement. Moreover, if the sample is contaminated, the measurement will be erroneous. For low resistance metals, these problems reduce the sensitivity of

the technique. In general, using the two-point probe technique, a resistance of less than $50\text{ k}\Omega$ cannot be measured.

2.3.2. Four-point Probe Technique

The four-point probe technique [2,3] overcomes many of the problems of the two-point probe technique. The probes are generally arranged in-line with equal probe spacing, but other probe configurations are possible. A current source forces a constant current through the ends of the sample bar. A separate ammeter measures the amount of current I passing through the bar. A voltmeter simultaneously measures the voltage V produced across the inner part of the bar. Alternatively, a voltage source could apply a voltage across the outer contacts, while an ammeter in series with this voltmeter measures the current flowing through the sample bar. The current path is identical to that of two-point probe configuration. However, the voltage is now measured with two additional contacts. Although the voltage path contains the probe resistance and the contact resistance as well, the current flowing through the voltage path is very low due to the high input impedance of the voltmeter. Hence voltage drops across the probe and contact resistances are very small and can be neglected and hence the measured voltage is essentially the voltage drop across the sample.

Figure 2 shows the four-point probe measurement technique on a rectangular bar of material of thickness w and width D . The four-point resistivity [22,23] in Ωm , of the bar is then given by

$$\rho = \frac{\pi}{\ln 2} w \left(\frac{V}{I} \right) F_1 F_2 \quad (2.9)$$

where V is the voltage measured by the voltmeter (in volts), I is the current measured by the ammeter (in amperes), F_1 and F_2 are geometric correction factors for the rectangular specimen. The correction factor F_1 depends on the specimen thickness w and the spacing between the voltmeter contacts, s . The correction factor F_2 depends on the specimen length A and width D .

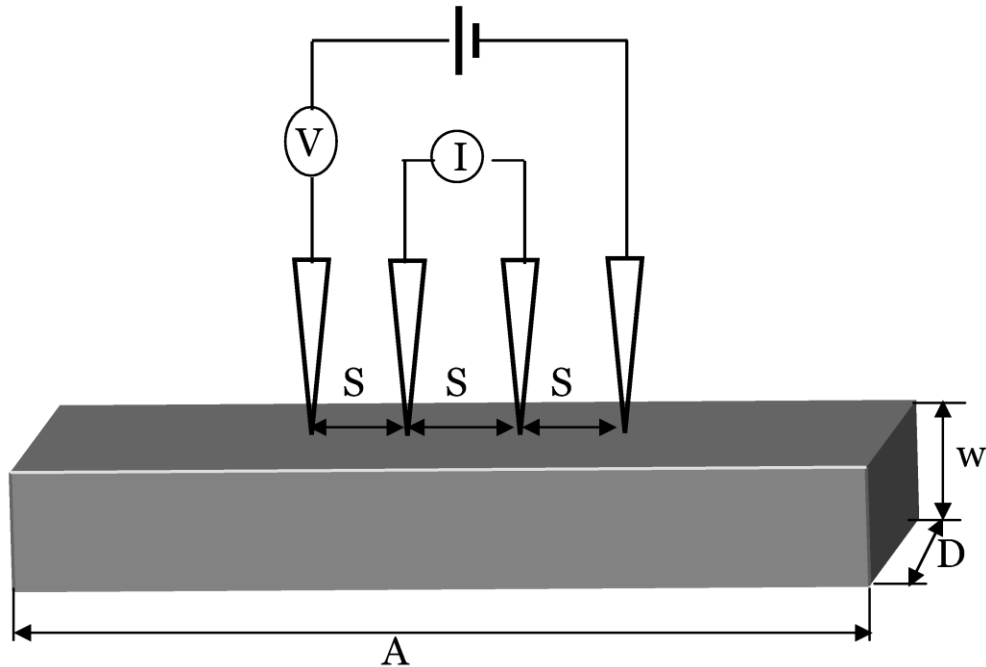


Figure 2.2. Schematic of a four-point probe technique

The four-point probe method has been extensively used to characterize electrical properties of metals [24], semiconductors [2,3,25,26], thin films [27-29], conducting polymer composites [30,31] etc under various temperatures and

vacuum conditions. By using separate electrodes for current injection and for the determination of the electric potential, the contact resistance between the metal electrodes and the material will not show up in the measured results. Because the contact resistance can be large and can strongly depend on the condition and materials of the electrodes, it is easier to interpret the data measured by the four-point probe technique than results obtained by two-point probe technique. The four-point probe method is an absolute measurement without a need for calibrated standard.

Although the four-point probe technique is simple to perform, it is sometimes difficult to analyze the experimental data. The difficulties arise mainly from geometrical considerations, with correction factors being necessary for non-infinite specimens. The probe samples a relatively large volume of the sample, thus preventing high-resolution measurements. In general, the resolution in four-point probe method depends on the spacing between the electrodes. The average spacing between the electrodes in conventional four point probe methods is between 0.5 to 1.5 mm. The spacing varies for different sample diameter and thickness. The four-point probe method is useful when the electrical conductivity of the sample is homogeneous in a volume that is large compared to the spacing of the probes, but it is ineffective in the presence of homogeneity over smaller spacing. For systems that exhibit short-range conductivity variations, the electrode spacing has to be reduced. However, the positioning of the electrodes becomes more difficult with the decrease of electrode spacing and increases the likelihood of positional errors in

measurements. As with two-point probe method, good ohmic contact and contamination-free samples are required for accurate measurements in four-point probe method. Finally, four point probe techniques provide average values of the electrical resistivity of the bulk material.

2.3.3. Electromagnetic Induction Methods

DC methods provide an accurate and direct way of measuring the electrical resistivity with high precision. However, they suffer from the thermoelectric and drift effects which introduce errors and are troublesome to eliminate. Also, AC methods are preferred to DC methods for resistance measurements when very small heat dissipation in the specimens is desirable or when the actual specimen resistance itself is extremely small. Alternating current potential drop (ACPD) technique [32] is a four-point probe technique with alternating currents passed through the probes. The principle of this technique is similar to that of DC four-point probe method except that AC currents are passed through the sample in ACPD technique. An advantage of the ACPD technique is that a lower measurement current can be applied in order to achieve a given sensitivity [33]. This reduces the risk of heating of the sample and any associated changes in the electrical conductivity. The ACPD technique suffers from the same disadvantages as the DC four-point probe technique. The dominant factor limiting the range of accurate and reproducible measurements of electrical

resistivity is the ability to establish proper electrical contact to the material in two point and four-point probe techniques. Surface preparation and subsequent contamination affect the electrical properties of a contact. Thus, a contactless technique of measuring electrical resistivity would eliminate these problems and also possesses many inherent advantages. The non-contact methods of AC measurement techniques use eddy currents to measure the electrical conductivity. The techniques are based on the principle of electromagnetic induction.

2.3.3.1. Eddy currents

Hans Christian Oersted discovered that a current-carrying conductor produces a magnetic field around it. This discovery provided the link between the phenomena of electricity and magnetism which had been previously regarded as unrelated. After Oersted discovered the magnetic effects of currents, many experiments were devised to detect the inverse effect, i.e. the flow of electric current due to a magnetic field, without success, mainly because a steady current flow was looked for. In 1831 Faraday found that a transient flow of current occurred in a close circuit when the magnetic flux through the circuit was changed. This is known as electromagnetic induction.

The process of generating current in a conductor by placing the conductor in a changing magnetic field is called induction. This is called induction because there is no physical connection between the conductor and the source of the magnetic field. The current is said to be induced in the conductor by the magnetic

field. When current is induced in a conductor, the induced current often flows in small circles that are strongest at the surface and penetrate a short distance into the material. These current flow patterns resemble eddies in a stream. Because of this presumed resemblance, the electrical currents are named eddy currents. Eddy currents are created when a moving conductor experiences changes in the magnetic field generated by a stationary object, as well as when a stationary conductor encounters a varying magnetic field. The generation of eddy currents in a conductor due to the excitation of a coil near it is shown schematically in Figure 2.3.

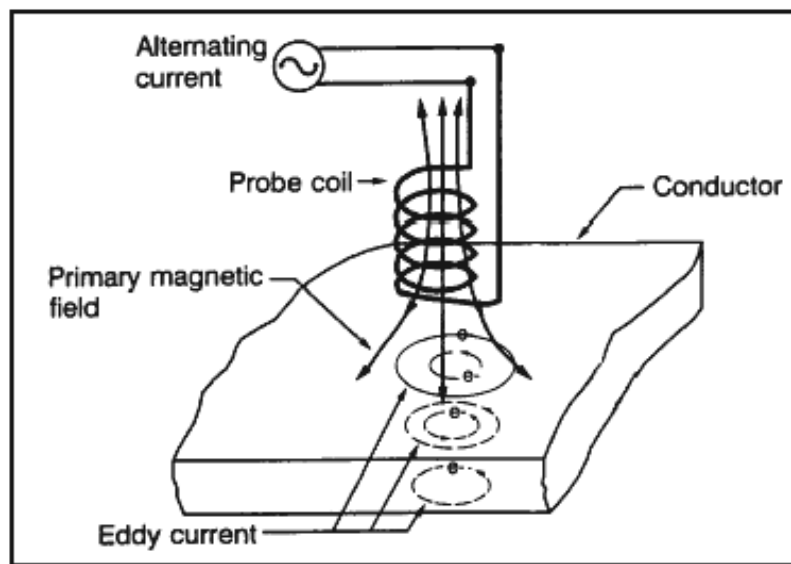


Figure 2.3. Generation of eddy currents in a conductor

Eddy currents are closed loops of induced current circulating in planes perpendicular to the magnetic flux. Eddy currents concentrate near the surface adjacent to an excitation source of the field and their strength decreases with distance from the source. Eddy current density decreases exponentially with depth. This phenomenon is known as the skin effect. The skin effect arises when

the eddy currents flowing in the test object at any depth produce magnetic fields which oppose the primary field, thus reducing the net magnetic flux and causing a decrease in current flow as the depth increases. Alternatively, eddy currents near the surface can be viewed as shielding the primary magnetic field, thereby weakening the magnetic field at greater depths and reducing induced currents. The depth that eddy currents penetrate into a material is affected by the frequency of the excitation current and the electrical conductivity and magnetic permeability of the specimen. The depth, at which eddy current density has decreased to $1/e$, or about 37% of the surface density, is called the standard depth of penetration. The depth of penetration of eddy currents inside a conductor is mathematically given by the expression

$$\delta = \sqrt{\frac{2}{\omega\sigma\mu}} \quad (2.10)$$

where ω is the frequency of the excitation, σ is the conductivity of the conductor and μ is the permeability of the conductor. It can be seen from the above equation that depth of penetration decreases with increasing frequency and conductivity and magnetic permeability. The effect of skin effect in a conductor is shown in Figure 2.4. At very high frequencies, eddy currents only penetrate a small distance into the surface of the conductor.

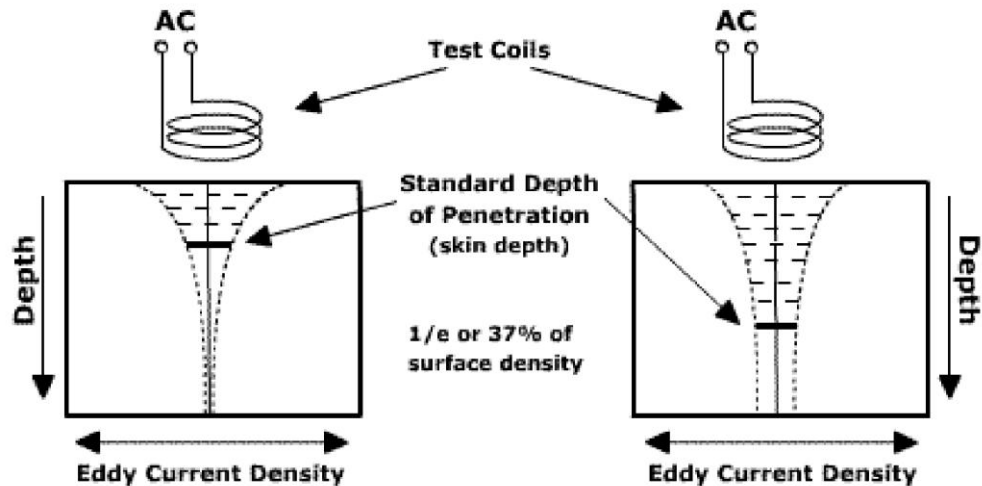


Figure 2.4. Skin effect in a conductor due to eddy currents

In eddy current methods, an electric field is induced in the conductor by a time-varying magnetic field source. By detecting the flow of the resulting eddy currents in the sample, the electrical resistivity can be determined. Various techniques to determine the flow of eddy currents can be used: a) measuring the change in the Q of a radio frequency solenoid [34]; b) measuring the change in terminal impedance of a coil [35] and c) measuring the change of phase of the secondary voltage of a transformer [36,37]. The most common method of detecting the eddy current flow in the conductor is the measurement of impedance changes in the coil. When the coil is excited by an AC signal, an oscillating magnetic field is generated around the coil. The time-varying magnetic field induces eddy currents in the conductor. The eddy currents in the conductor produce a magnetic field opposing the primary magnetic field. The opposing magnetic field produces changes in the impedance of the coil. Analysis of the electrical impedance of the coil provides information about the electrical conductivity of the metal. In the eddy current method of measuring electrical

conductivity, skin effect has to be taken into consideration. The skin effect limits the penetration depth of the eddy currents into the material. Since the penetration depth of the eddy current fields rapidly decreases with increasing frequency, care must be taken in selecting the frequency of the excitation of the magnetic field. Usually radio frequencies (100 kHz) are used to generate eddy currents in the samples to avoid skin effect problems.

2.3.3.2. Measurement of electrical properties using eddy currents

Over the past few decades, eddy current methods have been extensively used to measure the electrical properties of the materials. Zimmerman [35] developed a method in which the resistance and inductance of a coil are first measured by a suitable AC inductance bridge such as a Maxwell bridge. The specimen is then introduced into the field of the coil. The resistance and the inductance of the coil change due to the eddy currents induced in the specimen. The change in the impedance is measured from which the conductivity is measured. For specimens of simple geometry, relations have been obtained theoretically from which the electrical resistivity can be calculated. Audio frequencies must be used in order to ensure that the currents flow through the entire volume of the conductor and are not just limited to regions near the surface. A more convenient approach with wider applications has been developed by Bean *et al.* [38]. The methodology involves applying a current to a coil within which the specimen is placed for a time long enough to cause eddy current flow in the specimen, and then stop the current. As the flux emerges, the

voltage across a small pickup coil is observed on an oscilloscope, which is later used to calculate resistivity. Absolute resistivities can be calculated for specimens of regular cross-section. In 1961 Ogawa [39] reported a method for non-contact measurement of electrical conductivity and dielectric constants. A sample is placed in a rotating electric field, which exerts a torque on the sample. The torque is measured by the torsion of the thread which supports the sample. Later Khotkevich and Zabara [40] and Chaberski [41] also reported similar rotating magnetic field methods to characterize electrical resistivity of a spherical and cylindrical specimen. The resistivity is determined by measuring the moment of the forces acting on the sample due to induced eddy currents when placed in a rotating field. Hendrickson and Philbrook [42] developed an extremely sensitive method by adopting an alternating rotation. They enhanced the sensitivity by tuning the frequency of the alternating rotation to the resonant frequency of the mechanical system. These methods are based on a rotating electrical or magnetic field and hence the electrical or magnetic properties which can be measured are an average over different direction in a certain plane of the sample. A review of the many interesting contactless measurement techniques can be found in the paper written by Delaney and Pippard [43]. They reported five different methods for characterizing conductivity (resistivity), with or without a steady applied magnetic field. They are:

- (i) Low frequency AC induction, where the sample modifies the inductance of a coil
- (ii) Decay of eddy currents after a small, applied field is suddenly removed

(iii) Hard helicons

(iv) Soft helicons and

(v) Torque on a sample in a rotating magnetic field

In the decay method, the resistivity is calculated from the decay of a transient induced in the sample by switching a small DC magnetic field on or off. In the AC method the resistivity is calculated from the apparent susceptibility in an alternating field of constant frequency. Wejgaard and Tomar [44] suggested a simplified version of the AC method based on a phase angle measurement. In their method, they have used a phasemeter, a coil system and an electronic compensation circuit in addition to a standard oscillator and oscilloscope. Rajotte [45] developed a methodology to derive electrical conductivity from the measurement of the voltage induced in a magnetic probe at the surface of a metallic specimen. The specimen is subjected to an AC magnetic field by means of an inductive coil. One limitation of this technique is that the frequency of the excitation should be high enough such that the skin depth is not more than one-fifth of the sample thickness. Crowley and Rabson [46] developed a contactless electrical resistivity measurement system using induced currents in the sample. A primary coil is separated axially from a secondary coil and a sample is inserted between them. The voltage induced in the secondary coil is measured and related to the electrical resistivity by means of an equation relating the induced voltage to geometry of the coil, sample, frequency and resistivity. Flanders and Shtrikman [47] used a rotating sample magnetometer to do contactless conductivity measurements. In their method, the sample, in the shape of a rod,

rotates about an axis perpendicular to the magnetic field. The conductivity is measured through the voltage induced in coils by the sample in the magnetic field. Kraftmakher [48] determined the effective magnetic susceptibility of a cylindrical conductor in an axial ac magnetic field. The effective magnetic susceptibility of a conductor is an important parameter in determining electrical resistivity. The magnetic susceptibility depends on eddy currents in a sample and has no relation to usual magnetic properties. It depends on the frequency of the ac magnetic field, electrical resistivity and the shape of the sample. Pellicer-Porres *et al.* [49] measured susceptibility of metallic cylinders by studying the forces associated with the eddy currents. By relating the forces and susceptibility they determined conductivity of the cylinders. Iniguez *et al.* [50] measured conductivity of metallic tubes by measuring the screening of the magnetic field within the tube positioned inside a solenoid excited at low frequency. The low frequency was chosen so as to neglect the skin effect.

Eddy currents are also used to determine the electrical resistivity of highly anisotropic materials. Neighbor [51] extended the eddy current method of measuring electrical resistivity to anisotropic materials. Zeller *et al.* [52] used eddy currents to characterize electrical resistivity in anisotropic materials. Isono and Kotani [53] proposed a non-contact method which makes use of conversion of the energy of a mechanical vibration into Joule heat when an electrical conductor is forced to vibrate in a magnetic field. Using this method, electrical conductivity along any direction can be measured. This is useful if electrical conductivity of highly anisotropic samples needs to be measured. For

measurements of low resistivity of very pure samples, voltage decay at very long time is required. Therefore, in order to measure low resistivity of very pure samples, Riherd and Schreiber [54] proposed a modification to the conventional eddy current technique, such that shorter observation times are sufficient for accurate measurement of electrical resistivity of very pure metals.

The traditional method of measuring electrical resistivity of semiconductors is the four-probe method described previously. This technique is suitable for relatively low resistivity material but exhibits certain difficulties with high resistivity samples. The origin of the difficulties lies in the blocking nature of the metal-semiconductor pressure contacts used in the technique. Relatively higher pressures are applied on the contacts in order to minimize electrical problems and this can produce structural damage in the semiconductor sample. To avoid these problems non-contact resistivity measurement methods using eddy currents have been developed. Miyamoto and Nishizawa [55] used capacitive coupling to probe bulk charge carriers in semiconductors. Capacitive coupling eliminates the need for an ohmic contact, since at high frequencies, the capacitance offers a low impedance path for probing the resistivity of the bulk material. In another approach, Miller *et al.* [56] used inductive coupling to measure the electrical conductivity of semiconductor sample. In this method, the semiconductor sample is coupled to an amplitude-stabilized marginal oscillator. The sample absorbs power in the alternating magnetic field, which is proportional to the electrical conductivity. The magnitude of the power absorption is used to determine the conductivity. The inductive coupling has also been used to study

the minority carrier and majority carrier properties of semiconductors [57]. Wheeler *et al.* [58] used radio frequency AC signal to measure the bulk resistivity of II-VI compound semiconductors. They employed reflection measurements from a vector network analyzer to extract the resistivity of a semiconductor wafer.

2.3.3.3. Measurement of magnetic properties using eddy currents

Eddy current methods are used not only for electrical resistivity measurements, but also can be used to characterize magnetic properties of materials. Chaberski [41] measured the magnetic permeability of a ferromagnetic material by measuring the torque experienced by the sample when placed in rotating magnetic field. The measured torque is a function of the magnetic permeability. The magnetic susceptibility is then calculated using the torque and other factors such as the strength of the magnetic field, frequency of the field, sample geometry and density of the sample. Following a similar approach, Hendrickson and Philbrook [42] used eddy currents measure the magnetic susceptibility. The method consists of measuring the torque on a sample suspended in a uniform rotating magnetic field. The torque of the sample is measured as a function of the magnetic field plotted. The ratio of the angular deflection to the square of the magnetic field is proportional to the magnetic susceptibility. Using this technique magnetic susceptibility as low as 10^{-12} was measured. Tsukada and Kiwa [59] developed a magnetic property imaging system for detecting and analyzing three-dimensional magnetic field components. By analyzing the vector component maps the differences in

magnetic properties such as permeability, and residual magnetism were differentiated.

2.3.3.4. Eddy current NDE

One of the important applications of eddy currents is in the nondestructive evaluation of materials [5]. In eddy current inspection, a coil is located as near as possible to the material being tested and is excited by an AC signal at a given frequency. The time-varying currents induce a magnetic field near the coil and they in turn induce eddy currents in the material. The induced eddy currents produce a secondary magnetic field opposing the primary magnetic field of the coil. It is well known that the presence of defects, discontinuities modify the flow of currents in the material. If the coil or probe is scanned over a defect in the material, the impedance of the coil is modified. Thus, by monitoring the impedance changes in the coil, the presence of a defect in the material is detected.

The main components of an eddy current testing system are: ac magnetic field source, probe to detect the eddy current flux density in the conductor and electronics to convert the resulting signals into an interpretable form. In its simplest form, the eddy current probe consists of a single coil. In most cases, the source and the probe are the same. Figure 2.5 shows a typical arrangement of eddy current test probe and test material. The probe coil is placed adjacent to the flat surface of an electrically conductive material. The coil winding consists of several turns of wire, usually copper, wrapped around a circular coil. The turns of

the coil lie parallel to the surface of the test material. The axis of the coil is perpendicular to the surface of the test material. The associated magnetic field H induces the flow of electric currents, i.e. eddy currents, which follow circular paths in planes perpendicular to the direction of H . The coil and the metal sample form the primary and the secondary components of a transformer respectively, and the impedance of the coil is consequently affected by the behavior of the eddy currents. Neglecting its ohmic resistance, the impedance, at a frequency ω is purely inductive and has a value $Z_0 = j\omega L_0$, when completely removed from the test object and any other electrical conducting material. When the coil is located in the testing position, the value of the impedance changes at the same frequency to $Z = R + j\omega L$. This results in the change of the characteristic impedance of the test coil. The inductance changes from L_0 to L , and a resistive component R is introduced. The corresponding phase changes in the relevant electrical and magnetic vectors, \mathbf{B} , \mathbf{H} and \mathbf{J} are responsible for introducing the component R of the impedance. The impedance of the coil, and particularly the change in the impedance, is represented on an impedance plane which simultaneously shows the reactance and resistance of the coil. This is usually represented on the screen of an oscilloscope by displaying the real and imaginary parts of the impedance. The eddy current density around a defect would be different around the defect when compared to the current density without defect. The presence of a defect will interrupt or reduce the eddy current flow, thus decreasing the loading on the coil and increasing its effective

impedance. Thus, it is possible to detect defects in the material using eddy current testing.

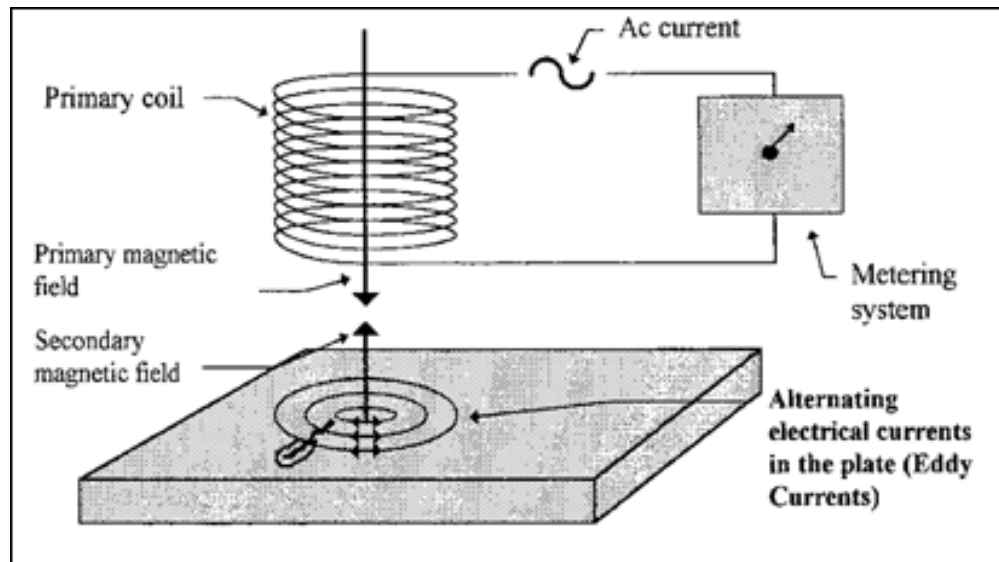


Figure 2.5. Schematic of eddy current inspection by a surface coil

The most important feature in eddy current testing is the way in which the eddy currents are induced and detected in the sample. This is dependent on the design of the probe, which can contain either one or more coils. A coil consists of a length of a cylindrical tube or rod, called a former. The former provides sufficient rigidity in the coil. The wire is usually made from copper to avoid magnetic hysteresis effects. The coil is usually embedded at the end of a rigid cylinder in which the coil itself is protected from damage, usually by a polymeric filler, which keeps the coil rigid. Eddy current probes are available in wide variety of sizes and shapes. The simplest type of probe is the single-coil probe which is most commonly used probe. These probes are also referred to as absolute probes. In some cases, a probe consisting of two coils is also used. In this configuration, the coils are arranged in a transformer fashion. The primary coil

induces eddy currents in the test object and the secondary coils acts as a detector. These probes enhance the signal-to-noise ratio and are very useful when detecting internal defects. These probes are also known as driver/pickup probes. The advantage of these probes is that the driver and pickup coils can be optimized separately. Two types of probes can be used: through-transmission probe and reflection probe.

The eddy current probes can be used in different configurations depending on the size and shape of the test material. Some of the commonly used configurations of the probe in eddy current testing are surface probes, encircling probes, and bobbin probes. Figure 2.5 shows the generation of eddy currents using a surface probe near the test material. This coil configuration is also known as pancake coil. It is useful in detecting flaws that are oriented perpendicular to the test surface. Encircling probes are usually used to inspect cylindrical shaped specimens. In this configuration, the coil is wound around the test specimen. These probes are commonly used to inspect solid bars. Bobbin probes are used to inspect hollow tubes and pipes.

Eddy current inspection is widely used in the nondestructive evaluation of materials in different industries. They are most often used in the testing of turbine blades and bolt holes in aircraft [60,61], nuclear reactor cooling tubes [62,63] and underwater structures and pipelines [64-67]. The eddy current method is also extensively used as a means of sizing surface cracks in welds. The simplest way to detect defects is to scan the test object with a single-coil probe and to look for abrupt changes in output signals resulting from sharp discontinuities in structure.

The presence of a small surface crack gives rise to a greater change in amplitude than in phase. For large surface cracks, however, an increase in size produces more change in phase than in amplitude. However, the maximum crack depth which can be measured with eddy currents is limited by the penetration depth. Various types of probes are used to detect cracks and other flaws depending on the sample geometry, material type and the type of flaw in the material [68].

In addition to the detection of defects in materials, eddy current inspection methods can be used for various other applications. Some of them include measuring electrical conductivity, determining magnetic permeability, evaluating dimensions etc. The measurement of electrical conductivity of a non-ferromagnetic metal is fairly straightforward both for obtaining absolute values for homogeneous materials and relative values for objects containing structural variations, e.g. localized heat treatment. The principle of measuring conductivity is based on the impedance variations with electrical conductivity at a fixed frequency with constant lift-off. The meter is calibrated using samples having known values of the electrical conductivity and the conductivity of the test material is given in terms of the conductivity of the standard in MSm^{-1} or %IACS. The eddy currents generated in the material depend on the structure and properties of material. Therefore, eddy current techniques can be used to determine material properties indirectly. The electrical conductivity can be related to heat treatment, grain size, alloy composition, and strength of the material.

Magnetic permeabilities are normally measured by using purely magnetic methods but the eddy current method can also be used to measure the magnetic permeability. In eddy current testing, the magnetic permeability of the material in the vicinity of the coil is affected by the strength of the exciting current. The magnetic permeability of ferromagnetic metals in the form of thin wedges can be measured by measuring the depth of penetration [69]. The standard sample with known conductivity and a ferromagnetic test sample are scanned from the thin edge with the same surface probe excited at the same input level and frequency. The output signals are observed during scanning. The measured penetration depths are related to the magnetic permeability.

Eddy current techniques are also used for the determination of various dimensions of the samples. They include cross sectional dimensions of cylindrical tubes and rods, thicknesses of thin metal plates and foils and of metallic coatings on metallic and non-metallic substrates and thicknesses of non-metallic coatings on metallic substrates. Dimensions of cylindrical tubes and rods are measured with either encircling probes or internal axial coils [70]. An important application of measurement of cross sectional dimensions of tubes is the detection and assessment of both external and internal corrosion. The thickness of a metal plate or foil on a non-metallic substrate is measured either with through-transmission method or with a surface-scanning reflection probe. The thickness of a thin layer of metal on a metallic substrate is measured using a single coil probe or a reflection probe. The requirement in this case is that the two metals have widely differing electrical conductivities. Thicknesses of non-

metallic coatings on metallic substrates are determined from the effect of lift-off on impedance. This method is widely used to measure thicknesses of paint and plastic coatings.

Eddy current testing system can be automated using scanning systems to improve the quality of the measurements. The automation involves using of a computer to locate and monitor the positions of the probes and to process the data collected by the probes. The operator variables such as wobble of the probe are greatly reduced due to automated scanning system.

2.3.3.5. Eddy current imaging

Conventional eddy current testing provides qualitative information regarding the presence or absence of cracks. However, the eddy current signal also contains quantitative information about the size and shape of the flaw in the material [71]. Therefore, imaging would provide quantitative information about the flaw in the material and also is a convenient way of presenting the eddy current signals in a form that can be interpreted visually. This technique is called eddy current imaging [72]. A two-dimensional eddy current image of the test surface can be obtained by attaching the probe coil to a computer controlled XY scanner and raster scanning the probe across the surface. The data is displayed as the plot of signal strength or phase angle shift as a function of position, similar to ultrasonic C –scans. Some of the first eddy current images were reported by McCary *et al.* [73]. They used a probe with a mean diameter of 5mm, a standard eddy current instrument, XY scanner and a microcomputer to collect the data and

control the scanning. Since then, eddy current imaging has been used extensively for the characterization of electrical and magnetic properties of materials [74-76]. Blodgett and Nagy [74] studied anisotropic grain noise in noncubic polycrystalline titanium alloys using eddy current imaging. Two-dimensional mapping of magnetic field fluctuations caused by local induced current flow disturbances due to the presence of any cracks or structural damage is obtained by scanning probe or scanning sample stage [77-79]. Tsukada and Kiwa [80] developed a magnetic property imaging system for detecting and analyzing three-dimensional magnetic field components. Time sequential normal and tangential maps of the magnetic field distribution were obtained. The spatial resolution in eddy current imaging is determined by the size of the coil being used. In conventional eddy current imaging systems, coil sizes range from few hundred microns to several mm depending on the size of the sample being tested. Therefore, the best spatial resolution one can obtain using eddy current imaging is of the order of few hundred microns.

There are many advantages of induction methods over conventional DC or AC four probe methods. The primary advantage is that it is completely non-contact technique; therefore, contact resistance is not a problem. Also, careful surface preparation is not necessary. Since no wires need to be attached to the sample, there is no possibility of contamination. The eddy current methods allow resistivity measurements on samples of various sizes and complex shapes. Also, eddy current methods are sensitive to small changes in the electrical and magnetic properties due to the localized nature of the eddy currents. Thus, these

methods can be used to detect very small variations in electrical conductivity [46,81]. Consequently, eddy current methods are sensitive to small cracks and defects. However, eddy current testing has some limitations too. Eddy current testing method is limited to electrically conductive materials or materials with electrically conductive components such as carbon fiber reinforced composites. The eddy current methods are essentially comparison methods and do not always give resistivity information directly. Therefore, standards for calibration have to be developed to measure the resistivity of a test material in terms of a standard. Also, flaws such as delaminations that lie parallel to the probe coil and probe scan direction are undetectable. The major limitation in eddy current testing and imaging is the spatial resolution of the technique. In eddy current imaging, if a flaw is much larger than the size of the eddy current probe, the eddy current image of the flaw will be well defined by the unprocessed data. However, if the flaw is smaller than the probe size, then the image would show the probe fields rather than fields of the flaw. Thus, the spatial resolution of eddy current imaging system depends on the size of the coils being used [74-75]. In a conventional eddy current testing, the coil diameter is in the range of few hundreds of microns. Thus, the resolution is of the order of hundreds of microns. The depth of penetration of the eddy currents is limited by the skin effect. Therefore, detection of subsurface flaws in very thick samples is not possible.

2.4. Microscale Electrical and Magnetic Property Measurement Techniques

The DC techniques like two-point probe and four-point probe techniques provide an easy and direct way of measuring electrical conductivity. However, these techniques provide an average conductivity value of the bulk material. The AC techniques, on the other hand, provide non-contact, local measurements of electrical conductivity, but the spatial resolution is hundreds of microns. While these techniques may be sufficient for bulk materials, they are not enough for the characterization of material properties on micro- and nanoscales. Therefore, new techniques were developed to characterize material properties on micro- and nanoscales. Some of these techniques are described below.

2.4.1. Eddy Current Microscopy

It was mentioned previously that the spatial resolution in eddy current imaging system depends on the size of the probe and is low if compared with standard microscopy. In most cases, the transverse dimensions of many flaws are equal to or smaller than the dimensions of manufacturable probes. Therefore, in order to detect smaller cracks, the resolution needs to be improved. One way of achieving high resolution is to employ smaller coils for imaging. The ability to detect and measure ultrasounds using mechanical oscillators has enabled the further development of eddy current microscopy techniques with better

spatial resolution than the conventional eddy current techniques. Palmer *et al.* [82] developed a scanning eddy current dynamometer to probe thin metallic films. The dynamometer was based on the measurement of force generated by a magnetic tip oscillating in close proximity to a conducting thin film attached to a mechanical oscillator. They have used the technique to detect cracks as large as 100 μm . A scanning magnetic flux microscope based on a superconducting quantum interference device (SQUID) to image eddy currents in patterned thin films was developed by Black *et al.* [83]. In their method, a small SQUID was used directly as a magnetic sensor. The SQUID was operated close to the sample surface and both the sample and the SQUID was place in liquid nitrogen. Using this technique they were able to image magnetic fields with a spatial resolution of 60 μm . The advantage of this technique is that it can be extended to imaging samples at room temperatures also. Karpen *et al.* [84] reported an eddy current microscopy imaging system capable of resolving defects with a 50 μm spatial resolution. Cleland and Roukes [85] developed a nanometer-scale mechanical electrometer to detect charge in semiconductor samples. Marchand *et al.* [86] developed giant magneto-resistance (GMR) based eddy current probes for high-resolution eddy current imaging. Using the GMR eddy current probes, they were able to detect flaws as small as 50 μm . The lateral variations in electrical resistivity of semi-conducting GaAs substrates were measured using contactless capacitive mapping technique [87]. The technique is also capable of imaging mesoscopic fluctuations in resistivity with a spatial resolution of less than 100 μm . Later, Green *et al.* [88] developed a high-resolution noncontact scanning

impedance imaging capable of achieving a spatial resolution of about 30 μm . Myungsik Kim *et al.* [89] developed a near-field scanning millimeter-wave microscope (NSMM) for surface imaging of electrical properties with spatial resolution better than 1 μm . The probe used in their experiments is a standard waveguide resonator coupled to a conventional metallic tip and operated at a frequency of 60 GHz. They observed millimeter-wave near-field images of patterned metal Cr films and $\text{YBa}_2\text{Cu}_3\text{O}_y$ thin films with a spatial resolution better than 1 μm . They also mapped the sheet resistance and electrical properties of surfaces by measuring the amplitude of transmission power and the resonant frequency shift of the resonator while scanning the surface.

2.4.2. Scanning Tunneling Microscopy

Any tool to successfully characterize a nanoscale system requires the capability of direct imaging coupled with a nanometer scale characterization capability. High resolution microscopic techniques, such as scanning electron microscopy (SEM), transmission electron microscopy (TEM), scanning tunneling microscopy (STM) and atomic force microscopy (AFM) can be used to obtain direct images of the material surface at the nanometer scale. Other surface analytical techniques, such as X-ray photoemission spectroscopy (XPS), ultraviolet photoemission spectroscopy (UPS), X-ray diffraction and low-energy electron diffraction (LEED) can only provide spatially averaged information.

Among these techniques, however, only STM, AFM, and STM-based spectroscopic techniques can provide a proper experimental tool for both imaging and characterization. These techniques have the characteristic that their resolution is not determined by the wavelength that is used for the interaction as in conventional microscopy but rather by the size of the interacting probe scanned over the sample surface. Thus the resolution that is achieved using these techniques is far superior to the wavelengths involved.

The invention of scanning tunneling microscope (STM) by Binnig *et al.* [90] in 1982 opened up the possibility of imaging material surfaces with spatial resolution much superior to the conventional microscopy techniques. The STM is the first instrument capable of directly obtaining three-dimensional images of solid surfaces with atomic resolution. STM utilizes tunneling current between a sharp conducting probe and the surface to construct an image of surface topography. In the STM, a fine metallic tip is brought within a nanometer from a conducting surface while a voltage is applied between them. At such a small separation distance, electrons from the tip can tunnel from the atom at the very end of the tip to the nearest atom on the sample surface and generate a current. This current is compared with a reference current and the error signal so generated is applied to a z-piezo, which moves the tip up or down in order to maintain a constant tunnel current as the tip is raster-scanned across the sample to record an image. Binnig *et al.* [90,91] used the electron tunneling in vacuum to develop scanning tunneling microscope. The lateral scanning allows a lateral

resolution of less than 1 nm and a vertical resolution of less than 0.1 nm, which is sufficient to define the position of single atoms.

Different applications of the STM in wide variety of research fields ranging from material science to biology can be widely found in literature [92-96]. While the STM was primarily developed as a method for topographic imaging of surfaces, several extensions of the STM have been developed to measure electrical and optical properties. One modification of the STM is the scanning tunneling potentiometer [97]. In this method, a bridge method is used to measure the spatial variations in potential across the sample as the tip is controlled and scanned to track the surface topography. An ac voltage is applied between the tip and the sample which generates an ac tunnel current. The amplitude of this current is then used to control the tip-sample spacing. This technique is useful for measuring nanoscale potential variations in micro and nanoscale devices such as Schottky barriers, *pn* junctions and heterostructures. Spin-polarized electron tunneling from a ferromagnetic sample to a nonmagnetic STM tip can be observed using spin-polarized scanning tunneling microscopy (SP-STM) [98]. This technique offers the capability of measuring magnetization at the atomic scale. The study of buried interfaces which are located far below the surface can be done by modifying the STM into a ballistic electron emission microscope (BEEM) [99,100]. Metal-semiconductor interfaces have been widely studied by this technique since its invention. BEEM is a three terminal device where the STM tip acts as an electron emitter. An STM tip is positioned close to the surface of a metal-semiconductor heterojunction. Electron tunneling from the tip to the

metal base electrode leads to injection of ballistic electrons into the base electrode which is typically about 100 Å thick. Since the injected ballistic electrons typically have attenuation lengths greater than 100 Å, they may propagate through the metal layer and thus allowing probing of the subsurface metal-semiconductor interface. By varying the voltage between tip and base, the energy distribution of the hot carriers can be controlled, and a spectroscopy of interface carrier transport may be performed. The BEEM method allows characterization of interface properties with nanometer spatial resolution and enables an energy spectroscopy of carrier transport. The technique is very sensitive to the carrier scattering at metal-semiconductor interfaces at high resolution. STM was also used to characterize the electronic properties of metallic nanoclusters deposited on semiconductor materials [101]. The STM is also used to implement four-point probe technique with nanoscale resolution [102].

2.4.3. Atomic Force Microscopy

Even though STM is capable of achieving atomic resolution, it can only be used on electrical conductors. This limitation has led to the invention of atomic force microscope (AFM) by Binnig and his co-workers [11] in 1986. The principle of AFM is similar to that of STM except that the tunneling tip is replaced by a force sensor. Since no electron tunneling is involved, AFM can be used on wide

range of materials including insulators. The details of AFM instrumentation and a detailed working principle of the AFM will be discussed in the next chapter. However, for the sake of continuity, a brief description of the principle of AFM is provided here. A sharp probe attached a flexible cantilever beam is raster scanned across the sample surface. The force interaction between the sample and the probe, as the probe approaches the sample surface causes the cantilever to deflect. These deflections are sensed by an optical detection mechanism. A topographic map of the sample surface is obtained by keeping the force constant while scanning the tip relative to the sample. A lateral resolution of about 0.2 nm and a vertical resolution of less than 0.1 nm have been achieved with AFM. Since the invention of AFM, it has evolved into one of the most powerful experimental tools for surface characterization of materials with nanometer scale resolution.

Although the initial applications focused on near-atomic resolution surface topography measurements, the AFM has also been used extensively to measure surface physical properties. Several new microscopic techniques, based on AFM have been developed to measure properties such as elastic modulus, magnetic, electrical and thermal properties in the nanometer regime. The families of instruments based on STM and AFM are commonly known as scanning probe microscopes (SPM). Some examples of scanning probe microscopes are ultrasonic force microscopy [103] for local elastic stiffness mapping, magnetic force microscopy [104] for magnetic property imaging, scanning Kelvin probe microscopy [105] for surface potential imaging, scanning thermal microscopy

[106] for local thermal conductivity mapping, electrostatic force microscopy [12] for electrical property mapping, scanning near-field optical microscopy [107] for optical properties. All scanning probe instruments are based on the same principle, i.e., scanning a local probe in near-field across the surface of a sample. While scanning is well established in microscopy, consequent near-field operation is a relatively novel approach in microscopy. The instruments differ only in the selective detection of different sample-probe interactions among the many kinds of interactions between the probe and the sample surface. This is accomplished by employing an appropriate probe for the particular tip-sample interaction. For example, if an electrical potential difference is externally applied, electrostatic interactions can be probed by using a conductive probe. Similarly, if a magnetic probe is used to scan a ferromagnetic sample, magnetostatic interactions can be probed. All scanning probe techniques are usually operated in the near-field regime of the interaction. The near-field imaging capability of AFM was exploited by many researchers to develop high-resolution material property imaging techniques based on AFM. The unique combination of nanoscale resolution, previously the domain of electron microscopy and broad applicability has led to the proliferation of SPM into virtually all areas of nanometer-scale science and technology.

2.4.3.1. Characterization of electric and dielectric properties using AFM

The general principle of characterizing electrical properties using AFM is to apply a bias voltage between a conducting tip and the sample surface and measuring the resulting electrical interactions at each point while scanning the surface. Some of the interactions are electrostatic forces, electric currents, resistance and capacitance. Various techniques are developed based on the measuring these interactions to study the electrical and dielectric properties of materials. Some of these techniques are briefly described here.

2.4.3.1.1. Electrostatic force microscopy

Electrostatic force microscopy (EFM) is an analytical AFM based technique capable of mapping the local electrical properties of materials by monitoring the attractive and repulsive interactions between a sharp conductive tip and the sample. In this technique, a bias voltage is applied between the sample and the conducting tip while the tip scans the surface. The resulting electrostatic forces and its local variations change the oscillation amplitude and phase of the AFM cantilever which are detected to create EFM images. Usually, stiffer single crystal silicon cantilevers are used. EFM can be used on metals, insulators, and ferroelectric materials. Martin *et al.* [12] modified an AFM to perform electrostatic force imaging and potentiometry of conductors and insulators. They measured tip-sample capacitance by applying an ac voltage at a frequency greater than the resonant frequency of the tip, and detecting the changes in the oscillations of the cantilever due to local variations in capacitance. Stern *et al.* [108] used an AFM to both deposit and image localized charge on

insulating surfaces with high lateral resolution. In their technique, a nickel tip electrochemically etched to a cantilever is mounted on a piezoelectric bimorph and oscillated at its resonant frequency. The changes in the resonance during scanning are detected by a lock-in amplifier and an optical interferometer. A bias voltage was applied between the tip and the sample to charge the sample surface. Using this methodology, they characterized samples of PMMA, single crystal sapphire, freshly cleaved mica and fused quartz. Later, Terris *et al.* [109] reported development of an electrostatic force microscopy with a lateral resolution of 0.2 μm . In their technique, an ac bias voltage was applied between the tip and an electrode behind the sample. The ac voltage induces an oscillating charge on the electrode. An equal and opposite charge is induced on the tip. The electrostatic force is then calculated by treating the tip-surface force as due to point charges and the tip-electrode force as from a capacitor. A sample of PMMA was characterized using this technique. Electrostatic force imaging using a two-pass scanning is also reported in literature [110,111]. In this method, the measurements are taken in two passes of the scan. In the first pass, the topography is obtained by intermittent contact of the tip with the sample surface. The tip is then lifted to a predetermined height and a bias voltage is applied between the tip and the sample. The image is obtained at a constant separation between the biased tip and the sample surface. Variations in phase or frequency shifts are then detected and processed to obtain electrostatic gradient images. The EFM is used in electrical failure analysis, detection of trapped charges,

quantifying potential difference between metals and semiconductors, testing electrical continuity, and performing electrical read/write.

A related technique to characterize surface potential of a sample is the surface potential imaging technique [16]. Surface potential imaging maps the electrostatic potential on the sample surface with or without a voltage applied to the sample. As the tip travels above the sample surface in lift mode, the tip and the cantilever experience a force wherever the potential on the surface is different from the potential of the tip. The force is nullified by varying the voltage of the tip so that the tip is at the same potential as the region of the sample surface underneath it. The voltage applied to the tip in nullifying the force is plotted versus the in-plane coordinates, creating the surface potential image.

2.4.3.1.2. Conducting AFM and tunneling AFM

Conducting AFM (c-AFM) [14,112,113] is a current sensing technique for the electrical characterization of conductivity variations in medium resistive samples. It can be used in either imaging or spectroscopic mode. In imaging mode, images of the electrical current are obtained, while in spectroscopy mode current-voltage or current-force spectra can be obtained. A DC bias voltage is applied between the sample and the conductive tip as the tip is scanned across the sample surface in contact mode. A feedback loop keeps the deflection of the cantilever constant and the local height of the sample is measured. A low noise current amplifier senses the resulting current (Fowler-Nordheim tunneling current) passing through the sample as a topography image is obtained simultaneously. The observed current can be used as a measure of the local

conductivity or electrical integrity of the sample. Using this technique current as low as 100 pA can be measured at a lateral resolution of about 10 nm. Olbrich *et al.* [112] demonstrated the applicability of c-AFM for the quantitative electrical characterization of thin SiO₂ films with thickness range of 3-40 nm on a nanometer scale length. The local oxide thickness was obtained with an accuracy of ± 0.3 nm. Oh and Nemanich [113] measured current-voltage characteristics of individual submicron islands of TiSi₂ less than 1 μm on Si(100) surfaces and imaged the variations in electrical conductivity among the islands. The technique can be applied to conductive polymers and other materials with limited or highly non-uniform conductivity. Conducting-AFM has been also used to explore variety of aspects of electrical properties such as surface conductivity [114], two-dimensional dopant profiling [115], nanopatterning [116], imaging and probing of InAs quantum dots [117]. The electrical characteristics of nanoscale structures were studied using c-AFM [118]. Other applications include identification of leakage paths, mapping of contaminants and different components in composite materials.

Tunneling AFM (TUNA) [14,112,119] is a technique similar to c-AFM, which is used to measure ultra-low currents on low-conductive samples. In this method, a DC bias voltage is applied between the sample and the conductive tip as the tip is scanned across the sample surface in contact mode. TUNA can map ultra-low currents in the range of 100 fA to 100pA at a lateral resolution of better than 10 nm. The TUNA method is extensively applied for the study of thin dielectric films used as gate oxide in field effect transistors. TUNA was used to

study variations in dielectric film thickness used in gate oxide layer, image defects in SiO₂ gate oxide thin film, study leakage current in ferroelectric films [120].

2.4.3.1.3. Scanning capacitance microscopy

Scanning capacitance microscopy (SCM) [15,121,122] is an AFM based technique, which detects the capacitance between the tip and the sample. This technique is primarily used to characterize 2-D carrier profiling and failure analysis of semiconductor devices. This technique is also used to characterize the properties of ferroelectrics. In the SCM, the sample (or the metallic tip) is covered with a thin dielectric layer, so that the tip-sample contact forms a metal-insulator-semiconductor (MIS) capacitor, whose capacitance-voltage behavior is determined by the local carrier concentration of the semiconductor sample. An AC bias voltage is applied between the tip and the sample. This generates capacitance variations, which are monitored using a GHz resonant capacitance sensor. This method is sensitive to variations smaller than attofarads capacitance. The capacitance variation is a measure for the local carrier concentration density and type (n- or p-type) and therefore is useful in high resolution two dimensional carrier profiling of semiconductor devices. Unlike EFM, which is operated in intermittent contact mode, SCM is usually operated in contact mode with a conductive tip. Topography and the capacitance images are obtained simultaneously. SCM provides information with a spatial resolution of about 10-20 nm [120].

2.4.3.1.4. Scanning spreading resistance microscopy

Scanning spreading resistance microscopy (SSRM) [120,122] is yet another AFM based technique to characterize variations in electrical resistance in the sample. SSRM provides two-dimensional information on the electrical conductivity or resistivity of the sample under study. An electrically conductive probe is used to measure local resistivity of the sample. When the probe is scanned over regions with different resistivity values, the electrical resistance formed by the probe-sample contact will vary proportionally. When the applied force exceeds a certain threshold force, the measured resistance is dominated by the spreading resistance. This technique can be equally applied for both conductors and semiconductors. A spatial resolution of 10-35 nm has been reported using this technique (123,124). SSRM images often complement images obtained by SCM, as SCM gives no signal on dielectrics and metals, whereas SSRM shows a big contrast between the two.

2.4.3.1.5. Scanning micro four-point probe techniques

Four-point probe technique has played an important role in understanding the electrical properties of solid state bulk materials and films for many decades. A conventional four-point probe used in four-point probe techniques is a macroprobe because the distance between the probes is usually 1 mm. Moreover, the macroprobes are inconvenient in many cases because of their size and the large contact forces exerted on the samples, while the in-plane electrodes cannot be repositioned. The four-point probe is particularly suited for systems with long-range conductivity variations compared to the electrode

spacing. The conventional four-point probe measurement in macroscale has limited sensitivity in nanoscale due to the comparatively large spacing between the four probes. For systems that show variations in electrical conductivity on microscale, it is preferable to reduce the electrode spacing below the characteristic scale of the variations. There is an interest in miniaturization of the four-point probes to obtain higher surface sensitivity, an increased spatial resolution and less damage to the sample. Several attempts have been made to reduce the electrode spacing in the four-point probe methods. Recently, Petersen *et al.* [125] fabricated micro four-point probes using silicon-based microfabrication technology to obtain higher spatial resolution. Electrode spacings of 8 and 20 μm were used in their experiments. Later Petersen *et al.* [126] used photolithography to fabricate micro four-point probes with an electrode spacing of about 1.1 μm . Bøggild *et al.* [127] later also used photolithographic techniques to fabricate four-point probes consisting of four soft and flexible metallized SiO_2 probes microcantilevers with an electrode spacing of 1.5 μm and a combination of conventional microlithography and electron beam deposition to fabricate four-point probes with electrode spacing of about 200 nm. Keller *et al.* [128] developed a micro four-point probe method to measure resistivity of fragile materials such as conducting polymers. The electrode spacing in this technique is between 10-20 μm . The above techniques provide electrical measurements at a given region with micro-scale resolution. However, the probes in these techniques are difficult to use for scanning because of problems in manipulating the force between the probe and the sample surface due to their structure and

rigidity. By combining the micro four-point probes with AFM, it is possible to image the electrical conductivity along with surface topography. Ju *et al.* [129] combined the principles of four-point probe technique and standard AFM to develop microscopic four-point probe technique. In their technique, an AFM probe was fabricated into four parallel electrodes isolated from each other separated by a distance of 1.0 μm . This instrument is capable of measuring both surface topography and local electrical conductivity simultaneously. Later, following a similar approach, Yoshimoto *et al.* [130] developed AFM based four-point probe technique by using PtIr-coated carbon nanotube tips with an electrode spacing of about 30 nm. Using this technique they were able to measure sample resistance as small as 2Ω , which is much smaller than the contact resistance. Nagase and his co-workers [131] reported a four-point probe AFM technique capable of imaging with sub- 100 nm resolution. In their technique, two Pt electrodes with a nanogap was fabricated using focused ion beam milling and integrated on a Si cantilever with Al electrodes. The minimum gap between the electrodes is about 20 nm.

2.4.3.1.6. Piezoresponse force microscopy

Piezoresponse force microscopy (PFM) is an AFM based technique to characterize the properties of ferroelectric materials [132,133]. In contrast to X-ray techniques, which are limited to averaged analysis of domain structure, PFM yields spatially resolved information on domain size, correlations, domain behavior near the inhomogeneities and grain boundaries. PFM can be used for imaging static domain structure in thin film, single crystals and polycrystalline

materials, selective poling of specified regions on ferroelectric surface. PFM is a modification of traditional AFM based on the detection of local vibrations of a cantilever induced by a probing AC signal applied between the conductive tip of an AFM and the bottom electrode of a ferroelectric sample. This method has been extensively used to characterize ferroelectric properties and piezoelectric measurements [134-136].

2.4.3.2. Characterization of magnetic properties using AFM

Shortly after the invention of atomic force microscope it was recognized that detection of magnetostatic interactions at a local scale was possible by using a ferromagnetic tip attached to the cantilever of an AFM. This resulted in a new scanning probe microscope known as magnetic force microscope (MFM). A ferromagnetic sample is then scanned using the magnetic probe. The near-field magnetostatic interaction for a typical probe-sample configuration is fairly strong and largely independent of surface contamination. In MFM, the imaging relies on the magnetostatic interactions between a magnetic tip and the ferromagnetic sample [104]. An image of the magnetic domains is constructed by measuring the long-range magnetic forces between the magnetic tip and the sample.

Martin and Wickramasinghe [19] were the first to build MFM based on the principles of AFM. A 25 μm diameter iron wire was used as the cantilever and the magnetic tip. The tip was formed by tapering the wire down and etching the end to form a 50 nm radius. The deflection and consequently the magnetic force were measured using an optical interferometer. They reported a spatial resolution of

100 nm- a substantial improvement over any magnetic imaging technique available at that time. After the first MFM was developed, it started to become a widely used method in magnetic materials research and in the development of magnetic devices. One of the most important applications of the MFM is in the magnetic recording industry [137-138]. The data storage industry currently utilizes MFM extensively to measure the magnetization distribution in magnetic recording media and heads in an effort to pack more data into a recording system [139,140]. Other applications in which MFM is useful are disk-failure analysis, characterization of local variations in the sensitivity of recording heads etc. MFM has also been used for the analysis of magnetic microstructures [141], observation of magnetization reversal processes [142], magnetic wires [143], magnetic dots [144], and also subsurface probing of current-carrying strips buried under insulating thin film. The MFM can also be used to image electrical properties. Hoffmann *et al.* [17] used MFM to map the electrical conductivity variations in Al_2O_3 -TiC sample. The vibrating cantilever in MFM generates eddy currents in the conducting sample. The opposing magnetic field generated by the primary magnetic field dissipates the vibration of the cantilever. By monitoring the reduction in the amplitude of the cantilever, a map of the local electrical conductivity variations is obtained. They have also used the same setup to image the magnetic properties without a magnetic tip.

The MFM has poor resolution, about 25 nm, compared to the AFM or the STM. The reason for this is that a larger volume of the tip interacts with the larger volume in the sample. The positive aspect of this long-range interaction is that

MFM is not very sensitive to surface contamination, and can even be used to study buried structures.

2.5. Summary

This chapter reviewed various measurement techniques to characterize electrical conductivity of materials on both bulk and micro- and nanoscales. While the two-point and four-point probe methods provide a direct and easy way of measuring electrical conductivity, they are not suitable for nanoscale measurements due to the electrode spacing. The electromagnetic induction methods provide localized measurement of conductivity with sensitivity to small crack detection. However, the spatial resolution of the induction methods is in micron range.

The characterization of properties on micro- and nanoscales is very important to the emerging fields of nanoscience and nanotechnology. These fields have wide range applications in different fields of materials, biology, sciences etc. Even though there is a lot of progress in the development of these materials, often there is a lack of techniques that have high resolution and sensitivity to local variations in the material properties. The invention of AFM has led to the development of numerous techniques based on AFM to characterize material properties. However, different modification needs to be done to the AFM in order to characterize these properties. For example, a bias voltage between a

conductive tip and the sample needs to be applied in order to map the electrical properties. For magnetic interactions, the sample is scanned with a vibrating ferromagnetic tip. Also, the cantilevers generally used for electrical property measurement by AFM are stiffer than conventional contact mode AFM cantilevers. Thus, these cantilevers may not be sensitive to small variations in the electrical conductivity of the sample. Eddy current methods are known to be sensitive to local variations in electrical properties of materials. Therefore, in this research work, the high spatial resolution of AFM and the high sensitivity of eddy current method are combined to develop a new methodology which can be used to characterize electrical conductivity variations in materials (bulk and nanomaterials) on micro- and nanoscales. The advantage of using induced currents in this methodology is that they can be used to characterize magnetic and dielectric properties as well. In order to characterize these properties a suitable probe is employed.

CHAPTER 3

SCANNING PROBE MICROSCOPY (SPM)

3.1. Introduction

This chapter gives an overview of the scanning probe microscopy techniques relevant to the present research work. The first technique that was developed in the SPM family is scanning tunneling microscopy. A brief introduction to the principle of STM and its applications is first presented. The tip-sample interaction forces in STM are discussed and are shown how these forces are exploited to develop the atomic force microscopy. A detailed description of the working principles of AFM along with the instrumentation used in this work is provided. Then, different imaging modes of AFM are discussed with the emphasis on those modes which will be used in the current research work. An account of the different interaction forces between various probes and sample surfaces in AFM is given. Finally, it is shown how these interaction forces can be used to build different AFM related techniques to image material properties on nanoscale.

3.2. Principle of Scanning Tunneling Microscopy

Giaever [145] proposed the principle of electron tunneling, which occurs if a potential difference is applied between two metals separated by a small distance. If the separation distance is small enough, a current will flow because of the ability of electrons to penetrate a potential barrier. To be able to measure the tunneling current, the separation distance between two metals must be no more than 10 nm. Binnig *et al.* [90,91] successfully combined electron tunneling in vacuum and scanning capability to build a scanning tunneling microscope. The vacuum provides the ideal barrier for tunneling and also dampens the external vibrations. The very high vertical resolution is obtained because the tunneling current varies exponentially as a function of distance between the probe and the metal surface. Typically, tunneling current decreases by a factor of 2 with an increase in separation distance by 0.2 nm.

A schematic of the STM is shown in Figure 3.1. The principle of the STM is straightforward. A sharp metallic tip is brought within 1 nm of a conducting surface while a voltage is applied between them. The gap separation between the tip and sample is so small that electrons from the tip can tunnel from the atom at the very end of the nearest atom on the sample surface and generate a current. This tunneling current is extremely sensitive to the gap, i.e., to the height of tip above the surface. The position of the tip in three dimensions is accurately controlled by piezoelectric drivers. The tip is scanned over a surface in the two lateral dimensions at a distance of 0.3-1 nm, while a feedback circuit constantly

adjusts the tip height, to keep the current constant. The STM can be operated in two modes: constant current or constant height. In the constant current mode, the tunneling current is compared with a reference current and the error signal generated is applied to a gap control z-piezo which moves the tip up or down in order to maintain a constant tunnel current as the tip is raster scanned across the sample surface to obtain an image. In the constant height mode, the tip is scanned across the surface at constant height and constant voltage while the current is monitored. The constant current mode is generally used for atomic scale images. In contrast to other electron microscopes and surface analytical techniques using electrons, STM can be operated in air and in liquids as well as in vacuum because there are no free electrons involved in the STM experiment. To achieve atomic resolution, vibration isolating is required. The stability can only be achieved by the combination of an effective vibration isolation system and a rigid design of the STM instrument. Since the technique requires current to flow between the sample and the tip, it cannot be used to characterize electrically insulating materials.

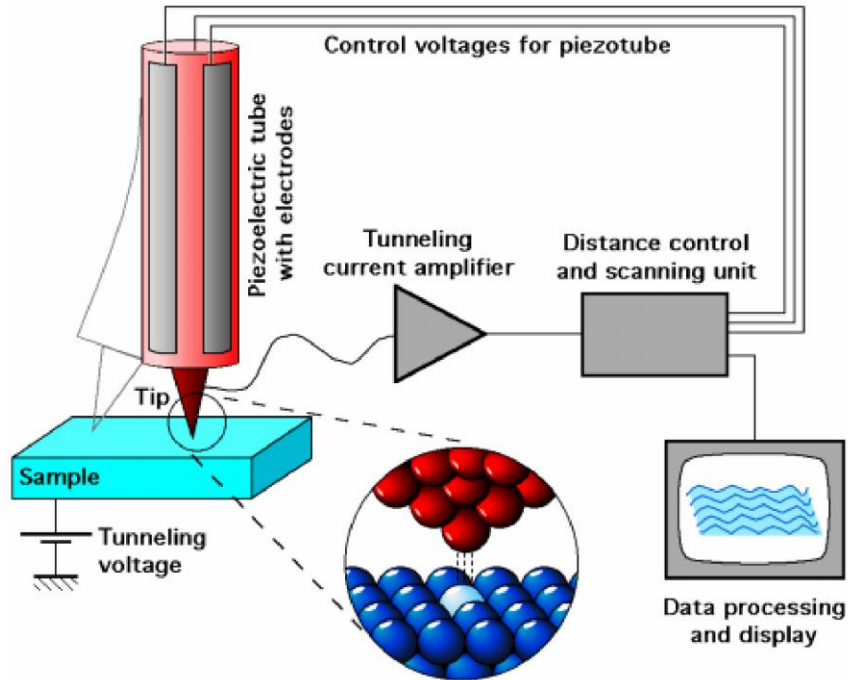


Figure 3.1. Schematic of a scanning tunneling microscope

The tunneling tip is the most crucial component of the STM. The geometry and the chemical identity of the tip influence both topographic and spectroscopic measurements. The best images are obtained when tunneling is limited to a single metallic atom at the end of the tip. STM cantilevers with sharp tips are typically fabricated from metal wires of tungsten, platinum-iridium, or gold and sharpened by grinding, field emission/evaporator, or electrochemical polishing/etching [146]. Electrochemical etching method has been widely used to manufacture STM tips.

An important aspect of STM measurements is the tip-sample interaction effects. Even though electron tunneling is used for topography measurements in STM, there will be other inter-atomic forces active between the tip and the sample. The role of atomic forces in tunneling, [147], has proven essential for the interpretation of STM images. At tip-sample separations of 10 Å and more, the

force interaction between the tip and sample surface is dominated by long-range van der Waals forces. At small tip-sample separations of only few Angstroms, the overlap of the wave functions of tip and sample surface is significant and short-range quantum-mechanical exchange-correlation forces become dominant which decay exponentially with increasing distance. The importance of force interactions in STM was first considered when STM was used to image graphite [148]. Giant corrugation amplitudes of up to several Angstroms were measured, which could not be explained by tunneling theory. Direct measurements of the force between the tip and the graphite sample while scanning in STM revealed the presence of high repulsive forces. Durig *et al.* [149] investigated short-range interatomic forces between metallic tips and samples during STM experiments by using a flexible cantilever beam as a sample holder. The forces were measured by measuring the static deflection of the cantilever beam. Later, Salmeron *et al.* [150] reported the effect of compressive and shear forces between the tip and sample surface in STM. They found that at typical gap resistances in STM, these forces have significant effects. While the additional influence of forces might not be desired for investigation of tunneling phenomena, these forces can be used to improved the quality of the STM images [149,151,152]

3.3. Atomic Force Microscopy

It was discussed in the previous section that a variety of interatomic forces act between the tip and the sample during the operation of a STM. The strength of these forces depends on the tip-sample separation. These interatomic forces between the probe and sample at small separation distances have been exploited to develop another type of scanning probe microscopy, called atomic force microscopy (AFM). Before the invention of the AFM, the forces of interaction between two bodies held at a distance were measured by a surface force apparatus [153]. The forces are measured between crossed cylinders of molecularly smooth mica sheets which were made to approach one another by using mechanical reduction mechanisms and piezoelectric transducers. The force can be measured by measuring the deflection Δz of a spring, on which one of the mica sheets is mounted and using Hooke's law $F = c \cdot \Delta z$, where c is the spring constant of the spring. The separation between the two mica surfaces is measured by means of an optical technique using multiple beam interference fringes. The surface force apparatus allowed study of forces for a wide range of separations. A force resolution of the order of 10^{-8} N is usually obtained. Surface profilometer was developed as a valuable means to study the surface roughness of materials including bulk insulators [154]. A topographic map is obtained by raster scanning a sample relative to a stylus tip. However, unlike STM, the stylus is in mechanical contact with the samples during scanning. The nominal radius of the stylus is about 1 μm , which is relatively large compared to STM tips. The

lateral resolution, therefore, is limited by the radius of the stylus. AFM can be regarded as a hybrid between a surface force apparatus (SFA) and a surface profilometer, but with much higher force and lateral resolutions.

3.3.1. Principle of AFM

Figure 3.2 shows the schematic diagram of a commercial AFM. The design of the AFM is similar to that of the STM except the sensor. The AFM uses a piezoelectric scanner to scan either the tip or the sample. The most commonly used scanner is a piezoelectric tube scanner. Piezoelectric tube scanners allow accurate, sub-angstrom positioning of the tip or sample in three dimensions. The scanner system comes in two designs. One is where the scanner is installed in the AFM head unit and the second one is where the scanner is attached below the sample stage. Depending on the scanner location, either the sample or the probe head will be raster scanned during imaging. Most of the commercial AFMs nowadays are designed with the scanner in the AFM head unit that holds the probe. The probe consists of a sharp tip attached to the end of a flexible cantilever which is connected to the scanner. The piezoelectric scanning system motion is controlled via the computer software in order to precisely position the sample for a scan. Piezo material allows precise control of the motion of the tip in the X, Y, and Z directions across the sample. During scanning, a laser light is focused on the back of the cantilever. The back face of the cantilever is coated with a thin layer of gold to enhance reflectivity. When the tip is brought into

contact with the sample surface, the tip experiences force due to intermolecular interaction between the tip and the sample. The force acting on the tip causes the cantilever to deflect. The deflection of the cantilever during scanning shifts the position of the laser spot which is reflected off the back of the cantilever. Usually, a four-quadrant position sensitive photo-diode detector is used to detect the position of the laser due to the deflection of the cantilever. The voltage difference between the top and bottom photodiodes provides the signal which is a sensitive measure of the cantilever vertical deflection. Surface topography is measured by laterally scanning the sample under the tip while simultaneously measuring separation dependent force between the tip and the surface. The interaction force between the tip and the sample is measured according to Hooke's law, $F = k\Delta z$, where k is the cantilever spring constant and Δz is the vertical displacement of the cantilever. To obtain topography information, the interaction force, F can be either recorded directly or used as a parameter for a feedback electronics system which maintains the force at a constant set value.

The lateral resolution of an AFM and related techniques depend on the diameter of the probe. Various commercial probes are available with a nominal probe diameter of 10-20 nm. By manufacturing a smaller, sharper tip, the resolution of the AFM can be improved.

Images from the AFM need to be processed. An ideal AFM is a noise free device that images a sample with perfect tips of known shape and has a perfectly linear scanning piezo. In reality, however, scanning devices are affected by distortions and these distortions must be corrected for. The distortions can be

linear and nonlinear. Linear distortions mainly result from imperfections in the machining of the piezo translators causing cross talk between the Z-piezo to the X- and Y-piezoes, and vice versa. Nonlinear distortions mainly result because of the presence of a hysteresis loop in piezoelectric ceramics. In addition, electronic noise may be present in the system. The noise is removed by digital filtering in real space or in the spatial frequency domain.

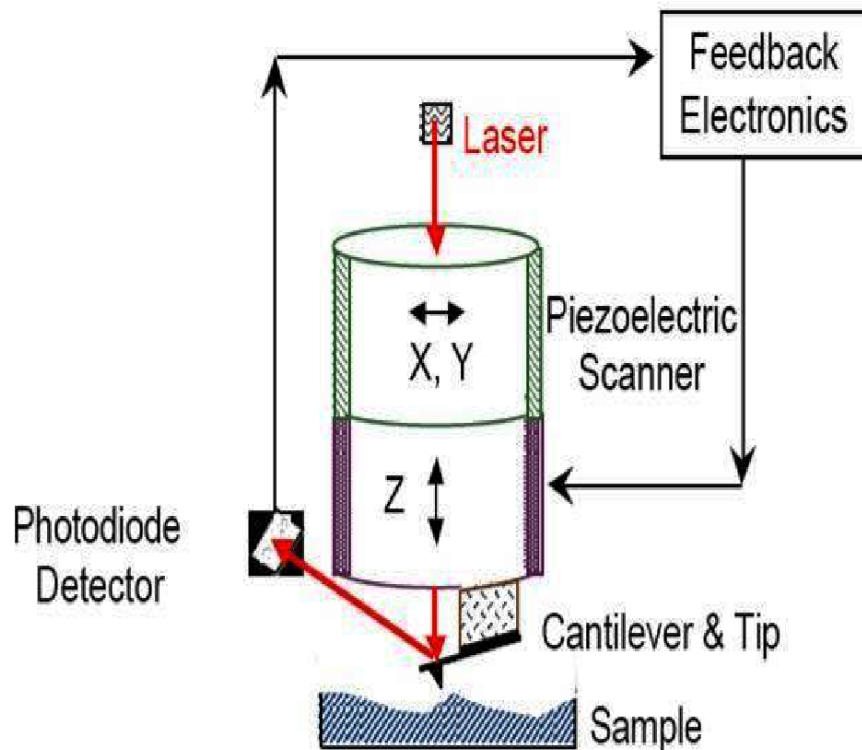


Figure 3.2. A schematic diagram illustrating the working principle of AFM

AFM probes the sample and makes measurements in three dimensions, x , y , and z , thus enabling the presentation of three-dimensional images of a sample surface. AFMs require neither a vacuum environment nor any special sample preparation, and they can be used in either an ambient or liquid environment. With these advantages AFM has significantly impacted the fields of materials

science, chemistry, biology, physics, and the specialized field of semiconductors.

3.3.2. Design and Instrumentation of AFM

Criteria for the design and instrumentation of AFM follow in many respects those for the STM, particularly concerning vibration isolation, positioning devices, scanning units, electronic feedback system and computer automation. The only components that are different in AFM are the force sensor and the cantilever deflection detection mechanism.

3.3.2.1. Force sensor

The performance of AFM and the quality of AFM images greatly depend on the instrument available and the probes used. The central element of a force microscope and its major instrumental difference from a scanning tunneling microscope is the spring which senses the force between the tip and the sample. For sensing normal tip-sample forces, the force sensor should be rigid in two axes and relatively soft in the third axis. This property is fulfilled with a cantilever beam, and therefore the cantilever geometry is typically used for force detectors. To achieve high sensitivity, a reasonably large deflection for a given force is desired. Therefore, the cantilever should be as soft as possible, i.e. the spring constant should be small enough to allow detection of small forces. On the other hand, a high resonant frequency is necessary in order to minimize sensitivity to

mechanical vibrations while scanning. In addition, a high resonant frequency of the cantilever allows for reasonably high scan speeds.

The force measuring cantilever in the AFM is a mechanical resonator. The resonances can be excited either by the surroundings or by the rapid movement of the tip. To avoid problems due to building or air induced oscillations, it is important to optimize the design of AFM for high resonant frequencies. The fundamental natural frequency, ω_0 , of any spring is

$$\omega_0 = \frac{1}{2\pi} \sqrt{\frac{k}{m_{eff}}} \quad (3.1)$$

where k is the spring constant in the normal direction and m_{eff} is the effective mass. The spring constant k of a cantilever with uniform cross section is given by

$$k = \frac{3EI}{L^3} \quad (3.2)$$

where E is the Young's modulus of the material, L is the length of the beam and I is the moment of inertial of the cross section. For a rectangular cross section with a width b and a height h , the moment of inertia is given by

$$I = \frac{bh^3}{12} \quad (3.3)$$

combining the above three equations,

$$\omega_0 = \sqrt{\frac{Ebh^3}{4L^3 m_{eff}}} \quad (3.4)$$

The effective mass can be calculated using Raleigh's method. For the case of a uniform beam with a constant cross section and length L the effective mass is given by [155]

$$m_{eff} = \frac{9}{20} m \quad (3.5)$$

substituting the above equation in the equation for ω_0 and noting that $m = \rho Lbh$, where ρ is the mass density,

$$\omega_0 = \left(\frac{\sqrt{5}}{3} \sqrt{\frac{E}{\rho}} \right) \frac{h}{L^2} \quad (3.6)$$

It is evident from the above equation that by choosing a material with a high ratio of E/ρ , the natural frequency can be increased. Alternatively, by optimizing the ratio h/L^2 , the resonant frequency can be increased. Therefore, for a large value of ω_0 and for a small spring constant, the mass and therefore the geometrical dimensions of the force sensor have to be as small as possible. This consideration leads directly to the idea of using microfabrication techniques for the production of cantilever beams.

Initial cantilevers have been cut by hand from thin metal foils or formed from fine wires. Tips for these cantilevers were prepared by attaching diamond fragments to the ends of the cantilevers by hand, or by electrochemical etching. Most commercial AFM cantilevers used today are microfabricated from silicon dioxide, silicon nitride or pure silicon using photolithographic techniques [155]. A variety of silicon and silicon nitride cantilevers are commercially available with micron-scale dimensions, spring constants ranging from 0.01 to 100 N/m, and resonant frequencies ranging from 5 kHz to over 300 kHz. The two most popular cantilevers are V-shaped and rectangular cantilevers [155]. The tip is usually pyramidal in shape and made of silicon or silicon nitride. The tip of the AFM

should be sharp in order to achieve high lateral resolution. In general, the lateral resolution of AFM depends on the sharpness of the tip.

3.3.2.2. Cantilever deflection measurement

The cantilever deflection measurement technique in AFM should have the following requirements: i) high sensitivity at the sub-Angstrom level and ii) the measurement technique should have negligible influence on the cantilever deflection itself and should not cause imaging artifacts. Several different techniques to detect the cantilever deflection have been used. These techniques are tunneling [156], capacitance [157] and optical interferometry [158] methods. In the original design of AFM by Binnig *et al.* [11], the cantilever deflection was measured using tunneling detector. However, the most common cantilever deflection detection system used in many commercially available AFM systems is the laser beam detection method [159]. For the AFM using the optical lever method a photodiode segmented into four closely spaced devices detects the orientation of the end of the cantilever. Initially, the light ray is set to hit the photodiodes in the middle of the two sub-diodes. Any deflection of the cantilever will cause an imbalance of the number of photons reaching the two halves. Hence the electrical currents in the photodiodes will be unbalanced. The difference signal is further amplified and is the input signal to the feedback loop. The output signal is proportional to the change in intensity on the segments. If the laser light beam moves between the upper and lower pairs of segments the

vertical deflection of the cantilever can be deduced from a proper treatment of all individual photocurrents:

$$\Delta I_{\text{vertical}} = (I_{\text{upper_left}} + I_{\text{upper_right}}) - (I_{\text{lower_left}} + I_{\text{lower_right}}) \quad (3.7)$$

The deflection can be measured to within 0.02 nm, so for typical cantilever spring constant of 10 N/m a force as low as 0.2 nN can be detected.

The scanning of a sample with an AFM can twist the microfabricated cantilever because of lateral forces and affect the images. When the tip is subjected to lateral forces, it will twist the cantilever and the light beam reflected from the end of the cantilever will be deflected perpendicular to the ordinary deflection direction. The twisting results in a horizontal deflection of the laser spot on the surface of the photodetector:

$$\Delta I_{\text{horizontal}} = (I_{\text{upper_left}} + I_{\text{lower_left}}) - (I_{\text{upper_right}} + I_{\text{lower_right}}) \quad (3.8)$$

For many investigations this influence of lateral forces is unwanted. The design of triangular cantilevers stems from the desire, to minimize the torsion effects. However, lateral forces open up a new dimension in force measurements. The lateral forces are used in lateral force microscopy [159] to study the frictional properties of materials. Beam deflection detection method offers the advantage of being capable of detecting simultaneously both lateral and vertical forces

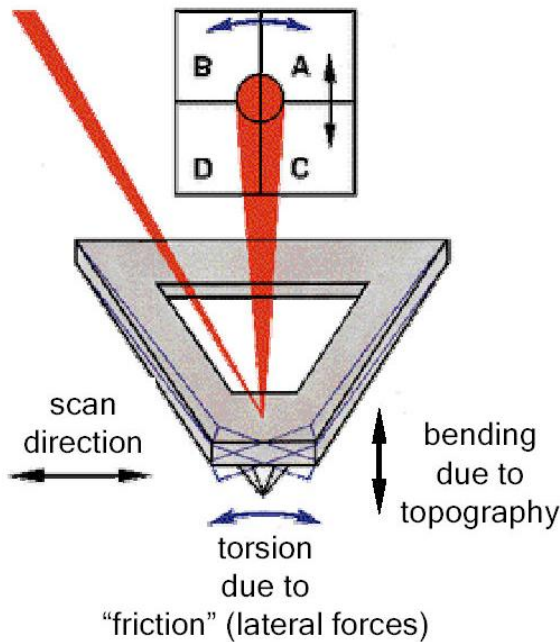


Figure 3.3. Optical beam deflection detection in AFM

3.3.2.3. Scanner

AFM uses a piezo-electric scanner to scan the tip across the surface. An electric field applied across a piezoelectric material causes a change in the crystal structure, with expansion in some directions and contraction in others. Scanning probe microscopes use the transverse piezoelectric effect, where the applied electric field E is perpendicular to the expansion/contraction direction. The most commonly used scanner is a tube scanner. They are widely used in AFM due to their simplicity and their compactness. The scanner is constructed by combining independently operated piezo electrodes for X, Y and Z into a single tube, forming a scanner which manipulates samples and probes with extreme precision in 3 dimensions. The outer electrode is segmented into four equal sectors of 90 degrees. Opposite sectors are driven by signals of the same

magnitude, but opposite sign. The inner electrode is normally driven by z signal. AFM systems can have the scanners installed in the AFM head or below the sample stage. Depending on the scanner location, either the sample or the probe head will be raster scanned during the imaging.

3.3.2.4. Feedback mechanism

A feedback control system is used in the AFM to keep the cantilever deflection constant. By measuring the difference signal in the photodiode quadrants, the amount of deflection can be correlated with a height. The feedback mechanism employed in the system enable the piezo-electric scanners to maintain the tip at a constant force (to obtain height information), or constant height (to obtain force information) above the sample surface. In constant force mode, as the tip is raster-scanned across the surface, the piezo will adjust the tip-sample separation so that a constant deflection set point is maintained. If there is surface asperity in the path of the tip as it scans the surface, the cantilever deflection will increase and the feedback electronics will move the z height of the scanner to the make the cantilever deflection back to the present point.

3.4. Probe-Sample Interactions in AFM

If two solids are in close proximity to each other a manifold of interactions manifesting themselves in forces can result. Some of these forces are van der Waals force, ion-ion core repulsion, capillary forces, adhesion, friction, etc. The diversity of the AFM stems from its basic operating principle - detecting the force between a sharp tip and the surface. The tip-sample force has long- and short-range contributions, which can be classified by their range and strength. Any separation of forces into categories will be arbitrary since all forces result from atomic and electronic interactions. However, the forces are usually classified according to the length scales on which they are significant. They are: (i) macroscopic forces that have a range of at least several nanometers, but are generally chemically independent and (ii) microscopic forces that are significant only at ranges of less than 1 nm, but much more sensitive to chemical identity of the atom under the tip. The AFM allows probing of a variety of attractive as well as repulsive forces, including van der Waals forces, ion-ion repulsion forces, electrostatic and magnetic forces, capillary forces, adhesion and frictional forces to mention a few.

3.4.1. Macroscopic Forces

It was mentioned above that AFM can measure variety of long-range macroscopic forces acting between the tip and the sample surface. Some of these macroscopic interaction forces between the AFM probe and the surface, like Van der Waals force and capillary forces are described briefly here.

3.4.1.1. Van der Waals force

The Van der Waals (VDW) force represents the electromagnetic interaction of fluctuating dipoles in the atoms of the tip and the surface. For two electrically neutral and non-magnetic bodies at relatively large separations, typically of the order of 1 nm or more, VDW forces usually dominate the interaction force between them. The VDW interactions lead to a negative interaction potential and thus to attractive forces. Therefore, small interactions between individual atoms of macroscopic tip and sample sum up to a resulting force on the order of several nanonewtons. Although this force is small by macroscopic standards, it exceeds the short-range chemical forces and usually dominates the probe-sample interaction. The VDW force does not vary much as a function of atomic species in comparison to chemical forces, and therefore acts as a long-range macroscopic force.

Assuming that the potential $V(r)$ between two atoms separated by a distance r is known, then the force between them is defined by the gradient of that potential given by

$$f(r) = -\nabla V(r) \quad (3.9)$$

For the VDW interaction the potential is given by

$$V(r) = -\frac{C_6}{r^6} \quad (3.10)$$

where C_6 is the interaction constant as defined by London [160] and is specific to the identity of the interacting atoms. The van der Waals forces usually increase in magnitude if the probe approaches the sample surface. If the outermost atom of the probe starts to penetrate the sample surface, short-range repulsive forces are introduced. Upon further approach of the probe into the sample, more and more interatomic interactions lead to a continuously increasing repulsion, while the overall long-range probe-sample interaction remains attractive in nature.

3.4.1.2. Capillary forces

Experiments performed using AFM must also consider the role of atmospheric humidity in the probe-sample interactions. In ambient conditions capillary forces can also be present. The presence of liquid water layers on the tip and/or the sample surface can introduce some discontinuous behavior in their interaction. At short-range distances, the liquid layers will *jump into contact*, forming a bridge of large meniscus radius between them. The meniscus causes huge attractive forces usually dominating all interactions. Moreover, the overall loading force exerted by the probe on the sample in presence of capillary force is greatly increased. This limits the resolution in contact mode and sometimes even leads to damage of the sample surface. The capillary forces can be avoided in two ways. The first one is to operate the AFM in ultra high vacuum conditions.

This reduces the adsorption of contaminants to a minimum. The second solution is to immerse both cantilever and sample in a suitable liquid [161].

Figure 3.4 shows a schematic of a sharp tip close to a sample surface. Long-range forces originate in the full volume and surface of the tip. They are shown by arrows in Figure 3.4. In addition to the above forces, other long-range forces like electrostatic and magnetostatic interactions may also occur if suitable environmental conditions are chosen or if external manipulations are undertaken in a suitable way. A detailed analysis of electrostatic and magnetostatic interactions in AFM will be discussed in a later section of this chapter.

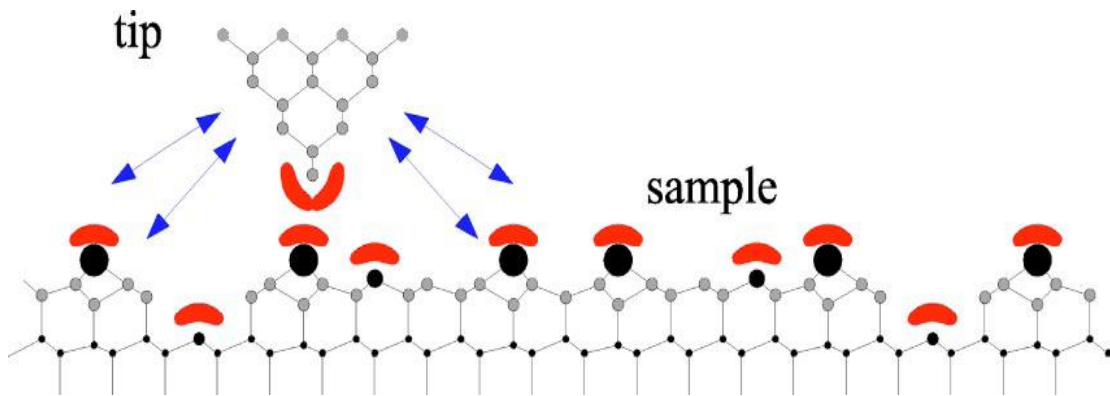


Figure 3.4. A schematic view of an AFM tip in close proximity to sample surface [162].

3.4.2. Microscopic Forces

Chemical forces rarely dominate the total force in SPM, yet they remain the most crucial interactions for understanding experimental images. The chemical forces define the atomic structure of the tip and surface and are responsible for atomic displacements when the tip is in proximity to the surface. The nature of chemical bonds that form in and between, the tip and surface are

intrinsically linked to the chemical forces. In AFM, they distinguish atomic identities and therefore are responsible for atomic resolution in images. Chemical short-range forces act when the orbitals of the tip and sample overlap, shown by crescents in Figure 3.4.

Figure 3.5 shows the interaction potential between probe and sample in AFM if the separation between them is successively decreased. As the tip approaches the sample surface, the cantilever follows the attractive force, where the probe is pulled toward the surface. Upon further approaching the probe to the sample more and more interatomic interactions lead to a continuously increasing repulsion, and the force increases steeply, while the overall long-range probe-sample interaction is still attractive. Thus the net interaction potential exhibits first a point of inflection, then an absolute minimum, followed by a situation where the repulsive short-range interactions just balance the attractive long-range interactions, and finally a regime where ultimately the repulsive interactions dominate the attractive interactions. In this regime the probe seriously penetrates the sample, first leading to elastic and finally to inelastic deformations. The potential energy between the tip and the sample causes a z component of the tip-sample force and a tip-sample spring constant. Depending on the mode of operation, the AFM uses the force or some entity derived from the force as the imaging signal.

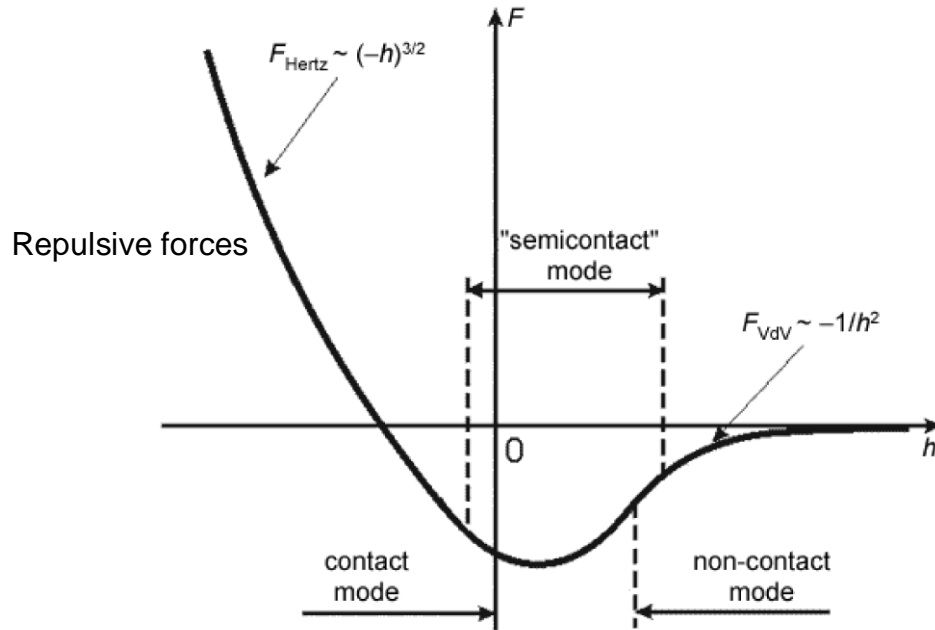


Figure 3.5. Interaction potential between the AFM probe and sample surface

3.5. Modes of Operation in AFM

AFM is operated primarily in two imaging modes: static and dynamic modes. The static mode is also referred to as repulsive mode or contact mode. As the name suggests, in this mode, the tip is always in contact with the sample surface. In the dynamic mode of operation, also referred to as attractive force imaging or noncontact mode, the tip is brought close to the sample surface within a few nm, and the cantilever is deliberately vibrated. In the two modes, surface topography is measured by laterally scanning the tip across the sample while simultaneously measuring the separation dependent force or force gradient between the tip and the surface. A brief description of the imaging modes of AFM is presented below.

3.5.1. Static Mode: Contact AFM

In the static mode of operation, the force translates into a deflection of the cantilever. The noise level of the force measurement is then given by the cantilever's spring constant k times the noise level of the deflection measurement. Because the deflection of the cantilever should be significantly larger than the deformation of the tip and sample, the cantilever should be much softer than the bonds between the bulk atoms in the tip and sample. Inter-atomic forces in solids are in a range of 10 N/m to about 100 N/m. Thus, typical values for k in the static mode are 0.01-5 N/m. In this respect, a small value for k increases the force sensitivity. Typically, V-shaped Si_3N_4 cantilevers with integrated pyramidal tips made of plasma enhanced chemical vapor deposition are used for contact mode imaging. Silicon nitride cantilevers are less expensive than other cantilevers. They are rugged and can be used for imaging in all environments. In the static mode, a sharp tip at the end of a cantilever is brought in contact with a sample surface. During initial contact, the atoms at the end of the tip experience a very weak repulsive force due to electronic orbital overlap with the atoms in the sample surface. With an AFM operated in the contact mode, topographic images with a vertical resolution of less than 0.1 nm (as low as 0.01 nm) and a lateral resolution of about 0.2 nm have been obtained [155]. With 0.01 nm displacement sensitivity, 10 nN to 1 pN forces are measurable [155].

The contact mode AFM can be operated in two modes: constant force and constant height. In constant force mode, a feedback control system is used in the

AFM to keep the cantilever deflection constant, i.e. a constant force is maintained throughout the scanning. As the tip is raster-scanned across the surface, the piezo will adjust the tip-sample separation so that a constant deflection set point is maintained. If there is surface asperity in the path of the tip as it scans the surface, the cantilever deflection will increase and the feedback electronics will move the z height of the scanner to make the cantilever deflection back to the preset point. The system electronics uses a feedback loop to maintain a constant deflection by adjusting the Z height as the sample is scanned in X and Y directions. The topography of the surface is imaged by correlating the X and Y scan position of the probe with the Z height of the scanner. The very first AFM observations have all been performed using constant force mode [11]. Many of the routine AFM investigations are frequently carried out in constant force mode. Since the feedback action is ultimately limited by the response time of the feedback circuit, the scan speed in the constant force mode is limited.

In many cases, where only the nanoscale topography of the sample surface is of interest, constant height mode is used. The constant height mode is used to obtain force information. This mode is achieved by limiting the feedback response to relatively low frequencies and by recording higher-frequency deflections as a function of probe position. In this mode the cantilever deflection and consequently force is allowed to change during scanning, while keeping the height constant. Since the cantilever deflection varies during the scanning, this mode is also called variable deflection mode. Compared with the constant force mode, significantly higher scan speeds can be achieved in the constant height

mode. However, AFM measurements in the constant height mode are more difficult to interpret since they are not equiforce surfaces. For small scanning areas the variation of the forces is usually negligible and the measurements can be interpreted similarly to the constant force mode.

It is helpful to discuss the formation of topography image in contact mode using the interaction potential between the sample and probe shown in Figure 3.5. The feedback set point for an operation in the constant force or constant height mode is chosen within the regime of overall repulsive interaction. This means that the probe exerts a certain force on the sample surface. In order to keep this force constant during the scanning of the surface, the probe has to follow the nanoscale corrugation of the sample surface. Thus, it is possible to obtain nanoscale resolution images of surfaces using AFM. Since the tip is always in contact with the sample surface during scanning, lateral forces will also be acting on the cantilever due to the friction between the tip and sample. Excessive lateral forces may be a problem for soft samples such as polymers and biological samples. In ambient environments, a layer of water vapor is usually formed on the sample surface. This leads to the formation of capillary forces resulting in jump to contact. This usually limits the spatial resolution achieved by contact mode AFM. Moreover, if the capillary forces are large enough, the sample surface may be damaged.

3.5.2. Dynamic Mode: Non-contact AFM

In the dynamic operation modes, the cantilever is deliberately vibrated. The dynamic mode of operation of the AFM is also known as non-contact mode or attractive force imaging. Non-contact mode AFM was introduced to use in situations where the tip contact may affect the sample surface in a subtle way. There are two basic methods of dynamic operation: amplitude modulation (AM) and frequency modulation (FM) operation. In AM-AFM [163], the cantilever is vibrated at a fixed frequency. Rectangular cantilevers with a spring constant in the range of 2-10 N/m are typically used for dynamic mode imaging. The stiffness of these cantilevers is high when compared to the stiffness of the contact mode AFM cantilevers. When the tip approaches the sample, elastic and inelastic interactions cause a change in both the amplitude and phase of the cantilever. These changes are used as the feedback signal. While the AM mode was initially used in a noncontact mode, it was later implemented at closer distances in ambient conditions involving repulsive tip-sample interactions. The change in amplitude in AM mode of AFM is not instantaneous with a change in tip-sample interaction but depends on the quality factor of the cantilever. Generally, the AM mode is slow with high Q-factor cantilevers. But high Q-factors are favorable for the reduction of noise. This limitation of AM-AFM has led to the development of FM-AFM. Albrecht *et al.* [164] combined high Q-factor and high speed by introducing the frequency modulation (FM) mode. Using the FM mode, the resolution improved dramatically and atomic resolution was obtained by reducing

the tip-sample distance and working in vacuum [165]. In FM-AFM, the cantilever with a resonant frequency f_0 and spring constant k is subjected to controlled positive feedback such that it oscillates with constant amplitude. In this method, the tip is brought close, but not in contact with the sample surface. The cantilever is then vibrated either in amplitude modulation mode or frequency modulation mode. The weak van der Waals attractive forces between the tip and surface are detected by the tip. Since the attractive forces from the sample are substantially weaker than the forces used by contact mode, the tip must be given a small oscillation so that the AC detection methods can be used to detect the small forces between the tip and the sample by measuring the change in amplitude, phase or frequency of the oscillating cantilever in response to force gradients from the sample. In the dynamic mode the force gradient is obtained by vibrating the cantilever and measuring the shift of resonant frequency of the cantilever. To obtain the topography of the surface, the interaction force (in this case, the attractive van der Waals forces) is either recorded directly or used as a control parameter for a feedback circuit that maintains the force derivative at a constant value. Although in this technique there is no damage to the sample, it is slow and is difficult to use, and hence is rarely used outside research environments.

3.5.3. Tapping Mode AFM

If the amplitude modulation (AM) AFM is operated in such a way the external excitation frequency is much lower than the resonant frequency, it

results in a quasi-static measurement. Consequently, this mode then can be viewed as a hybrid between the static and dynamic AFM. This mode of operation of the AFM is called intermittent contact AFM or tapping mode AFM. In the contact mode AFM, huge lateral forces are being applied to the tip during scanning and resulting in the wear of the tip and damage to samples. To minimize the effects of friction and the lateral forces on the topography measurements and to avoid damage to samples, tapping mode AFM is used [166,167]. Tapping mode AFM is used to image samples that are very soft or easily damaged or contaminated by continuous contact with tip, e.g. biological samples or soft polymers. In this mode of AFM, the cantilever/tip assembly is vibrated at the resonance frequency of the cantilever (usually 50-500 KHz) using a sinusoidal wave by a piezo mounted above it. The piezo motion causes the cantilever to oscillate with high amplitude when the tip is not in contact with the surface. The oscillating tip is then moved toward the surface until it begins to lightly tap the surface. During scanning, the vertically oscillating tip alternately contacts the surface and lifts off the surface. A feedback loop keeps the average normal force constant.

As the cantilever begins to intermittently contact the surface, the cantilever oscillation is necessarily reduced due to energy loss caused by the tip contacting the surface. As the cantilever begins to intermittently contact the surface, the resonant characteristics of the cantilever are changed. The reduction in oscillation amplitude is used to identify and measure surface features. Rectangular silicon single crystal cantilever with integrated pyramidal tips are

generally used in tapping mode applications. The tip and cantilever are an integrated assembly of single crystal silicon produced by etching techniques. These probes are much stiffer than the silicon nitride cantilevers used in contact mode AFM. Tapping mode inherently prevents the tip from sticking to the surface and causing damage to the sample during scanning. Unlike contact and noncontact modes, it has sufficient oscillation amplitude to overcome the tip-sample adhesion forces. There are no shear forces since the applied force is always vertical.

In addition to the above described modes, AFM can also be operated in lift mode. Lift mode is not an analytical mode, but a measurement approach that allows the imaging of relatively weak but long-range interactions while minimizing the influence of topography. Lift mode can be used in both static and dynamic imaging modes. Measurements are taken in two passes across each scan line; each pass consists of one trace and one retrace. In the first pass, topographical data is taken in tapping mode on one trace and retrace. The tip is then raised to the lift scan height and a second trace and retrace is performed while maintaining a constant separation between the tip and the local surface topography. Long range interactions are detected during this second pass. Using lift mode, topographical features are virtually absent from the image with the long-range forces.

3.6. Force-Distance Curves in AFM

To determine the optimum settings for the cantilever tip-material interaction in topographic measurements, it is often useful to directly record the force on the cantilever as the probe tip is brought close to the surface of the sample and then pulled away. This gives information about the long-range attractive or repulsive forces between the tip and the sample surface, elucidating local chemical and mechanical properties like adhesion and elasticity. Force curve [168] is a plot of the force between the tip and the sample as their distance is changed. This is the most important feature in an atomic force microscope. Many of the features in the images as well as modification of AFM to image other physical properties other than topography depend upon the understanding of the various probe sample interactions. Optimizing the force acting on the tip becomes essential to obtain good quality images. The force applied should not be so low that the tip gets retracted from the surface and also should not be too high that the tip indents the surface. An optimum force has to be applied by the tip on the surface. This optimum force can be identified by obtaining force curves.

A typical experimental force curve obtained by an AFM is shown in Figure 3.6. Force curves typically show the deflection of the free end of the cantilever as the fixed end of the cantilever is brought vertically towards and then away from the sample surface. Experimentally, this is done by applying a triangle wave voltage pattern to the electrodes for the z-axis scanner. This causes the scanner to expand and then contract in the vertical direction, generating relative motion

between the cantilever and sample. The deflection of the free end of the cantilever is measured and plotted at many points as the z-axis scanner extends the cantilever towards the surface and then retracts it again. By controlling the amplitude and frequency of the triangle wave voltage pattern, the distance and the speed the AFM cantilever tip travels during the force measurement can be varied.

Some of the important features along a typical force curve are shown schematically in the Figure 3.6. The beginnings of the cantilever's travel (A) not in contact with the surface. In this region if the cantilever feels a long-range attractive (or repulsive) force it will deflect downwards (or upwards) before making contact with the surface. As the tip is brought very close to the surface, it may jump into contact (B) if it feels sufficient attractive force from the sample. Once the tip is in contact with the surface, cantilever deflection will increase (C) as the fixed end of the cantilever is brought closer to the sample. If the cantilever is sufficiently stiff, the probe tip may indent into the surface at this point. In this case, the slope or shape of the contact part of the force curve (C) can provide information about the elasticity of the sample surface.

After loading the cantilever to a desired force value, the process is reversed. As the cantilever is withdrawn, adhesion or bonds formed during contact with the surface may cause the cantilever to adhere to the sample (D) some distance past the initial contact point on the approach curve (B). A key measurement of the AFM force curve is the point (E) at which the adhesion is broken and the cantilever comes free from the surface. This can be used to

measure the rupture force required to break the bond or strength of adhesive forces.

One of the first uses of force measurements was to improve the quality of the AFM images by monitoring and minimizing the attractive forces between the tip and surface. Large adhesive forces can reduce imaging resolution, damage the sample and probe and/or create unwanted artifacts. The force measurements in AFM are now increasingly used not only for improving the quality of images but also to investigate various types of forces between the surfaces, measuring the thickness of the adsorbed molecular layers, nano-indentation studies.

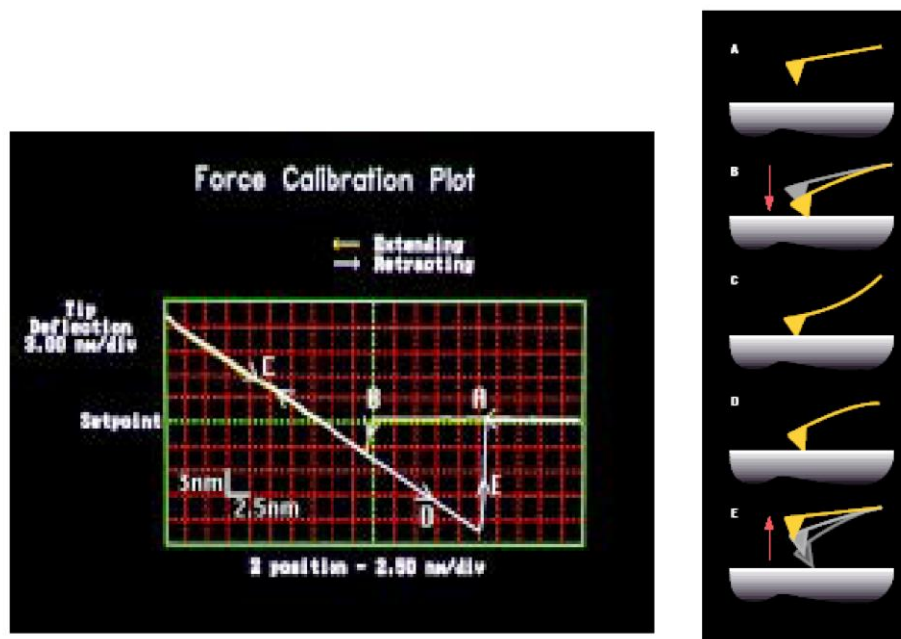


Figure 3.6. Typical experimental force-distance curve and the points along a force curve

3.7. Electrostatic and Magnetostatic Interactions in AFM

Previously, it was mentioned that at relatively large separation distances, long-range forces such as van der Waals force and capillary force dominate the interaction between the probe and sample. This is true for any given experiment since it represents the general behavior of two solids brought into sufficiently close proximity. However, a couple of additional long-range interactions can result if suitable environmental conditions are chosen or if external manipulations are undertaken in a suitable way. These forces are electrostatic and magnetostatic interactions of a charged probe and a ferromagnetic probe respectively with the samples. These long-range electrostatic and magnetostatic interactions in AFM can be used to map the electrical and magnetic properties respectively.

3.7.1. Electrostatic Interactions

If a potential difference V is applied between the probe and sample, the resulting Coulomb force is given by

$$F_c = \varphi(d)V^2 \quad (3.11)$$

where φ depends on the geometry of the probe, on the local geometrical configuration of the sample surface, on the dielectric environment and explicitly on the probe-sample spacing d . If the probe-sample arrangement is modeled by

a simple parallel-plate capacitor with an electrode area A involving a dielectric medium of relative constant ϵ_r , then ϕ can be written as

$$\phi(d) = \frac{\epsilon_0 \epsilon_r A}{2d^2} \quad (3.12)$$

where ϵ_0 is the dielectric constant of vacuum. The difference in surface potential of the probe and tip produces an electrostatic energy given by

$$E_{elec} = \frac{1}{2} CV^2 \quad (3.13)$$

where C is the tip-sample capacitance.

The long-range electrostatic interactions can be exploited to image different electrical and dielectric properties using AFM. For example, if a bias voltage is applied between the conductive tip and the sample, and if the AFM is operated in lift mode, the cantilever is sensitive to the long-range electrostatic forces between the tip and the sample. Coulomb interactions provide an additional long-range attractive contribution. Charges of equal sign on probe and sample would in contrast lead to repulsive forces. Thus, a map of electrostatic variations of the sample surface can be obtained. Similarly, if the tip and probe are operated in contact mode, currents can be measured. This mode is called tunneling AFM or conductive AFM. The Coulomb force given in Eq. (3.11) exhibits a square dependence in the local electrical potential which opens up the possibility to measure potential variations across the sample surfaces. Since ϕ depends on the relative dielectric constant of the sample surface, the electrostatic interactions resulting in the capacitance forces can be used to measure the dielectric properties of the sample surface. (For example,

piezoresponse force microscopy) Also, it has been demonstrated that the electrostatic interactions can also be applied for nonelectrical measurements in order to separate topographical influences from the long-range interactions of interest [169]

3.7.2. Magnetostatic Interactions

If the probe and the sample are both ferromagnetic, then the resulting long-range magnetostatic interactions can either be repulsive or attractive. For a ferromagnetic tip and sample, the magnetic force contribution can be calculated by first estimating the magnetic moment of the tip and then applying

$$F = \nabla(m.B) \quad (3.14)$$

where m is the magnetic moment and B is the magnetic flux density. For a setup with a ferromagnetic tip and a paramagnetic/diamagnetic sample the force will be due to the interaction of the induced moment in the sample and the diverging field of the tip.

The additional long-range interaction forces can be utilized to modify the AFM to characterize magnetic properties. In order to detect the local magnetostatic interactions using an AFM, both the probe and the sample have to be ferromagnetic. The interactions can be imaged by using lift mode so that the long range interaction effects can be isolated from the topographic effects, so that the topography and the magnetic forces can be imaged simultaneously. One

of the most important derivatives of noncontact AFM is the magnetic force microscopy (MFM). The microscope's cantilever is attached with a ferromagnetic tip. The magnetic tip is raster-scanned near the sample surface. The sample's magnetic volume and surface charges lead to a locally varying magnetostatic interaction, which is then detected by either DC (static) or AC (dynamic) detection techniques. AC detection techniques are sensitive to the resonant frequency of the cantilever, depending on the force gradient between the tip and sample. Both the force and force gradient are related to the magnetic field or spatial derivatives of the magnetic field from the sample.

In general, MFM consists of a sharp magnetic tip attached to a cantilever positioned near the sample surface. The cantilever is mounted on a piezoelectric scanner and is driven at a frequency just above the resonant frequency of the cantilever. The oscillating tip is raster scanned across the sample surface in lift mode. In lift mode, the topography of the surface is obtained first in tapping mode and then the tip is raised to a pre-determined height (typically 10-500 nm) above the sample surface. The magnetic tip interacts with the stray magnetic field emanating from the sample. The surface topography is scanned while being monitored for the influence of magnetic forces. These influences are measured using the principle of force gradient detection. The force or force gradient which is exerted on the scanned tip by the sample is measured as a function of the tip position. The presence of magnetic forces on the tip modifies the effective spring constant and shifts the resonance frequency of the cantilever. The frequency shift is detected in three ways: phase detection, which measures the cantilever's

phase of oscillation relative to the piezo drive; amplitude detection, which tracks variations in oscillation amplitude; and frequency modulation, which directly tracks shifts in resonant frequency. Phase detection and frequency modulation generally produces results that are superior to amplitude detection. The topographic and magnetic images are obtained simultaneously. MFM requires ferromagnetic probes that interact with the near-surface stray magnetic fields of the sample. In order to equip microfabricated cantilevers with some magnetic sensitivity, they have to be coated with magnetic thin films. This is usually done by thermal evaporation or sputter deposition of suitable ferromagnetic metals or metal compounds.

3.8. MFM Based Eddy Current Microscopy

In conventional magnetic force microscopy, an oscillating ferromagnetic probe is scanned above the sample surface. The magnetostatic force acting on the cantilever is measured and used to image the magnetostatic variations across the sample surface. In most cases, this magnetostatic interaction is used to generate an image of local magnetic properties. However, according to Faraday's law, an oscillating magnetic field induces eddy currents in a conducting material. Therefore, in the case of MFM, the oscillating probe should induce eddy currents in the sample. Consequently, the forces due to the eddy currents generated in the sample affects the oscillation of the cantilever.

Based on this principle, Hoffmann *et al.* [17] developed an eddy current microscopy technique capable of imaging local electrical conductivity variations with nanometer scale resolution. The technique involves vibrating a cantilever with a magnetic tip above a conducting surface. The oscillating magnetic probe induces eddy currents in the material. These currents lead to an electrodynamic interaction between the probe and sample. The eddy currents in the conducting sample generate opposing magnetic field resulting in the change of the amplitude of the vibrating magnetic tip. Silicon cantilevers with resonant frequencies ranging from 20 to 60 kHz and with spring constants ranging from 0.3 to 3 N/m are used. For conductivity mapping, the cantilevers were first coated by a 90 nm Cr layer. The AFM was operated in lift mode. The topography of the sample is obtained first and then the cantilever is lifted to a height of about 30-50 nm, based on the topography of the sample. When the tip is lifted, it is sensitive only to the long-range magnetic forces between the tip and the probe. Electrical conductivity images were obtained on a sample consisting of TiC precipitates in Al₂O₃ matrix. When the tip scanned over the insulating matrix, the oscillating cantilever does not show much variation in the amplitude or phase. On the other hand, when the tip is scanned over the conductive precipitates, eddy currents are generated in the precipitates producing an opposing magnetic field. As a consequence, the oscillation of the probe is affected, leading to a contrast in the phase, amplitude or frequency-shift. The amplitude gets dampened due to the opposing magnetic field. Thus the conducting region appears with dark contrast due to the reduction in amplitude, while insulating region appears with bright

contrast. The changes in the vibration characteristics of the cantilever are used to image local variation in electrical conductivity. A phase shift of 1° is also detected. Using this technique, Hoffmann *et al.* reported electrical conductivity images with a lateral resolution of about 100 nm.

In contact mode AFM, the sample surface is prone to damage due to excessive forces between the tip and the sample surface. This is due to the fact that the tip is always in contact with the sample surface. In MFM, in spite of relatively large separation distances, there is a potential for sample perturbation. If the stray field of the magnetic tip is too high the magnetization of the sample can be affected during scanning. In order to circumvent this problem, Hoffmann and his co-workers used the same experimental setup, but with a non-ferromagnetic tip, to image the magnetic properties in a nondestructive way. In order to image magnetic properties, the silicon probe was coated by a nonmagnetic Au thin film with a thickness of 60 nm. The probe is oscillated at close proximity to the magnetic samples. In this way, eddy currents are induced within the probe, giving rise to a contrast based on local variations in magnetic properties. Using this experimental configuration, they imaged the magnetic domains in commercial hard disk recording heads and a soft magnetic material.

Even though a significant improvement in spatial resolution can be obtained by the eddy current microscopy developed by Hoffmann *et al.*, for a conventional magnetic tip, the damping force is expected to be very weak [170] and hence the technique is not expected to be sensitive to small variations in electrical conductivity. While developing a theoretical model of the changes

caused by eddy current to the vibration characteristics of the cantilever, Hirsekorn *et al.* [170] raised concerns about the sensitivity of the system used by Hoffmann *et al.*, for small changes in electrical conductivity. Recently, following an approach similar to that of Hoffmann *et al.*, Lantz *et al.* [18] developed an eddy current imaging system with magnetic probes with large magnetic stray field to improve the sensitivity of the eddy current microscopy. The large magnetic field strength is generated by attaching FeNdBLa spherical magnetic particles with radii ranging from 650 to 1000 nm to the end of single crystal silicon cantilever. The cantilevers used have a typical spring constant of 2-2.5 N/m and a resonant frequency of 60-70 kHz. The magnetic stray field of the permanent magnet is at least six orders of magnitude larger than magnetic thin film coated tip used by Hoffmann *et al.* Resistivity measurements were demonstrated on a silicon test structure with a staircase doping profile having varying resistivities. Even though the sensitivity of the system is greatly enhanced, the spatial resolution that was achieved was of the order of the size of the magnetic particle used, in this case, about 650 nm. In order to improve the lateral resolution, they performed the same experiment in UHV conditions where the absence of viscous damping effects results in an increase in the quality factor of the cantilever and thus an increase in the minimum measurable dissipation force. A lateral resolution of about 180 nm was achieved in vacuum. However, the spatial resolution is still poor than the 100 nm resolution achieved reported by Hoffmann *et al.*

3.8.1. Improving Spatial Resolution and Sensitivity in Eddy Current Microscopy

From the above discussion it is evident that using the conventional magnetic force microscopy configuration it is difficult to achieve both high spatial resolution and high sensitivity to local variations in electrical conductivity. A definite way of improving the sensitivity to local variations in conductivity is to use a permanent magnetic particle as a tip. However, this is not always practical, particularly when nanoscale spatial resolution is needed. Another way of increasing the sensitivity is to improve the ability of the cantilever to detect small variations in the forces due to the variations in the property. In general, with a decrease in the spring constant of the cantilever, the ability of the cantilever to detect small forces increases, thus increasing the sensitivity of the force detection. However, in conventional magnetic force microscopy techniques, a stiffer cantilever, vibrated at its resonant frequency, is used in order to make the cantilever sensitive only to the long-range magnetic forces. But by using a stiffer cantilever, it is difficult to measure small forces generated due to very small variations in the electrical conductivity. Therefore, for better sensitivity, a *flexible* cantilever is recommended. However, the cantilever has to be operated in such a way that it is not deliberately vibrated but only sensitive to long-range magnetic forces. The magnetic tips used in conventional magnetic force microscopy techniques have small magnetic field strength. Therefore, the eddy current density that can be induced in the sample material is limited. Moreover, the

strength of magnetic field cannot be increased and hence the eddy current density cannot be adjusted in different materials. An alternative to this would be to externally control the eddy current density generated in the sample and use a commercially available magnetic probe. Thus, the eddy current density in the material can be independently adjusted according to the electrical conductivity of the sample.

The above considerations led to the development of a high-resolution electrical conductivity imaging technique described in this dissertation. The technique is based on a simple principle- detecting the relevant forces due to the interactions between a probe and the sample. These interactions occur due to the generation of the electromagnetic forces in the materials. To detect the changes in the local electrical conductivity of the sample, a magnetic tip is used to map the secondary magnetic field generated by the eddy currents in the sample. To improve the resolution and the sensitivity of the measurement the following were adapted:

(i) a flexible cantilever

(ii) an electromagnetic coil to independently adjust the eddy current intensity in different materials. Instead of vibrating the cantilever, in this technique, the sample is placed in a time-varying magnetic field generated by the coil.

In addition, to separate the topography and the electrical conductivity images from the signal coming out of the AFM photodiode detector, a detector electronics consisting of a lock-in amplifier and an oscilloscope is used. Thus, the topography and the conductivity images can be obtained simultaneously.

The scanning eddy current imaging technique described in this dissertation is capable of imaging magnetic and ferroelectric properties in addition to the electrical conductivity, with some modifications. The major modification is using a different probe for different property. The objective of this research work is to show how a local probe can be used to detect various probe-sample interactions in order to build a multiple material characterization technique based on a single instrument. By combining the principles of AFM and eddy currents, these techniques are capable of achieving high spatial resolution and high sensitivity to local variations in material properties.

CHAPTER 4

DEVELOPMENT OF SCANNING EDDY CURRENT FORCE MICROSCOPY (SECFM)

4.1. Introduction

The principles of working of an AFM and the various interactions between the probe and the sample surface are described in detail in the last chapter. This chapter describes how the AFM is modified to measure the eddy current forces and image the local electrical conductivity variations. The most important element of the AFM is the force sensor. In order to achieve maximum sensitivity, the cantilever should be able to detect small forces generated by the eddy currents in the experiment. Therefore selecting an appropriate cantilever with the required spring constant is important for enhancing the sensitivity of the technique. A mathematical model is first developed to calculate the magnitude of the eddy current forces in a typical metal. The model describes the electrodynamic interactions between the magnetic field of eddy currents and a magnetic tip. The eddy current forces are calculated theoretically for a typical metal. Based on the calculated forces, a suitable cantilever is selected.

To solve an electromagnetic field problem, one must start from the Maxwell's equations. Maxwell's equations are a set of four equations that describe the properties of electric and magnetic fields and relate them to their sources, charge density and current density. The Maxwell's equations have to be modified to accommodate the quasi-static nature of the eddy currents. The modified Maxwell's equations along with necessary boundary conditions are used to calculate the magnetic field strength generated by the eddy currents in a metallic thin plate sample. The magnetic field strength of a typical magnetic tip used in magnetic force microscopy is calculated using monopole and dipole approximations. After calculating the magnetic field strengths of eddy currents and the magnetic tip, the interaction force between the magnetic fields is calculated using a simple mathematic model. The selection of a suitable AFM cantilever sensitive to the calculated eddy current forces is described. Also, a suitable electromagnetic coil is designed for inducing eddy currents in the sample material.

Finally, the necessary modifications to convert the traditional AFM into an eddy current imaging system are described. The modifications are external instrumentation to generate, control the eddy currents in the material and detect the eddy current signals coming out of the photo-diode detector of the AFM. The separation of topography and electrical conductivity images from the AFM signal is discussed. The experimental measurement of eddy current forces is described.

4.2. Maxwell's Equations

The state of excitation which is established in space by the presence of electric charges is said to constitute an electromagnetic field. It is represented by two vectors, \mathbf{E} and \mathbf{B} , called the electric field and magnetic induction respectively. The relation between \mathbf{E} and \mathbf{B} are given by a set of four fundamental equations, namely, Gauss's law for electric fields, Gauss's law for magnetic fields, Faraday's law, and Ampere's law. The four laws, in integral form, are given by:

$$\text{Gauss's law for electricity: } \oint_{\substack{\text{closed} \\ \text{surface}}} \vec{E} \cdot d\vec{A} = \frac{Q_{enc}}{\epsilon_0} \quad (4.1a)$$

$$\text{Gauss's law for magnetism: } \oint_{\substack{\text{closed} \\ \text{surface}}} \vec{B} \cdot d\vec{A} = 0 \quad (4.1b)$$

$$\text{Faraday's law: } \oint \vec{E} \cdot d\vec{s} = -\frac{d\phi_B}{dt} \quad (4.1c)$$

$$\text{Ampere's law: } \oint \vec{B} \cdot d\vec{s} = \mu_0 i_{enc} \quad (4.1d)$$

where ϵ_0 is the electric permittivity of free space, μ_0 is the magnetic permeability of free space, and J is the volume current density. The electric permittivity of free space has the numerical value of

$$\epsilon_0 = 8.85 \times 10^{-12} C^2 / Nm^2 \quad (4.2)$$

and the magnetic permeability of free space has the numerical value of

$$\mu_0 = 4\pi \times 10^{-7} N / A^2 \quad (4.3)$$

The Gauss's law for electricity (Eq. (4.1a)) states that the electric flux through any closed surface equals the charge enclosed (Q_{enc}). Gauss' law is the basic theorem of electrostatics. It is a necessary consequence of the inverse-square law of Coulomb. The flux tubes of a static electric field originate and end on electric charges. On the other hand, tubes of magnetic flux are continuous. They have no sources or sinks. This is a fundamental difference between static electric and magnetic fields. Since it is continuous, the number of magnetic flux tubes entering a volume must leave it. This is given by Gauss's law for magnetism, Eq. (4.1b). The Faraday's law states that a changing magnetic field induces an electric field. In other words, a changing magnetic flux ($d\phi/dt$) induces an emf in the conductor. This phenomenon is known as electromagnetic induction. The negative sign in Faraday's law indicates the direction of the magnetic field. This is explained by Lenz's law which states that the induced currents set up a magnetic field which opposes the cause of the induced current. Ampere's law states that the line integral of magnetic field along any closed path is directly proportional to the net electric current crossing any surface bounded by the closed path.

The four fundamental laws of electromagnetics in differential form are given as

$$\text{Gauss's law for electricity: } \nabla \cdot E = \frac{1}{\epsilon_0} \rho \quad (4.4a)$$

$$\text{Gauss's law for magnetism: } \nabla \cdot B = 0 \quad (4.4b)$$

$$\text{Faraday's law: } \nabla \times E = -\frac{\partial B}{\partial t} \quad (4.4c)$$

$$\text{Ampere's law: } \nabla \times B = \mu_0 J \quad (4.4d)$$

where ρ is the charge density and J is called current density.

The set of equations given in Eq. 4.4(a-d) represent the state of electromagnetic theory over a century ago when Maxwell began his work. However, Maxwell noticed a fundamental flaw in the Ampere's law. If divergence is applied to Eq. (4.4d), we have

$$\nabla \cdot (\nabla \times B) = \mu_0 (\nabla \cdot J) \quad (4.5)$$

Since divergence of a curl is always zero, the left hand side of Eq. (4.5) must be zero. However, the right side of the equation is not always zero. For steady currents, $\nabla \cdot J = 0$, but evidently when dynamic currents are involved the divergence cannot be zero. Thus Ampere's law is bound to fail for non-steady currents. A qualitative analysis of the failure of Ampere's law for non-steady currents can be provide by taking an example of charging up a capacitor. Suppose, a capacitor with two conducting plates separated by a distance d , is being charged. While the capacitor was charging, positive charge accumulates on one plate, and negative charge accumulates on the other, but no current passes between the plates. A capacitor is essentially a gap in a circuit, but because of its nature, the circuit is still complete. However, using Ampere's law to find the magnetic field at a point in space, it is possible to select one closed loop passing through the capacitor, so that no current passes through the closed loop. This would indicate that there was no magnetic field at that point. However, if another closed loop is selected for the same point such that it passes through the wire this time, current flows in the wire and hence there would be a magnetic

field at the same point. Clearly, this is a contradiction. Maxwell corrected the Ampere's law by introducing a new term to the equation of the Ampere's law.

Applying continuity equation ($\nabla \cdot \mathbf{J} = -\frac{\partial \rho}{\partial t}$) and Gauss's law (Eq. (4.4a), the divergence of \mathbf{J} can be written as

$$\nabla \cdot \mathbf{J} = -\frac{\partial \rho}{\partial t} = -\frac{\partial}{\partial t}(\epsilon_0 \nabla \cdot \mathbf{E}) = -\nabla \cdot \left(\epsilon_0 \frac{\partial \mathbf{E}}{\partial t}\right) \quad (4.6)$$

Maxwell added the term $\epsilon_0 \frac{\partial \mathbf{E}}{\partial t}$ to the Ampere's law and the modified Ampere's law is given by

$$\nabla \times \mathbf{B} = \mu_0 \mathbf{J} + \mu_0 \epsilon_0 \frac{\partial \mathbf{E}}{\partial t} \quad (4.7)$$

Such a modification to the Ampere's law changes nothing, as far as magnetostatics is concerned: When \mathbf{E} is constant, the original Ampere's law still holds good. In fact, Maxwell's term is hard to detect in ordinary electromagnetic experiments. However, it plays a crucial role in the propagation of electromagnetic waves. From the modified Ampere's law, it can be clearly seen that just as a changing magnetic field induces an electric field, a changing electric field induces an electric field. Maxwell termed the extra term used in Ampere's law the displacement current.

The final form of the Maxwell's equations after the correction to the Ampere's law in differential form is given as:

$$\begin{aligned}
\nabla \cdot \mathbf{E} &= \frac{1}{\epsilon_0} \rho \\
\nabla \cdot \mathbf{B} &= 0 \\
\nabla \times \mathbf{E} &= -\frac{\partial \mathbf{B}}{\partial t} \\
\nabla \times \mathbf{B} &= \mu_0 \mathbf{J} + \mu_0 \epsilon_0 \frac{\partial \mathbf{E}}{\partial t}
\end{aligned}
\tag{4.8}$$

Together with the force law

$$\mathbf{F} = q(\mathbf{E} + \mathbf{v} \times \mathbf{B})
\tag{4.9}$$

the Maxwell's equations summarize the entire theoretical content of classical electrodynamics. In free space, where ρ and \mathbf{J} vanish, the Maxwell's equations in differential form reduce to:

$$\begin{aligned}
\nabla \cdot \mathbf{E} &= 0 \\
\nabla \cdot \mathbf{B} &= 0 \\
\nabla \times \mathbf{E} &= -\frac{\partial \mathbf{B}}{\partial t} \\
\nabla \times \mathbf{B} &= \mu_0 \epsilon_0 \frac{\partial \mathbf{E}}{\partial t}
\end{aligned}
\tag{4.10}$$

4.2.1. Maxwell's Equations in Matter

The set of equations given by Eq. (4.8) gives the Maxwell's equations in general. However, when the materials are subjected to electric and magnetic polarization, the Maxwell's equations need to be reformulated in terms of the interactions of the materials with the fields. Maxwell's equations in matter are formulated in terms of free charges and currents.

An electric polarization \mathbf{P} produces a bound charge density given by

$$\rho_b = -\nabla \cdot P \quad (4.11)$$

Similarly a magnetic polarization (or magnetization) M results in a bound current given by

$$J_b = \nabla \times M \quad (4.12)$$

Any change in the electric polarization involves a flow of bound charge which must be included in the total current. This current density, denoted by J_p is given by

$$J_p = \frac{\partial P}{\partial t} \quad (4.13)$$

This polarization current has nothing to do with the bound current \mathbf{J}_b . The latter is associated with magnetization of the material and involves the spin and orbital motion of electrons; \mathbf{J}_p , on the other hand, is the result of the linear motion of charge when the electric polarization changes. The total charge density can then be separated into two parts: bound and free charge densities.

$$\rho = \rho_f + \rho_b = \rho_f - \nabla \cdot P \quad (4.14)$$

The current density is separated into three parts:

$$J = J_f + J_b + J_p = J_f + \nabla \times M + \frac{\partial P}{\partial t} \quad (4.15)$$

Gauss's law can now be written as

$$\nabla \cdot E = \frac{1}{\epsilon_0} (\rho_f - \nabla \cdot P) \quad (4.16)$$

The above equation can also be written as

$$\nabla \cdot D = \rho_f \quad (4.17)$$

where D is known as electric displacement and given by

$$\mathbf{D} = \epsilon_0 \mathbf{E} + \mathbf{P} \quad (4.18)$$

The Ampere-Maxwell law becomes

$$\nabla \times \mathbf{B} = \mu_0 \left(\mathbf{J}_f + \nabla \times \mathbf{M} + \frac{\partial \mathbf{P}}{\partial t} \right) + \mu_0 \epsilon_0 \frac{\partial \mathbf{E}}{\partial t} \quad (4.19)$$

Eq.(4.19) can also be written as

$$\nabla \times \mathbf{H} = \mathbf{J}_f + \frac{\partial \mathbf{D}}{\partial t} \quad (4.20)$$

where \mathbf{H} can be written as

$$\mathbf{H} \equiv \frac{1}{\mu_0} \mathbf{B} - \mathbf{M} \quad (4.21)$$

\mathbf{H} is called the magnetic field strength. Faraday's law and Gauss's law for magnetism are not affected by the separation of charge and current into free and bound parts, since they do not involve ρ or \mathbf{J} . Therefore, the Maxwell's equations in matter can be summarized as

$$\begin{aligned} \nabla \cdot \mathbf{D} &= \rho_f \\ \nabla \cdot \mathbf{B} &= 0 \\ \nabla \times \mathbf{E} &= -\frac{\partial \mathbf{B}}{\partial t} \\ \nabla \times \mathbf{H} &= \mathbf{J}_f + \frac{\partial \mathbf{D}}{\partial t} \end{aligned} \quad (4.22)$$

The Maxwell's equations given by Eq. (4.22) reflect a convenient division of charge and current into free and nonfree parts. However, since the equations contain both \mathbf{E} and \mathbf{D} , and both \mathbf{B} and \mathbf{H} , they must be supplemented by appropriate constitutive relations. In electromagnetics, there are four fundamental constitutive relationships to describe the response of a medium to a variety of electromagnetic input. Two of them describe the relationship between the electric

field E and the conductive current J , and the electric displacement D , and the other two describe the relationship between the magnetic field H and the magnetic induction B , and the magnetic polarization M . These relations depend on the nature of the material. For linear media, the constitutive relations are given by the following equations:

$$J = \sigma E \quad (4.23)$$

$$D = \varepsilon E \quad (4.24)$$

$$B = \mu H \quad (4.25)$$

$$M = \chi H \quad (4.26)$$

where σ is the electric conductivity, ε is the dielectric permittivity, μ is the magnetic permeability, and χ is the magnetic susceptibility. For a more convenient mathematical manipulation and using the SI unit system, the electric permittivity and magnetic permeability can be written as

$$\varepsilon = \varepsilon_r \varepsilon_0 \quad (4.27)$$

$$\mu = \mu_0 \mu_r \quad (4.28)$$

where ε_r and μ_r relative dimensionless values of dielectric permittivity and magnetic permeability of a given material respectively. The Maxwell's equations are of profound importance and together with boundary conditions, continuity and other auxiliary relations, form the basic tools for the analysis of electromagnetic problems.

4.3. Electromagnetic Field Equations

Problems involving magnetic fields and current flow are formulated in terms of differential or integral equations as described above. A differential equation describes the behavior of the magnetic field, or some related quantity, at a point in terms of the local source current density. The equation is then solved within a given region, and the influence of sources outside the region is conveyed to the solution by the boundary conditions. Integral equations, on the other hand, express the field in terms of all the sources, the effect of the sources being summed to derive the resultant field. Even though the integral approach seems to be a better way of solving than the differential equation approach, integral equations are usually much more difficult to solve. One reason is that the time rate of change of the magnetic field produces eddy currents, so that the field also appears in the integrand. Hence in the following analysis of the electromagnetic fields, differential approach is taken to solve the electromagnetic fields.

It can be seen from the last two equations of Eq. (4.28) that the electric field and magnetic field from Ampere's law and Faraday's law are coupled with each other. They clearly show the coupling nature of the electromagnetic induction. However, it is relatively more cumbersome to solve those equations mathematically. If the two equations can be de-coupled, it would be easy to solve these equations for the fields.

Consider the Maxwell-Ampere law

$$\nabla \times \vec{H} = \vec{J} + \frac{\partial \vec{D}}{\partial t} \quad (4.29)$$

Applying curl on both sides of Eq. (4.35), we have

$$\nabla \times (\nabla \times \vec{H}) = \nabla \times \vec{J} + \nabla \times \frac{\partial \vec{D}}{\partial t} \quad (4.30)$$

Substituting Eq. (4.29) and Eq. (4.30) in the above equation,

$$\nabla \times (\nabla \times \vec{H}) = \nabla \times (\sigma \vec{E}) + \nabla \times \left(\epsilon \frac{\partial \vec{E}}{\partial t} \right) \quad (4.31)$$

From vector algebra,

$$\nabla \times (\nabla \times \vec{H}) = \nabla (\nabla \cdot \vec{H}) - \nabla^2 \vec{H} \quad (4.32)$$

where ∇^2 denotes the Laplace operator given by

$$\nabla^2 = \frac{\partial^2}{\partial x^2} + \frac{\partial^2}{\partial y^2} + \frac{\partial^2}{\partial z^2} \quad (4.33)$$

and

$$\nabla \times (\sigma \vec{E}) = \sigma (\nabla \times \vec{E}) + (\nabla \sigma) \times \vec{E} \quad (4.34)$$

Substituting Eq. (4.38) and Eq. (4.40) in Eq. (4.37), we have

$$\nabla (\nabla \cdot \vec{H}) - \nabla^2 \vec{H} = \sigma (\nabla \times \vec{E}) + (\nabla \sigma) \times \vec{E} + \nabla \times \left(\epsilon \frac{\partial \vec{E}}{\partial t} \right) \quad (4.35)$$

Now, using Eq. (4.31), and the fact that divergence of B is zero, the first term on the left hand side of Eq. (4.41) reduces to

$$\nabla (\nabla \cdot \vec{H}) = \nabla \left(\frac{1}{\mu} \nabla \cdot \vec{B} \right) = 0 \quad (4.36)$$

Using the Faraday's law from Eq. (4.28), Eq.(4.41) can now be written as

$$-\nabla^2 \vec{H} = \sigma \left(-\frac{\partial \vec{B}}{\partial t} \right) + (\nabla \sigma) \times \vec{E} + \epsilon \frac{\partial}{\partial t} (\nabla \times \vec{E}) \quad (4.37)$$

$$= \sigma \left(-\frac{\partial \vec{B}}{\partial t} \right) + (\nabla \sigma) \times \vec{E} - \epsilon \frac{\partial}{\partial t} \frac{\partial \vec{B}}{\partial t} \quad (4.38)$$

For a linear magnetic or nonmagnetic material of constant conductivity, $\nabla \sigma = 0$, and also using the constitutive relation, $\mathbf{B} = \mu\mathbf{H}$, Eq. (4.44) becomes

$$\nabla^2 \vec{H} = \sigma\mu \frac{\partial \vec{H}}{\partial t} + \epsilon\mu \frac{\partial^2 \vec{H}}{\partial t^2} \quad (4.39)$$

Using the same argument and similar approach a similar equation for electric field using the Faraday's law can be obtained and is given by

$$\nabla^2 \vec{E} = \sigma\mu \frac{\partial \vec{E}}{\partial t} + \epsilon\mu \frac{\partial^2 \vec{E}}{\partial t^2} \quad (4.40)$$

Eq. (4.39) and (4.40) are the de-coupled equations of the Faraday's law and Ampere-Maxwell's law and only one physical quantity either the electric field or the magnetic field appears in one equation.

In a variable field of frequency ω , the time variation of the electric field is in a simple harmonic form given by

$$\vec{E}(t) = E e^{-i\omega t} \quad (4.41)$$

The first and second derivatives of Eq. (4.41) are given by

$$\frac{\partial \vec{E}}{\partial t} = -i\omega \vec{E} \quad (4.42)$$

and

$$\frac{\partial^2 \vec{E}}{\partial t^2} = -\omega^2 \vec{E} \quad (4.43)$$

Substituting Eqs. (4.42) and (4.43) into Eq. (4.40),

$$\nabla^2 \vec{E} = -i\sigma\mu\omega \vec{E} - \epsilon\mu\omega^2 \vec{E} \quad (4.44)$$

Eq. (4.44) can be re-written as

$$\nabla^2 E = -\omega^2 \epsilon\mu \left(1 + \frac{\sigma}{\omega\epsilon} i \right) \vec{E} \quad (4.45)$$

or

$$\nabla^2 E + k^2 E = 0 \quad (4.46)$$

where

$$k^2 = \omega^2 \epsilon \mu \left(1 + \frac{\sigma}{\omega \epsilon} i \right) \quad (4.47)$$

Following a similar approach with magnetic field, we can derive a similar equation for magnetic field given by

$$\nabla^2 \vec{H} + k^2 \vec{H} = 0 \quad (4.48)$$

Eqs. (4.52) and (4.54) are known as Helmholtz equations. It is clear that in Eq. (4.53), if the second term in the bracket on the right hand side has a value much higher than one, then k^2 has a significant imaginary part so that the Helmholtz equation essentially represents diffusion equation. On the other hand, if it is much less than one, k^2 has a significant real part so that the Helmholtz equation essentially represents a wave equation. The term k is related to the penetration depth of the electromagnetic field into a conductor.

If $\sigma \gg \omega \epsilon$, Eqs. (4.45) and (4.46) can be written as

$$\nabla^2 \vec{H} \approx \sigma \mu \frac{\partial \vec{H}}{\partial t} \quad (4.49)$$

$$\nabla^2 \vec{E} \approx \sigma \mu \frac{\partial \vec{E}}{\partial t} \quad (4.50)$$

In this case, electrical conductivity is the controlling parameter in the process. Thus, the above equations represent a conductive, or diffusion process, similar to the diffusion equation used to describe heat conduction. Mathematically, it is a

parabolic equation. The eddy currents usually can be described by the diffusion equations shown above. If $\sigma \ll \omega\epsilon$, then Eqs. (4.45) and (4.46) can be written as

$$\nabla^2 \vec{H} \approx \epsilon\mu \frac{\partial^2 \vec{H}}{\partial t^2} \quad (4.51)$$

$$\nabla^2 \vec{E} \approx \epsilon\mu \frac{\partial^2 \vec{E}}{\partial t^2} \quad (4.52)$$

In these equations, the dielectric permittivity is the prevailing parameter. Dielectric polarization is the controlling process than the conduction. Thus, the above equations represent the process of wave propagation, similar to mechanic waves. Mathematically, this is a hyperbolic equation.

4.3.1. Boundary Conditions

When solving partial different equations in a given region it is necessary to specify sufficient information on the boundary of the region to make the solution unique. Maxwell's equations in differential form govern the interrelationships between the field vectors and associated source densities at points in a given medium. For a problem involving two or more different media, the differential equations pertaining to each medium provide solutions for the fields that satisfy the characteristics of that medium. These solutions need to be matched at the boundaries between the media by employing boundary conditions, which relate the field components at points adjacent to and on one side of a boundary to the field components at points adjacent to and on the other side of the boundary. The

boundary conditions arise from the fact that the integral equations involve closed paths and surfaces whether they lie entirely in one medium or encompass a portion of the boundary.

The boundary conditions are obtained by considering one integral equation at a time and applying to a closed path encompassing the boundary. Let the quantities pertinent to medium 1 and 2 be denoted by subscripts 1 and 2 respectively, and \mathbf{a}_n be the unit vector normal to the surface. Let all normal components at the boundary in both media be directed along \mathbf{a}_n and denoted by a subscript n , and all tangential components at the boundary in both media be denoted by subscript t . Let ρ_s and \mathbf{J}_s be surface charge density and surface current density on the boundary respectively. Then the boundary conditions corresponding to Maxwell's equations in integral form can be summarized as

$$\mathbf{a}_n \times (\vec{\mathbf{E}}_1 - \vec{\mathbf{E}}_2) = 0 \quad (4.53 \text{ a})$$

$$\mathbf{a}_n \times (\vec{\mathbf{H}}_1 - \vec{\mathbf{H}}_2) = \vec{\mathbf{J}}_s \quad (4.53 \text{ b})$$

$$\mathbf{a}_n \cdot (\vec{\mathbf{D}}_1 - \vec{\mathbf{D}}_2) = \rho_s \quad (4.53 \text{ c})$$

$$\mathbf{a}_n \cdot (\vec{\mathbf{B}}_1 - \vec{\mathbf{B}}_2) = 0 \quad (4.53 \text{ d})$$

or, in scalar form, the boundary conditions are written as

$$E_{t1} - E_{t2} = 0 \quad (4.54 \text{ a})$$

$$H_{t1} - H_{t2} = J_s \quad (4.54 \text{ b})$$

$$D_{n1} - D_{n2} = \rho_s \quad (4.54 \text{ c})$$

$$B_{n1} - B_{n2} = 0 \quad (4.54 \text{ d})$$

In words, the boundary conditions state that at a point on the boundary, the tangential components of \mathbf{E} and normal components of \mathbf{B} are continuous,

whereas the tangential components of \mathbf{H} are discontinuous by the amount equal to J_s at that point, and the normal components of \mathbf{D} are discontinuous by the amount equal to ρ_s at that point. The direction of \mathbf{J}_s relative to that of $(\mathbf{H}_1 - \mathbf{H}_2)$ is given by given Eq. (4.53 b).

4.4. Classification of Fields

While every macroscopic field obeys Maxwell's equations in their entirety, depending on their most dominant properties, it is sufficient to consider a subset of, or certain terms only, in the equations. The primary classification of fields is based on their time dependence. Fields which do not change with time are called static fields. Fields which change with time are called dynamic fields. Static fields are the simplest kind of fields, because for them $\partial/\partial t = 0$ and all terms involving differentiation with respect to time go to zero. Dynamic fields are the most complex, since for them Maxwell's equations in their entirety must be satisfied, resulting in wave type solutions. However, if certain features of the dynamic field can be analyzed as though the field were static, then the field is called quasi-static field. If the important features of the field are not amenable to static field analysis, they are generally referred to as time-varying fields. However, in general, quasi-static fields are also time-varying fields. Since, in most general case, time-varying fields give rise to wave phenomena involving velocity of propagation, and time delay, it can be said that quasi-static fields are those time-

varying fields for which wave propagation effects can be neglected. The eddy current problem solution in this work is solved by assuming that the eddy current fields are quasi-static in nature.

4.5. Eddy Current Problem

The field and current variations for conductors subjected to varying external magnetic field are assumed to be sufficiently slow such that the field distribution at any moment of time can be described as static and created by the currents existing at this moment. The validity of this approach is determined by the quasi-static condition of the eddy currents. Quasi-static condition requires that the wavelength λ of the electromagnetic field should be much greater than the dimension of the conductor [171]. For quasi-static fields, it is assumed that the electric and magnetic fields are propagated instantaneously. That means, the displacement current determined by $\partial D/\partial t$ can be neglected. Generally,

$$\frac{\partial D}{\partial t} \sim \epsilon_0 \epsilon' \omega E \quad (4.55)$$

The current density inside a conductor is related to the electric field E by the Ohm's law given by (7) with a constant conductivity σ . Eq. (7) remains valid when the field frequencies are small compared to the inverse mean free time of the electrons in the conductor. For typical metals at room temperatures this condition is satisfied up to the infrared region of the spectrum. In good conductors, i.e. metals with conductivity $\sigma \gg \epsilon_0 \epsilon' \omega$ throughout the whole

frequency interval where the Ohm's law holds, and therefore the conduction current density J is much larger than the displacement current $\partial D/\partial t$. Thus, the displacement current within conductors can be neglected with respect to conductive current for quasi-static fields. This is true even at high frequencies because, usually conductors with high conductivity are generally used.

4.5.1. Eddy Current Field Equations

In view of the quasi-static nature of the eddy currents, the Maxwell's equations have to be modified. Therefore, for eddy current field problems, the Maxwell equations, modified to accord with the quasi-static case, are

$$\nabla \times \vec{E} = -\frac{\partial \vec{B}}{\partial t} \quad (4.56 \text{ a})$$

$$\nabla \cdot \vec{B} = 0 \quad (4.56 \text{ b})$$

$$\nabla \times \vec{H} = \vec{J} \quad (4.56 \text{ c})$$

The constitutive relations for the eddy currents remain the same as given by Eqs. (4.23)-(4.26).

Using Ohm's law, $J = \sigma E$, Eq. (4.56 c) can be written as

$$\nabla \times H = \sigma E \quad (4.57)$$

Applying curl on both sides of Eq. (4.58)

$$\nabla \times (\nabla \times H) = \nabla \times \sigma E \quad (4.58)$$

Substituting Eq. (4.32) and Eq. (4.34) in Eq. (4.59)

$$\nabla(\nabla \cdot H) - \nabla^2 H = \sigma(\nabla \times E) + (\nabla \sigma) \times E \quad (4.59)$$

Now, substituting Eq. (4.25) into Eq. (4.56 b), we have

$$\nabla \cdot (\mu H) = 0 \quad (4.60)$$

From the product rule in vector algebra, the above equation can be written as

$$\nabla \cdot (\mu H) = \mu(\nabla \cdot H) + H \cdot (\nabla \mu) = 0 \quad (4.61)$$

so that

$$\nabla \cdot H = -H \cdot \left(\frac{1}{\mu} \nabla \mu \right) \quad (4.62)$$

substituting Eq. (4.62), Eq. (4.56 a), and Eq. (4.57) into Eq. (4.59), and using Eq. (4.25), we obtain

$$\nabla^2 H = \sigma \mu \frac{\partial H}{\partial t} - \nabla \left(H \cdot \frac{1}{\mu} \nabla \mu \right) - \frac{1}{\sigma} (\nabla \sigma) \times (\nabla \times H) \quad (4.63)$$

Inside a linear magnetic or nonmagnetic material of constant conductivity, $\nabla \mu = 0$ and $\nabla \sigma = 0$. Therefore, Eq. (4.63) reduces to the simpler form

$$\nabla^2 \vec{H} = \sigma \mu \frac{\partial \vec{H}}{\partial t} \quad (4.64)$$

Eq. (4.64) is the well-known equation of the theory of heat propagation.

Eq. (4.64) represents differential equations of the vector quantities \mathbf{H} which have in general three special components varying with time. The components of these equations may be written out for various coordinate systems. A coordinate system is chosen for a problem so that the boundary conditions of the problem may be incorporated as simply as possible. In the Cartesian coordinate system the Eq. (4.64) is expressed by the following three equations:

$$\begin{aligned}
\frac{\partial^2 H_x}{\partial x^2} + \frac{\partial^2 H_x}{\partial y^2} + \frac{\partial^2 H_x}{\partial z^2} &= \sigma\mu \frac{\partial H_x}{\partial t} \\
\frac{\partial^2 H_y}{\partial x^2} + \frac{\partial^2 H_y}{\partial y^2} + \frac{\partial^2 H_y}{\partial z^2} &= \sigma\mu \frac{\partial H_y}{\partial t} \\
\frac{\partial^2 H_z}{\partial x^2} + \frac{\partial^2 H_z}{\partial y^2} + \frac{\partial^2 H_z}{\partial z^2} &= \sigma\mu \frac{\partial H_z}{\partial t}
\end{aligned} \tag{4.65}$$

Eddy currents result directly from Faraday's law and generally have three components in space. However, in many technical cases the problem of eddy currents can be considered in two-dimensional space. In such cases two situations are discussed: (a) H excitation and (b) J excitation. In the first case the magnetic field strength has one component only while the eddy current density is expressed by two components. In the second case the eddy current density has one component and the magnetic field strength has two. The latter, however, is usually described in terms of the magnetic vector potential which has also one component.

In a variable field of frequency ω all quantities depend on the time through a factor $e^{j\omega t}$. The time derivative in the case of the magnetic field intensity can be expressed as

$$H(t) = He^{j\omega t} \tag{4.66}$$

so that

$$\frac{\partial \vec{H}}{\partial t} = -j\omega \vec{H}$$

Equation (4.64) can then be written as

$$\nabla^2 H = j\omega\sigma\mu H \tag{4.67}$$

or

$$\nabla^2 H = k^2 H \quad (4.68)$$

where

$$k^2 = j\omega\sigma\mu \quad (4.69)$$

The constant k is connected with the so-called penetration depth of an electromagnetic wave. From Eq. (4.69) it is evident that the constant k has a complex value. It can be written as

$$k = \sqrt{j\omega\sigma\mu} = (1+j)\sqrt{\frac{\mu\sigma\omega}{2}} = \frac{1+j}{\delta} \quad (4.70)$$

The quantity δ is known as penetration depth and is given by

$$\delta = \sqrt{\frac{2}{\omega\sigma\mu}} \quad (4.71)$$

It can be seen from the above equation that depth of penetration decreases with increasing frequency and conductivity and magnetic permeability.

4.5.2. Boundary Conditions

The Maxwell's equations for the quasi-static case, given by Eqs. 4.56 (a-c) are complemented by the interface conditions which ensure that the magnetic field solution is unique in the case of non-homogeneity of the region. They result from the physical features of the electromagnetic field and are as follows:

$$n \cdot (\vec{B}_1 - \vec{B}_2) = 0 \quad (4.72)$$

$$n \times (\vec{H}_1 - \vec{H}_2) = 0 \quad (4.73)$$

where '1' and '2' denote two sub-regions on the interface of which the above conditions hold, and n is the unit vector normal to the interface. Eq. (13) is under the assumption that there is no surface current and it is always fulfilled in low frequency and finite conductivity problems. The interface conditions are called boundary conditions when the region considered is surrounded by an environment, which enforces the field behavior on its boundary. For non-ferromagnetic materials we can simply conclude that the magnetic field intensity H and magnetic induction B are continuous at the boundary: $H_1 = H_2$.

The continuity of the tangential field components H_t together with the fact that $\nabla \times H = 0$ outside the conductor results in the continuity of the normal component of the rotation $(\nabla \times H)_n$. Consequently, the quantity $(\sigma E)_n$ is also continuous on the surface of the conductor. Outside the conductor $\sigma = 0$. Hence, the normal component of the electric field E_n inside the conductor also vanishes at the boundary as well as the current density normal component J_n so that $E_n = 0$, $J_n = 0$ on the surface. From the above discussion it can be concluded that in the quasi-static approximation a variable magnetic field does not create free charges on the surface of the conductor.

4.6. Theoretical Modeling of Eddy Current Forces

When a metal is placed in a time-varying magnetic field, electromagnetic forces act on the material due to the generation of eddy currents. The

experimental technique described in the current work detects the forces due to the eddy currents in a sample material by means of an AFM cantilever. The sensitivity of force measurement in AFM depends on the spring constant of the cantilever. For higher sensitivity, the cantilever should be able to detect very small interaction forces. Therefore, it is important to know forces generated in a metal subjected to an AC magnetic field and the spring constant of the cantilever capable of measuring those forces. In this section, a theoretical model is developed to describe the electrodynamic interactions between the sample and AFM cantilever-tip and then calculate the forces due to eddy current in a metal. In order to determine the eddy current forces, magnetic fields due to eddy currents in the sample and the magnetic field of the tip have to be determined individually. Based on the eddy current forces, a suitable cantilever is designed.

4.6.1. Eddy Current Forces

Lenz's law predicts a force that opposes the motion of a conductor passing through a non-uniform magnetic field. Motion of the conductor's free charge through the field results in magnetic forces that drive current in the conductor. This current, in turn, interacts with the magnetic field and results in a net magnetic force acting on the conductor. This current is called an eddy current. Eddy current forces are important from a practical point of view. For example, the eddy current forces are used as braking force in trains. In this work,

eddy current forces between a magnetic tip and the magnetic field generated by eddy currents are used to characterize the electrical conductivity of the sample. The contrast in the images obtained is explained based on the eddy current forces generated in different materials. Thus, eddy current force is an important parameter in this study. The following theoretical modeling of the eddy current forces helps to design an appropriate cantilever sensitive to the forces generated by the eddy currents.

Before attempting to model the eddy current forces, it is important to know the assumptions made in solving the eddy current problem. For the analysis of eddy current fields, the following assumptions are made:

1. The conducting media are assumed to be non-magnetic in nature i.e. $\mu_r = \text{constant}$. This is a basic assumption which makes the problem linear.
2. The conducting media are assumed to be homogeneous and isotropic. These conditions imply constant conductivity and electrical permittivity at every point of the medium and in every direction.
3. All excitations vary sinusoidally with time, with angular frequency $\omega = 2\pi f$. The frequencies considered in this study are assumed to be low i.e. in the radio frequency range. Moreover, by choosing radio frequencies, the skin depth is chosen to be larger than the thickness of the samples studied in this work.
4. The displacement current is neglected because at the low frequencies, the dimensions of the system are small compared with the

wavelength. This assumption has the consequence that the charge distribution on the conducting surface of the material is absent.

5. The sample material is neither electrically nor magnetically polarizable.

To evaluate the eddy current force, the magnetic field strength in the sample generated by the eddy currents and the magnetic field strength of the magnetic tip have to be determined independently.

4.6.2. Magnetic Field Due to Eddy Currents in the Sample

A schematic of the experimental configuration is shown in Figure 4.1. A small cylindrical coil of radius a , with number of turns (N), placed under a nonmagnetic electrically conducting sample is excited by a time-varying electromagnetic signal. The diameter of the coil is much smaller than the lateral dimensions of the sample. The thickness (t) of the sample is very small compared to the diameter of the coil. The electromagnetic signal through the coil produces a uniform magnetic field within the diameter of the coil. \mathbf{B}_0 is the normal component of the uniform magnetic field. The time-varying normal component of the magnetic field generates eddy currents in the sample. The effect of the tangential component is neglected. The magnetic field generated by the eddy currents in the sample is assumed to be uniform within the diameter of the coil.

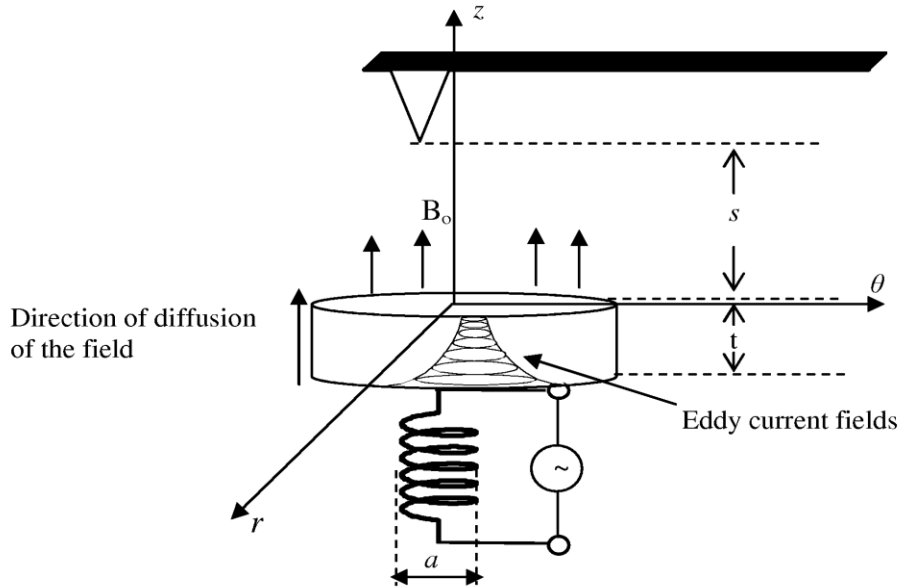


Figure 4.1. A non-magnetic electrical conductor placed in time varying external magnetic field. The eddy current density decreases exponentially as a function of increasing thickness of the conductor.

Maxwell's equations in differential form, together with the constitutive relations and boundary conditions, allow for the unique determination of the fields of \mathbf{E} , \mathbf{B} , \mathbf{D} , and \mathbf{H} for a given set of source distributions with densities \mathbf{J} and ρ . However, in some cases, the solution can be simplified if the fields can be derived from electromagnetic potentials. The potentials are scalar potential and vector potential. In this analysis, a scalar potential approach is taken to simplify the solution.

The eddy current density, \mathbf{J} that is generated in the sample in turn generates a secondary magnetic field \mathbf{H} . The Maxwell's electromagnetic equations provide the relationship between \mathbf{J} and \mathbf{H} as,

$$\nabla \times \vec{H} = \vec{J} \quad (4.74)$$

$$\nabla \times \vec{J} = -(j\omega\mu_0\sigma H_z + j\omega\sigma B_0)e_z \quad (4.75)$$

where ω is the angular frequency of the signal exciting the coil, μ_0 is the magnetic permeability of the free space, σ is the conductivity of the material, H_z is the magnetic field strength in the normal direction to the sample, \mathbf{e}_z is a unit vector in the z-direction and $\nabla^2 = -1$. In the case of eddy currents, the fields are quasi-stationary and hence the displacement currents can be neglected.

In cylindrical coordinates, the current density \mathbf{J} can be represented by a scalar potential function $u(r)$ [172] as

$$\vec{J} = \frac{1}{t} (\nabla \times u(r)) \vec{e}_z \quad (4.76)$$

Using Eq. (4.76) in Eq. (4.74) results in

$$\nabla \times \left(H - \frac{1}{t} u(r) \right) \vec{e}_z = 0 \quad (4.77)$$

From the above equation, the z-component of \mathbf{H} created in the sample due to the eddy current generation can be written as

$$H_z = \frac{1}{t} u(r) \quad (4.78)$$

By substituting Eq. (4.76) in Eq. (4.75) the scalar potential function $u(r)$ for the region $0 \leq r < a$ can be written as

$$\frac{\partial^2 u}{\partial r^2} + \frac{1}{r} \frac{\partial u}{\partial r} = j\omega\mu_0\sigma u(r) + j\omega\sigma t B_0 \quad (4.79)$$

Following Krakowski [173] the solution to Eq. (4.79) can be written as,

$$u(r) = \frac{tB_0}{\mu_0} \left[\frac{I_0(kr)}{I_0(ka)} - 1 \right], \quad 0 \leq r \leq a \quad (4.80)$$

where

$$k = \sqrt{\omega\mu_0\sigma} e^{j\frac{\pi}{4}} \quad (4.81)$$

$$I_0(kr) = ber(kr) + j bei(kr) \quad (4.82)$$

$$I_0(ka) = ber(ka) + j bei(ka) \quad (4.83)$$

where $I_0(kr)$ and $I_0(ka)$ are zeroth order Bessel functions. The constant k is related to the penetration depth of the electromagnetic waves into the sample and is of great importance in the eddy current testing. The constant k can be written in terms of the penetration depth as $k = (1+j)/\delta$ where δ , is the depth of penetration or skin depth.

In accordance with Eq. (7), the current density in the plane of the sample \vec{J}_θ , can be calculated as

$$\vec{J}_\theta = -\frac{1}{t} \frac{du}{dr} = \frac{kB_0}{\mu_0} \left[\frac{I_1(kr)}{I_1(ka)} \right] \quad (4.84)$$

where

$$I_1(ka) = \exp\left(-j\frac{\pi}{4}\right) [ber(ka) + j bei(ka)] \quad (4.85)$$

$I_1(ka)$ is a first order Bessel function. Once the scalar potential function $u(r)$, is calculated, the normal component of the secondary magnetic field strength in the sample (H_{sample}) generated due to eddy currents can be calculated using Eq.(4.78). This normal magnetic field interacts with the magnetic field of the magnetic tip of the AFM.

4.6.3. Magnetic Field of the Tip

The tip used in this study is in the form of a cone that is coated with a thin film of magnetic cobalt. A schematic of the magnetic tip used in this study is shown in Figure 4.2.

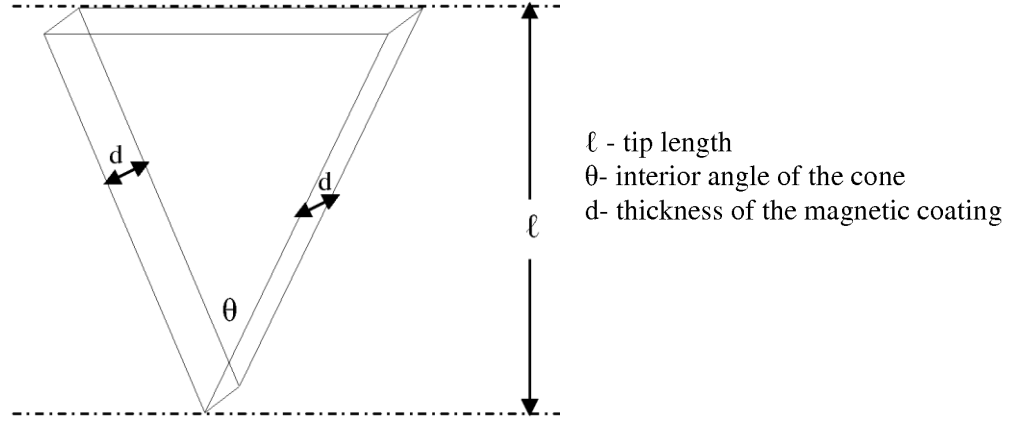


Figure 4.2. Schematic of a cone shaped AFM magnetic tip along with its dimensions

A magnetic tip with a magnetization \mathbf{M} creates a magnetic field $\mathbf{H}_{\text{tip}}(\mathbf{r})$ [170] given by,

$$\vec{H}_{\text{tip}}(s) = \frac{1}{4\pi} \int_V d^3r_i \left\{ \frac{3\vec{M}(s-r_i)}{|s-r_i|^5} (s-r_i) - \frac{\vec{M}}{|s-r_i|^3} \right\} \quad (4.86)$$

where r_i is the location within the magnetic coating of volume V and s is the distance between the tip end to the sample surface. The magnetic field of the tip can be obtained by modeling the tip with dipole or monopole approximation. If the dimensions of the tip are small compared to the distance between the tip and sample surface, then the magnetic tip can be considered as a dipole. In this case, the magnetic field can be obtained by substituting $r_i = 0$. Thus, the magnetic field for dipole approximation is given by

$$\begin{aligned}\vec{H}_{TD}(s) &= \frac{1}{4\pi} \left\{ \frac{3\vec{M} \cdot s}{s^5} s - \frac{\vec{M}}{s^3} \right\} \int_v d^3 r_i \\ &= \frac{1}{4\pi} \left\{ \frac{3m \cdot s}{s^5} r - \frac{m}{s^3} \right\}\end{aligned}\quad (4.87)$$

where $m = \mathbf{MV}$ is the dipole moment of the tip. The dipole approximation uses the assumption that all dimensions of the volume of the magnetic coating of the tip are small compared to its distance to the sample surface. A typical value for the length of the tip is usually between $3\mu\text{m} - 10\mu\text{m}$ and the distance between sample and the tip is approximately 100 nm . Therefore, the dipole approximation is not valid for the present case. If the square of the dimensions within a cross-section of the tip is small compared to the square of its distance to the sample surface, then the tip can be modeled using monopole approximation. Additionally, the cross section of the tip should be constant throughout the length l of the tip and the tip should be long compared to the distance between the tip and the sample surface. In general, however, the cross-section of the tip is not constant throughout the length of the tip. But the length of the tip is long compared to the tip-sample separation. Moreover, if the tip is assumed to be a cone of small interior angle, the condition that the square of the cross-sectional dimensions of the tip being smaller than the square of the separation distance will be satisfied. Therefore, the monopole approximation is valid for a typical magnetic tip used in AFM. In such case, the magnetic tip of the tip is given by [170]

$$\vec{H}_{ipM} = -\frac{q}{4\pi} \frac{r_i}{s^3} \quad (4.88)$$

where q is the monopole moment of the tip and is given by

$$q = \frac{MV}{l} \quad (4.89)$$

which is magnetized along the z-axis.

Eq. (4.78) and Eq. (4.88) give the magnetic field strength generated by the sample and the tip respectively. To determine the forces due to the eddy currents, we assume that the magnetic field of the tip [$\mathbf{H}_{\text{tip}}(\mathbf{r})$] is concentrated at the end of the tip. The eddy current generated magnetic field in the sample (\mathbf{H}_z) is located at a point along the axis of the electromagnetic coil in the sample. The eddy current force is then calculated using the magnetic field strengths of the sample and the tip.

When there is no sample between the coil and the magnetic tip, the interaction is between the magnetic field of the coil and the stray magnetic field of the tip. For a coil of N turns, and length l , an AC current I produces a magnetic field given by

$$H_{\text{coil}} = \frac{NI}{l} \quad (4.90)$$

The force of interaction between the magnetic field of tip and the coil, F_{TC} is calculated as

$$F_{\text{TC}} = 4\pi\mu_0 d^2 H_{\text{tip}} H_{\text{coil}} \quad (4.91)$$

where d is the separation distance between the tip and the coil. When a metallic sample is introduced between the tip and the coil, eddy currents are generated in the metal and they screen the magnetic field reaching the tip, thus decreasing the force experienced by the tip. The force between the magnetic tip and the magnetic field due to eddy currents in the sample is then given by

$$F_{TS} = 4\pi\mu_0 d^2 H_{tip} H_{sample} \quad (4.92)$$

The difference in the forces given by Eqs (4.91) and (4.92) is called eddy current force which is a function of the sample conductivity.

As an example, the theoretical eddy current force for a typical electrical conductor is determined. The electromagnetic coil that is used in the experiments has radius (a) of 6mm and has 100 turns of 36 gauge copper wire. The field (B_0) that is generated at the top of the coil when a current of 86 mA flows through is approximately 17 kA/m. The thickness of the magnetic coating (d) and the volume of the coating of the tip (V) are taken as 60 nm and $4.2 \times 10^{-19} \text{ m}^3$ respectively. The magnetization, M of the coating is approximately 114 kA/m [174]. In a typical metallic, electrically conducting sample, with an electrical conductivity of $10^7 (\Omega\text{m})^{-1}$, the theoretical eddy current force is approximately in the range of 50 pN at a separation distance of 100 nm.

4.7. Selection of Cantilever and Tip

For high vertical and lateral resolutions, a very sharp tip attached to an extremely low spring constant cantilevers has to be used. Measuring small forces (0.1nN or lower) using an AFM requires a cantilever with a spring constant typically in the range of 0.05-1 N/m [155]. Based on the theoretical calculation of the eddy current forces, if a cantilever with a magnetic film coated tip is to be sensitive to small changes in eddy current forces, the spring constant should be

smaller than 0.5 N/m. The sensitivity of most single crystal silicon cantilevers used in traditional MFM has higher stiffness with a spring constant of 2 N/m or higher and hence may be only marginally suitable for eddy current force imaging. Therefore, a cantilever with a spring constant in the range of 0.05-1 N/m is required for higher sensitivity. While attempting to design such probes, we came across a commercially available [175] magnetic film coated tip attached to a cantilever with a spring constant of 0.1 N/m with a nominal tip radius of 10 nm. The force sensitivity of this cantilever is within the range of the calculated theoretical eddy current forces in a typical electrically conducting nonmagnetic metal. The spring constant of the cantilever used in this study is much lower than the spring constant of the cantilevers used by Hoffmann *et al.* and Lantz *et al.*

4.8. Scanning Eddy Current Force Microscope

As described in previous chapter, a standard AFM, which can image the surface topography, can be converted to image material properties after some modifications. The eddy current imaging system based on AFM also requires modifications to the standard AFM. In this study, a Digital Instruments DI 3000 AFM was used to convert it into an eddy current imaging system. The modifications to the AFM are external electronic instrumentation which facilitates the imaging electrical conductivity images. These modifications doesn't affect the routine surface topography imaging of AFM; rather, the electronic instrumentation

helps acquiring both surface topography and electrical conductivity images simultaneously at a given location on the sample surface. A schematic of the experimental setup used to image electrical conductivity with external modifications is shown in Figure 4.3. Dimension 3000 AFM is a multimode instrument that can be used in different imaging modes. The cantilever deflection is measured by optical method using a four-quadrant photodiode detector. The maximum scan area of the scanner in the AFM is about 100 μm . A commercially available magnetic tip-cantilever was selected for the purpose of electrical conductivity imaging. The cantilever is a V-shaped cantilever with an average spring constant of 0.1 N/m, which is in the range of the suitable spring constant to measure pico-Newton forces generated by eddy currents in metals. A typical cantilever used in this study is shown in Figure 4.4. The cantilever is made of silicon nitride with a resonant frequency of about 25 kHz. The typical dimensions of the cantilever are 153 μm in length and 44 μm in width. The tip is coated with a thin layer of Co/Cr. The thickness of the magnetic coating is in between 10-250 nm. The magnetic tip has a nominal radius of approximately 10 nm.

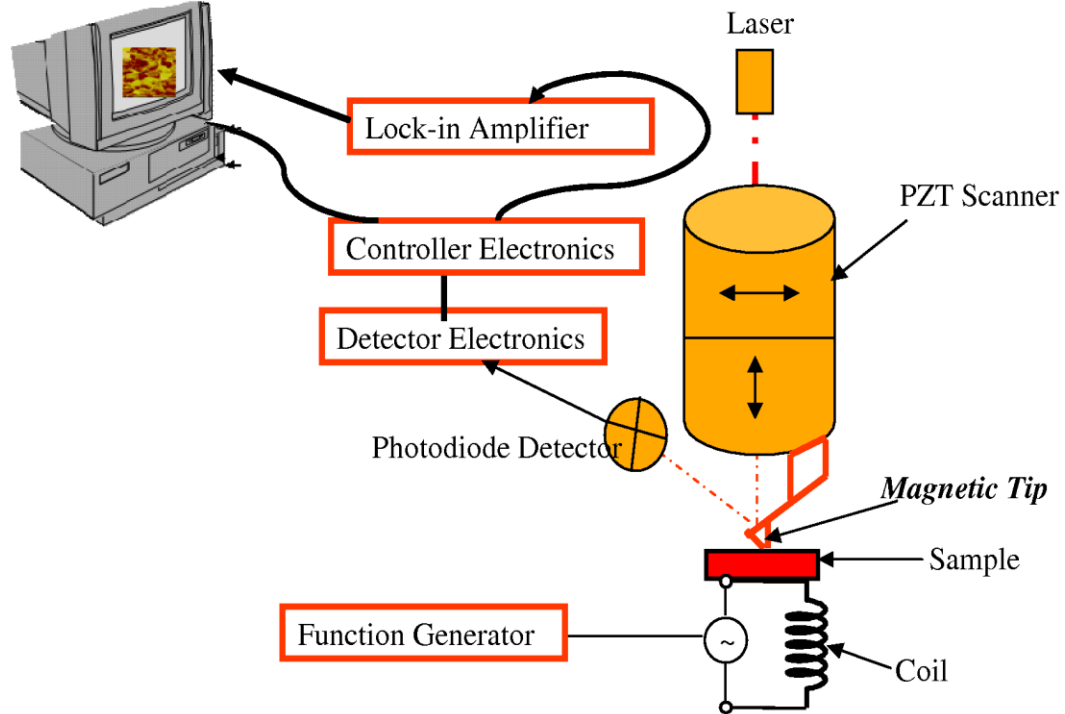


Figure 4.3. Schematic of AFM-based eddy current imaging system

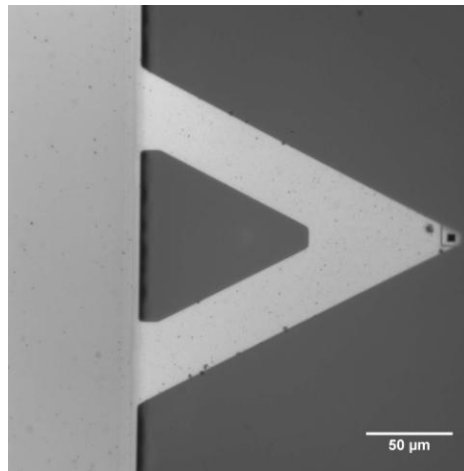


Figure 4.4. V-shaped cantilever used in the experiments. The tip is attached at the end of the cantilever.

For the purpose of generating eddy currents in the sample material, a tiny air-core electromagnetic coil is designed. The coil has a radius of 6 mm and was wound with 100 turns of 36 gauge copper wire. The sample is placed on a small

diameter coil. One face of the sample faces the circular end of the coil. The opposite face of the sample faces the cantilever with the magnetic film coated tip. The coil is excited by a sinusoidal radio frequency signal from a signal generator (hp 33120A) with appropriate frequency and amplitude. The current in the coil generates alternating magnetic field around it. The axial magnetic field near the circular end is intersected by the sample. The changing magnetic field generates eddy currents in the sample. The strength of the eddy currents exponentially decreases as the distance increases from the coil into the sample. The circular eddy currents in the sample produce a magnetic field that is opposing the magnetic field of the coil. The combined electromagnetic force of oscillating magnetic field and the eddy currents in the conducting sample produces oscillations of the magnetic tip-cantilever. For the purpose of measuring eddy current forces, the cantilever-tip is positioned in a static position over a single point on the sample. The oscillation amplitude of the cantilever due to eddy current forces is detected by the four-quadrant photo-detector. The eddy current force is then determined by multiplying the amplitude with the spring constant of the cantilever. The amplitude of the oscillation of the cantilever is dependent proportional to the conductivity of the sample material.

For imaging the electrical conductivity of the sample surface, the tip is raster-scanned across the sample surface. The AFM is operated in lift mode. The surface topography is first obtained and then the tip is raised to a certain height and the resulting tip-sample interactions are measured. In the case of electrical conductivity imaging, the interactions are long-range magnetic forces between

the magnetic tip and the magnetic field generated by the eddy currents in the sample. Thus, electrical conductivity imaging is performed in non-contact fashion. The output of the photo-detector and the signal that excites the coil are fed into a lock-in amplifier (SR 844). A lock-in amplifier is used to measure the amplitude and phase of signals buried in noise. It acts as a narrow band pass filter which removes much of the unwanted noise while allowing through the signal which is to be measured. The frequency of the signal to be measured and hence the passband region of the filter is set by a reference signal, which has to be supplied to the lock-in amplifier along with the unknown signal. The reference signal must be at the same frequency as the modulation of the signal to be measured. The lock in amplifier measures the differential amplitude and the difference in the phase between the signal to the coil and the photo-detector signal. The difference in amplitude and the phase detected by the lock-in amplifier is proportional to the electrical conductivity of the material beneath the magnetic tip. Both amplitude and phase can be used to obtain conductivity images. The output of the detector can be seen on the screen of an oscilloscope. The output of the lock-in amplifier and the controller electronics of the AFM are used to generate surface topography and electrical conductivity images sample simultaneously. The current experimental set up is similar to that of a conventional eddy current testing. However, in the current set up, the pick-up coil is replaced by a sharp magnetic probe. The resolution in this case is purely dependent on the diameter of the probe rather than on the size of the coil. The coil in this case allows controlling the eddy current density in the material.

One of the advantages of the new technique is that it can be used to characterize other material properties like magnetic, magneto-acoustic and ferroelectric properties in addition to the electrical properties. This is accomplished by utilizing an appropriate probe to measure the interactions between the induced currents and the materials. Experimentally, this requires some modifications. The modifications are the type of the probe used and the imaging mode employed to image the interactions between the probe-sample. To image electromagnetic acoustic interactions, a non-magnetic tip is used to scan the metallic sample in contact mode. For imaging magnetic properties, a non-magnetic tip in contact mode is used. For ferroelectric measurements, a magnetic tip in contact mode and lift mode is used.

CHAPTER 5

CHARACTERIZATION OF ELECTRICAL CONDUCTIVITY OF BULK CONDUCTORS

5.1. Introduction

The previous chapter described the modifications to a standard AFM to develop an eddy current imaging system. This chapter presents the application of the technique for the characterization of electrical conductivity of bulk conductors. Eddy current forces are experimentally measured on single crystal samples of copper, cadmium, aluminum and platinum. The experimental forces are compared with theoretical and finite element model results. The effect of separation distance between the tip and the sample is studied. The forces are then used to quantitatively measure the electrical resistivity of a single crystal copper sample. The imaging capabilities of the new technique are demonstrated first by imaging 7 μm diameter carbon fibers reinforced in a polymer matrix. Then, the technique is used to image small changes in electrical conductivity. A polycrystalline titanium alloy with two phases having a small electrical conductivity variation is chosen for this purpose. The contrast in both cases is explained based on the eddy current forces generated in the material. The

magnitude of the eddy current forces is proportional to the electrical conductivity. The variation in the electrical conductivity in the eddy current images of the titanium alloy is expressed in terms of eddy current forces measured in different materials previously. Finally, the spatial resolution of the technique is determined by imaging carbon nanofibers reinforced in a polymer matrix.

5.2. Materials

For the purpose of calibrating the eddy current force, three single crystal metallic samples of copper, cadmium, aluminum and a polycrystalline platinum were chosen. The electrical conductivity of the chosen samples are respectively $5.961 \times 10^7 (\Omega\text{m})^{-1}$, $3.745 \times 10^7 (\Omega\text{m})^{-1}$, $1.36 \times 10^7 (\Omega\text{m})^{-1}$, and $0.94 \times 10^7 (\Omega\text{m})^{-1}$.

For the purpose of demonstrating the imaging capability of the instrument to map the electrical conductivity variations, two samples were selected. The first sample is a carbon fiber reinforced polymer composite sample. Carbon fibers with an average diameter of $7 \mu\text{m}$ were reinforced in a polymer (PEEK) matrix. The polymer composite sample was chosen because of its huge variations in the electrical conductivity between the conductive fibers and the insulating polymer matrix. The second sample is a titanium alloy, Ti-6Al-4V with dual phases. Ti-6Al-4V has duplex microstructure with α and $(\alpha+\beta)$ phases. The $(\alpha+\beta)$ grains consist of platelets of α and the β phase with the β phase present in between the α plates. The α phase grains are fairly large and uniformly spread across the

sample. The titanium alloy was chosen because of its richness in the variations of electrical conductivity. The α phase of the alloy has a hexagonal close pack (hcp) crystal structure and the β phase has body centered cubic (bcc) crystal structure. It is known based on the crystal structure differences that the electrical conductivity of the α phase (hcp) is different compared to that of the β phase (bcc) [176]. Further more, the electrical conductivity of hcp structure is anisotropic while that of the bcc structure is isotropic. The combination of the presence of electrical conductivity anisotropy mixed with an isotropic structure makes Ti-6Al-4V sample unique for electrical conductivity imaging using this technique.

5.3. Experimental Setup

The experimental setup to image electrical conductivity described in the previous chapter was used to image the electrical conductivity of the composite and titanium alloy samples. During operation, a small electromagnetic coil placed under the sample is excited with a sinusoidal signal of appropriate frequency and amplitude using a signal generator. The oscillating magnetic field generates eddy currents in the sample. The combined electromagnetic force that results from the coil's oscillating magnetic field together with opposing magnetic field that is generated by the eddy currents in the conducting sample produces oscillations of the cantilever. The oscillation amplitude detected by the photo-

detector and the signal from the function generator are fed into a lock-in-amplifier. The output of the lock-in-amplifier and the controller electronics of the AFM are used to develop surface topography and eddy current microscopy images.

The AFM was operated in the lift mode. In the lift mode, the sample surface topography is obtained in the first pass and then the tip is raised to a user-selected height (usually 100 nm) and is scanned over the sample surface to obtain eddy current images. The area scanned in most cases is less than 100 mm and to a first approximation the electromagnetic field distribution over this area can be considered uniform.

The eddy current force as measured in the present experimental configuration can be described, as a reduction in the force, between the magnetic tip and the magnetic field of the coil, due to the presence of a nonmagnetic metallic sample between the magnetic-tip and the coil. The eddy current force on each of the samples was measured in two steps. In the first step, an insulator was placed on the coil and excited with an AC signal. The force experienced by the AFM magnetic tip-cantilever due to the magnetic field generated in the coil was then measured (F_{Ins}). In the second step, the insulator was replaced by the metallic sample and the force is measured (F_M) similar to the first step. The difference between the two forces [$F_{Ins} - F_M$] is the eddy current force in the sample and is directly dependent on the electrical conductivity of the metallic sample.

To determine the eddy current forces, the magnetic tip was positioned at a fixed distance from the surface of the sample. The electromagnetic coil was excited with a sinusoidal voltage to operate at the cantilever at its resonant frequency. The sinusoidal oscillations of the cantilever were recorded on the insulator and then on the metal. The experiment was repeated for several distances between the sample and the magnetic tip-cantilever. The oscillation amplitude and the dynamic spring constant of the cantilever were used to determine the eddy current force for all the samples.

5.4. Results and Discussion

In the following sections, results of eddy current force measurements and eddy current images obtained on different metals are presented and discussed.

5.4.1. Experimental Eddy Current Force Measurement

To demonstrate the force measuring capabilities of the instrument, the technique was first used to compare the amplitude of the oscillating cantilever when the tip was positioned over a single crystal copper sample with the analogous amplitude when the tip is positioned over an electrical insulator. The magnetic tip was positioned at a distance of 50 nm from the surface of both the copper and the insulator. A coil placed under the sample was excited with a

sinusoidal voltage. The frequency was varied and it was observed that the maximum amplitude of oscillation occurred at a frequency of 82 KHz. This was one of the resonant frequencies of the cantilever. When the cantilever was on the epoxy the resonant frequency was observed to be 87 kHz. The magnetic tip-cantilever oscillations were recorded at 82 kHz when the tip was positioned on the epoxy matrix (insulator) and then on the copper single crystal. Figure 5.1 compares the amplitudes of the vibrations of the cantilever over copper and insulator. Over the insulator the magnetic tip senses the magnetic field generated by the coil without shielding and hence the amplitude of oscillations was significantly large. On the other hand, when the magnetic tip was positioned over the copper, the amplitude of oscillation was reduced. The oscillating magnetic field produces eddy currents in copper, which in turn generate an opposing magnetic field, thus partially screening the field sensed by the magnetic tip. As the electrical conductivity increases, the eddy current density increases and a much higher damping of the oscillations will be observed. The conductivity of copper is $5.961 \times 10^7 \text{ } (\Omega\text{m})^{-1}$ and at the frequency of 82 kHz, the skin depth was larger than the actual thickness of the sample. Thus the entire sample can be considered to be in a uniform magnetic field. In the single crystal copper, the electrical conductivity is uniform throughout the sample. Hence, the eddy current force will be constant at all regions of the single crystal copper.

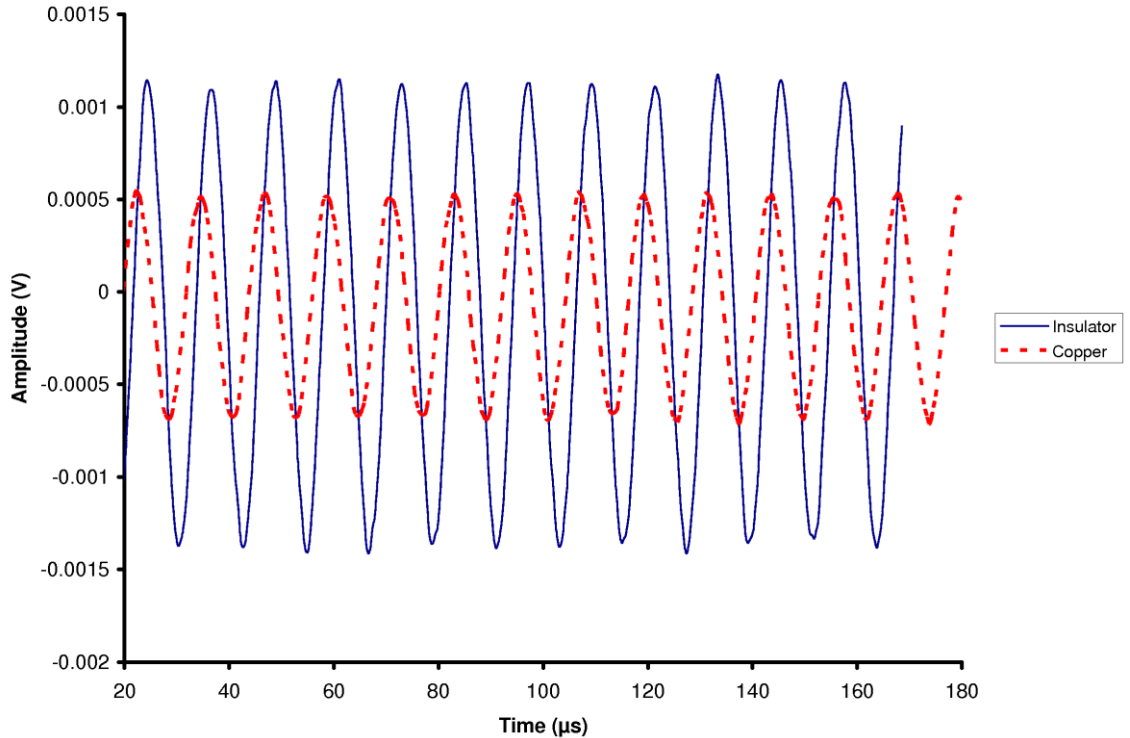


Figure 5.1. Comparison of cantilever vibration amplitudes over copper and insulator at a frequency of 82 KHz. The waveform on copper has been slightly shifted in time to show the waveforms separately.

The amplitude of the oscillations can be used to evaluate the electromagnetic force between the sample and the magnetic tip. The force on the magnetic tip can be calculated using the Hooke's law. It has been found that in some cases, the spring constant values provided by the manufacturer are up to a factor of two or more in error compared to their original value [177]. Moreover, the cantilever in our experiments was used at the resonant frequency of the cantilever. Therefore, for accurate measurement of the force, the spring constant of the cantilever needs to be modified by the quality factor, Q of the cantilever to obtain dynamic spring constant. Several methods were proposed to calculate the effective spring constant of AFM cantilevers. For the V-shaped cantilever, the most popular approach to the analytical evaluation of its normal spring constant

is the use of parallel beam approximation (PBA) [178]. The fundamental principle of the PBA is that the V-shaped cantilever is approximated by two rectangular cantilevers joined in parallel. Then, by calculating the spring constant of the rectangular cantilever, the spring constant for the V-shaped cantilever can be obtained. However, when adapting the PBA approximation, the width and length of the rectangular arms are chosen appropriately. The correct dimensions that need to be considered in PBA approximation are shown in Figure 5.2. Therefore, the original V-shaped cantilever is equivalent to a cantilever which has its skewed rectangular arms replaced by a single unskewed rectangular plate of length L_1 and width $2W_1$ as shown in Figure 5.2.

Sader *et al.* [179] developed a method to determine the spring constant of a rectangular AFM cantilever by measuring resonant frequency and quality factor of the cantilever in air, and plan view dimensions of the cantilever. In their method, the spring constant k is given by

$$k = 0.1906\rho_f(2W_1)^2 L_1 Q \Gamma_i \omega_f^2 \quad (5.1)$$

where ρ_f is the density of the air, Γ_i is the imaginary component of the hydrodynamic function, Q is the quality factor of the cantilever, W and L_1 are the equivalent dimensions of an unskewed rectangular cantilever, and ω_f is the resonant frequency. The hydrodynamic function depends on the Reynolds number and is independent of the cantilever thickness and density. The Reynolds number, Re , is given by

$$Re = \frac{\rho_f \omega W^2}{4\eta} \quad (5.2)$$

where η is the viscosity of the surrounding fluid, in this case, air. Then, the imaginary component of the hydrodynamic function Γ_i is given by

$$\Gamma_i = \frac{b_1}{\sqrt{\text{Re}}} + \frac{b_2}{\sqrt{\text{Re}}} \quad (5.3)$$

where b_1 and b_2 are constants and the values are 3.8018 and 2.7364 respectively.

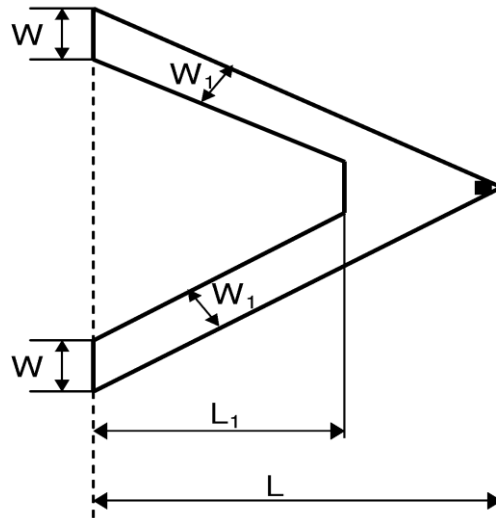


Figure 5.2. A schematic of the AFM cantilever used in the experiments showing dimensions. The tip is shown as a solid rectangle at the end of the cantilever.

The quality factor of the cantilever was obtained from the resonance curve of the cantilever and found to be about 13.5. The equivalent dimensions, L_1 and W_1 , of the V-shaped cantilever are taken as 90 μm and 34 μm respectively. The resonant frequency of the cantilever is taken as 82 kHz. The density and the viscosity of the air are taken as 1.18 kg m^{-3} and $1.86 \times 10^{-5} \text{ kg m}^{-1}\text{s}^{-1}$ respectively. The dynamic spring constant of the cantilever was then calculated using Eq. (5.1) and was found to be 0.18 N/m. Using the dynamic spring constant the force experienced by the magnetic tip on the epoxy and on the copper were evaluated to be 54 pN and 13 pN respectively. The difference between the two forces

caused by the eddy currents in the copper sample was 41 pN. The eddy current force calculated using the theoretical model for copper was approximately 30 pN.

The experimentally measured eddy current force at a separation distance of 50 nm between copper sample and the magnetic tip is in good agreement with the theoretically calculated value. In order to test the eddy current force over the entire range of separation distances, the amplitude of oscillation was measured at several fixed distances up to 3000 nm. The amplitude was then converted into force and plotted against separation distance. The effect of separation distance between the magnetic tip and the sample on the eddy current force is shown in Figure 5.3. The force-distance curve shows that at smaller separation distances the force is very large and that the force decreases dramatically as the separation distance increases. From the theoretical calculations, the eddy current force distance curve is expected to follow inverse square law over the entire range of distance. Even in classical MFM the force-distance curves which are supposed to follow an inverse square law do not exhibit this behavior at all separation distances. The reasons have been described as being due to the contribution of other forces in the distance ranges. This is also true in the case of eddy current forces. The inverse square law is observed between distances of 50-200 nm. Beyond distances of 500 nm the eddy current forces are weak and the amplitude of vibration is in the same range as thermal noise. This explains the saturation behavior observed in Figure 5.3 after a separation distance of 500 nm.

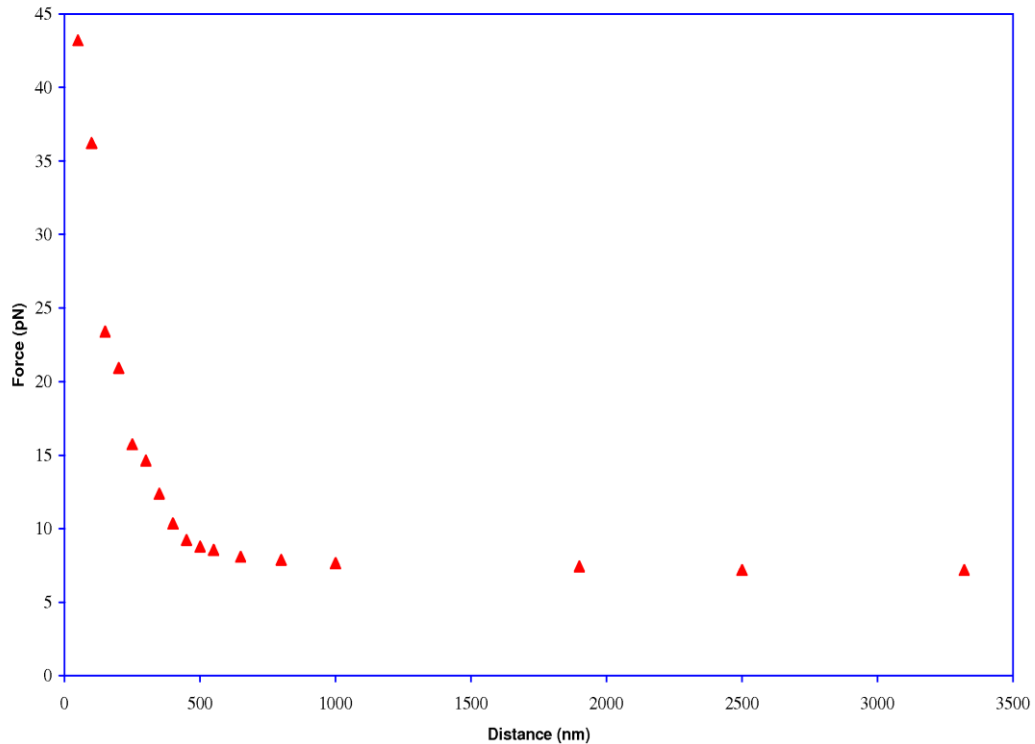


Figure 5.3. Eddy current force in the copper sample as a function of separation distance between the magnetic tip and the sample.

Figure 5.4 compares the amplitudes of the oscillations of the cantilever for different metals. The amplitude of oscillations was obtained at a frequency of 82 kHz and at a fixed distance of 50nm from the surface of the sample. It is observed that the peak to peak amplitude is different for different metals. In the metallic materials, platinum has the largest amplitude and copper has the least amplitude. Cadmium and aluminum are in between. In general, the amplitude of oscillation decreases with increasing electrical conductivity of the metals. The amplitude of oscillations, on the insulator is at least five times higher than that of the metals. Hence, it was not included in the figure for a direct comparison. The difference between the amplitude of oscillations between the insulator and the metallic samples is attributed to the generation of eddy currents in the metal.

In an insulator, the magnetic field generated by the coil passes through the insulator without attenuation. Hence, the entire magnetic field generated by the electromagnetic coil is sensed by the magnetic tip, producing large amplitude oscillations of the cantilever. On the other hand, in the presence of a metal, the oscillating electromagnetic field generates eddy currents in the metal shielding significant portion of the magnetic field that is sensed by the magnetic tip. The amplitude of oscillations of the cantilever on the metal is at least five times smaller than on insulator, because of the shielding effect.

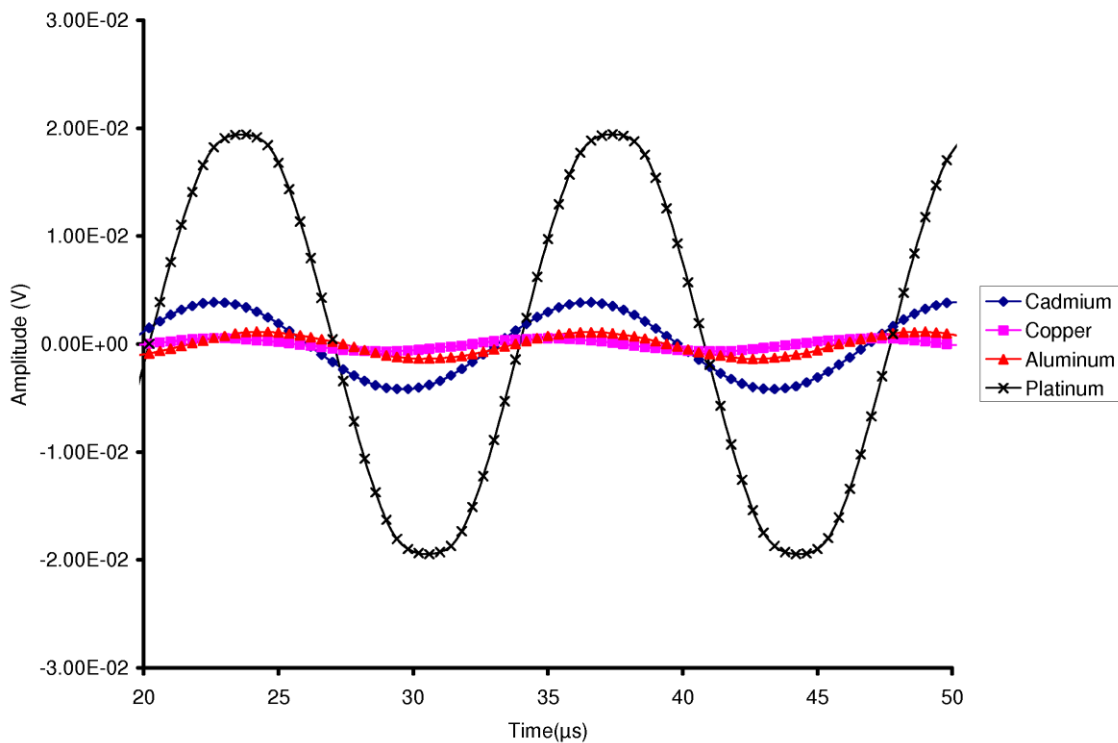


Figure 5.4. Amplitude of oscillation of the AFM cantilever on different metallic samples. The waveforms on the metals have been slightly shifted in time to show the waveforms separately.

The amplitude of the oscillations can be used to evaluate the electromagnetic force between the sample and the magnetic tip. The force on the

magnetic tip can be calculated using the Hooke's law with the knowledge of spring constant of the cantilever. The dynamic spring constant of 0.18 N/m was determined using the resonance curve for the cantilever. Using the dynamic spring constant the force experienced by the magnetic tip on the insulator, copper, aluminum, cadmium and platinum were measured to be 80 pN, 15 pN, 24 pN, 50 pN and 65 pN respectively. The eddy current force in a metal is the difference between the force due to the insulator (F_{ins}) and the force due to the metal (F_m). Thus, the resulting eddy current forces on metallic single crystals of copper, aluminum, cadmium and platinum are 65 pN, 56 pN, 30 pN, and 15 pN respectively. Figure 5.5 shows a plot of the variation of eddy current force with electrical resistivity of metallic materials. The eddy current force is directly proportional to the electrical resistivity of the metals examined.

The interaction of the magnetic field due to the eddy currents and the magnetic field of the tip gives rise to electromagnetic force experienced by the magnetic tip. The theoretical calculations based on the above equations for eddy current force at a separation distance of 50 nm is approximately 55 pN, 40 pN, 32 pN and 20 pN for copper, aluminum, cadmium and platinum respectively. The experimentally measured eddy current forces on the same metallic single crystals are 65 pN, 56 pN, 30 pN, and 15 pN respectively. The experimental measurements are in reasonably good agreement with the simple theoretical calculations.

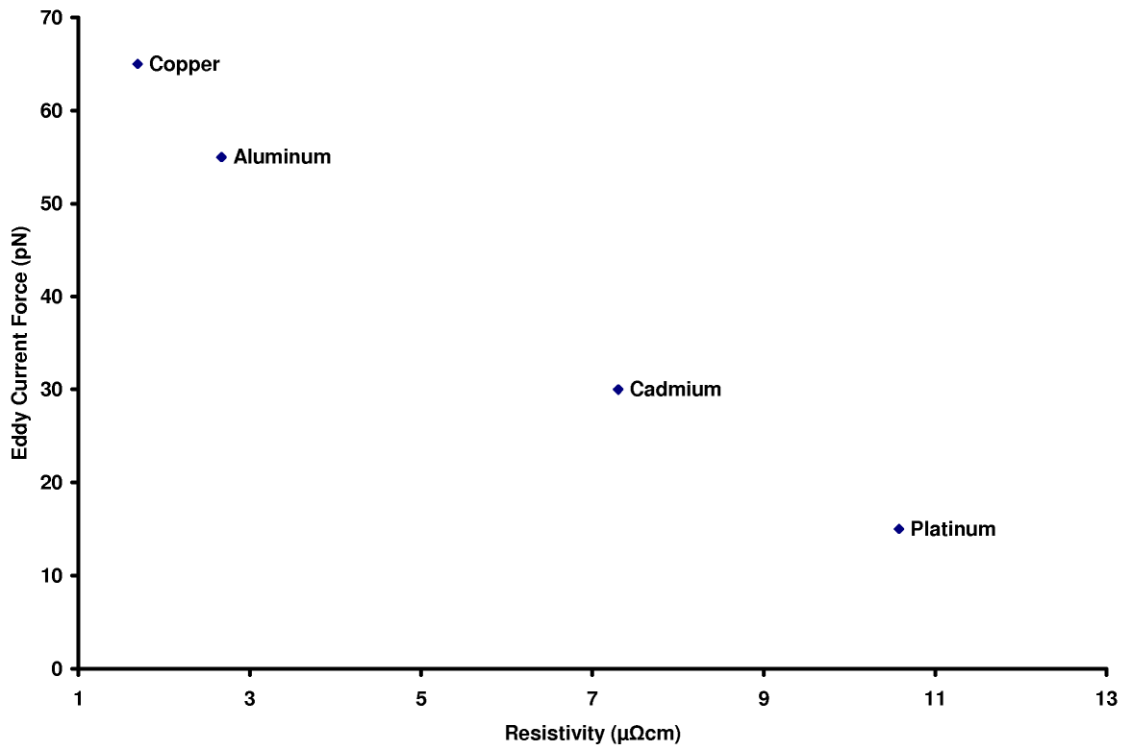


Figure 5.5. Variation of eddy current force as a function of electrical resistivity in different metals.

5.4.2. Finite Element Modeling of Eddy Current Forces

The finite element analysis (FEA) method is a powerful computational technique for approximate solutions to a variety of real world engineering problems having complex domains subjected to general boundary conditions. The basis of FEA relies on the decomposition of the domain into a finite number of sub-domains (elements) for which the systematic approximate solution is constructed by applying the variational or weighted residual methods. In effect, FEA reduces the problem to that of a finite number of unknowns by dividing the domain into elements and by expressing the unknown field variable in terms of

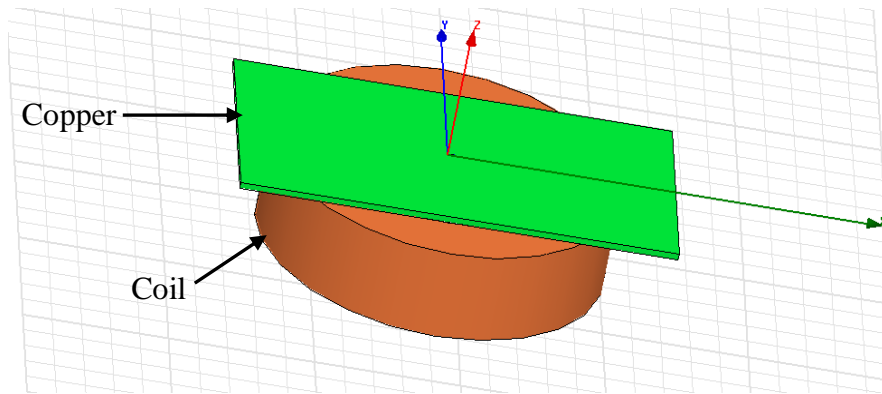
the assumed approximating functions within each element. These functions are defined in terms of the values of the field variables at specific points, referred to as nodes. Nodes are usually located along the element boundaries, and they connect adjacent elements. Finite element methods can be used to solve electrical, structural, thermal, fluid and other engineering problems. The finite element method is one of many accepted methods of numerically solving complicated fields where analytical solutions are not sufficient. Finite elements have proven to be very robust for general electromagnetic analysis.

Maxwell 3D is an interactive software package that uses finite element analysis (FEA) to solve three-dimensional electric, magnetostatic, eddy current and transient problems. Maxwell solves the electromagnetic field problems by solving Maxwell's equations in a finite region of space with appropriate boundary conditions and when necessary, with user-specified initial conditions in order to obtain a unique solution. In Maxwell 3D, the fundamental unit of the finite element is a tetrahedron (four-sided pyramid). These tetrahedral elements are constructed together to build a finite element mesh. The desired field in each element is approximated with a 2nd order quadratic polynomial known as basis function. All other quantities are determined from the field solution in part or in all of the solution space. Once the tetrahedral elements are defined, the finite elements are placed in a large sparse matrix equation, which is then solved using standard matrix solution techniques such as Gaussian elimination or Choleski conjugate gradient method.

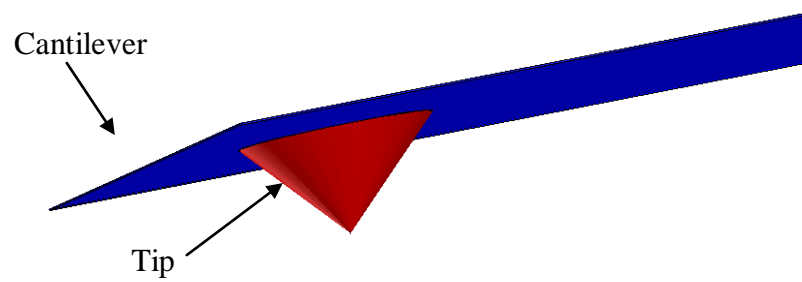
To model the eddy current microscopy, we used the eddy current solution type of Maxwell 3D. The eddy current solver computes steady state, time-varying (AC) magnetic fields at a given frequency. It is assumed that all the objects are stationary. Magnetic field (H) and magnetic scalar potential are the two quantities that are computed using this solver. Current density (J) and magnetic flux density (B) are automatically calculated from the magnetic field (H). Derived quantities such as force, torque, energy and inductances can be calculated from the basic field quantities.

The model showing coil, sample, tip and cantilever of the eddy current microscope is shown in Figure 5.6. The coil used in our experiments was built using 100 turns of Gauge 36 Copper wire. The radius and height of the coil are 3 mm and 3 mm respectively. A single crystal copper sample was used to compute the eddy current forces. The thickness of the copper sample was 200 μm . In the eddy current microscopy experiments, frequency of excitation is an important parameter in obtaining better quality images. It is important to excite the coil at the resonant frequency of the cantilever so that the cantilever vibrates with maximum amplitude. For the single crystal copper sample, the resonance occurred at a frequency of 82 KHz. Therefore, the model was analyzed at a frequency of 82 KHz. The coil was excited with a current of 130 mA corresponding to the frequency of 82 KHz. The tip is modeled as a cone with the base of the tip as 4 μm and diameter of 10 nm. The tip is coated with 60 nm thick cobalt coating to make the tip magnetic. The cantilever was modeled as a rectangular cantilever with dimensions of 170 μm X 36 μm X 0.06 μm . The tip was

positioned at a distance of 50 nm from the sample surface and the model was analyzed for force on the tip. The force in the z-direction was calculated as 52 pN. The theoretical and experimental eddy current forces on the copper sample were 70 pN and 55 pN respectively. Thus, the force obtained using Maxwell 3D model are in good agreement with theoretical and experimental forces. In addition to the forces in z-direction, Maxwell 3D predicted forces in x and y directions. The force in x direction was about 35 pN. This shows that there are lateral forces acting on the tip and consequently, there would be lateral deflections of the cantilever. One of the major advantages of an atomic force microscope is that it can detect both normal and lateral deflections of the cantilever. Since the eddy currents exert normal and lateral forces on the tip, the flexible cantilever in the AFM of the eddy current system can detect the lateral eddy current forces. This is not possible in the conventional eddy current testing methods unless a probe is positioned in the lateral direction. The lateral force can be used to obtain eddy current images in the lateral direction. Thus the AFM based eddy current imaging system is capable of obtaining eddy current images in both normal and lateral directions. The eddy current density (J) and magnetic field strength (H) vector distribution in the copper sample is shown in Figure 5.7 and Figure 5.8 respectively.



(a)



(b)

Figure 5.6. Maxwell 3D model showing (a) coil, sample, and (b) tip and cantilever

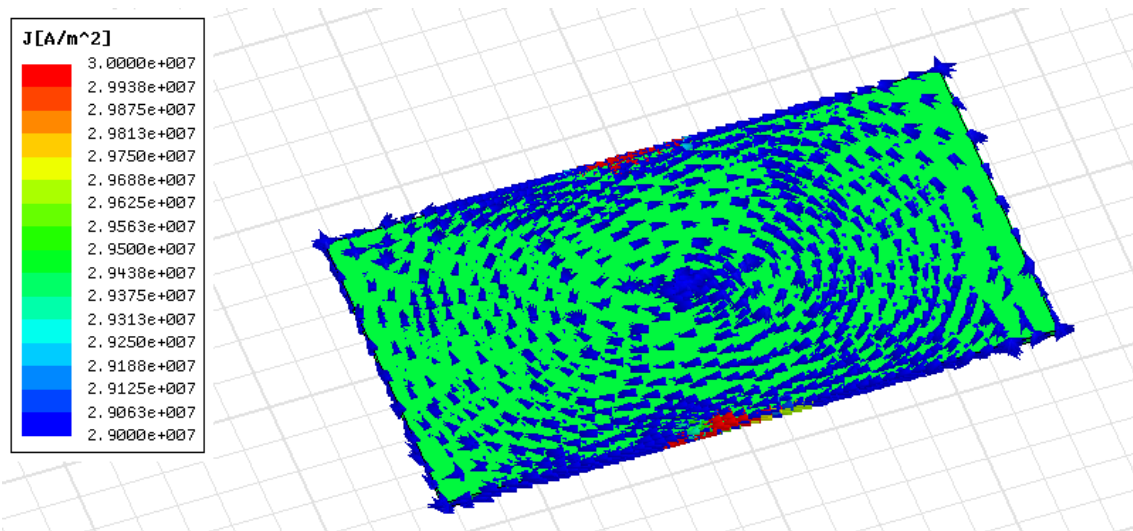


Figure 5.7. Eddy current density (J) in the copper sample

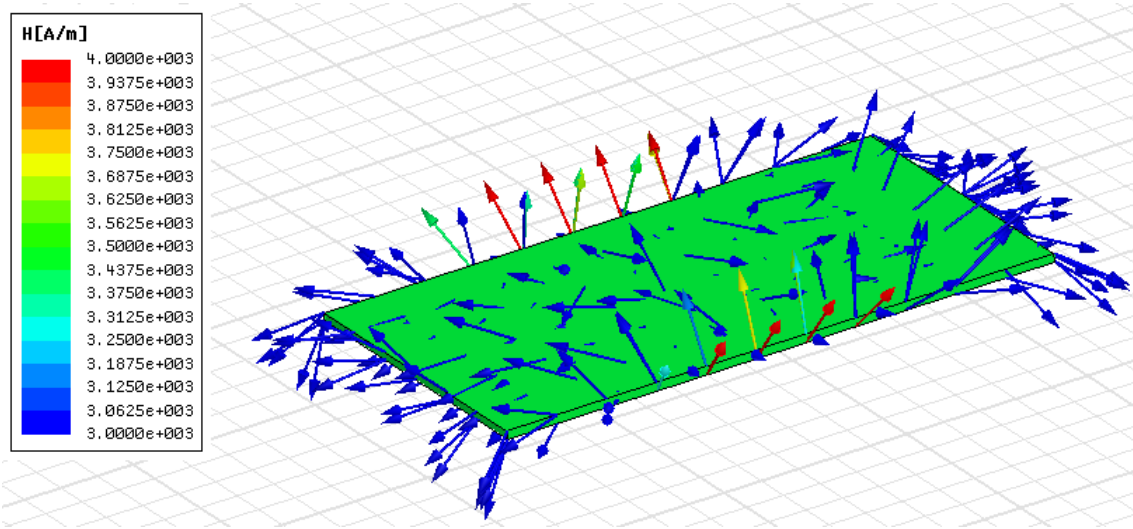


Figure 5.8. Magnetic field strength vector (H) in the copper sample

5.4.3. Quantitative Measurement of Electrical Resistivity

Eddy currents can be associated with the magnetization and described by a complex magnetic susceptibility. The experimental characterization of susceptibility is made by inductance measurements [180-182], generally using an induction bridge driven at audio frequencies. After solving Maxwell's equations with proper boundary conditions, the susceptibility can be related to the conductivity. In this way it is possible to determine the electrical conductivity with a noncontact setup. In this work, we use the quasi-static nature of the eddy currents to determine diamagnetic susceptibility of metals. The equivalent magnetization is experimentally characterized by eddy current force

measurements. Forces associated with eddy currents are important from a practical point of view.

The relation between forces and eddy currents can be derived by several methods. The simplest method is to calculate directly the forces appearing on the eddy currents due to the magnetic field. It can also be characterized by calculating first the magnetization and then employing the usual expressions describing forces on magnetized media.

The force on a magnetized medium is given by [183]

$$F_z = \frac{\mu_0 \chi_m S}{2} [H_z^2(z)] \quad (5.1)$$

where S is the cross section surface. H_z is the normal component of the magnetic field generated by the eddy currents. Since the susceptibility associated with eddy current is very small, it is assumed that the magnetic field is not appreciably disturbed after introducing the sample in the electromagnetic field. It is also assumed that $\mu = \mu_0$.

The sample used in this experiment is a thin wire of copper with a diameter of 250 μm and a length of 0.1 mm. The copper wire is embedded in an epoxy. The coil used to generate eddy currents in the sample has a radius of 0.6 mm and a height of 0.8 mm with 100 turns. The magnetic field generated by a solenoid turns N and length l is given by

$$H = \frac{NI}{l} \quad (5.2)$$

Therefore, value of the quantity in the brackets in Eq. (5.1) is

$$H^2 = 4.02 \times 10^{10} I^2 \quad (5.3)$$

so that Eq. (5.1) can be written as

$$F = \frac{\mu_0 \chi_m S}{2} [4.02 \times 10^{10} I^2] \quad (5.4)$$

where μ_0 is the magnetic permeability of the free space given by $4\pi \times 10^{-7}$ N/A², and S is the cross section area of the copper wire.

The magnetic susceptibility associated with eddy currents for a cylindrical geometry is given by [171]

$$\chi_m = \frac{J_2 \left[\frac{(1+i)a}{\delta} \right]}{J_0 \left[\frac{(1+i)a}{\delta} \right]} \quad (5.5)$$

where δ is the skin depth of the eddy currents given by

$$\delta = \sqrt{\frac{2}{\mu_0 \sigma \omega}} \quad (5.6)$$

J_0 and J_2 are Bessel functions of the first kind, and a is the radius of the cylinder.

Eq. (5.2) can be expanded in a power series about $a/\delta = 0$. The result up to the second order is given by

$$\chi_m = \frac{1}{8} i a^2 \mu_0 \sigma \omega - \frac{1}{48} a^4 \mu_0^2 \sigma^2 \omega^2 \quad (5.7)$$

In the power series expansion of χ_m only the even terms, for which χ_m is real, contribute to the force. Imaginary terms are related to dissipation losses. Thus, the force is equated to the real part of χ_m . The first real term in Eq. (5.4) is the second order expansion. Therefore, the magnetic susceptibility is given by

$$\chi_m^{(2)} = -\frac{\mu_0^2 \sigma^2 \omega^2 a^4}{48} \quad (5.8)$$

The minus sign in Eq. (5.5) indicates the diamagnetic character of the magnetization, because eddy currents screen the applied magnetic field.

The copper wire embedded in the epoxy is placed on the coil and is excited by a radio frequency sinusoidal signal. The frequency of the excitation was varied and a maximum amplitude was observed at a frequency of 84 kHz, which was one of the resonant frequencies of the cantilever. Therefore, the excitation frequency of the coil was set at 84 kHz. The sinusoidal excitation of the coil produces a time-varying magnetic field around the coil which in turn induces eddy currents in the sample. As a consequence, forces are acted upon the eddy currents which are given by Eq. (5.1). These forces are measured by a magnetic tip which is attached to the AFM cantilever. The strength of the forces is directly proportional to the conductivity of the material. The forces on the cantilever are measured as a function of input current to the coil.

Figure 5.9 shows a plot of the eddy current forces as a function of the square of the current to the coil. According to Eq. (5.4), a plot between the force and current should follow a straight line behavior. As expected, the plot shown in Figure 5.9 follows a linear behavior. The net forces acting on the eddy currents act upward, indicating the diamagnetic behavior of the eddy currents in the copper sample. According the Eq. (5.4), the slope of this line is determined by the diamagnetic susceptibility whose slope is determined by the diamagnetic susceptibility related to eddy currents. The calculated susceptibility of the copper wire from the plot is $\chi_m = -7.2 \times 10^{-6}$. The value diamagnetic susceptibility of the copper in the literature is -9.7×10^{-6} at room temperature. The experimental value

agrees with the value provided in the literature. Once the susceptibility is known, Eq. (5.5) can be used to calculate the conductivity of the sample. Thus, it is possible to quantitatively measure the electrical conductivity using the scanning eddy current force microscopy.

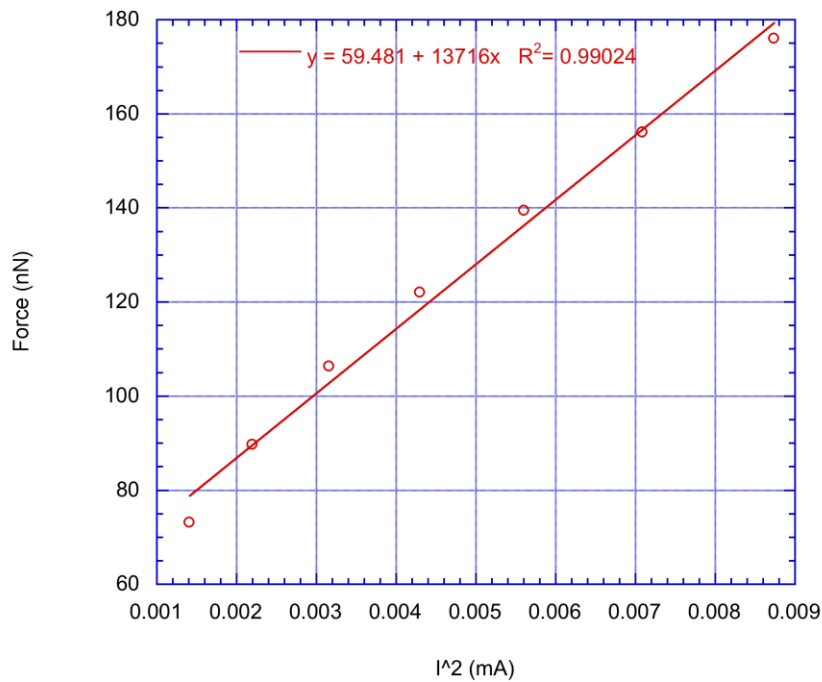


Figure 5.9. Forces on the cantilever due to eddy currents measured as a function of the input current to the coil. Line corresponds to linear fit of the data.

5.4.4. Imaging Local Electrical Conductivity Variations

The previous section described in detail the experimental measurement of eddy current forces in different metals. It was seen that the magnitude of the eddy current force is a function of the material conductivity. Thus, the eddy current forces can be used to map the electrical conductivity of the sample. As the conductivity changes, the magnitude of the eddy current forces changes. This

leads to variation in the forces as the tip scans the surface. Thus, by measuring the changes in eddy current forces locally, it is possible to image the variations in the local electrical conductivity. This section demonstrates the imaging capability of the scanning eddy current force microscopy of materials having different electrical conductivities.

Eddy current imaging requires optimization of the coil operating conditions and the cantilever characteristics. Although the cantilever can vibrate at any frequency that excites the coil under the sample, to obtain high sensitivity, it is necessary to operate at the resonant frequencies of the cantilever. To obtain the resonance characteristics of the cantilever coupled with the sample, the coil is connected to one port of a network analyzer (HP 8753D) and the output of the photo-diode detector of AFM is connected to the second port. The input frequency to the coil was continuously varied from 10 kHz to 500 kHz. The network analyzer treats the coil-sample-magnetic tip-cantilever-photo-detector combination as a two-port electrical network. Although several network characteristics can be measured, for the particular application the transmission characteristics (S_{21}) are important. The S_{21} parameter as a function of frequency for titanium alloy sample is shown in Figure 5.10. Maximum transmission and hence the resonance peaks were observed at frequencies of 92 and 275 KHz, and 510 kHz. Many smaller resonance peaks were observed up to frequency of 1 MHz. While the images can be obtained at any of these frequencies, images obtained at 92 kHz would show good contrast, since maximum amplitude was observed at 92 kHz. The resonance peak was observed to be at 92 kHz in

titanium alloy, while in copper the resonance was observed at a frequency of 82 kHz. The difference in the resonant frequency may be attributed to many factors including thickness, electrical conductivity, eddy current forces, skin depth etc. Therefore, the frequency of excitation needs to be carefully chosen for different material for better contrast in the images. A network analyzer can be used to measure the resonance characteristics at every position while scanning the magnetic tip cantilever and thereby obtain eddy current images. That procedure, however, is time-consuming. Hence, a function generator is used to set the frequency at the resonant frequency and perform electrical conductivity imaging.

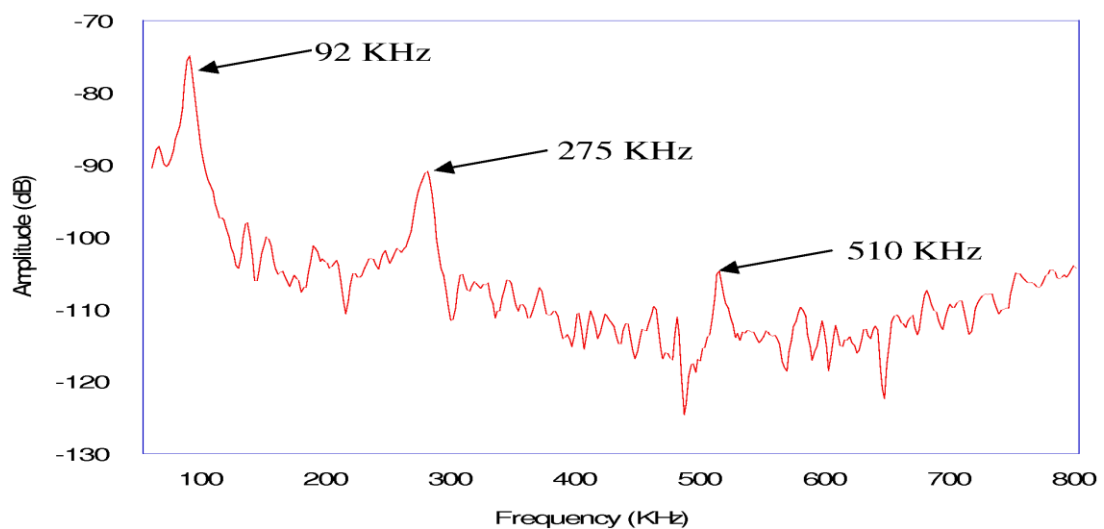


Figure 5.10. Vibration spectra of the AFM cantilever positioned on titanium alloy showing multiple resonance peaks

5.4.4.1. Carbon fiber reinforced composite material

This sample was chosen because of huge variation in electrical conductivity between carbon fibers and polymer matrix. The carbon fibers are electrically conducting while the polymer matrix is an insulator. Figure 5.11 shows the topography and electrical conductivity images obtained simultaneously

on the composite sample. The contrast in the AFM image is due to variation of surface height and brighter regions indicate higher surface heights. The surface height of the features in this image is about 500 nm, with a scan area of 30 μm X 30 μm . The images are obtained at a frequency of 85 kHz, which is one of the resonant frequencies of the cantilever for the composite sample. The carbon fibers appear bright in the image compared with the polymer matrix. The image on the right shows the eddy current image of the same region.

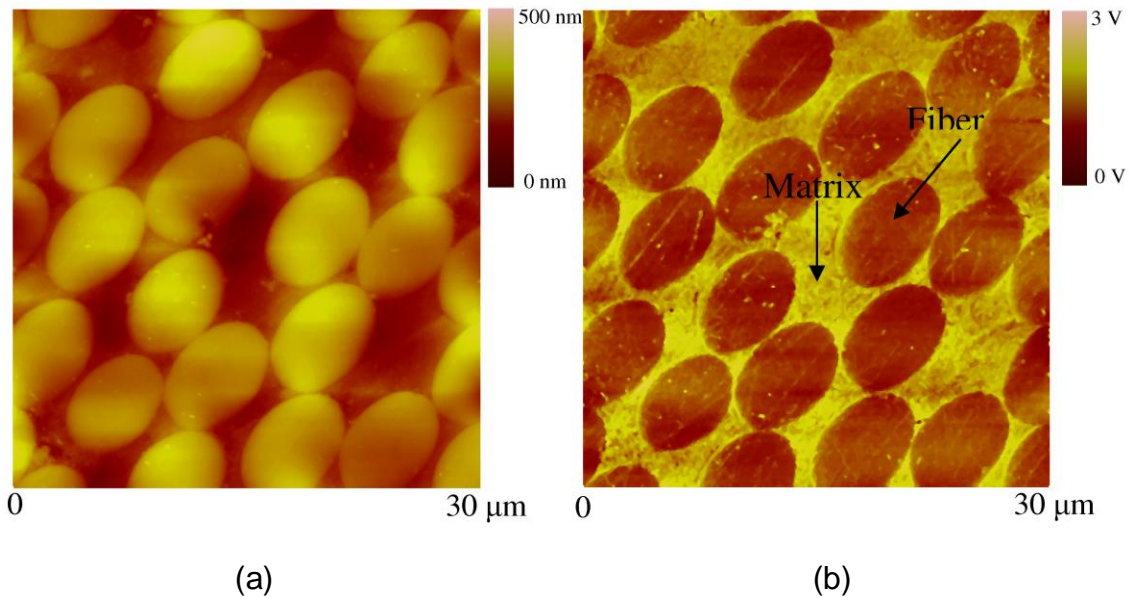


Figure 5.11. (a) Surface topography and (b) electrical conductivity images of carbon fibers reinforced in PEEK matrix. The conductive fiber and insulating matrix are shown by arrows in the eddy current image.

In the eddy current image the fibers are seen with dark contrast and the polymer matrix with a bright contrast. This difference in the contrast between the fibers and the matrix is due to the variations in the conductivity of fiber and polymer. The electrical resistivity of carbon and the polymer matrix is 0.006 $\Omega\text{-cm}$ and $1 \times 10^{15} \Omega\text{-cm}$ respectively. Thus, there is a large variation in the conductivity

of carbon and the matrix. The large difference in the conductivities of the fiber and matrix provides significant contrast in the eddy current image. The matrix is almost an insulator and the magnetic field generated by the coil passes through with out damping, producing large amplitude of vibration of the tip-cantilever. Large amplitude produces significant output voltages from the photo-detector. When the tip is located on the carbon fiber which has significant conductivity, the oscillating magnetic field generated by the coil produces eddy currents. The amplitude of the magnetic tip-cantilever sees reduced amplitude compared with polymer matrix. Reduced amplitude of the cantilever produces lower output voltage from the photo-detector. Thus the carbon fiber appears darker than the polymer matrix in the eddy current image. Consequently, in eddy current images, darker contrast indicates higher conductivity regions and brighter contrast indicates less conductivity regions. The arrows on the eddy current image show the conductive fibers and nonconductive matrix.

A section analysis of a region of the electrical conductivity image is shown in Figure 5.12. The section analysis shows the conductivity variations between the carbon fiber and the matrix. The image on the right shows the conductivity profiles of the region selected. It can be seen that the profile above the center line represents the matrix and the profile below the center line represents the fiber. This is due to the fact that the conductive fibers dampen the oscillation of the cantilever and hence is seen with lower amplitudes in the section analysis. A higher magnification conductivity image of the composite is shown in Figure 5.13. This allows a closer examination of the fiber-matrix interface region. Along with

the image a section analysis is also presented. The section analysis shows the conductivity variations in fiber and matrix along with the sharp variation in the conductivity at the interface. It can also be seen from this analysis that, at some regions there is a sharp transition in conductivity profiles at the boundary of matrix and fiber, while at other regions there is a gradual transition at the boundary, as shown by arrows in the image. In composite materials, it is very important for the proper bonding between the fiber and the matrix at the interface for maximum strength. Therefore, characterization of interface is important to estimate the strength of the composite. It can be seen from the above results that this technique is capable of imaging the interface between the fiber and the matrix with high resolution. Thus, this technique is well suited for the characterization of the interface in composite materials based on the variations in electrical conductivity.

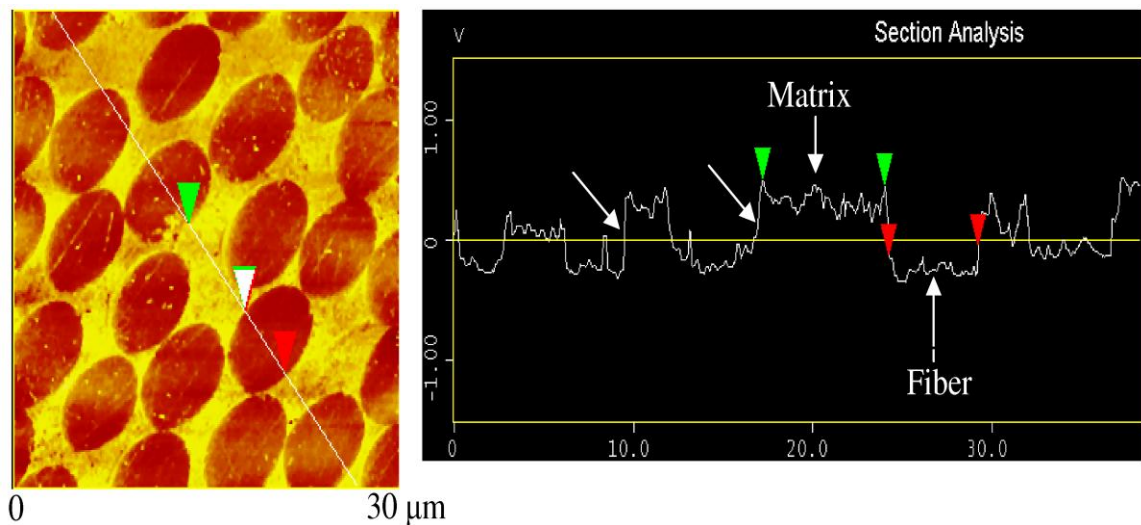


Figure 5.12. A section analysis of the eddy current image of fibers and matrix showing the variations in eddy current force.

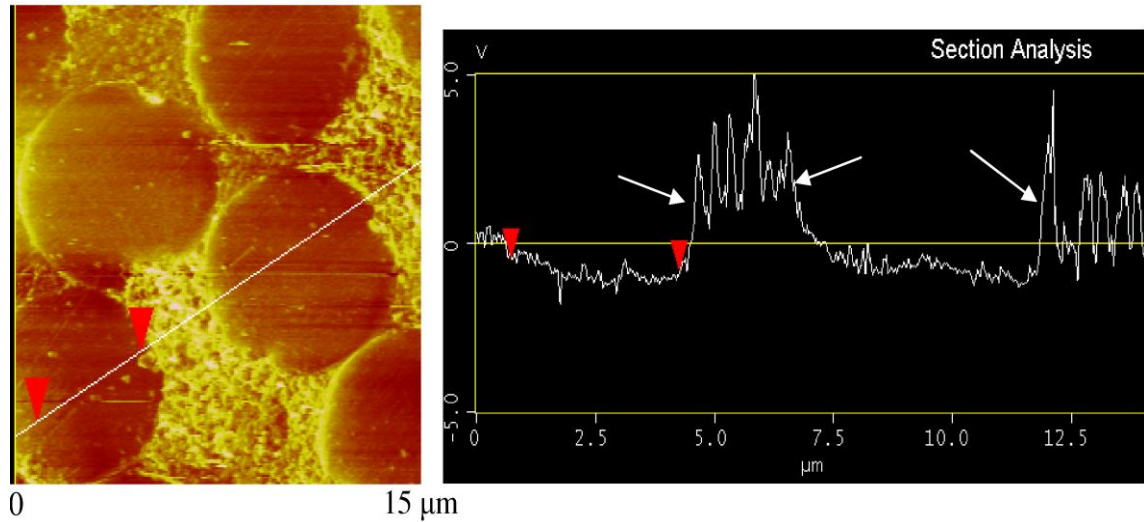


Figure 5.13. Section analysis of a high magnification eddy current image showing the variations in eddy current force at the interface of matrix and fiber.

5.4.4.2. Ti-6Al-4V alloy

The eddy current imaging of carbon fiber-polymer matrix shows that when the conductivity differences are several orders of magnitude, electrical conductivity images with a good contrast can be obtained. The electrical conductivity across single crystal metallic surfaces is constant and hence the eddy current forces do not vary. On the other hand, in polycrystalline metals, while the electrical conductivity is constant within individual grains, near the grain boundaries, it can be significantly different. In addition, in electrically anisotropic metals, the electrical conductivity can also vary from one grain to other due to crystallographic orientation difference. The scanning eddy current force microscopy is used to investigate electrical conductivity variations and the microstructure in polycrystalline metals. A titanium alloy, Ti-6Al-4V is chosen for the imaging electrical conductivity. Ti-6Al-4V alloys are used in high performance aerospace applications that require high toughness, good fatigue strength, and

good corrosion resistance. Titanium exists in two crystal structures: hexagonal close packed (α -phase) and body centered cubic (β -phase). The two phases often exist together in α - β alloys. The sample used in this experiment is a dual phase Ti-6Al-4V alloy consisting of both α and β phases. The microstructure of the dual phase titanium alloy consists of circular primary α grains with a grain size of about 10-20 μm and fine lamellar α + β platelets. The electrical conductivity of the two phases is expected to be close. The microstructure of Ti-6Al-4V is very sensitive to heat treatment conditions [184]. A small change in heat treatment temperature significantly changes the microstructure of the material. In order to test the feasibility of imaging small changes in conductivity, the electrical conductivity images of Ti-6Al-4V sample are obtained. Two types of titanium alloy samples are studied: a rectangular piece of Ti-6Al-4V alloy in as-is condition and a previously fatigue fractured dog-bone sample of Ti-6Al-4V. The fatigue fractured sample was polished for an optical finish and slightly etched near the fractured region.

Figure 5.14 shows the surface topography and the electrical conductivity image of an unetched titanium alloy. The image was obtained with a scan size of 30 μm and at an excitation frequency of 92 kHz. The surface topography image shows clearly the primary α -phase grains at a surface height of 80 nm. On the other hand, in the electrical conductivity image, only some grain boundaries can be seen clearly, while there is no contrast among other grains. The α -phase of this alloy has HCP structure which has electrical anisotropy. Therefore, if the grains are oriented in different directions, it will lead to different electrical

conductivity along that particular direction. Therefore, the grains that are oriented in different directions give produce variations in the eddy current force measured by AFM cantilever, thus giving rise to a contrast difference between the grains. The grains that are oriented in the same direction, however, do not show any variation in the electrical conductivity and thus the eddy current force measured by the cantilever is same giving rise to uniform contrast. On closer observation, lamellar structure can be seen in the eddy current image.

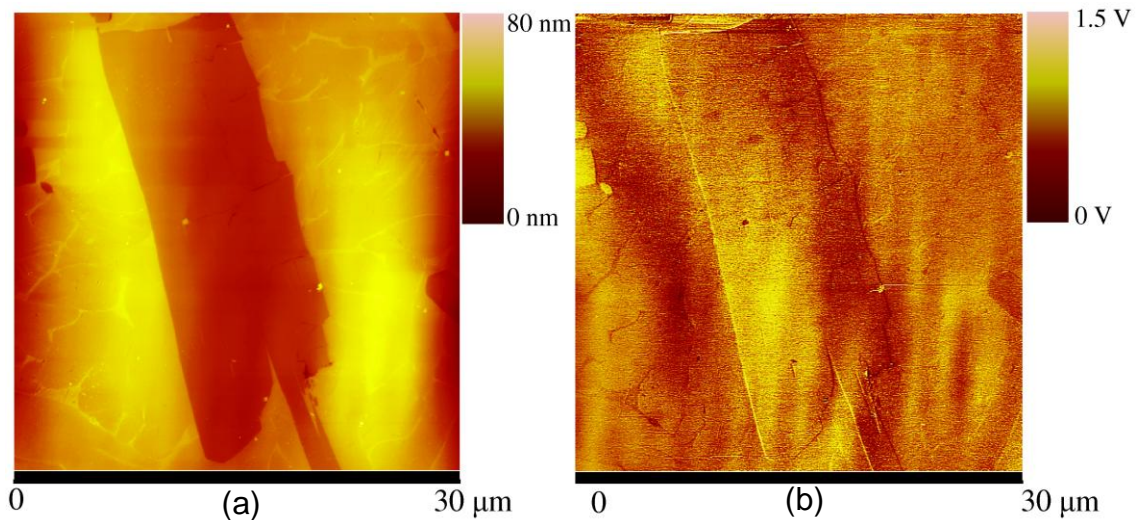


Figure 5.14 (a) Surface topography and (b) electrical conductivity image of Ti-6Al-4V alloy. The excitation frequency of the coil was 92 kHz

Figure 5.15 shows surface topography and eddy current images acquired simultaneously on the fatigue-fractured Ti-6Al-4V sample. The image was obtained on an area of $(50 \times 50) \mu\text{m}^2$ at an excitation frequency of 92 kHz. The surface topography image shows α grains, the $(\alpha+\beta)$ grains and α platelets inside $(\alpha+\beta)$ grains with a maximum vertical height of 800 nm. The β phase that is present between the two α platelets cannot be observed clearly in the topography image. Moreover, polishing and light etching have produced very

small surface height variation between the two phases. This may make it more difficult to observe the β phase in the AFM topography image. On the other hand, the eddy current force image shows quite good contrast. The large α grains, the $(\alpha+\beta)$ grains and the α platelets inside $(\alpha+\beta)$ grains can be observed with significant contrast. Some of the large α grains that appear as a single grain in the AFM image appear to be consisting of smaller grains and α plates when viewed in the eddy current image. The contrast observed in the eddy current image of the titanium sample is due to the difference in the electrical conductivities of α and β phases. Since the eddy current force changes with electrical conductivity variations, the eddy current forces due to the two phases are different. The scale bar in the eddy current image represents the output voltage from the photodiode detector, which is proportional to the electrical conductivity. When the magnetic tip scans over the more conductive regions of the sample, the amplitude of the vibration of the cantilever reduces due to the generation of the eddy currents. This results in lower output from the photodiode detector. Thus the higher conductivity regions appear with dark contrast in the eddy current image. On the other hand, when the tip scans over less conductive regions, the damping of the vibrations of the cantilever is relatively small and the output of the photodiode detector is relatively large. Hence less conductive regions appear relatively bright in the eddy current image. On closer observation, contrast among large α grains can also be observed in the eddy current force image. Thus, the eddy current force image shows significantly more structure than the AFM surface topography image.

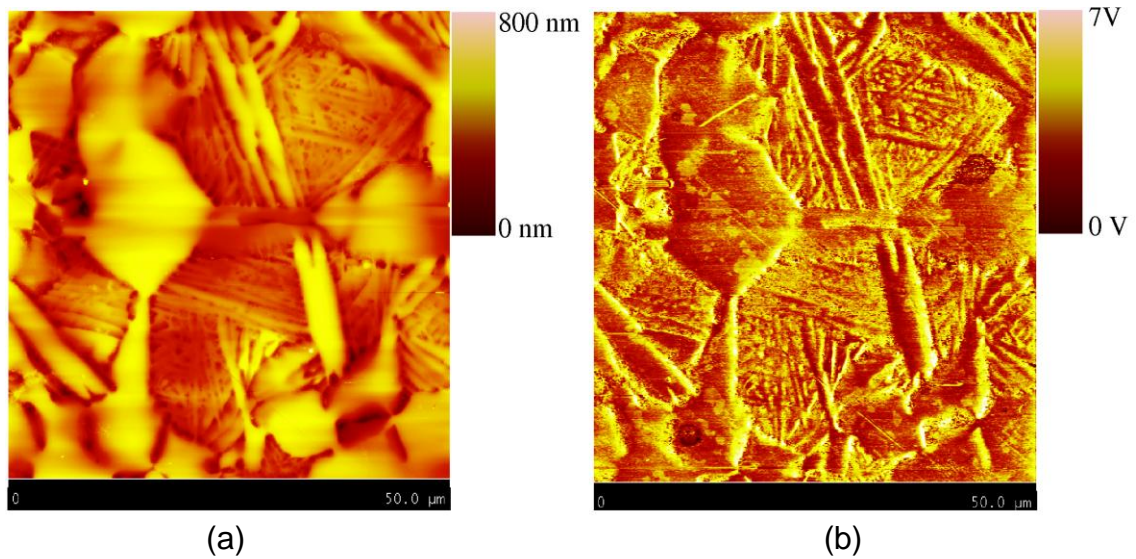


Figure 5.15. (a) Surface topography and (b) electrical conductivity images of Ti-6Al-4V. The coil was excited at a frequency of 92 kHz.

The hexagonal phase has anisotropic electrical conductivity. In pure titanium the electrical resistivity in the basal plane is $45.35 \mu\Omega \text{ cm}$ and $48 \mu\Omega \text{ cm}$ in a plane normal to basal plane [176]. This anisotropy in electrical conductivity leads to crystallographic orientation dependence conductivity. Thus different grains may have slightly different crystallographic orientation and hence different electrical conductivity. These variations in the conductivity of α grains give rise to a different contrast in the eddy current image. Thus the eddy current image on the titanium shows that the technique is sensitive to the small changes in the electrical conductivity of the material.

In a single crystal copper the experimental measurement of the eddy current force was found to be approximately 41 pN. This was observed to be in good agreement with theoretical calculations. The theoretical model shows that the electrical conductivity is the most important physical parameter for determining the eddy current force and the variations of eddy current force with

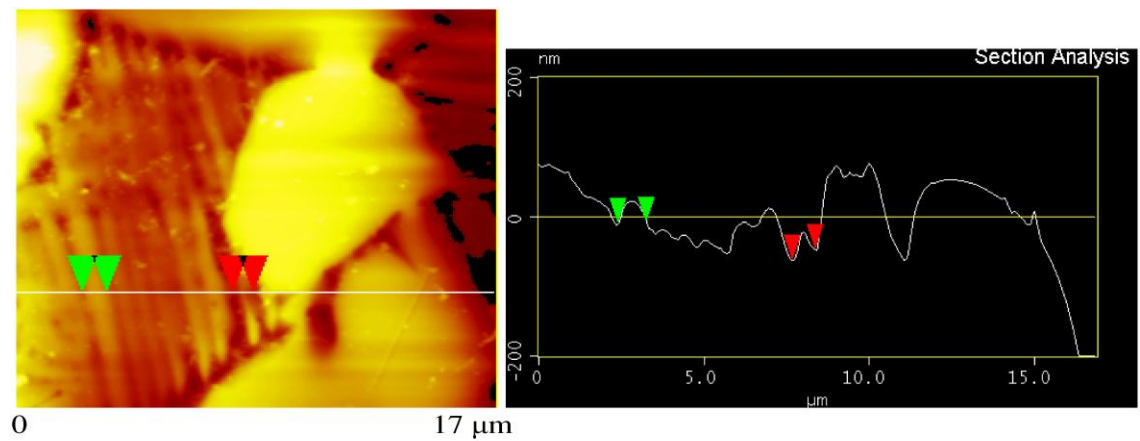
conductivity. At a fixed frequency, for a fixed distance between the sample and the magnetic tip, the eddy current force changes with the changes in electrical conductivity of the sample. Thus, an eddy current force image is a representation of the electrical conductivity variation. In single crystals, the eddy current force is constant across the surface and hence the image will have no contrast. In cubic metals the electrical conductivity is isotropic; because of this the eddy current forces across a polycrystalline cubic metallic surface will be uniform and no contrast will be observed as in the case of single crystals. On the other hand, the electrical conductivity in HCP metals is anisotropic. The electrical conductivity parallel and perpendicular to the *c*-axis in HCP materials is different. Thus in polycrystalline HCP metals like titanium, the eddy current force will vary with the crystallographic orientation of the individual grains. Assuming that the difference between the two conductivities is similar to that of pure titanium, the eddy current forces are calculated to be 1.6 nN and 1.77 nN respectively. The grains having random crystallographic orientation will have eddy current forces between the two extreme values. Thus the contrast observed in the α grains of the eddy current image shown in Figure 5.15 can be attributed to the variation of the electrical conductivity among individual α grains.

The β phase has body centered cubic (BCC) crystal structure. The conductivity of the β phase is significantly different compared to α phase and electrical conductivity of the β phase is isotropic. The difference in the electrical conductivity between the two phases and the anisotropy in conductivity of the α phase enhances the contrast in eddy current images. These factors help in the

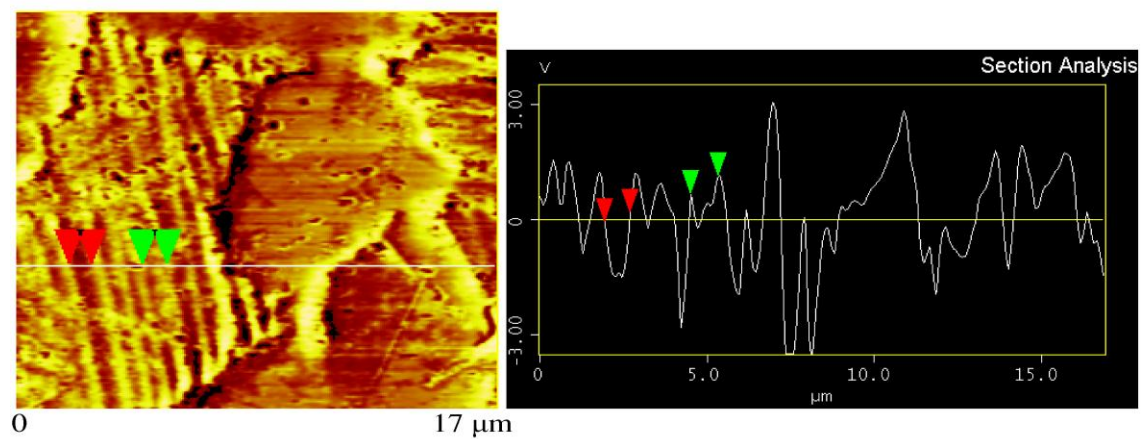
observation of multiple grains, platelets in large grains that appear to be single grain in AFM topography images. Although the surface roughness among the different phases and platelets are very small to show significant contrast in AFM images, the electrical conductivity is significantly different among different phases of the material and the anisotropy of electrical conductivity enhances the contrast in eddy current images. The contrast in eddy current images has been explained based on the physics based simple theoretical model of the eddy current force and the variation of distance between sample and the magnetic tip. It is possible to develop finite element based methods to examine the local electrical conductivity variation.

Figure 5.16 takes a closer look at the platelets in the titanium alloy. A single line scan across both the images showing the variations in topography and conductivity respectively is also shown in the figure. The image shows a line scan across the topography and electrical conductivity images of titanium alloy showing the variations in topography and conductivity. In some regions it has needle like grains of alpha phase within a large grain. The surface topography image shows the needle like grains oriented in different directions with surface height variation. The contrast is fuzzy and identifying individual needle structured grains is difficult. On the other hand the eddy current force image shows each and every needle structure with enhanced contrast at the boundary. The contrast at the grain boundary is quite strong because of significant change in the conductivity and due to modification of the eddy currents near the boundary. Generally, it is well known that the conductivity is modified near the grain

boundaries due to extra scattering of the electrons. While the lamellar structure in the AFM image of α and β phases does not show much variation in the surface topography, the same phases in the eddy current force images distinctly show two different contrasts. This is shown in the section analyses of the topography and eddy current force images. The widths of the dark and bright phases shown in the line scan of the eddy current force image are 560 nm and 520 nm respectively.



(a)



(b)

Figure 5.16 (a) Surface topography and the corresponding line scan across the line shown in the topography. (b) Electrical conductivity image and the corresponding line scan across the line shown in the eddy current image of Ti-6Al-4V sample. The excitation frequency of the coil was 92 kHz.

Figure 5.17 shows the topography and electrical conductivity images obtained very near the crack initiation and propagation regions of the fatigue-fractured titanium sample obtained at an excitation frequency of 92 kHz. The image shows the surface topography with primary α grains and the lamellar structure with a maximum surface height of 600 nm. The contrast within the grains is not clearly seen at this magnification. However, the eddy current force image shows the structure within the α grains clearly, in addition to the lamellar structure. The structure shows parallel features with dark contrast, similar to lamella structure. These parallel platelets could be the lamella formed during the heat treatment. Also, features with bright contrast can be seen in the image near the $\alpha+\beta$ lamellar structure and also within the α grain. These features are shown by arrows in Figure 5.17. The corresponding surface topography image did not show any such features. It is well known that the electrical conductivity around a crack is significantly different than the conductivity in a region without a crack. When eddy currents flow through the material which has cracks in it, the eddy current density is different near the crack when compared to other regions without the presence of cracks. Usually, electrical conductivity is more near the cracks. In the electrical conductivity images obtained by scanning eddy current force microscopy, brighter regions correspond to higher conductivity regions. Since the features indicated by the arrows show brighter contrast, they could be the cracks due to the fatigue fracture of the sample. A higher magnification eddy current force image of the fine crack is shown in Figure 5.18. A line scan across the fine crack is also shown in the Figure. The width of the crack shown by the

line scan in the image is about 115 nm. In addition, other small cracks can also be seen in the image. Thus, this technique can also be used to detect very fine cracks in materials which cannot be resolved by AFM topography image.

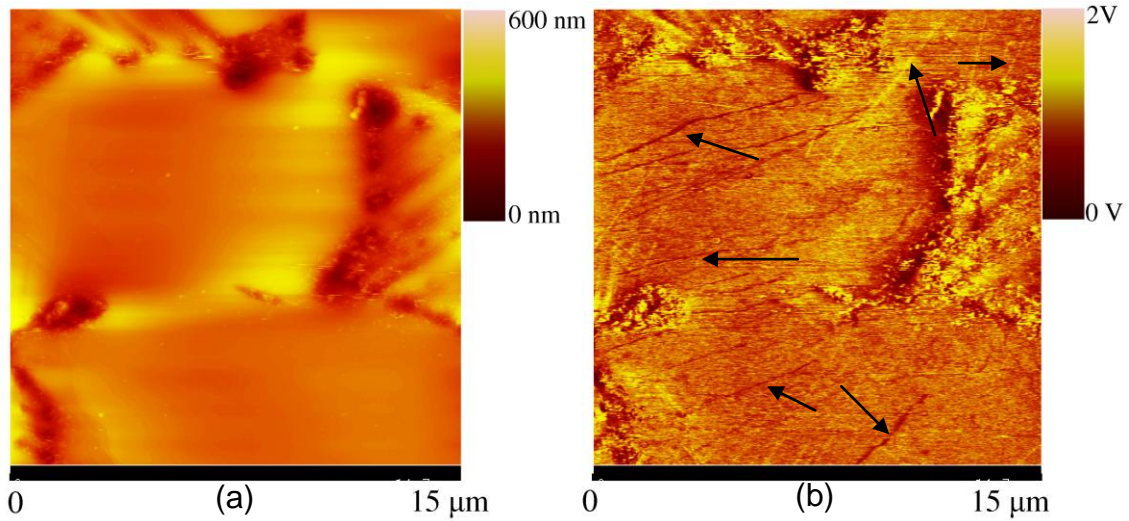


Figure 5.17 (a) Surface topography and (b) electrical conductivity image obtained very near the crack initiation region of the fatigue fractured titanium sample. The electrical conductivity image shows lamellar structure with dark contrast within α grain and also very fine cracks with bright contrast as indicated by arrows. The frequency of the excitation was 92 kHz.

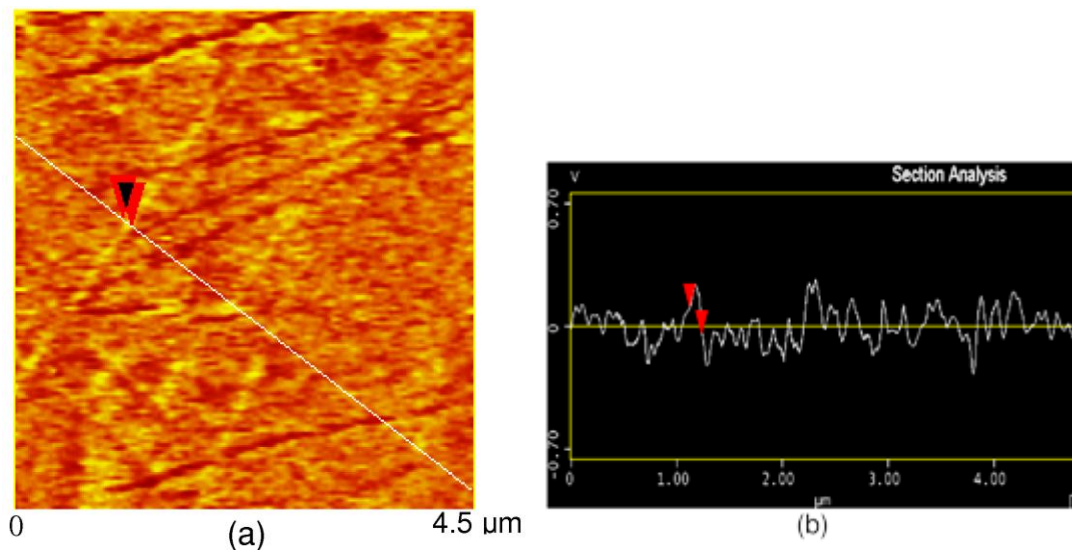


Figure 5.18 (a) A high magnification electrical conductivity image showing fine cracks in fatigue fractured titanium sample (b) Line scan across the crack showing the size of the crack. The coil was operated at a frequency of 92 kHz.

Figure 5.3 shows that the eddy current force decreases as the distance between the sample and the magnetic tip increases. Although these measurements were performed on copper, the essential features of the curve are expected to be similar in other conducting materials. In polycrystalline materials, especially in HCP metals, the eddy current forces depend on the crystallographic orientation and the electrical conductivity of the grain. Thus the eddy current force on different grains is expected to be different for a particular distance between the sample and the magnetic tip. Hence the contrast in the images will vary with the distance between the sample and the magnetic tip. To examine the role of separation distance between the sample and the magnetic tip on the contrast in eddy current images, images of the same region of the sample were obtained at several separation distances. The contrast in the images was observed to degrade with the increase of distance between the sample and the magnetic tip. The features that are sharp at distances of 50 – 100 nm become blurry as the distance increased to 200 nm. The degradation of contrast can be explained based on Figure 5.3, which shows that the eddy current force decreases with increasing distance and becomes negligible at distances larger than 500 nm. To obtain eddy current images with better contrast, it is therefore necessary to keep the distance between the sample and the magnetic tip in the range of 50 – 150 nm depending on the electrical conductivity of the sample.

An important factor in the eddy current imaging is the role of skin depth. The eddy currents diffuse from the bottom of the sample through the thickness of the sample. Hence, the force between the conducting sample and the magnetic

tip is an average over the thickness of the sample. If the sample's electrical conductivity is inhomogeneous in the thickness direction the eddy current force is an average over the sample thickness. While this appears to be a limitation of the technique, it may be advantageous in imaging subsurface features like defects or crack that cause inhomogeneities in electrical conductivity. This fact is effectively used in non-destructive evaluation of materials using eddy current testing [185].

The experimentally measured eddy current forces on the single crystal samples can be used in the data scale of the conductivity image of the titanium sample. Figure 5.19 shows the surface topography and electrical conductivity images showing the α and β phases in the form of platelets at a frequency of 92 kHz with a scan size of 15 μm . While the previous images showed the data scale of the conductivity image in terms of the output voltage of the photodiode detector, this image shows the data scale in terms of eddy current force. These forces were calculated experimentally on single crystal metallic samples. The magnitude of the eddy current forces is proportional to the electrical conductivity. Thus, force data can be related to the local variations in electrical conductivity. When the magnetic tip scans over the more conductive regions of the sample, the amplitude of the vibration of the cantilever reduces due to the generation of the eddy currents. This results in lower output from the photodiode detector. Thus the higher conductivity regions appear with dark contrast in the eddy current image. On the other hand, when the tip scans over less conductive regions, the damping of the vibrations of the cantilever is relatively small and the output of the photodiode detector is relatively large. Hence less conductive

regions appear relatively bright in the eddy current image. The electrical conductivity of titanium is $0.18 (\Omega\text{m})^{-1}$ and the conductivity is in between the conductivity of the platinum and an insulator. From Figure 5.5, the eddy current force for titanium is expected to vary between the eddy current force for platinum and insulator. The maximum and minimum eddy current force on the titanium sample was about 14 pN and 3 pN respectively. The scale bar in the eddy current image represents the variation of the eddy current force in the region where the image was taken. From Figure 5.5, it can be seen that as the electrical conductivity increases, the eddy current force increases. The darker regions (higher conductivity) in the image correspond to higher eddy current forces and the brighter regions (lower conductivity) correspond to lower eddy current forces.

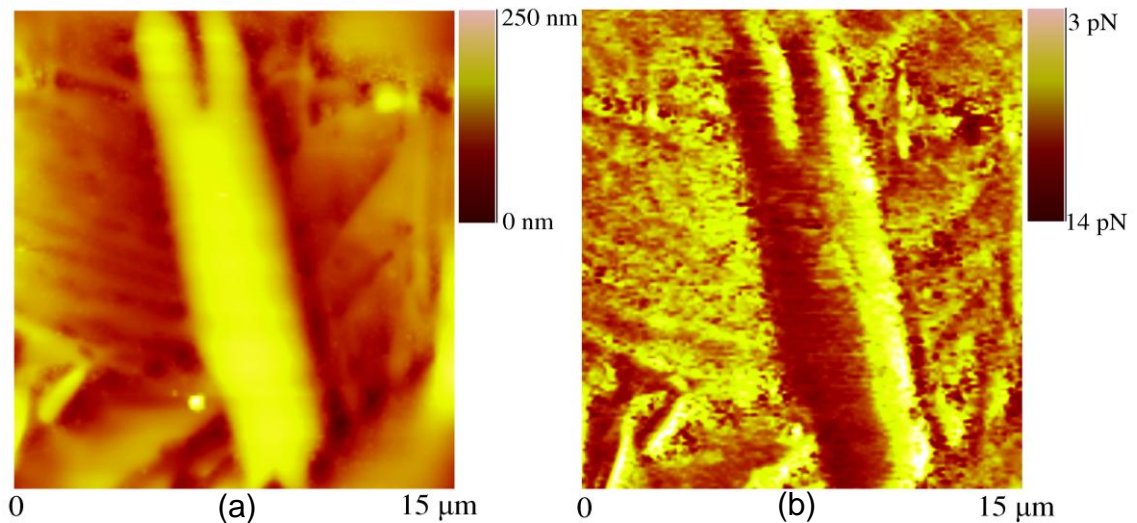


Figure 5.19. (a) Surface topography and (b) relative electrical conductivity images of $\alpha + \beta$ platelets in Ti-6Al-4V sample. The scale bar for electrical conductivity image is provided in terms of eddy current force. Excitation frequency 92 kHz.

5.4.5. Spatial Resolution

The Ti-6Al-4V sample that was used for eddy current imaging of the grain structure had no features that were smaller than a micron. Thus, we could not examine the spatial resolution of our eddy current imaging system with that sample. To examine the spatial resolution of the system, a composite sample consisting of carbon nanofibers reinforced in a polymer matrix was used. The diameters of the fibers are in the range of 20 – 100 nm and the length is known to be in the range of fraction of microns to tens of microns. The carbon fibers are electrically conductive while the polymer matrix is an insulator. Eddy current imaging is an excellent method to examine the distribution of carbon fibers in the matrix because of the huge conductivity difference between the matrix and the carbon fibers. This sample could also be used to examine the spatial resolution by imaging the smallest diameter carbon nano-fiber.

Figure 5.20 shows the topography and eddy current images of carbon nanofibers embedded in an epoxy matrix, together with the response signals from a single scan line each image. The images were obtained with a total scan size of 625 nm in each direction at an excitation frequency of 85 KHz. This allowed the examination of the smallest possible nanofiber. The carbon nanofibers appear with darker contrast in the eddy current image due to the reduction of the cantilever amplitude when compared to the amplitude on the epoxy. To examine the spatial resolution, one of the carbon nanofibers was chosen and single scan line response signals from the topography image and

from the eddy current image are presented. It can be seen from the analysis that a particle of 25 nm diameter can be resolved in eddy current images. In the current experiments, a magnetic tip with a nominal diameter of 20 nm was used for imaging. Although features smaller than 25 nm may be resolved, the magnetic field sensed by the tip may be larger than the diameter of the tip. In general, the spatial resolution in an AFM depends on the diameter of the probe as well as the interaction forces between the tip and the sample [186,187]. It is known that long range interaction forces between the tip and the sample degrades the spatial resolution [188,189]. In the experiments, the magnetic forces generated due to the eddy currents are long range interaction forces and the magnetic tip experiences an average force from the region larger than the size of the tip. Hence the spatial resolution in eddy current image is slightly larger than the diameter of the tip.

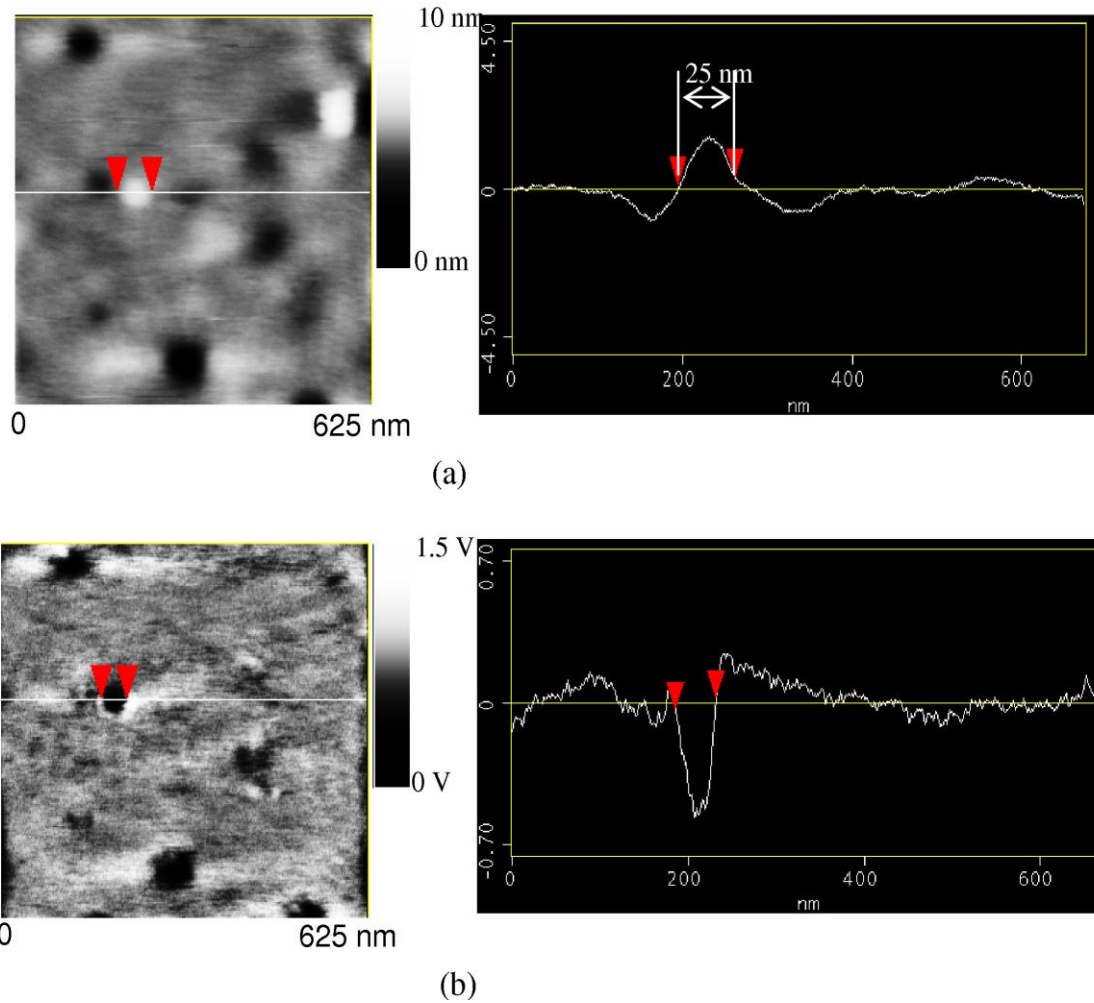


Figure 5.20. Images and single-scan-line response signals from carbon nanofibers in an epoxy matrix. (a) Surface topography and (b) eddy current (relative electrical conductivity). Frequency 85 kHz.

5.5. Conclusions

This chapter discussed the application of the scanning eddy current force microscopy for the characterization of electrical conductivity of bulk conductors. The eddy current forces are experimentally measured on single crystal metallic samples and compared with theoretical and finite element models. The results

show that the experimental forces are in good agreement with theoretical and finite element models. The magnitude of the eddy current forces in the samples is shown to be a function of the electrical conductivity of the material. The effect of separation distance between the magnetic tip and the sample surface on the eddy current force is studied. The forces between the magnetic tip and the eddy currents are used to quantitatively measure the electrical resistivity of micron sized copper wires. The results are in agreement with the resistivity values in literature. The instrument was first used to map the electrical conductivity of a carbon fiber composite sample. The contrast in the eddy current force image is explained based on the huge electrical conductivity difference between the fibers and the polymer matrix. The instrument is then used to show that the technique is capable of imaging very small variations in electrical conductivity. This is accomplished by imaging the microstructure of a dual-phase polycrystalline titanium alloy. The eddy current image distinguished different phases in the sample and also facilitated the observation of different grains by significantly increasing the image contrast. The contrast in the eddy current force images is attributed to the anisotropy of the electrical conductivity of the α phase and the difference between the conductivity of the α and the β phase. The spatial resolution of the eddy current imaging system was determined by imaging carbon nanofibers reinforced in a polymer matrix. Nanofibers as small as 25 nm in diameter are observed with good contrast. Since the magnetic field sensed by the magnetic tip may be larger than the diameter of the tip, the resolution is in the range of 30–50 nm. Based on the response of the magnetic tip to the excitation

of the electromagnetic coil, the instrument can be used to perform eddy current imaging at multiple frequencies.

CHAPTER 6

CHARACTERIZATION OF ELECTRICAL AND ELECTROMAGNETIC PROPERTIES OF NANOSTRUCTURED MATERIALS

6.1. Introduction

The previous chapter demonstrated the ability of the new technique to characterize electrical conductivity of bulk conductors with nanometer scale resolution. Since the scanning probe methods are used extensively to characterize nanomaterials, the new technique is also applied to characterize electrical properties of nanostructured materials. Two types of nanostructured materials are studied: nanofibers and metallic nanoparticles.

Ever since the development of carbon nanotubes by Iijima [190], researchers have been investigating carbon nanotubes for use in high strength applications, due to their remarkable physical properties [191]. Carbon nanotubes exhibit high strength and a relatively low density. During the last decade, there have been several research works to study CNT reinforced polymer matrix composite systems. Even though the carbon nanotubes hold much promise for many applications, there are several unresolved issues. The major problems are related to the dispersion of the CNTs in the matrix and the adhesion between the nanotubes and the matrix. Therefore, as an alternative,

carbon nanofiber (CNF) is increasingly used as a low-cost version of CNT. Although the mechanical properties of CNF are not as good as those of CNT, the modulus of elasticity and the strength of CNT's are still relatively high (192).

A literature search in the field of CNF reinforced composites shows that majority of research efforts mainly focuses on the manufacturing and processing related issues of the composites. The characterization of nanocomposites is done by traditional techniques such as tensile and bending tests. However, these characterization techniques are macroscopic in nature. Further more, the homogeneous dispersion and adhesion of the fibers to the matrix is a major concern in CNF reinforced composites. Therefore, the newly developed technique is used to characterize the carbon nanofibers embedded in a polymer matrix. The technique is also used to study the distribution and dispersion of the fibers in the polymer matrix.

Metallic nanoparticles display fascinating properties that are quite different from those of individual atoms, surfaces or bulk materials [193]. They are a focus of interest for fundamental science and, because of their huge potential in nanotechnology, they are the subject of intense research effort in a range of disciplines. Applications, or potential applications, are diverse and interdisciplinary. They include, for example, use in biochemistry, in catalysis and as chemical and biological sensors, as systems for nanoelectronics and nanostructured magnetism (e.g. data storage devices), where the drive for further miniaturization provides tremendous technological challenges and, in medicine, there is interest in their potential as agents for drug delivery.

The reduction of the size of metals results in significant changes in the electromagnetic properties compared with the bulk metals. In particular, the electromagnetic response of nanometer dimension metal particles has attracted a lot of attention during the last decade [194-196]. It is well known that the noble metallic nanoparticles, like gold and silver exhibit remarkable optical properties, viz, strong colors. These particles acquire a characteristic color due to plasmon resonance. Plasmon resonance occurs due to coherent oscillation of the conduction band electrons induced by the incident EM field at optical frequencies. This phenomenon finds applications in many fields of science and engineering, and sensing. For example, the enhancement of electrical field around the particles can be used to enhance surface enhanced Raman scattering. In biological sciences, gold nanoparticles have been used to label organic substances or biological material. The surface plasmon resonance exhibited by metallic nanoparticles is usually characterized using near-field optical techniques such as scanning near-field optical microscopy (SNOM) [197,198]. In these techniques, the *electric field* around the nanoparticle is usually sensed and imaged. The spatial resolution of conventional optical techniques is limited by the wavelength of the light. In SNOM, the diffraction limit is overcome by performing measurements with the optical source or detector held much closer to the sample than the wavelength of the light. In this near-field regime, the attainable spatial resolution is now dependent on the size of the source or detector. The SNOM has been used to detect plasmon resonances in colloidal metallic nanoparticles. When a small spherical metallic nanoparticle is

excited by electromagnetic radiation, the oscillating electric field causes the conduction electrons oscillate coherently. The plasmon resonances in the metallic nanoparticles occur in the optical frequency range and they result in powerful localized sources of electric field. The plasmon frequency can be used to calculate the metal dielectric constant.

While the high-frequency electromagnetic properties of nanoparticles have been extensively studied and reported in literature, very little information is available on the low-frequency interaction of electromagnetic waves with nanoparticles. In this experiment, the interaction of low-frequency electromagnetic waves with metallic nanoparticles is studied.

6.2. Materials and Experiment

A nanocomposite thin film with vapor grown carbon nanofibers (VGCF) inside a polymer matrix is used in this experiment. Nanocomposite films were fabricated with vapor phase grown carbon nanofibers (Pyrograf III PR-24-LHT, Applied Science, Cedarville Ohio). Most of the nanofibers are agglomerated in bundles of 20-200 micrometers in diameter (Figure 6.1(a)). The individual nanofibers are about 100 nanometers in diameter (Figure 6.2(b)) and highly graphitic. It is a processing challenge to de-agglomerate the raw material and uniformly disperse into a polymer resin. In this study, we dispersed the nanofibers into a solution of high performance thermoplastic polymer in DMAC at

a loading of 5 wt% (relative to the polymer). The solution was exposed to high shear conditions using laboratory and pilot plant equipment for about 1 hour. The resulting solution was cast onto a glass plate using a doctor blade, and heat was applied to evaporate the solvent. The resulting free standing films were then analyzed with SEM. While most of the nanofibers were well dispersed, some agglomerates of approximately 10-20 micrometers still remained.

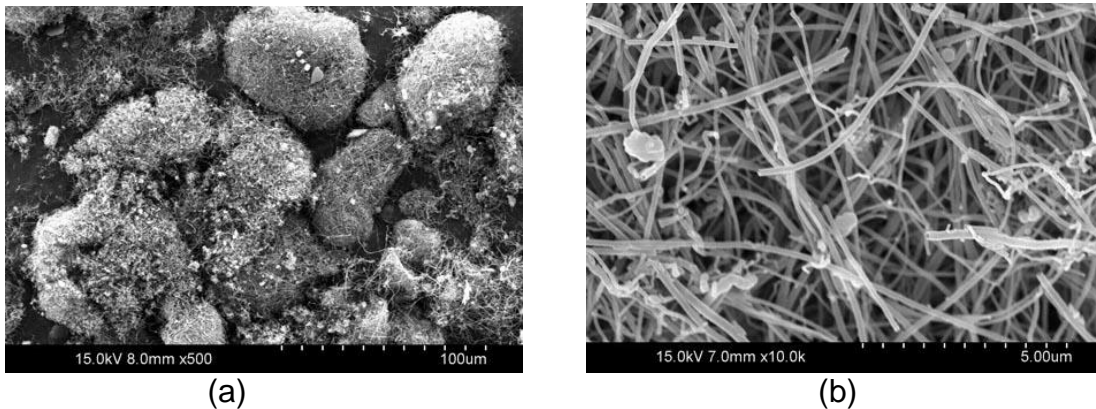


Figure 6.1. High resolution SEM images of raw Pyrograf III carbon nanofibers, a) 500X magnification, showing agglomerated nature of raw materials, and b) 10kX magnification showing individual nanofibers within agglomerate.

Nanoparticles of platinum are synthesized by a process known as Through Thin Film Ablation (TTFA) [199]. In TTFA, a thin film target is ablated in vacuum through a transparent support. The nanoparticles thus synthesized are not agglomerated and have a uniform size distribution. Figure 6.2 shows a SEM micrograph of platinum nanoparticles synthesized using TTFA. The experimental setup used in this study is similar to that used for imaging bulk conductors.

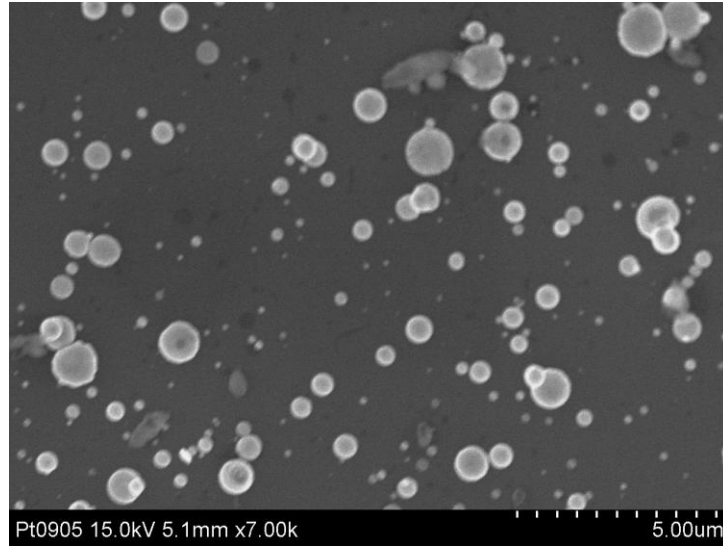


Figure 6.2. SEM micrograph of platinum nanoparticles synthesized by through thin film ablation.

6.3. Results and Discussion

In this section, eddy current images of carbon nanofibers reinforced in polymer composite and platinum nanoparticles are presented.

6.3.1. Carbon Nanofiber Polymer Composite

Figure 6.3 shows the AFM topography and electrical conductivity images obtained on the nanocomposite sample at an excitation frequency of 85 kHz. The images show carbon nanofibers in the polymer matrix in an area of $5\ \mu\text{m} \times 5\ \mu\text{m}$. The topography of the nanocomposite film shows small hazy features in the AFM images. Even though nanofibers are present in this image, it is difficult to clearly

distinguish the fibers from the matrix features. On the other hand, the eddy current image obtained in the same region shows a set of features with darker contrast. Based on the contrast obtained on the previous carbon fiber reinforced composite sample, the darker features are the carbon nanofibers in the polymer matrix. Some of the carbon nanofibers are shown by arrows in the eddy current force image. The brighter regions are the lower conductivity polymer matrix. When the magnetic tip scans over the insulating polymer matrix, the magnetic field of the coil directly reaches the magnetic tip resulting in larger amplitudes of the cantilever. This translates to a brighter contrast in the eddy current force image. On the other hand, when the tip scans over the conductive fibers, the magnetic field is screened by the eddy currents generated by the carbon fibers thus resulting in reduced vibration amplitude of the cantilever. This means that the conductive fibers would appear with darker contrast in the eddy current force image. The improved contrast in the eddy current image can be used to study the size distribution of the carbon fibers in the matrix. Fibers with sizes ranging from 30 nm to 150 nm can be seen in this region. The eddy current image can also be used to quantitatively analyze the distribution and dispersion of the nanofibers in the matrix. The area fraction of the carbon nanofibers in this image (5 μm X 5 μm) is found to be approximately 8.2 %. Figure 6.4 shows the carbon nanofibers obtained in a different region of the sample with a scan area of 1 μm at a frequency of 85 kHz. The fibers appear to be well dispersed in this region compared to the previous region and they are more spherical in this region. The

size distribution of the carbon fibers in this region is more uniform in this region with an average size of about 100 nm.

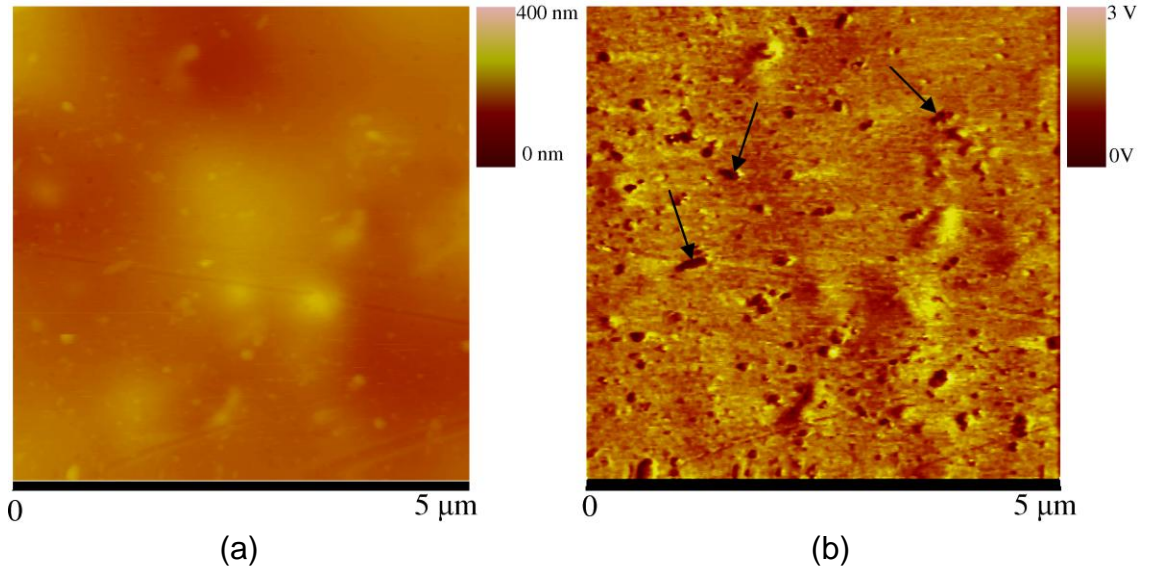


Figure 6.3. (a) Surface topography and (b) electrical conductivity images of a carbon nanofiber composite thin film. Arrows on the eddy current image indicate some of the nanofibers. Frequency of the excitation 85 kHz.

Figure 6.5 shows the topography and eddy current image obtained at another region of the nanocomposite sample. The image was taken with a scan size of $1.97 \mu\text{m} \times 1.97 \mu\text{m}$ and at a frequency of 85 kHz. Carbon nanofibers can be seen in the eddy current image with reduced contrast compared to the nonconductive polymer matrix. On closer observation of the eddy current image, an agglomeration of the residual catalyst particles or carbon black can be observed in the image shown by the rectangular region, while the same cannot be clearly seen in the topography image. Another interesting feature of this image is indicated by an arrow in the eddy current image. The bottom region around the fiber is brighter than the top region, indicating that there is less conductivity around the bottom region than the top region. It is well known in

standard eddy current testing that presence of debonding, delaminations or crack would alter the conductivity around the defects [5]. Thus, this change in the contrast would imply a fiber pull out from the matrix. A magnified image of the debonded fiber is shown in Figure 6.6. A conductivity profile along the debonded fiber is shown on the right side. It can be seen from this analysis that the conductivity changes sharply around the fiber where there is a pullout from the matrix. If the fiber is not pulled out from the matrix there would be a gradual transition in the conductivity profile instead of a sharp transition.

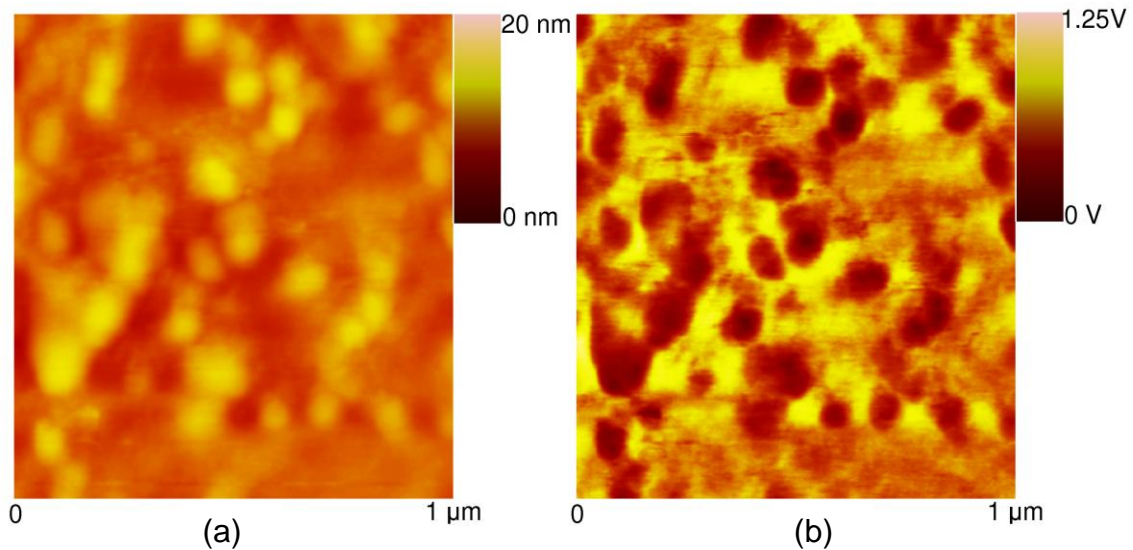


Figure 6.4. (a) Surface topography and (b) electrical conductivity images of carbon nanofibers. The images show a uniform size distribution and better dispersion of nanofibers in the polymer matrix. Excitation frequency 85 kHz.

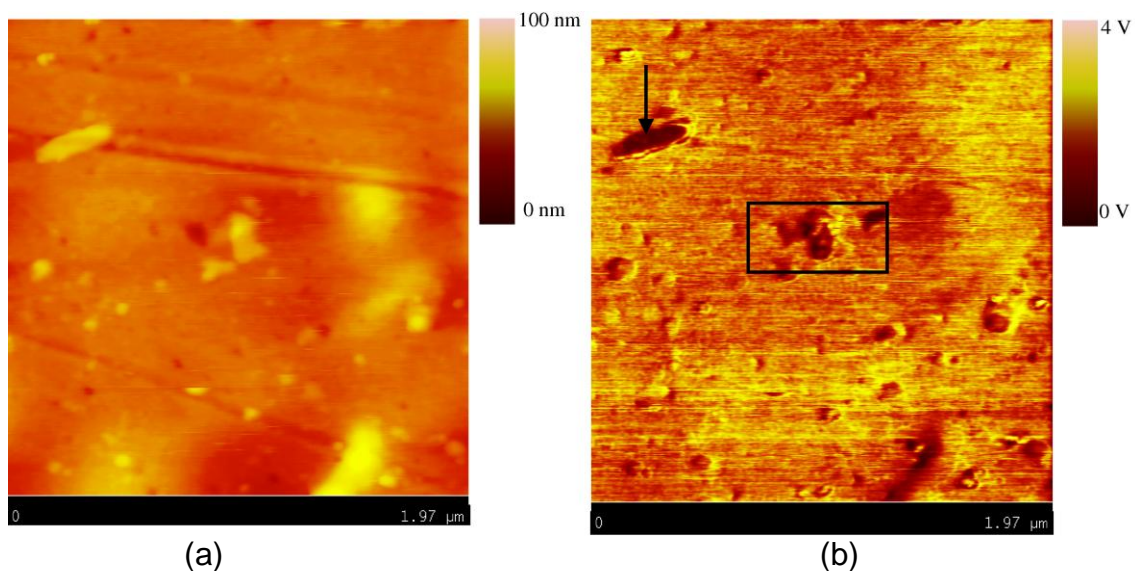


Figure 6.5. (a) Surface topography and (b) electrical conductivity images obtained at another region of nanocomposite thin film. The arrow indicates the fiber pull-out from the matrix. The frequency of excitation was 85 kHz.

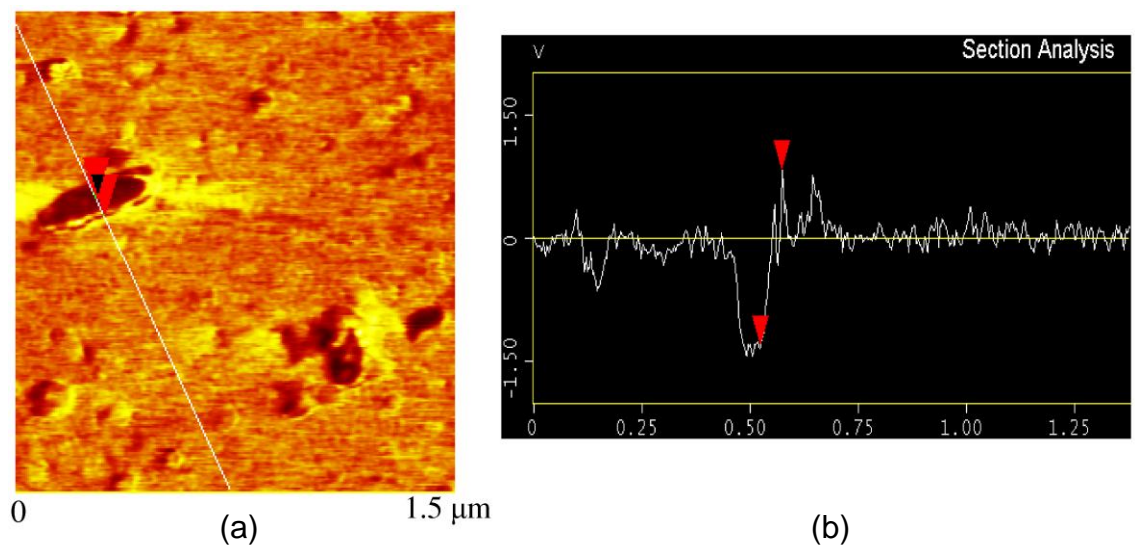


Figure 6.6. (a) Magnified image of the carbon nanofiber showing the separation of fiber from the matrix. (b) Single line section analysis of the fiber showing the variation in the conductivity near the interface.

6.3.2. Metallic Nanoparticles

Figure 6.7 shows surface topography and the eddy current force image of an individual platinum nanoparticle. The electromagnetic coil was operated at a frequency of 85 kHz. Surface topography image shows that the particle is almost spherical with an approximate diameter of 250 nm. The eddy current force which is related to the electrical conductivity of the metallic particle, on the right hand side shows a darker contrast varying uniformly across the nanoparticle.

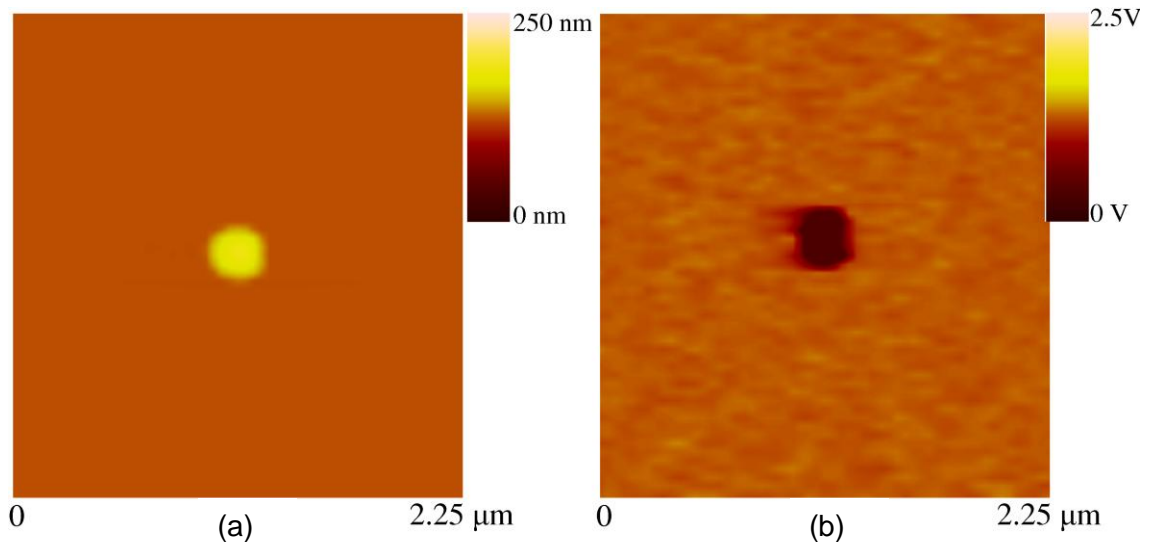


Figure 6.7. (a) Surface topography and (b) eddy current images of an individual nanoparticle of platinum. Frequency of excitation 85 kHz.

Figure 6.8 shows an image of another single nano-particle obtained at an excitation frequency of 85 kHz. The surface topography image is similar to the image of diameter 250 nm nano-particle shown in Figure 6.7. The approximate diameter of the nanoparticle measured using surface topography image is 500 nm. The contrast in the image indicates that the surface height changes across the image and being highest at the center. On the other hand the image contrast

in the eddy current force image is dramatically different. The particle appears to have split into two parts right in the middle with dark and bright contrast. Since the contrast is related to the local electrical conductivity, it appears as though the particle has two different electrical conductivities. It is tempting to interpret that the particle has two different conductivities. Since the material is just platinum it is almost impossible to have two conductivities in a 500 nm particle of metal without additives. Moreover, it is extremely improbable that the conductivity changes exactly in the middle.

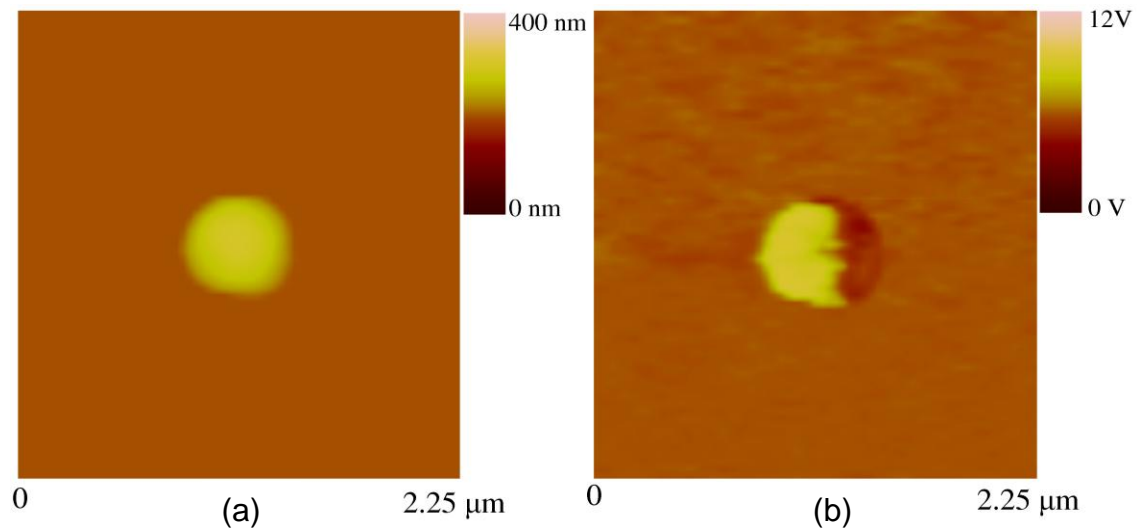


Figure 6.8. (a) Surface topography and (b) eddy current images of a 500 nm platinum nanoparticle. The surface topography looks similar to the previous image, but the eddy current force image shows the particle is split into bright and dark regions. Frequency 85 kHz.

Figure 6.9 shows the surface topography and the eddy current images of platinum nanoparticles at a different region of the sample. The image was obtained at an excitation frequency of 85 kHz. The image shows three platinum nanoparticles of different size. While the topography image of the platinum nanoparticles appears similar to that of previous images, the eddy current image

distinctly shows different contrast among the nanoparticles. Two nanoparticles with diameters 500 nm and 200 nm respectively can be seen at the top half of the image with a contrast similar to that of eddy current image of the nanoparticle seen in Figure 6.8. Another nanoparticle with a diameter of about 800 nm is also seen in the image. The nanoparticle appears as if the particle is split into three different parts. Here again, it is highly improbable that electrical conductivity with in a nanoparticle will change so dramatically.

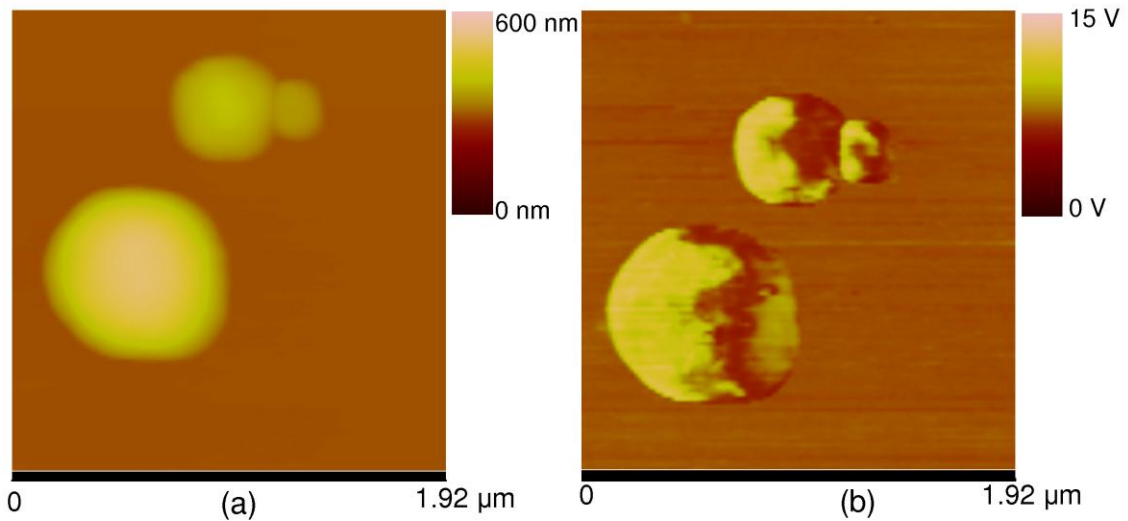


Figure 6.9. (a) Surface topography and (b) eddy current images of platinum nanoparticles. While two smaller particles are split into half showing two different contrasts, the bigger particle is split into three parts showing bright-dark-bright contrast within the particle. Frequency 85 kHz.

The eddy current images shown in Figures 6.7-6.9 can be compared with surface plasmon resonance images on spherical metallic nanoparticles reported extensively in the literature using optical techniques [194-198]. In general the features are very similar. When electromagnetic waves at optical frequencies are used to excite metallic nanoparticles, they undergo plasmon oscillations and the plasmon resonance modes of the particles at different wavelengths can be

imaged using optical techniques. Moreover, the plasmon resonances result in powerful localized sources of electric field and this enhancement of electrical field around the nanoparticle can also be observed using optical techniques like SNOM [198]. The distribution of the electric field around the nanoparticles is explained based on the scattering theory developed by Mie [200]. Mie's scattering theory deals with the calculation of the attenuation of an unpolarized monochromatic light beam after it has been passed through a medium containing spherical particles.

In view of the similarity of the plasmon resonance images of nanoparticles reported in the literature to the images shown in Figures 6.7-6.9, it appears the images show the resonance behavior of the nanoparticles. In the experiment, a magnetic tip is used to sense the magnetic field generated by the eddy currents in the nanoparticles. While the optical techniques image the *electric field* around the nanoparticle at optical frequencies, the current technique images the *magnetic field* around the nanoparticle at radio frequencies. Therefore, the question that now arises is what is the source of the contrast seen in the magnetic field images of nanoparticles excited with low frequency electromagnetic radiation?

It is well known that in bulk metals, in presence of an external magnetic field, low frequency electromagnetic waves can propagate as helicons [201,202]. In the presence of a magnetic field the screening of magnetic field is reduced. Because of the Lorentz force acting on the electrons, they move in a much less random fashion. This new constraint on their motion prevents the electrons from

responding completely to the electric field of the electromagnetic field. When the Lorentz force dominates the motion of the electrons, a low-frequency electromagnetic wave can propagate in a highly conducting medium. Helicons are circularly polarized electromagnetic waves that propagate with very low phase velocity, smaller by a factor of 10^5 - 10^{10} compared with the velocity of light in vacuum, with very low attenuation. It can be shown in the framework of the kinetic theory that the helicons can exist only at low frequencies $\omega \ll \omega_c$. Qualitatively, the helicon propagation can be described as follows: when the mean free path of electrons is sufficiently large and the frequency ω of the wave is low enough, the electrons affected by the Lorentz force would drift in the direction perpendicular to the plane formed by the uniform magnetic field \mathbf{B}_0 and the electric field of the wave. The current created by such a drift is called Hall current. It is perpendicular to the electric field \mathbf{E} of the wave and causes no dissipation. The other processes leading to the wave propagation in a metal, i.e. the induction of the variable magnetic field by virtue of the Ampere law and the induction of the variable electric field of the wave by virtue of Faraday law, are also non-dissipative. Consequently, the electromagnetic energy is conserved and in the absence of collisions the wave does not attenuate.

A quantitative description of the helicon waves in metals can be obtained by using Maxwell's equations. The local conditions, viz., $\omega\tau \ll 1$, and $kl \ll 1$ are satisfied. Here, ω is the excitation frequency, τ is the relaxation time of the electrons, $k = 2\pi/\lambda$ is the helicon wave vector and l is the electron mean free path. The local conditions are practically always fulfilled for the frequencies $\omega < 10^8 \text{ s}^{-1}$.

Helicon resonance modes in metals can be observed whenever the helicon frequency approaches the cyclotron frequency, i.e. $\omega \rightarrow \omega_c$. The cyclotron frequency ω_c , is given by

$$\omega_c = \frac{eB_0}{m^* c} \quad (6.1)$$

where e is the electron charge, B_0 is the static magnetic field, m^* is the effective mass of the electron and c is the speed of light. The phase velocity of the helicons, v_{ph} , is given by [201]

$$v_{ph}^H = \sqrt{\frac{cB_0\omega}{4\pi ne}} \quad (6.2)$$

where n is the electron density. It can be seen from the above equation that the phase velocity of the helicon does not depend on the electron effective mass, and it is proportional to the square root of the magnetic field and frequency. The helicon frequencies are small compared to the cyclotron and plasma frequencies. Thus, phase velocity of helicons is smaller than the speed of the light. At typical metallic densities, the plasma frequency, $\omega_p = 10^{16} \text{ sec}^{-1}$; for a frequency $\omega = 10^7 \text{ sec}^{-1}$ and $\omega_c = 10^{11} \text{ sec}^{-1}$, the phase velocity of a helicon is approximately 30 m/s. Helicons in metals are extremely slow waves. Their velocity is small relative to the velocity of light and small compared to typical particle velocities. The only velocity comparable with the velocity of the helicon is the sound velocity.

The remarkable fact about the helicon is that its magnetic field is much larger than the magnetic field of an ordinary electromagnetic wave with the same

electric field. Usual electromagnetic waves possess a magnetic field $B \sim E/c$, while $B_H = \frac{E}{v_{ph}} \gg \frac{E}{c}$. Hence the field of the helicon wave is mainly magnetic.

Generally, helicon wave propagation and its resonance have been observed in high purity metals only at very low temperatures [203,204]. At low temperatures, the mean free path length of the electrons in high purity metals is of the order of few millimeters. Helicon wave propagation has been reported in a number of metals [205,206]. Most often rectangular samples with flat and parallel boundaries of a few millimeters thickness are used. An electromagnetic coil in MHz range is used to excite helicon wave into the metal. The sample and the coil are placed in a static magnetic field ranging from 1-100 kG and cooled to liquid helium temperatures. The changes in the impedance of the coil are measured as the magnetic field is varied. Both standing wave and traveling wave measurements have been performed. Spherical samples have been used to observe both transverse and longitudinal helicon resonance. Helicon resonance modes in metals can be observed when the excitation frequency approaches the cyclotron frequency (Eq. 6.1). In a typical metal placed in an external static magnetic field of 1 kG, the cyclotron frequency is about 10 MHz. Therefore, to observe helicon resonances in bulk metallic samples, the frequency of the electromagnetic waves should be in MHz range. It is clear from the above discussion that in order to measure helicon resonances, the mean free path length of the electrons should be of the same order as the thickness of the sample, and the excitation frequency should approach the cyclotron frequency.

In nano-metals, at room temperature, the electron mean free path is of the order of the diameter of the particles. For example, the electron mean free path of gold at room temperature is about 50 nm. However, the cyclotron resonance frequency at a magnetic field of 1kG is approximately 10^6 - 10^7 Hz. To observe helicon resonances at room temperature the electromagnetic frequencies have to be in the range of 10-100 MHz. The examination of Eq. (6.1) indicates that for helicon wave propagation to occur at low frequencies in nano-metals, either the effective mass has to be large or the static magnetic field should be extremely high.

Recently, Pendry *et al.* [207] have shown that the effective mass of electrons can be dramatically increased in artificial metallic lattice structures. They used thin metallic wires with a radius of 1 μm assembled into a periodic lattice and analyzed for the plasmon frequency of the artificial structure. They derived an expression for the effective mass of electrons of the new structure which depends on the radius of the wire and the lattice spacing. Applying the method to a lattice structure of aluminum wires of diameter of 1 μm with a lattice spacing of 5 mm, it has been shown that the effective mass of the electron increases by four orders of magnitude. Therefore, by confining electrons to thin wires, an enhancement of their mass was achieved by 4 orders of magnitude so that they are as heavy as nitrogen atoms. Consequently, with an increase in the effective mass of electrons and reduced effective density, the plasma frequency was reduced to GHz range rather than UV or optical frequency ranges. The key to the suppression of the plasma frequency is that the structure is made of *thin*

wires. By reducing the radius of the wire, it was possible for the increase in the effective electron mass, which in turn reduces the plasma frequency. In a thick wire structure, the plasma frequency corresponds to a free space wavelength of approximately twice the lattice spacing. Therefore, it is clear from the above discussion that by employing micro- or nanostructures it is possible to decrease the plasma frequency. Also, the cyclotron frequency depends on the effective electron mass. In view of the increase in the effective mass of electrons for a thin wire structure, it can be observed that the cyclotron frequency will also reduce accordingly. Thus, the cyclotron frequency for an artificial structure could be reduced down to kHz range.

Following similar arguments, for noble metal (Au, Ag, etc), assuming a diameter of 200 nm, and 1 μm spacing, it can be shown that the effective mass of the electron increases by two orders of magnitude and the effective electron density decreases by three orders of magnitude. Substituting this data into Eq. (6.1), the cyclotron resonance frequency is found to be few hundred kHz in a magnetic field of 1 kG, and the phase velocity of helicons from Eq. (6.2) is found to be less than 100 mm/s. Thus it appears it is possible to generate helicon waves and resonances in nano-metal structures at very low frequencies even at room temperatures. Since the nature of a helicon wave is mainly magnetic, a magnetic tip scanning above the nanoparticle would image the magnetic field due to the helicon wave. Therefore, it is possible to image helicon waves and their resonance modes using the experimental configuration. The configuration of the experimental set up is similar to the experimental setups used in longitudinal

helicon resonance, except that a low spring constant magnetic tip-cantilever is used instead of an electromagnetic coil. This enables the imaging of the helicon resonance modes with nanometer scale resolution which is not possible when a coil is used to detect the helicon resonance modes. The surface plasmon images are distribution of electric field around the nanoparticles and while the helicon resonance images are magnetic field distribution. This further enhances the argument that the resonances observed are due to helicons in nano-metal particles.

Figure 6.10 shows a line scan across the platinum nanoparticle shown in Figure 6.7. It shows that the magnetic force distribution gradually decreases from the center of the image. The image contrast can be further understood based on the magnetic lines of force. The eddy currents generated in the nano-particle are circular and concentric with increasing diameter. The orientation of the magnetic field is perpendicular to the sample surface parallel to the magnetic field of the magnetic tip. Since the direction of the magnetic field changes every half cycle of the excitation the region closest to the magnetic tip the “pole” appears as a magnetic pole of the nano-particle sphere. It appears as though that the nano-particle has become a tiny magnet with pole direction aligned perpendicular to the sample surface with the poles interchanging at the frequency of the electromagnetic excitation frequency. It may be assumed that this is the fundamental helicon resonance. The approximate velocity of the helicon is about 400 m/s. If this is the fundamental resonance, the next resonance should occur in this spherical nano-metal particle at a frequency approximately 180 kHz.

Although, it is possible to excite the coil at 180 kHz to generate helicons, the sensitivity of the detecting magnetic-tip cantilever at this frequency should be high and similar to the sensitivity at fundamental frequency. An examination of the cantilever response to different frequencies showed that at 180 kHz the response is very weak and hence detection of second resonance is difficult. Alternatively, if a nano-particle with 500 nm can be identified, then the second resonance of the helicon could be detected at 90 kHz. In this case, the sensitivity of the cantilever is not changed and hence it is appropriate to use a 500 nm particle to detect the second helicon resonance if it is there.

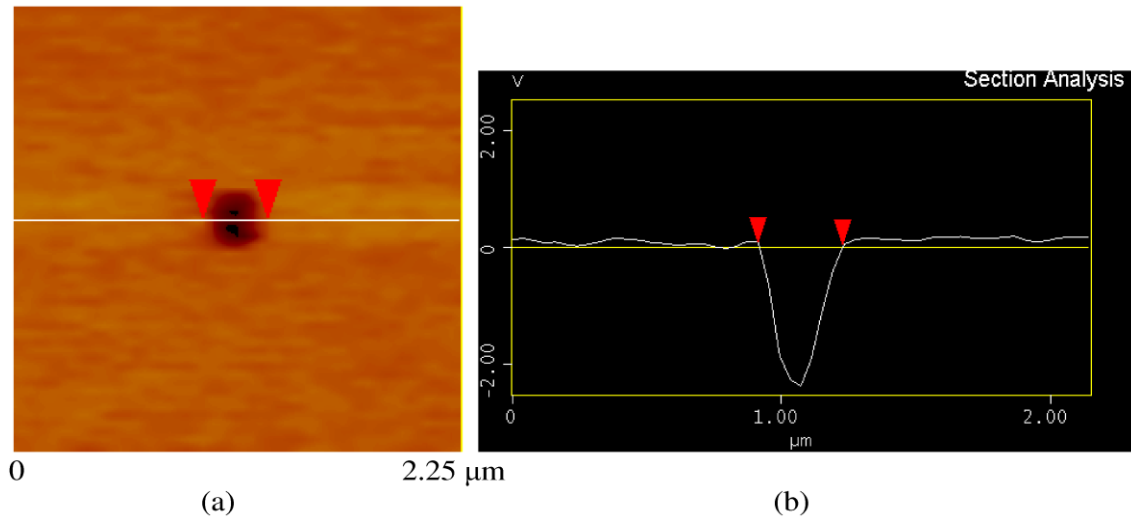


Figure 6.10. (a) Eddy current image of the platinum nanoparticle and (b) line scan across the nanoparticle showing the magnetic field variation across the nanoparticle. The size of the nanoparticle is about 250 nm.

Figure 6.11 shows the section analysis of the magnetic field image of a 500 nm platinum nanoparticle. The variation of the magnetic field across the diameter of the particle can be seen in the section analysis. Based on the above discussion, this could be the second helicon resonance mode of the nanoparticle. A closer observation of the line scan shows that the particle is not exactly split

into half. The bright region of the nanoparticle is longer than the dark region. This could be because the nanoparticle in this case is not a perfect sphere. Thus it appears the shape of the particle affects the magnetic field distribution in the nanoparticle. Since the contrast can be related to the magnetic forces, the contrast in the image appears as though two tiny hemispherical magnets are placed adjacent to each other with their poles in reverse direction. The section analysis of the 800 nm diameter nanoparticle shown in Figure 6.9 is shown in Figure 6.12, showing the third resonance mode of the helicon wave.

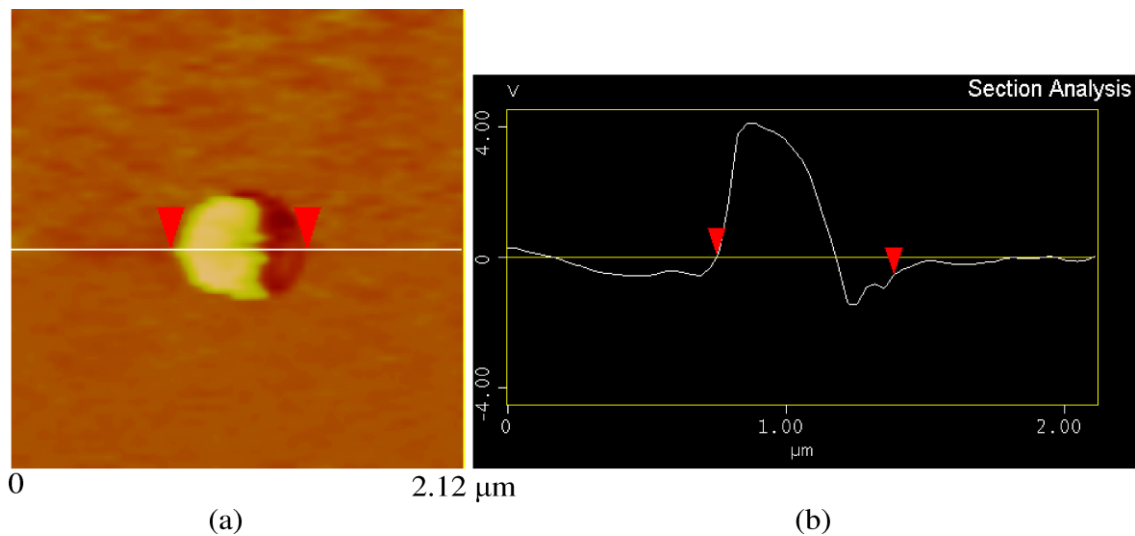


Figure 6.11. (a) Eddy current image of the individual platinum nanoparticle showing the second resonance mode of helicon wave. (b) Section analysis showing the variation of magnetic field across the line. The size of the nanoparticle is about 500 nm.

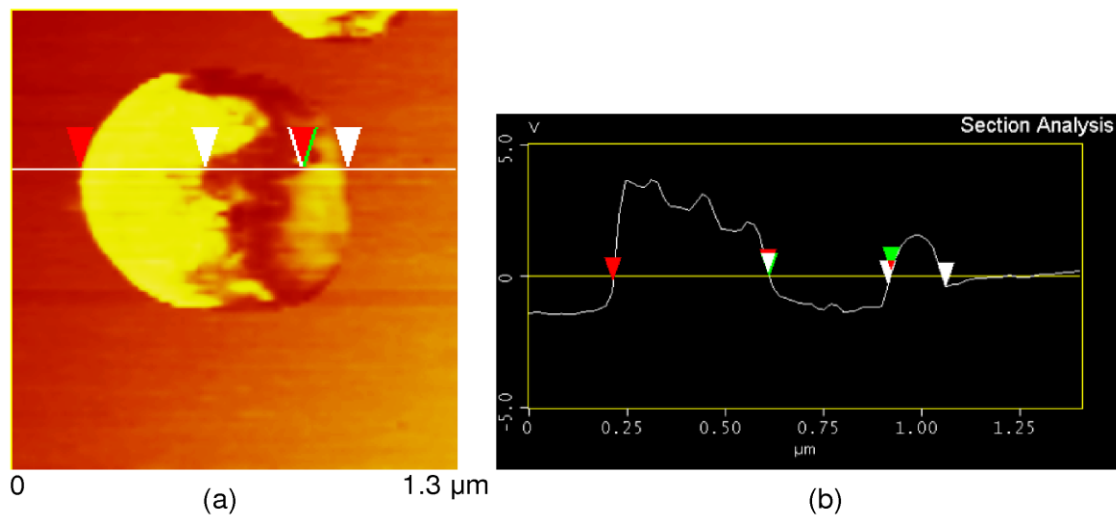


Figure 6.12. (a) Eddy current image of an individual nanoparticle showing the third resonance mode of helicon wave (b) corresponding section analysis of the nanoparticle showing the variation of magnetic field across the line. The size of the nanoparticle is about 800 nm.

The magnetic field images of the platinum nanoparticles excited with low frequency electromagnetic field can be compared with the magnetic lines of force of spherical particles subjected to electromagnetic radiation. The magnetic lines of force of spherical particles for different resonance modes are schematically shown in Figure 6.13. The nanoparticle with dark contrast is the first resonance mode of the particle. The corresponding magnetic lines of force show concentric lines in the spherical particle. An image of single particle with bright and dark contrast with a split in the middle appears to be consistent with the second resonance mode of the helicon in the particle. The lines are semicircular with their direction reversed in the two parts of the particle. Higher order resonances have been observed in bigger particles in the sample showing regions of bright and dark band contrast. The shapes of the resonances have been observed to change with the diameter as well as the shape of the particle. The contrast can

be explained based on accommodating tiny magnetic inside the particle with alternating the magnetic poles such that no two adjacent magnetic poles are alike.

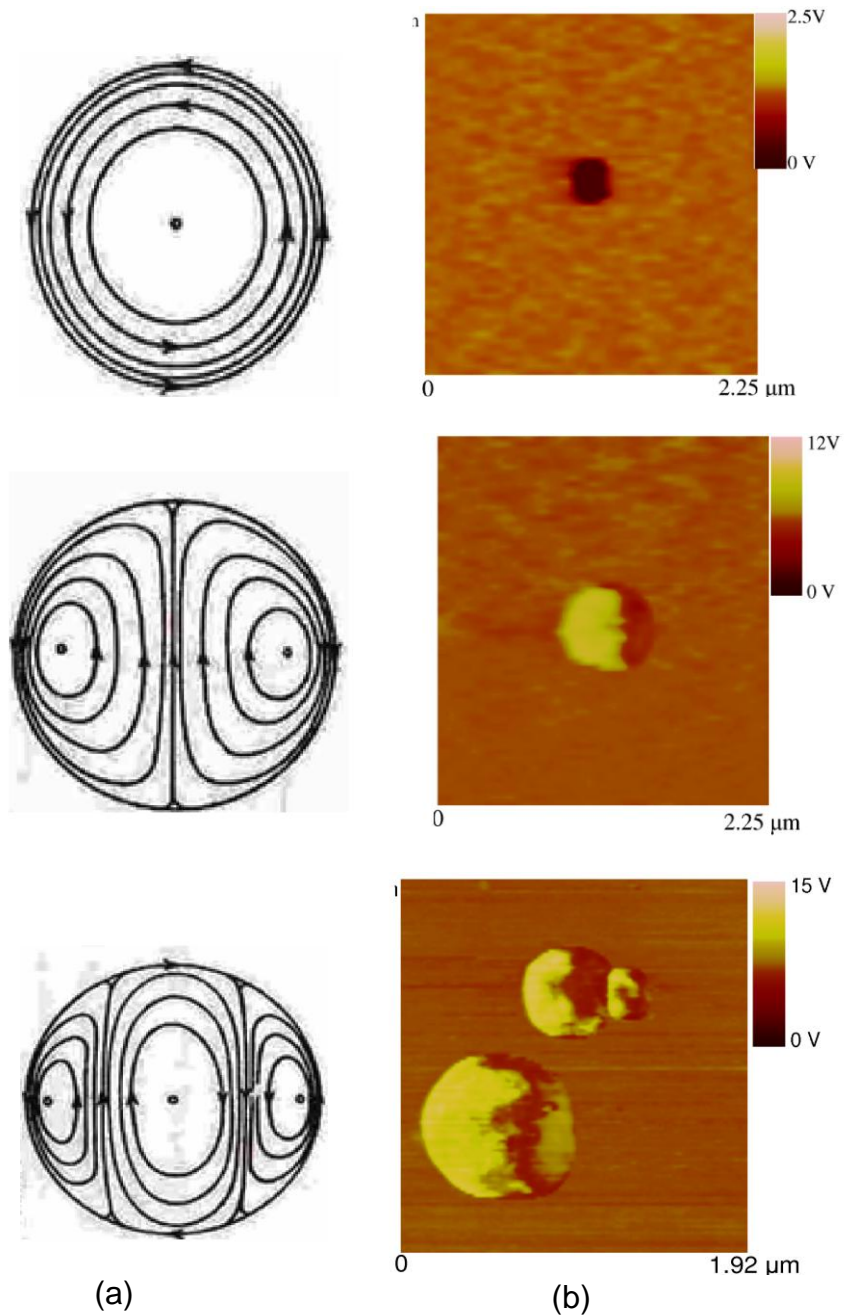


Figure 6.13 (a) Magnetic lines of force for the first, second, and third resonance modes in spherical particles [200]. (b) Magnetic field images of platinum nanoparticles.

The AFM surface topography and eddy current force images of the sample over a large area $50\ \mu\text{m} \times 50\ \mu\text{m}$ at an excitation frequency of 85 kHz is shown in Figure 6.14 shows that the size and the interparticle distance of the nano-particles vary. The average interparticle distance is $2\ \mu\text{m}$ and the diameter varies over few tens of nanometer to 500 nm. For approximate calculations an average diameter of particles and an average interparticle spacing of few microns were used. Following Pendry *et al.* [207] the effective mass of the electron was found to be $7.243 \times 10^{-29}\text{kg}$, the plasma resonance frequency to be $2.8 \times 10^{10}\text{Hz}$ and the cyclotron resonance to be 880 kHz. The helicon velocity was determined to be 200 m/s. Assuming these average values, the first helicon resonance should occur in 250 nm diameter particle at 85 kHz and the second resonance is expected to occur at the same frequency in a 500 nm particle and the third resonance mode at 750 nm. These are comparable to the experimental observations.

Although the calculations assume periodic arrangement of square array, Pendry *et al.* [207] have shown that for significant decrease of plasmon resonance frequency the actual lattice geometry may not be significant. Similar arguments are expected to hold good for cyclotron and helicon resonances and hence we believe even though the sample doesn't have regular periodic array of nano-metal particles still helicon resonances can be observed. The experiments conducted by Pendry *et al.* on artificial structure clearly showed the plasmon resonance frequency shifted dramatically from optical range to microwave region. However, the behavior of each of the member of the structure, if the dimensions

and the lattice spacing are different, has not been investigated. On the other hand, the experimental configuration developed in this work allows visualizing the helicon resonances in individual members of the structure with varying dimensions of the metallic nano-particles and inter-particle spacing.

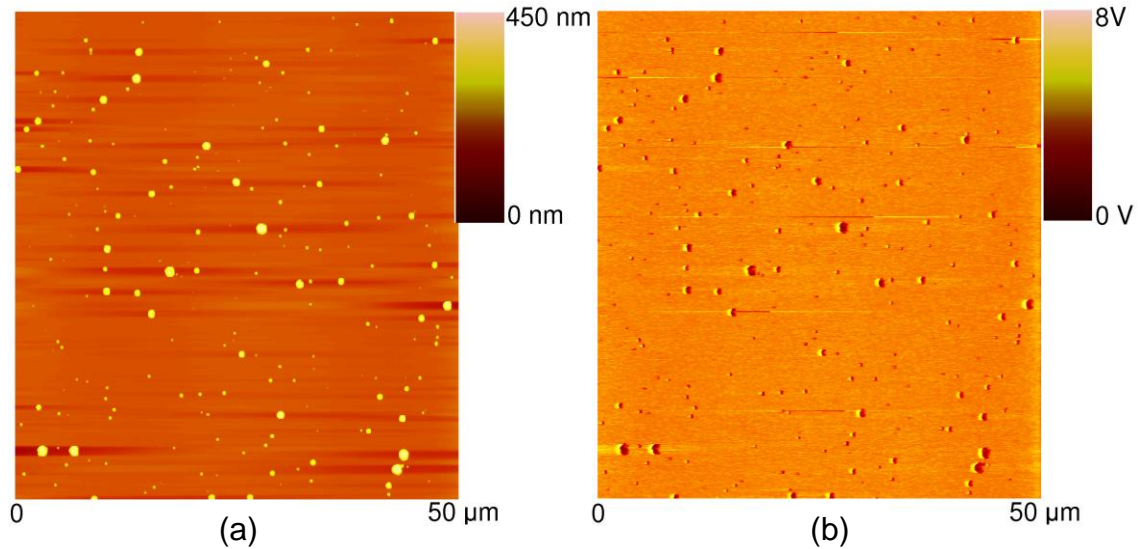


Figure 6.14 (a) Surface topography and (b) eddy current images showing the distribution of platinum nanoparticles. Frequency 85 kHz.

6.4. Conclusions

The application of the scanning eddy current force microscopy to characterize nanostructured materials is discussed in this chapter. The distribution and dispersion of carbon nanofibers reinforced in polymer matrix is studied using eddy current force imaging. The low-frequency electromagnetic properties of metallic nanoparticles are studied using the eddy current imaging technique. It is shown that helicon resonances in metallic nanoparticles can be detected and imaged at low frequencies. This is possible due to the increase in

the effective mass of electrons in the nanoparticles, which decreases the cyclotron frequencies into kHz range. The possibility of imaging helicons in metallic nanoparticles along with enhancement of magnetic field around nanoparticles opens up new avenues of research particularly in sensing applications.

CHAPTER 7

GENERATION, DETECTION AND IMAGING OF ELECTROMAGNETIC ACOUSTIC FIELDS

7.1. Introduction

Ultrasonic waves are normally generated by applying an alternating electric field to a piezoelectric transducer or an alternating magnetic field to a magnetostrictive transducer. These techniques produce coherent pulses of ultrasound over a very wide range of frequencies. However, the acoustic transducers have to be bonded to the test material. The bonding becomes increasingly difficult at high frequencies and is often undesirable in soft single crystals. It is well known that acoustic waves can also be generated in metals when they are placed in an electromagnetic field. When a metal is placed in electromagnetic field, eddy currents are generated in the metal and the electrons collide with the lattice producing local strains in the lattice. These strains cause the lattice to vibrate thus producing acoustic waves in the solid. The discovery of acoustic resonances due to electromagnetic radiation in metals without contact has led to the development of electromagnetic acoustic transducers (EMAT) [208,209]. These transducers are extensively used in NDE applications [210-212]. The experimental setup for an EMAT consists of a pulse generator which

drives a small coil placed close to the plane face of a metallic sample so that a time-varying magnetic field is generated at the surface of the sample. The time-varying magnetic field induces eddy currents in the sample. The induced eddy currents produce acoustic vibrations within the material. However, the amplitudes generated by the acoustic waves are extremely small. Therefore, for detecting these small amplitudes, an amplification of the signal is necessary. This is usually accomplished by the presence of a static magnetic field which increases the amplitude of the strains in the lattice thus allowing the detection of the acoustic signals with better signal-to-noise ratio. When a static external magnetic field B_0 of few kilogauss is applied to the sample, an acoustic wave is generated within the skin depth of the eddy currents. A quartz transducer is attached to the other face of the sample which is used to amplify the acoustic signal and displayed. In some cases, the coil that excites the magnetic field can itself be used as the detector.

Even though an external static magnetic field enhances the amplitude of the acoustic fields generated through electromagnetic fields, it has been shown that an efficient generation of sound can be achieved even in the absence of an external magnetic field. Southgate [213] showed that when there is no external static magnetic field, a slowly attenuating acoustic shear wave can be generated when the sample is placed in an electromagnetic field at low frequencies. An experimental setup similar to that of an EMAT can be realized by scanning a *magnetic* tip over a metallic sample placed in an electromagnetic field. However, the resultant interactions between the magnetic tip and the eddy currents involve

both eddy current forces and acoustic interactions. Thus, it is very difficult to interpret the contrast in the resulting images. Therefore, in this study, the combination of eddy currents and AFM is used to develop an EMAT-type system which can generate and detect the ultrasonic waves in a metallic sample by means of electromagnetic excitation without the presence of an external static magnetic field. This is made possible by the fact that AFM cantilever can measure very small amplitudes. Therefore, an external magnetic field is not required to measure and image acoustic fields generated by electromagnetic fields. An image of the sample is obtained by scanning a non-magnetic tip attached to the AFM cantilever in contact mode. The image contrast is explained based on the local acoustic fields generated in the material. The advantages of the new methodology and potential applications are discussed.

7.2. Materials and Experiment

Single crystal samples of copper, aluminum and cadmium were used to measure the amplitude of the acoustic waves generated by the electromagnetic field. For the purpose of imaging, the Ti-6Al-4V alloy used for electrical conductivity mapping was used. A non-magnetic tip attached to a cantilever of spring constant 0.12 N/m was used. The sample was placed on the electromagnetic coil and was excited with a radio frequency AC signal. The AFM was operated in contact mode. The thicknesses of the samples are chosen in

such a way that the skin depth of the eddy currents at the excitation frequency was larger than the thickness of the samples.

7.3. Results and Discussion

In this section, the results of electromagnetic acoustic field amplitudes in single crystal metallic samples are presented. Later, the acoustic field images of titanium alloy, placed in electromagnetic field are presented.

7.3.1. Detection of Acoustic Amplitudes in Single Crystal Metallic Samples

Figure 7.1 plots the amplitude of the AFM cantilever while in contact with the sample surface as a function of the input voltage to the electromagnetic coil in single crystal samples of copper, aluminum and cadmium. The thickness of each of the samples is 0.1 mm. One face of the sample surface is placed on the coil, while the other is in contact with the AFM tip. While the tip is in contact with the sample surface, the coil is excited with different frequencies and the frequency at which the cantilever vibrates with maximum amplitude is chosen. The frequency of excitation for copper, aluminum and cadmium is 80 kHz, 75 kHz, and 72 kHz respectively. The tip is positioned at a point on the each of the sample surfaces and the input voltage to the coil is varied and the cantilever vibration is monitored. It can be seen from Figure 7.1 that when the tip is in

contact with cadmium, the cantilever vibration amplitude was highest for any input voltage to the coil. Copper and aluminum showed a similar trend until a voltage of $4 V_{p-p}$ and after that the cantilever vibrated with more amplitude in aluminum than in copper. While the plot is linear for aluminum, it showed a quadratic behavior in cadmium. The plots in Figure 7.1 clearly indicates that the AFM was able to detect the amplitude of the ultrasonic waves generated in the samples.

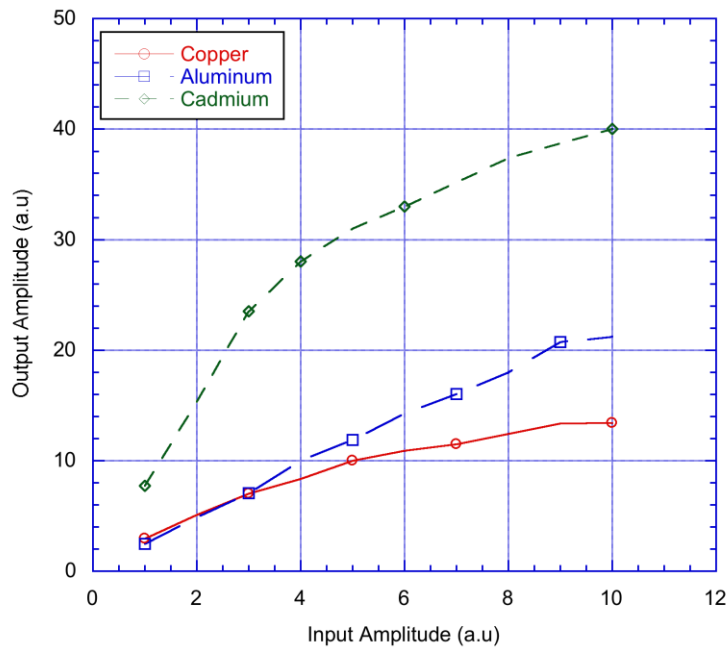


Figure 7.1. Amplitude of the AFM cantilever plotted as a function of the input voltage to the coil for copper, aluminum and cadmium single crystal samples.

In conventional EMATs ultrasonic waves are generated at the surface of a metal sample at room temperature when a static magnetic field is applied to the eddy current distribution induced by a small coil excited at megahertz frequencies. At megahertz frequencies the eddy currents are confined to a thin surface layer defined by skin depth, δ and the external magnetic field due to the

coil is screened from the interior of the metal. For a good conductor at room temperature δ is about 25 μm at 10 MHz, whereas the acoustic wavelength λ is in the range 300-600 μm . In the absence of a static field the electronic and ionic currents in a surface layer of thickness δ act in opposite directions and effectively cancel each other. The electrons are constantly in collision with the ions, transferring their excess momentum to the ions at each collision. The currents thus balance out and the incident electromagnetic energy is dissipated as Joule heat. However, when a steady magnetic field is applied a new force, Lorentz force acts on the electrons thus creating an imbalance in currents. If the static magnetic field is applied along the same direction as that of the coil magnetic field, the Lorentz force is longitudinal, resulting in a variation of the electron charge density along the perpendicular direction to the coil field. An internal electric field along this perpendicular direction will be set up to maintain local charge neutrality. This field generates an ultrasonic wave in longitudinal direction. A transverse ultrasonic wave can be generated if the static magnetic field is applied in a direction perpendicular to the field of the coil.

In the current experiments, the skin depth of the eddy currents at the excitation frequencies used for the samples is larger than the thickness of the sample. Therefore, skin effect need not be taken into account and there will be no screening of the magnetic field. This leads to considerable acoustic displacements in the material which can be detected by a flexible cantilever in contact with the sample surface. Thus, it is possible to generate acoustic waves in a conductor using the eddy current experimental setup without an external

magnetic field. It can be seen that cadmium generated large acoustic amplitudes, while copper generated least acoustic amplitude. Therefore, it appears that acoustic waves with larger amplitudes are generated in material with less conductivity and decreases with an increase in the conductivity.

7.3.2. Imaging Acoustic Fields Generated by Electromagnetic Fields

It was shown in the previous section that by positioning a nonmagnetic tip in contact with the metallic surface, it is possible to detect the acoustic amplitudes generated in the metal due to an electromagnetic excitation. If the same tip is raster scanned across the sample surface, the variations in the acoustic amplitudes can be imaged in metals. Figure 7.2 shows the surface topography and acoustic field image showing the microstructure of the Ti-6Al-4V alloy. The image was obtained with a scan area of 100 μm while the coil was excited with a frequency of 85 kHz. The acoustic field image clearly shows the grain boundaries with better contrast than the conductivity image obtained previously. However, the α and β phases that were seen with different contrast in electrical conductivity image are seen with near-uniform contrast in acoustic field image. This indicates that the local elastic properties of the two phases are not significantly different. It is well-known that grain boundaries appear with better contrast in acoustic imaging techniques because at the boundary, the acoustic amplitudes are significantly larger than in the grain. Therefore, the images

provide information about variations in local elasticity and stiffness in the material.

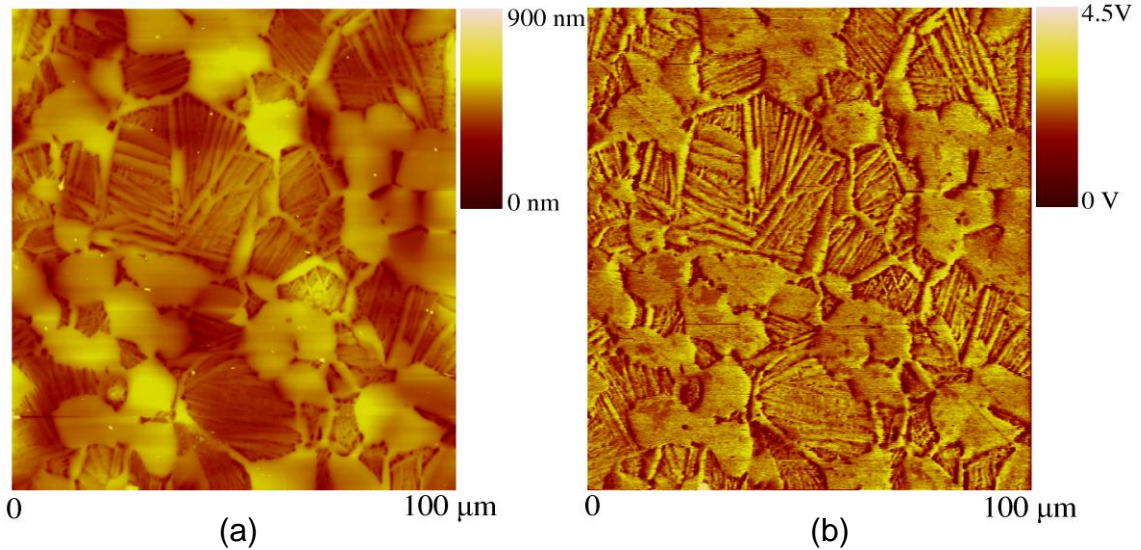


Figure 7.2. (a) Surface topography and (b) acoustic amplitude images obtained on a dual-phase polycrystalline Ti-6Al-4V sample. Excitation frequency: 85 kHz.

Figure 7.3 shows a magnified surface topography and acoustic field images at a frequency of 85 kHz and a scan area of 50 μm . In this image, variation in contrast between different α grains can be observed. The contrast among these grains is due to the anisotropy of the α phase. As mentioned in a previous section, the α phase of Ti-6Al-4V exhibits HCP crystal structure. The elastic modulus of the crystal structure parallel and perpendicular to c-axis of HCP structure is quite different. Thus, if the grains are oriented in different directions, it will lead to a different contrast in the acoustic image, while grains oriented in similar directions will have uniform contrast. Moreover, in this image, some of the lamellar regions show different contrast at the boundaries indicating different grain orientations.

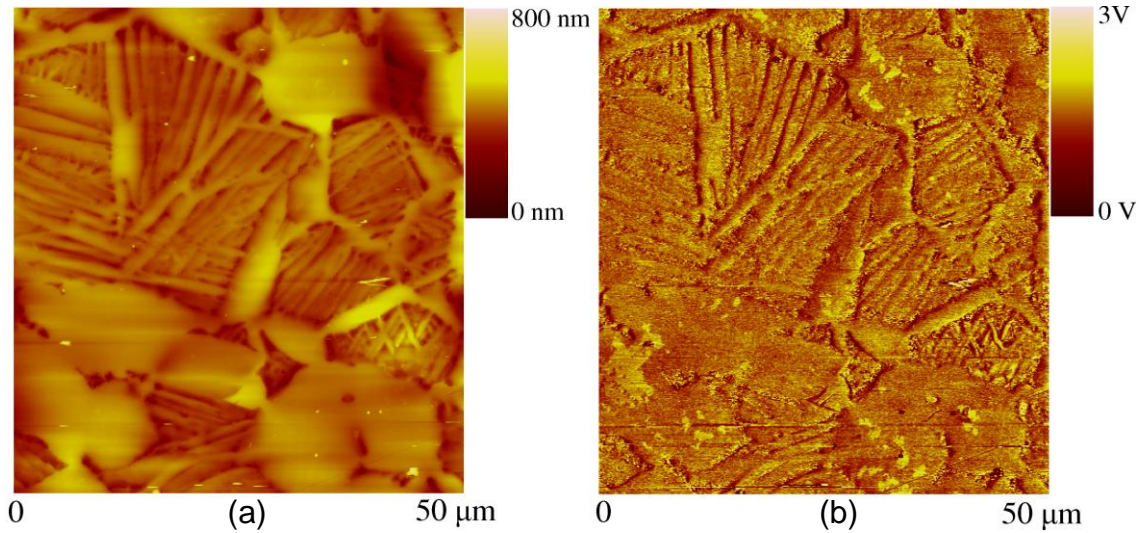


Figure 7.3. A higher magnification (a) surface topography and (b) acoustic field images of Ti-6Al-4V showing the contrast difference in the grains. Frequency of excitation: 85 kHz.

7.4. Conclusions

Electromagnetic generation of acoustic fields in metals at low frequencies is shown by an experimental setup involving a coil and a non-magnetic tip attached to a flexible cantilever of an AFM. The detection of acoustic amplitudes in single crystal metallic samples has been shown using this setup. An image of the local variations in acoustic fields was obtained in a titanium alloy by scanning the tip across the surface while the sample is placed in an electromagnetic field generated by a coil. The images show that local elasticity and stiffness variations can be imaged with nanometer scale resolution. Grain to grain contrast and grain boundary contrast was observed clearly in the images. The experimental setup described here is similar to EMAT which are used to generate acoustic waves in

metals at megahertz frequencies in the presence of an external static magnetic field in a noncontact fashion. The EMATs are extensively used in nondestructive testing of materials. However, the current experimental setup does not require the presence of an external static magnetic field. Ultrasonic imaging [103,214,215] using atomic force microscopy has been studied extensively. In these techniques a piezoelectric transducer is used to generate ultrasonic waves in the sample and the resulting acoustic interactions are mapped to generate an image of local elastic properties. The contrast observed in the magneto-acoustic imaging is very similar to that of ultrasonic AFM. Therefore, this technique provides an avenue to image local elastic properties with nanometer resolution without an acoustic transducer. This technique will be particularly useful when acoustic bonding is a major concern or imaging single crystal samples.

CHAPTER 8

CHARACTERIZATION OF MAGNETIC PROPERTIES

8.1. Introduction

In general, to characterize magnetic properties using an AFM, a ferromagnetic probe is attached to the cantilever and is used in lift mode to image the magnetic interactions between the tip and the sample. However, if the stray field of the probe is too high, the magnetization of the sample will be affected, particularly for soft magnetic samples. Hence AFM cantilevers with high spring constants have been used for magnetic imaging, and high coercivity magnetic tips have been fabricated to avoid changes due to tip magnetization. Nevertheless, the interpretation of the magnetic contrast in traditional MFM images is difficult due to the tip magnetization. Another drawback of conventional magnetic force microscopy is that, in lift mode, the spatial resolution and sensitivity are often poor. Thus, development of AFM based magnetic imaging techniques using nonmagnetic tips is highly desirable. Hoffmann *et al.* [17] described an AFM based experimental setup to image magnetic domains of a soft magnetic material using a non-magnetic probe. In their experiments, they used a non-magnetic conducting tip attached to a silicon cantilever of an AFM to

scan the magnetic domains. The conducting tip, when oscillated near the sample induces eddy currents within the tip. The vibration characteristics of the tip are dependent on the magnetic properties of the sample below the tip. Therefore, an image obtained in this setup gives information about magnetic properties of the material.

Magnetostriction is one of the most important properties of magnetic materials. When a magnetic field is applied to a magnetic material, strains are generated in the material. This phenomenon is known as magnetostriction. Strains can also be generated by the magnetic force acting on the material as a whole, by the magnetic forces acting on the magnetization of each of the domains in the material and by the electromagnetic forces between the magnetization and an eddy current. The strain generated in the entire material can be considered to be noise, because it does not provide any microscopic information. When an alternating magnetic field is applied to a ferromagnetic material, electromagnetic forces induce strains in the material depending on the frequency of the field. Measurement of the strains due to microscopic magnetic forces due to magnetization of domains, magnetostriction, and electromagnetic forces reveals local variations in magnetic properties along with elastic properties. Moreover, the phenomenon of strain generation in magnetic materials depends on the magnetization of the domains. Therefore, domain structure can also be observed by studying these strains. The relative contribution of the three strains depends on the measurement conditions.

In this study, an experimental technique capable of imaging magnetic properties using an AFM which detects magnetostrictive interactions between a nonmagnetic tip and ferromagnetic material is described. The interactions detected by this technique are quite different from the conventional magnetic property imaging techniques based on atomic force microscopy. The detection and imaging of magnetostrictive interactions using an AFM results in the imaging of magnetic domains with high sensitivity and high spatial resolution when compared to conventional MFM techniques. The technique is first applied to characterize a sample consisting of both magnetic and non-magnetic nanoparticles. While the magnetic nanoparticles exhibit magnetostriction behavior, the non-magnetic particles do not show any magnetic properties. Therefore, the magnetostriction is used to identify the magnetic particles and can also be used to study the distribution and dispersion of the nanoparticles. This technique provides a simple methodology to identify magnetic and nonmagnetic regions which cannot be accomplished by electron microscopy or other techniques. The experimental setup is then used to detect and image small changes in local magnetostriction behavior of amorphous and nanocrystalline magnetic ribbon materials. The magnetic domains in these materials are also imaged and the contrast in the images is explained based on the strains caused by the magnetic field which depends on the magnetization of individual domains.

8.2. Materials and Experiment

Nanoparticles of iron and carbon were deposited on a silicon substrate using through thin film ablation (TTFA) process [199]. In this process, a target consisting of thin films of iron and carbon is ablated using a laser. The target was prepared by RF magnetron sputtering and consisted of a thin layer of Fe that was deposited onto a fused silica support. A thin layer of C was sputtered-deposited on top of the Fe. The resulting nanoparticles of iron and carbon are collected onto a silicon substrate positioned few mm from the target. The process results in a more uniform distribution and dispersion of nanoparticles compared to the standard laser ablation process.

Amorphous and nanocrystalline magnetic ribbons of the nominal composition FeSiBNbCu alloy are used to study the local variations in magnetostriction behavior. These materials are also known as FINEMET alloys [216]. The details of processing of these materials can be found elsewhere in the literature [215-218]. The nanocrystalline magnetic ribbon of FINEMET alloy is produced by the controlled devitrification of the amorphous ribbon and is composed of two magnetic phases- nanosized crystallites embedded in a residual amorphous matrix. The nanocrystalline ribbons exhibit exceptionally soft magnetic properties which arise from a very small magnetostriction [219]. With an increase in annealing temperatures, the magnetostriction in nanocrystalline magnetic material rapidly decreases and in fact, in fully nanocrystallized state, the effective magnetostriction is close to zero.

A non-magnetic tip, made of Si_3N_4 with a nominal radius of 20 nm, attached to a cantilever with a spring constant of 0.1 N/m, is used in this study. The cantilever-tip is scanned in contact mode across the surface of the ferromagnetic material which is placed in an electromagnetic field generated by a coil driven at the resonant frequency of the cantilever coupled with the sample surface. The strains caused by magnetostriction and electromagnetic forces are detected by the tip which causes the cantilever to oscillate with an amplitude, which is proportional to the local magnetostrictive properties of the material.

8.3. Results and Discussion

In this section, magneto-elastic images of iron and carbon nanoparticles deposited on silicon substrate are obtained to distinguish between the magnetic iron and non-magnetic carbon nanoparticles. Electrostrictive images of amorphous and nanocrystalline magnetic ribbons are also presented.

8.3.1. Iron and Carbon Nanoparticles

Figure 8.1 shows the surface topography and magneto-elastic images of iron and carbon nanoparticles. The images were obtained with a scan area of $2.78 \mu\text{m} \times 2.78 \mu\text{m}$ at an excitation frequency of 91 kHz. The surface topography image shows nanoparticles with different sizes at a maximum vertical height of 200 nm. It is difficult to identify iron and carbon nanoparticles from the

topography image alone. However, careful observation of the magneto-elastic image on the right reveals nanoparticles showing different contrast. When the tip is scanned over iron nanoparticles, due to their magnetic property, they show magnetostriction behavior causing strains in the nanoparticle. This causes the cantilever to deflect with relatively more amplitude. On the other hand, when the tip scans the carbon nanoparticles, no strain is observed. Thus, the cantilever deflects more near ferromagnetic regions giving rise to brighter contrast than nonmagnetic regions. Consequently, the particles with dark contrast are carbon nanoparticles and the regions with bright contrast correspond to iron nanoparticles. Some of the particles are shown by arrows. On closer observation, it can be seen that an agglomeration of iron and carbon nanoparticles is seen with bright and dark regions next to each other, as shown by the box in the Figure 8.2. The size of iron nanoparticles ranges from 200 to 270 nm and carbon ranges from 50 to 80 nm.

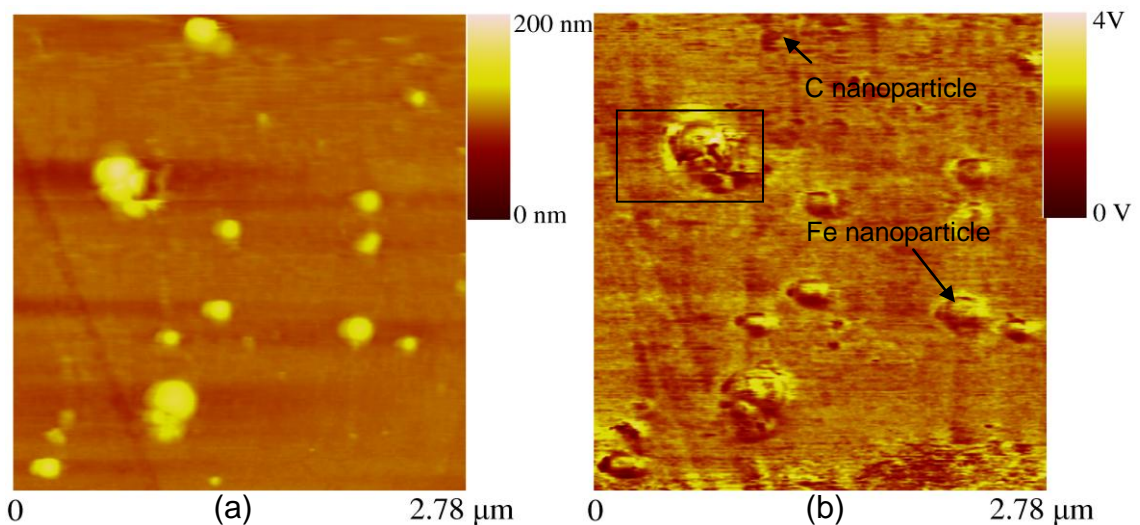


Figure 8.1. (a) Surface topography and (b) magneto-elastic images of the sample containing Fe and C nanoparticles. Excitation frequency: 91 kHz.

Figure 8.2 shows the surface topography and magneto-elastic images of the nanoparticles in another region of the sample. The images were obtained in an area of $3.87 \mu\text{m} \times 3.87 \mu\text{m}$ at a frequency of 91 kHz. In this region, it can be seen that the more number of iron nanoparticles are present than carbon nanoparticles. The size distribution of the nanoparticles is similar to that of previous region.

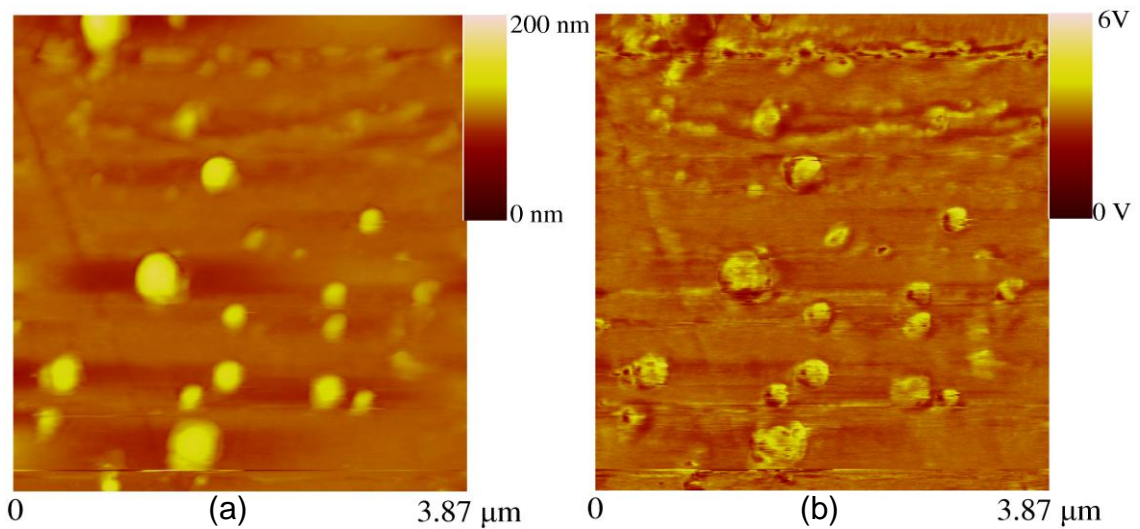


Figure 8.2. (a) Surface topography and (b) magneto-elastic images of Fe and C nanoparticles showing more number of iron nanoparticles than the carbon nanoparticles. Excitation frequency: 91 kHz.

8.3.2. Amorphous and Nanocrystalline Magnetic Ribbons

Figure 8.3 shows simultaneously obtained surface topography and magnetostriction images of amorphous magnetic FINEMET alloy sample. The images were taken with a scan size of $1.33 \mu\text{m} \times 1.33 \mu\text{m}$ at an excitation frequency of 58 kHz. The surface topography of the sample shows uniform contrast indicating a flat surface profile. The maximum vertical height of the

topography is 3 nm. The corresponding magnetostriction image shows bright and dark regions indicating variations in magnetostriction locally in the material. The bright regions in the image correspond to the regions having higher strains and consequently more magnetostrictive. Since the strains produced by magnetostriction depend on the magnetization of each domain, the magneto-elastic image can be used to identify magnetic domains. If the magnetostriction or the electromagnetic forces between the magnetization and eddy currents contributed to the image contrast, then the bright and dark regions would represent magnetic domains [220]. An example of such domains is shown by arrows in Figure 8.3.

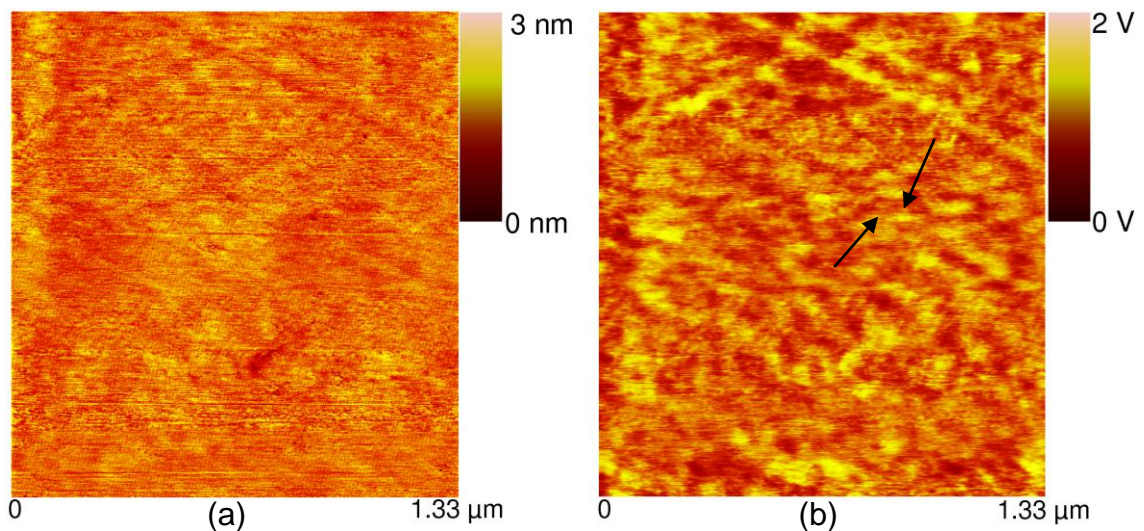


Figure 8.3. (a) Surface topography and (b) magneto-elastic images of amorphous FINEMET magnetic ribbon sample. Magnetic domains can be observed in the magneto-elastic image and are indicated by arrows. Frequency of excitation: 58 kHz.

Figure 8.4 shows the magneto-elastic image at another location on the amorphous sample at the same excitation frequency. This region has circular bright and dark regions which are magnetic domains and the size of the domains

is large in this region. The amplitude of the vibration of the cantilever is higher in this region as seen by the higher output voltage from the photodiode detector of AFM. This would indicate that locally the magnetostriction is higher than the other region. The amorphous magnetic ribbons exhibit higher saturation magnetostriction. This is confirmed by the larger strains produced by the amorphous sample which can be clearly seen in magneto-elastic images. In this region also, the magnetostriction is the dominant factor that contributed to the contrast in the magneto-elastic image. Thus the bright and dark region corresponds to the magnetic domains as shown by arrows in Figure 8.4.

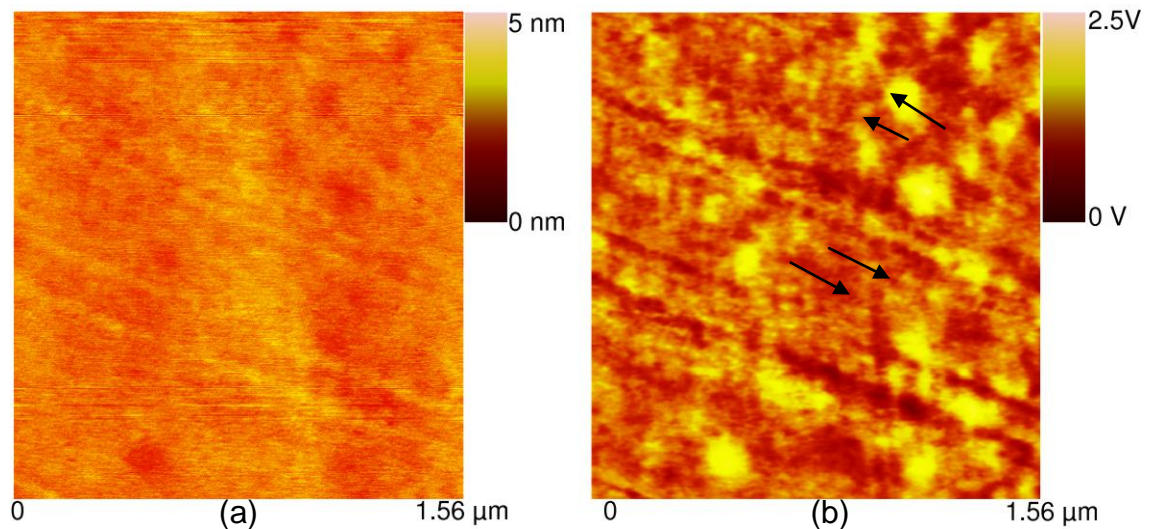


Figure 8.4. (a) Surface topography and (b) magneto-elastic image of amorphous magnetic ribbon sample. The magneto-elastic image shows relatively large circular magnetic domains. Some of the domains are indicated by arrows. Frequency of excitation: 58 kHz.

The magneto-elastic images obtained on nanocrystalline FINEMET magnetic ribbon sample showed the formation of nano-sized crystals due to the annealing of amorphous sample. The size of the nano crystals ranges from 50 nm-100 nm. Figure 8.5 shows the surface topography and the corresponding

magneto-elastic image obtained with a scan size of $3.27 \mu\text{m} \times 3.27 \mu\text{m}$ at an excitation frequency of 58 kHz. The topography image shows the nanocrystals embedded in amorphous matrix with a maximum vertical height of 200 nm. Most of the nanocrystalline phase appears with dark contrast indicating a decrease in the magnetostriction of the material. However, some regions show dark and bright regions indicating the presence of a small effective saturated magnetostriction. An agglomeration of nanocrystals is also observed in this region.

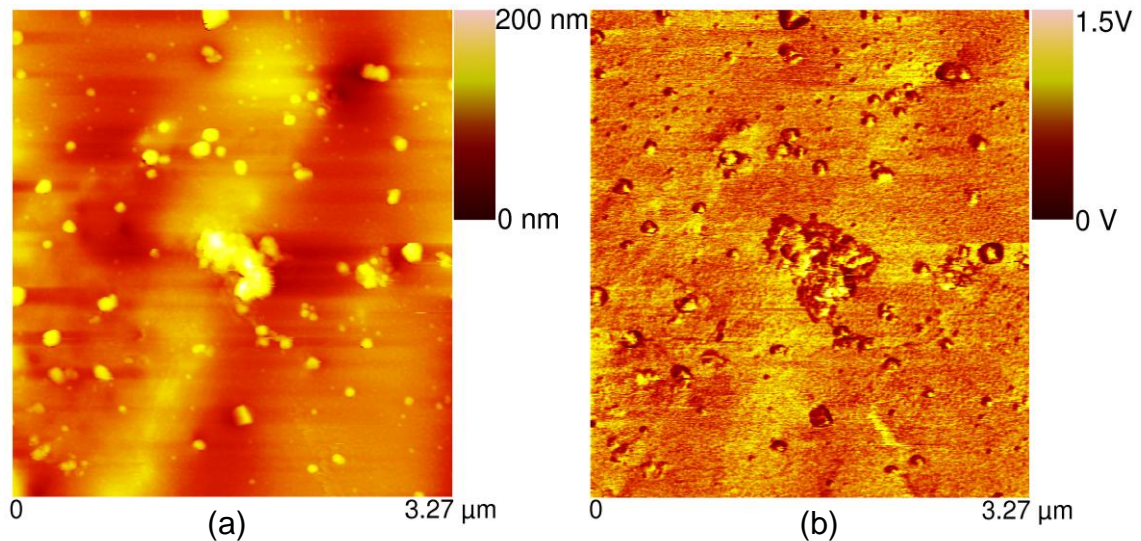


Figure 8.5. (a) Surface topography and (b) magneto-elastic images of nanocrystalline magnetic ribbon sample. Frequency of excitation: 58 kHz. Nanocrystalline phase can be observed in the images.

Figure 8.6 shows a magnified image of the nanocrystalline phase of the FINEMET alloy sample at a frequency of 58 kHz. The domains can be clearly seen in this image. Within a domain the magnetostriction is saturated. The saturation gives rise to a deformation which is dependent on the magnetization direction of the domain. At the domain wall the magnetic moments changes direction, resulting in the deformation of material. The magnetization of the

sample is in-plane and the external magnetic field is perpendicular to the plane. Therefore each of the domains is subjected to rotational forces and consequently the amplitude of AFM cantilever is large near the domain walls. If the microscopic magnetic forces contribute to the domain image, the domain walls would appear bright in the magneto-elastic image [220]. A domain wall is shown by arrow in Figure 8.6. A line profile across the domain wall in the nanocrystal shows a width of 40 nm. Therefore, it appears that the magnetic forces contributed to the contrast in this region of the sample.

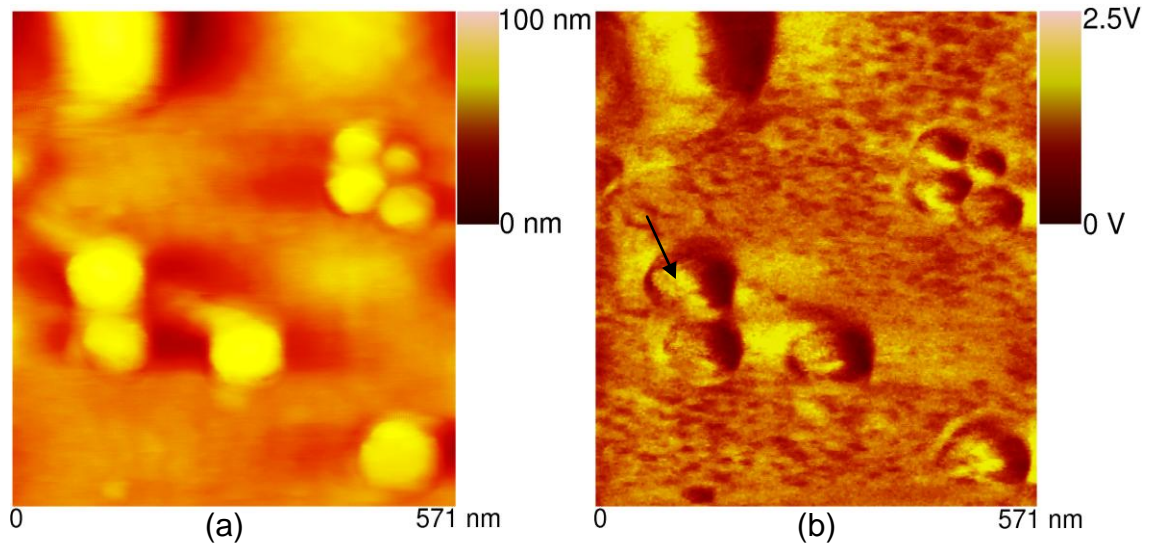


Figure 8.6. A high magnification (a) surface topography and (b) magneto-elastic images of the nanocrystalline FINEMET alloy magnetic ribbon. A domain wall with a width of 40 nm is shown by arrow. Frequency of excitation: 58 kHz.

8.4. Conclusions

An experimental setup based on AFM is presented to image magneto-elastic interactions in ferromagnetic materials. A non-magnetic tip is used to scan

the surface of a ferromagnetic sample placed in the electromagnetic field of a tiny coil excited at resonant frequency of the AFM cantilever. The ac magnetic field generates strains in the material which is detected by the AFM cantilever to obtain an image of local magnetostriction of the sample. The technique is used to identify magnetic iron nanoparticles from nonmagnetic carbon nanoparticles deposited on a silicon substrate. The technique is also used to study the magnetostrictive properties of amorphous and nanocrystalline magnetic materials. The local magnetostriction properties depend on the magnetization of the domains. Therefore, this technique is used to image the magnetic domains in the sample. The nanocrystals in nanocrystalline magnetic ribbon sample are imaged using the technique. The magnetostriction behavior of a nanocrystalline magnetic material is expected to be small. This is confirmed in the magneto-elastic images obtained on the nanocrystalline sample. Most of the nanocrystalline phase appears dark indicating a small magnetostriction. Magnified images of the magneto-elastic interactions show that the deformation of the material due to magnetization direction reversal in domains leads to a higher amplitude of AFM cantilever near the domain wall. Consequently, the domain wall can be imaged due to the microscopic magnetic forces acting on the domains. The width of the magnetic domain wall is about 50 nm. The magnetostrictive imaging using an AFM will be a useful technique when imaging magnetically soft materials, which are otherwise difficult to be imaged due to sample magnetization in conventional magnetic force microscopy techniques.

CHAPTER 9

CHARACTERIZATION OF FERROELECTRIC PROPERTIES

9.1. Introduction

A ferroelectric material is an insulating system with two or more discrete stable or metastable states of different nonzero electric polarization in zero applied electric field, referred to as spontaneous polarization. For a system to be considered ferroelectric, it must be possible to switch between these states with an applied electric field. When an electric field is applied to a piezoelectric material, strains are generated in the material due to the converse piezoelectric effect. In addition to the piezoelectric effect, electrostriction and electrostatic interactions can also be observed when a ferroelectric or piezoelectric material is subjected to an external electric field. Electrostriction refers to the generation of strains in ferroelectric or dielectric materials when an external electric field is applied to the material. This phenomenon is similar to that of magnetostriction in ferromagnetic materials.

Various techniques have been developed to characterize ferroelectric materials using AFM. Piezoresponse force microscopy (PFM) is one of the most

widely used AFM based technique to study the ferroelectric properties [132-136]. This technique has been used extensively to study at nanometer scale, the local piezoelectric properties, ferroelectric domain imaging, spontaneous polarization distribution, etc. In this method, a bias voltage is applied between a conducting tip and the ferroelectric sample. Also, an electrode is attached to the sample material, so that bias voltage can be applied to the sample material. The piezoelectric response of the surface is detected as the first harmonic component of bias-induced tip deflection. A significant challenge of the piezoelectric measurements is that the tip motion can be due to a combination of piezoelectric, electrostrictive and electrostatic interactions. The relative contribution of these interactions depends on the measurement conditions. As mentioned above, the piezoelectric behavior represents a linear relation between the strain and applied field. If the strain depends on the square of the applied field, the interaction is mainly due to electrostriction of the material. Therefore, careful analysis of the contrast in the images is needed for accurate measurement of ferroelectric properties. The piezoresponse force microscopy has also been used for quantitative measurement of piezoelectric coefficient in ferroelectric materials [221]. High-voltage PFM was also used for the measurement of piezoelectric coefficient in single crystal of RbTiOPO_4 [222]. In this method, a high voltage stress is applied via plain electrodes between the sample and tip. However, this method cannot be used in ionic conducting ferroelectrics such as KTiOPO_4 (KTP), due to the possibility of electrical breakdown. Therefore, for ionic conducting ferroelectrics, PFM may not be suitable.

In this study an alternative technique based on AFM is proposed to study the local electrostrictive and piezoelectric properties of ferroelectric materials. In this method, the ferroelectric sample is placed in an electromagnetic field generated by a coil. The electric field component of the electromagnetic field interacts with the polarized states of the ferroelectric. This results in the generation of strains in the material. The strains are measured by a magnetic tip-cantilever of an AFM and a map of local electrostrictive properties of the material is obtained with nanometer resolution. Depending on the frequency of the applied field, both piezoelectric and electrostriction properties can be imaged. Since the strain produced by electrostriction or piezoelectricity is dependent on the polarization behavior, ferroelectric domains can be imaged using this technique. Ionic conducting KTP samples are characterized using this technique. Since the samples are conducting, conductivity images can also be obtained. The contrast in the images is explained based on the local variations of electrostriction or piezoelectric properties and/or conductivity. An advantage of the new technique is that no bias voltage is required to be applied between the tip and sample. Therefore, the possibility of damage to the sample is not present. Even though ionic ferroelectric material is characterized, the technique can equally be applied to any ferroelectric or dielectric material.

9.2. Materials and Experiment

Ferroelectric properties of four samples of uncoated potassium titanyl phosphate KTiOPO_4 (KTP) crystals processed by different methods were studied in these experiments. KTP crystals exhibit excellent nonlinear optical properties, used in frequency doubling by second-harmonic generation and optical parametric oscillations [223-225]. The four samples were labeled as K0557, KTP4, KTP6, and HGTR KTP. The dimensions of all the samples were 10 x 5 x 1 mm.

A magnetic thin film coated tip with a nominal diameter of 20 nm attached to a cantilever with a spring constant of 0.1 N/m is scanned across the sample surface in contact mode. The electric field of the coil electromagnetic field interacts with the ferroelectric material leading to strains in the material. The strains generated in the sample deflect the cantilever, the oscillations of which are dependent on the local electrostrictive properties of the material.

9.3. Results and Discussion

In this section, results of electrostrictive and piezoelectric interaction measurement using AFM in different KTP samples are presented. Images of ferroelectric interactions in KTP samples are presented.

9.3.1. Detection of Electrostrictive and Piezoelectric Interactions in KTP crystals

Figure 9.1 plots the amplitude of the vibration of the AFM cantilever when positioned over a single point on the four KTP samples at a frequency of 85 kHz. Of the four samples, three samples except HGTR KTP show a linear behavior. It implies that, at a given frequency, the samples, KTP4, KTP6, and K0557 exhibit piezoelectric behavior. The slope of the linear plot is related to the piezoelectric coefficient of the sample. The fourth sample, HGTR KTP does not show a linear behavior, but shows a quadratic behavior indicating that the sample shows electrostrictive behavior at a given frequency. It means that electrostriction interactions can be obtained at $2f$ frequency.

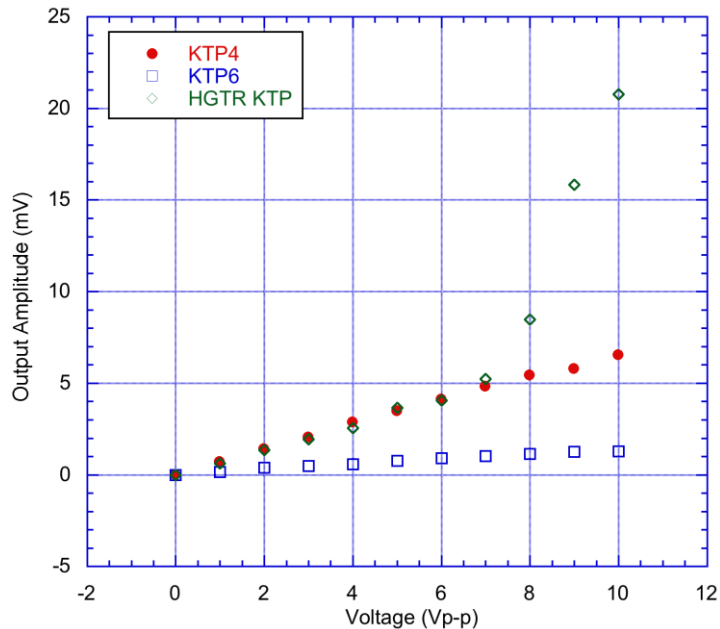


Figure 9.1. Amplitude of the AFM cantilever plotted as a function of the input voltage applied to the coil for the different KTP crystal samples.

KTP crystals are ionic conducting ferroelectrics with relatively high conductivity. Therefore, eddy currents can be generated in the material. For measuring piezoelectric or electrostrictive interactions, the magnetic tip needs to be in contact while taking measurements. However, if a conductivity mapping is needed, the tip can be scanned in a non-contact fashion to detect local variations in electrical conductivity. To study the effect of separation distance between the tip and sample on electrical conductivity measurements, eddy current forces were measured between the magnetic tip and magnetic fields generated by eddy currents. Figure 9.2 shows a plot of amplitude of the cantilever vibration as a function of separation distance between tip and the sample for K0557, KTP4, and HGTR KTP samples. The plots show that with an increase in the separation distance, the amplitude of cantilever vibration gradually decreases and after a certain distance the amplitude becomes constant. At any separation distance, K0557 produced larger amplitudes of AFM cantilever. Consequently, eddy current forces in K0557 sample would be the highest among all the samples.

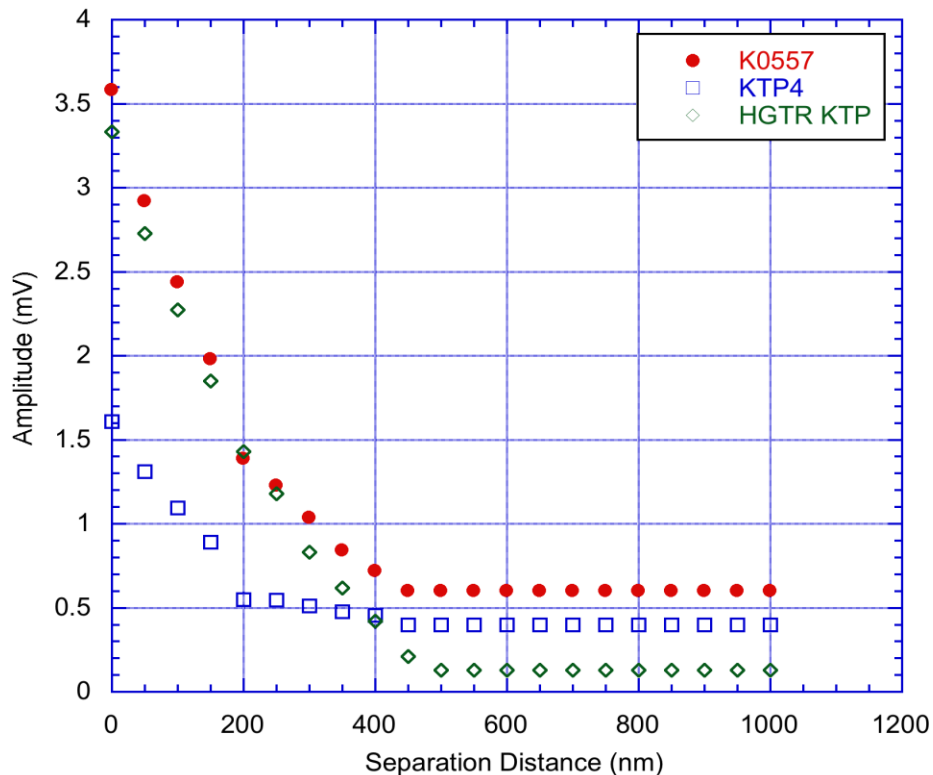


Figure 9.2. Amplitude of AFM cantilever vibration plotted as a function of separation distance between magnetic tip and sample surface for different KTP crystal samples.

9.3.2. Imaging Ferroelectric Interactions in KTP crystals

By scanning the magnetic tip across the ferroelectric sample surface, it is possible to map the ferroelectric interactions between the magnetic tip and the eddy currents generated in the sample. This section presents preliminary imaging results obtained on four different KTP samples. Figure 9.3 shows surface topography and ferroelectric image obtained on KTP6 at a scan area of $1.51 \mu\text{m} \times 1.51 \mu\text{m}$ and excitation frequency of 90 kHz. The image is obtained in contact mode and hence will have both eddy current interactions and

piezoelectric or electrostrictive interactions. Therefore, interpreting the contrast needs careful analysis. The topography image shows circular features with a maximum height of 50 nm. The eddy current image on the right shows some interesting features. Circular features with dark contrast can be seen in this image, which are not seen in the corresponding surface topography image. These features are shown by arrows. A ferroelectric material switches between polarization states in the presence of an external field. While the dark features seen in the image can be K^+ ions which are conductive, they are not seen in the corresponding topography image. Therefore, these features might be the ferroelectric domains formed when the electric field interacts with the sample.

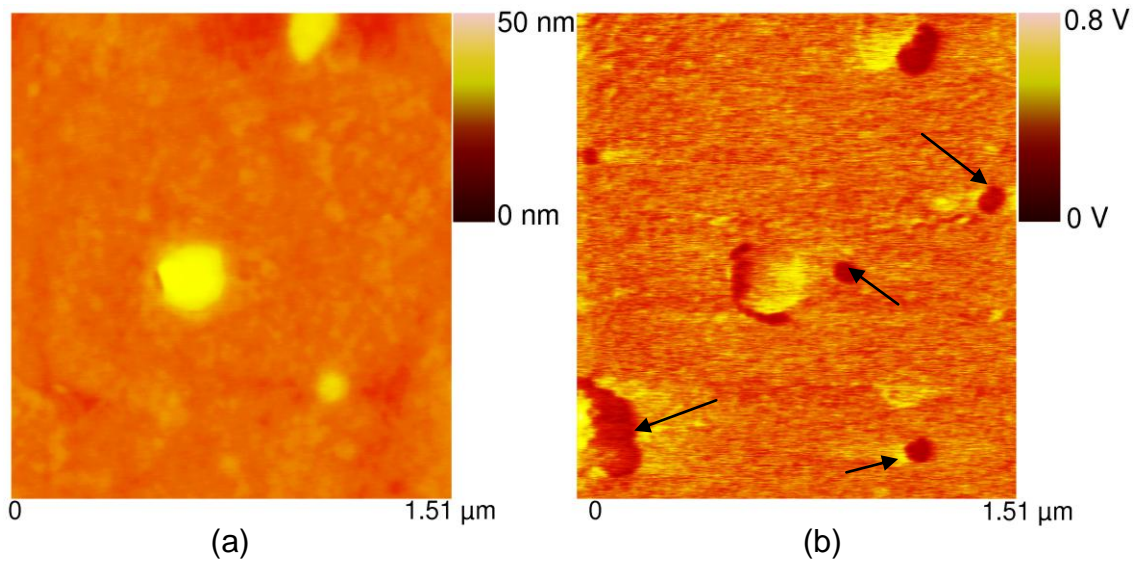


Figure 9.3. (a) Surface topography and (b) eddy current images of KTP6 sample. Frequency of excitation: 90 kHz.

Figures 9.4-9.6 show surface topography and eddy current Images obtained on KTP4, HGTR KTP, and K0557 samples respectively all obtained at a frequency of 90 kHz. KTP4 and HGTR KTP images show similar features.

Precipitates introduced during the processing of the material can be observed in both the images. However, the precipitates show different contrast in different regions, as indicated by arrows in Figure 9.4 and 9.5. The difference in contrast could be due to electrical conductivity variations or electrostriction behavior or ferroelectric domains. The images obtained on K0557, shown in Figure 9.6 did not show any precipitates. The surface topography image on this sample shows parallel bands with a width of 200 nm and a maximum height of 20 nm. However, the eddy current image shows bright-dark contrast within these bands. The plot between the input voltage and the output amplitude of the cantilever for K0557 showed a quadratic behavior indicating the strong electrostriction interactions in the sample. Therefore, the contrast difference in this image could be due to the local variations in the electrostriction. Consequently, the features indicate the ferroelectric domains of the sample.

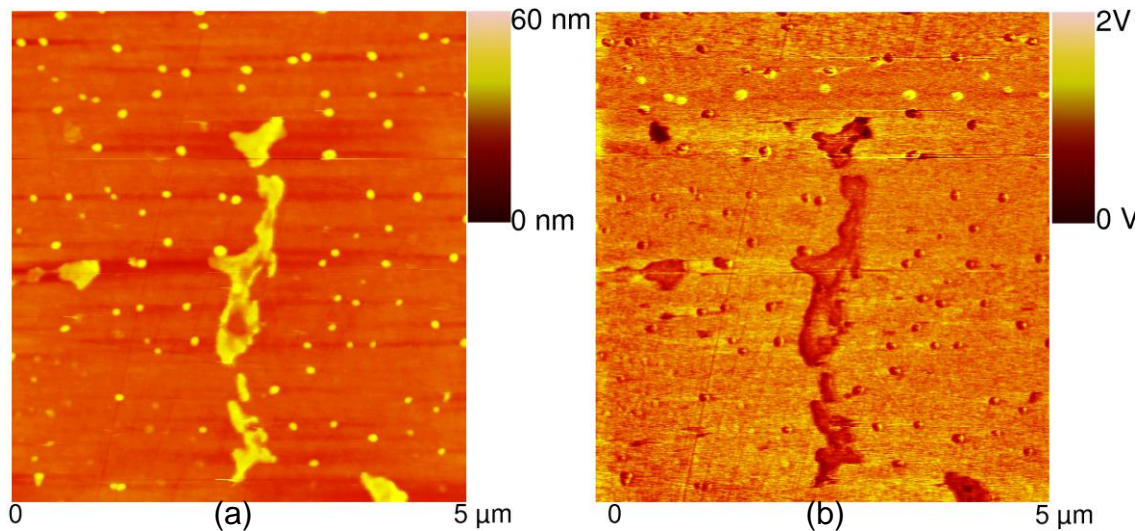


Figure 9.4. (a) Surface topography and (b) eddy current images of KTP4 sample. Frequency of excitation: 90 kHz.

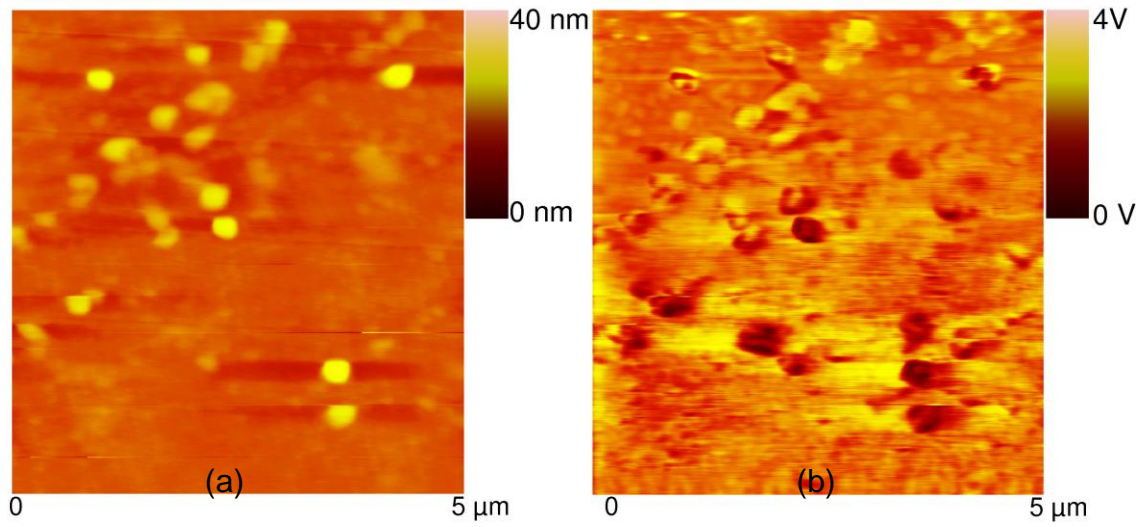


Figure 9.5. (a) Surface topography and (b) eddy current images of HGTR KTP sample. Frequency of excitation: 90 kHz.

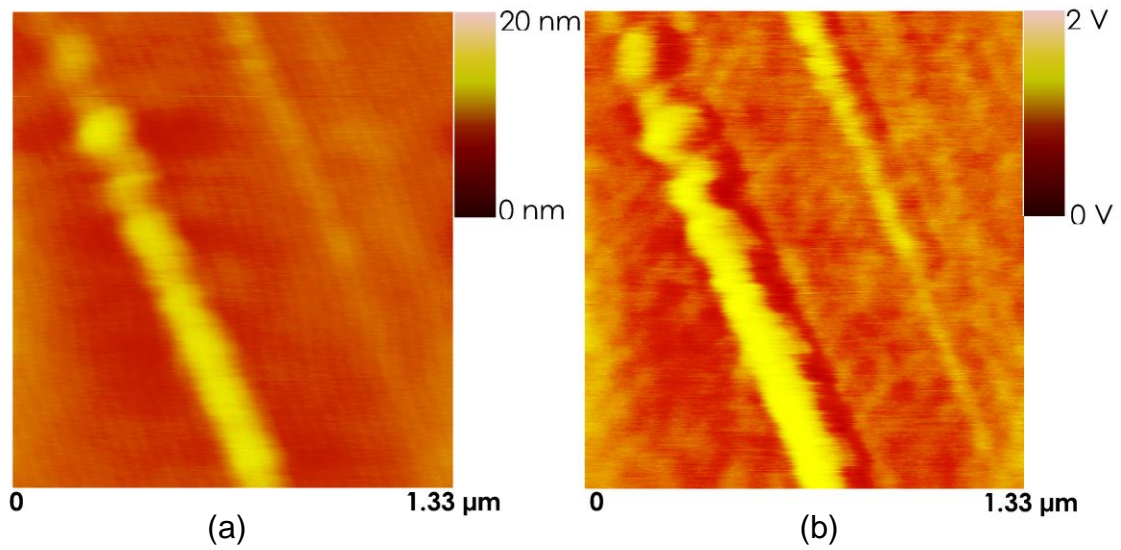


Figure 9.6. (a) Surface topography and (b) eddy current images of K0557 sample. Frequency of excitation: 90 kHz.

9.4. Conclusions

A new methodology to measure and image ferroelectric properties with nanometer scale resolution is presented. The technique is based on the combination of an AFM and electromagnetic fields. A ferroelectric sample is placed in an electromagnetic coil excited with radio frequency signal. The electric field generates strains in the material through electrostriction and piezoelectricity. The strains are measured by a magnetic tip attached to a flexible cantilever. An image is obtained by scanning the tip across the sample surface in contact mode. Samples of KTP crystals processed under different conditions are characterized using this technique. Plots between the input voltage to the coil and the output amplitude of the cantilever are shown for the samples. The results show that while some samples exhibit a linear behavior, other samples showed a quadratic behavior indicating the presence of both piezoelectric and electrostrictive interactions. Eddy current images obtained on the four samples show different contrast in each of the samples. This difference in contrast could be due to local variations in ferroelectric properties. Moreover, the KTP crystals are ionic conducting samples with relatively higher conductivity than other ferroelectric materials. Therefore, the contrast in the images could also be due to local variations in electrical conductivity. The results presented in this chapter are only preliminary results and further studies need to be conducted on these samples to explain the mechanism of contrast seen in the eddy current images of ionic conducting ferroelectric materials.

CHAPTER 10

SUMMARY AND CONCLUSIONS

The research work in this dissertation presents a new AFM based methodology to measure and image electrical properties of materials with nanometer scale resolution and high sensitivity to local variations in electrical conductivity. A conventional AFM is modified to measure forces due to induced currents in conducting materials placed in a time-varying external magnetic field. A small electromagnetic coil is used to generate eddy currents in conducting samples. The eddy currents are acted up on by forces ranging from few picoNewtons to nanoNewtons. A theoretical model based on solution to Maxwell's equations with appropriate boundary conditions is developed to determine the magnitude of eddy current forces generated in a typical metal placed in an external electromagnetic field. The model is also used to describe the electrodynamic interactions between the magnetic field of a typical MFM tip and the magnetic field generated by eddy currents. For a typical metallic material, the theoretical eddy current forces were found to be approximately 50 pN. Based on the theoretical force calculations, for maximum sensitivity, a cantilever with a spring constant of 0.1 N/m was selected for measuring eddy

current forces. The selected spring constant is capable of measuring sub-picoNewton forces. Also, a suitable electromagnetic coil is designed to generate the required eddy current densities in the samples. By externally generating eddy currents in the samples using a coil, eddy current densities can be independently adjusted in different materials depending on conductivity, frequency of excitation, skin depth etc.

The sample is placed on a small electromagnetic coil. One face of the conducting sample faces the circular end of the coil, while the opposite face of the sample faces a magnetic tip-cantilever of the AFM. The coil is connected to a radio frequency signal generator. The coil generates a time-varying magnetic field around it. The oscillating magnetic field of the coil induces eddy currents in the conductor. The eddy currents produce an opposing secondary magnetic field in a direction opposite to the primary magnetic field. The secondary magnetic field of the eddy currents interacts with the magnetic tip causing the cantilever to deflect. The deflection of the cantilever is measured by a lock-in amplifier which compares the output of the AFM cantilever with the input to the coil. The output from the lock-in amplifier is used to separate surface topography and electrical conductivity images simultaneously.

The experimental setup is first used to measure eddy current forces in different metallic samples. Eddy current forces in single crystal samples of copper, cadmium, aluminum and polycrystalline platinum were measured. The samples were embedded in an epoxy and polished to an optical finish. The sample is placed on the coil and the coil is connected to the signal generator. For

maximum sensitivity, the frequency of the coil was varied while looking for a maximum amplitude of the cantilever vibration. The resonant frequency of the cantilever coupled to the sample was determined. The signal generator was then set at the resonant frequency and tip was positioned at a distance of 50 nm above the sample surface. The force acting on the cantilever due to eddy currents was measured. This was repeated for all the samples. The results show that very small forces, of the order of 15 pN can be measured using this technique. The effect of separation distance between the tip and sample on the magnitude of eddy current forces was studied. The results showed that at small separation distances, the eddy current forces were highest and with an increase in the distance, the eddy current forces rapidly decreased. It was also shown that the magnitude of the eddy current forces strongly depend on the electrical conductivity of the sample. The experimentally measured eddy current forces on different metals were compared with theoretical results and they were in good agreement. A finite element model of the electrodynamic interactions of magnetic tip and the magnetic field due to eddy currents in metals was developed using an electromagnetic analysis software Maxwell 3D. The resulting eddy current forces are also computed. The finite element model results were in good agreement with theoretical and experimental forces.

The imaging capability of the newly developed instrument was demonstrated by imaging the electrical conductivity of 7 μm carbon fiber reinforced in polymer matrix. The contrast in the eddy current force image is explained based on the huge electrical conductivity difference between the fibers

and the polymer matrix. High-resolution eddy current images of the interface between the fiber and matrix were obtained. Therefore, this technique can be effectively used to study the interfacial properties of composites with nanometer resolution. The methodology is then applied to demonstrate that the technique is capable of imaging very small variations in electrical conductivity. This is accomplished by imaging the microstructure of a dual-phase polycrystalline Ti-6Al-4V alloy with an approximate difference of 6% in electrical conductivity between the two phases and within the α phase. The eddy current image distinguished different phases in the sample and also facilitated the observation of different grains by significantly increasing the image contrast. The contrast in the eddy current force images is attributed to the anisotropy of the electrical conductivity of the α phase and the difference between the conductivity of the α and the β phase. The spatial resolution of the eddy current imaging system was determined by imaging carbon nanofibers reinforced in a polymer matrix. A spatial resolution of 25 nm was obtained using the technique. Since the magnetic field sensed by the magnetic tip may be larger than the diameter of the tip, the resolution is in the range of 30–50 nm. Thus, it is demonstrated that high resolution and high sensitivity to local electrical conductivity variations can be achieved using the newly developed technique. Moreover, based on the response of the magnetic tip to the excitation of the electromagnetic coil, the instrument can be used to perform eddy current imaging at multiple frequencies.

Since the AFM is extensively used for the characterization of nanomaterials and nanostructures, the newly developed technique was also

used to characterize the electrical properties of nanostructured materials. Two types of nanostructured materials were characterized: carbon nanofibers and platinum nanoparticles. The results show that the eddy current images can be successfully used to study the distribution and dispersion of carbon nanofibers in the polymer matrix. The interface region of the fibers and the matrix was examined with nanometer scale resolution, thus facilitating characterization of interface and possible delaminations or fiber pull-out from the matrix. Therefore, the eddy current imaging can be a useful tool for the characterization of nanocomposites.

The electromagnetic properties of metallic nanoparticles have been studied extensively and vast amounts of literature are available on this subject. Generally, the electromagnetic properties are characterized using optical techniques such as NSOM and SERS. These techniques operate at optical frequencies and image the plasmon resonances of the metallic nanoparticles. Moreover, these techniques image the local enhancement in electrical field around the nanoparticles. The interaction of low-frequency electromagnetic fields with metallic nanoparticles has not been reported in the literature, to the best knowledge of the author. Therefore, in this study, the local electromagnetic properties of platinum nanoparticles subjected to low frequency electromagnetic fields are studied. The eddy current images of platinum nanoparticles show that it is possible to image the helicon wave propagation and its resonance modes in nanometals. Generally, helicon wave resonance modes are observed in thicker metallic samples excited at MHz frequencies at low temperatures. The helicon

wave propagation in nanometals is explained based on the increase of effective mass of electrons in metallic mesostructures. The increase in the effective mass of electrons reduces the cyclotron frequencies from MHz to kHz range. In the experiments, the images are obtained at a frequency of 90 kHz. Since the excitation frequency is approaching the cyclotron frequency, it is possible to excite helicon resonance modes in nanometals at room temperatures. The nature of the helicon wave is predominantly magnetic and thus the magnetic field of the helicon wave propagating in the nanoparticle can be imaged using a magnetic tip attached to the AFM cantilever. The possibility of imaging helicon waves in nanometals at room temperatures opens up a new avenue for variety of applications, most notably in sensors.

The eddy current force imaging utilizes interactions between induced currents and the conducting sample to build an image of local electrical conductivity variations. However, the induced currents interact with different materials and gives rise to different interaction forces. If these interaction forces can be imaged using an appropriate cantilever-tip system, new imaging modes can be developed. Therefore, the newly developed technique was also used to characterize magneto-acoustic, magneto-elastic and ferroelectric properties.

When a metallic material is subjected to electromagnetic fields, strains due to the collisions of the electrons with the lattice are developed in the material. These strains cause the lattice to vibrate thus generating acoustic waves in the metal. The amplitudes of the acoustic waves generated are very small. The electromagnetic generation of acoustic waves has led to the development of

EMATs which are extensively used in NDE applications. In a traditional EMAT, a static magnetic field is used to increase the amplitudes of vibrations. However, if an AFM cantilever-tip is in contact with the metal placed in electromagnetic field, the cantilever can measure the extremely small amplitudes due to acoustic waves. In such case, the external magnetic field is not necessary. Therefore, in this study, acoustic waves generated due to electromagnetic fields in metals measured and imaged using AFM. A plot between the input voltage and the output of the AFM cantilever was obtained for different single crystal metallic samples. The thicknesses of the samples are smaller than the electromagnetic skin depth at the excitation frequency. The results show that the generation of acoustic waves in metals is a function of the electrical conductivity as well as the elastic properties of the metals. Acoustic amplitude images were obtained on the Ti-6Al-4V alloy in contact mode AFM. The images showed a better contrast in the acoustic amplitude image. Grain-to-grain contrast and strong grain boundary contrast were observed in the acoustic images. The contrast observed in the images is similar to the ultrasonic AFM images which utilize a piezoelectric transducer to generate acoustic waves in a sample and the AFM cantilever to detect and map the acoustic amplitudes.

When a ferromagnetic material is placed in an external magnetic field, the sample dimensions change due to the magnetostriction phenomenon. Therefore, if an AFM tip is placed in contact with the ferromagnetic material subjected to electromagnetic field, the resulting image maps the local variations in magneto-elastic properties of the sample. Also, a magnetic tip is not needed in this case.

A *non-magnetic* tip is used to scan the surface of a ferromagnetic sample placed in the electromagnetic field of a tiny coil excited at resonant frequency of the AFM cantilever. The ac magnetic field generates strains in the material which is detected by the AFM cantilever to obtain an image of local magnetostriction of the sample. The technique is used to identify magnetic iron nanoparticles from nonmagnetic carbon nanoparticles deposited on a silicon substrate. The technique is also used to study the magnetostrictive properties of amorphous and nanocrystalline magnetic materials. The local magnetostriction properties depend on the magnetization of the domains. Therefore, this technique can also be used to image the magnetic domains in the sample. The contrast in the images can be explained based on the local variations of the magnetostriction of the samples. The images obtained on amorphous magnetic ribbon material show high magnetostriction of the material. When the amorphous material is heat treated, the nanocrystalline phases develop in the material. The magnetostriction the nanocrystalline phase is expected to be small. The magneto-elastic image of the nanocrystalline phase shows that the local magnetostriction is small when compared to the amorphous phase of the same material. Magnified images of the magneto-elastic interactions show that the deformation of the material due to magnetization direction reversal in domains leads to a higher amplitude of AFM cantilever near the domain wall. Consequently, the domain wall can be imaged due to the microscopic magnetic forces acting on the domains. The width of the magnetic domain wall is about 50 nm. The magnetostrictive imaging using an AFM will be a useful technique when imaging magnetically soft materials, which

are otherwise difficult to be imaged due to sample magnetization in conventional magnetic force microscopy techniques.

Finally, the technique was used to characterize ferroelectric materials. A ferroelectric sample is placed in an electromagnetic coil excited with radio frequency signal. The electric field generates strains in the material through electrostriction and piezoelectricity. The strains are measured by a magnetic tip attached to a flexible cantilever. An image is obtained by scanning the tip across the sample surface in contact mode. Four different samples KTP crystals, processed under different conditions are characterized. Preliminary results on the four samples were presented. Since KTP is an ionic conductor, the contrast in the images could be explained due to variations in electrical conductivity in addition to the local ferroelectric property variations. Therefore, the analysis of the contrast in ionic conducting ferroelectric materials needs careful interpretation. More studies are needed to explain the contrast mechanism in ferroelectric materials using the new technique.

In summary, the techniques developed in this dissertation can be used to study local variations in different material properties, like electrical conductivity, magnetic, magneto-acoustic and ferroelectric properties with nanometer scale resolution and high sensitivity. The most important feature of all the techniques described in this work is how the induced currents are exploited to image different material properties without applying any bias voltage or any extensive modifications to the AFM. Simple modifications to AFM would result in characterization of multiple material properties offering ease of use and

versatility. The only modifications required to image these properties are the selection of an appropriate tip and using a suitable imaging mode of AFM. These techniques would find many applications in different areas of nanotechnology including advanced micro- and nano-NDE applications and sensing applications.

CHAPTER 11

FUTURE WORK

A new AFM based methodology to characterize multiple material properties is developed and discussed in this dissertation. However, several research topics that surfaced during the course of this investigation could not be studied due to time constraints. A few of those topics for future research listed below.

1. Eddy current forces on copper, aluminum and cadmium were measured in this study. However, eddy current forces on other metals of different electrical conductivities could be obtained and used as calibration standards for future imaging. Also, finite element models can be developed to model the interactions between the magnetic tip and the eddy currents in different metals.
2. The eddy current forces can be used to measure electrical resistivity of the samples. In this study, the magnetic susceptibility of copper is measured using eddy current forces. The same analysis can be extended to different materials.

3. The frequency spectra of the cantilever coupled with the sample showed that the cantilever has multiple resonance peaks. The images in this study were obtained at one resonance frequency. The effect of the multiple frequency imaging on the contrast in different materials can be studied.
4. In the electrical conductivity images shown in this study, the normal component of the eddy current force is measured and imaged. However, the finite element analysis of electrodynamic interactions between magnetic tip and copper showed that there are lateral eddy current forces on the cantilever. The lateral forces give rise to the twisting motion of the AFM cantilever resulting in a torsion. The deflections of the cantilever due to the lateral forces can be used to obtain an image of the torsional eddy current force in the material. The torsional eddy current forces are expected to give rise to a strong contrast near the boundaries, thus enhancing the contrast seen in images. Moreover, cracks which are parallel to the eddy current field cannot be imaged using the normal eddy current force component. In such cases, the lateral forces will be able to detect the cracks with much better contrast.
5. It is well known that the presence of defects cracks significantly modify the eddy current density around them. Therefore, the eddy current AFM technique can be effectively used to detect cracks or characterize fractured surfaces with nanoscale resolution. Moreover, this technique can also be effectively used to detect sub-surface cracks, since the eddy currents pass through the thickness of the sample.

6. Eddy current images of metallic nanoparticles showed a dramatic contrast difference between the nanoparticles. The contrast in the images was explained based on the helicon resonances in the nanoparticles. More studies need to be done on different metallic nanoparticles to explore in more detail about the contrast mechanisms in nanoparticles. The effect of size, shape, and electrical conductivity of nanoparticles can be studied. Also, it is interesting to study the possibility of measuring local dielectric properties of individual nanoparticles using this technique.
7. The contrast mechanism in the eddy current images of ferroelectric materials needs to be studied in detail. The images on different ferroelectric materials needs to be obtained and compared to study the effect of conductivity and local ferroelectric properties on the contrast. Also, images can be obtained using both magnetic and non-magnetic tips to study the differences in images.

REFERENCES

1. Heany, M. B. 1999. *Electrical conductivity and resistivity*. In *The measurement, instrumentation and sensors handbook*, ed. John. G. Webster. Boca Raton: CRC Press.
2. Smits, F.M. 1958. Measurements of sheet resistivity with the four-point probe. *Bell Syst. Tech.J.* 7:711-718.
3. Valdes, L.B. 1954. Resistivity measurements on Germanium for transistors. *Proc. Inst. Radio Engrs.* 42: 420-427.
4. Czichos, H., Saito, T., and Smith, L. 2006. *Handbook of Materials Measurement Methods*. Berlin: Springer.
5. Libby, H.L. 1971. *Introduction to Electrodynamic Nondestructive Test Methods*. New York: Wiley-Interscience.
6. Gleiter, H. 2000. Nanostructured materials: basic concepts and microstructure. *Acta. Mater.* 48: 1-29.
7. Padmanabhan, K. A. 2001. Mechanical properties of nanostructured materials. *Materials Science and Engineering A* 304-306: 200-205.
8. Millo, O., Katz, D., Cao, Y., and Banin, U. 2000. Scanning tunneling spectroscopy of InAs nanocrystal quantum dots. *Phys. Rev. B* 61: 16773-16777.
9. Imura, K., Nagahara, T., and Okamoto, H. 2004. Imaging of surface plasmon and ultrafast dynamics in gold nanorods by near-field microscopy. *J. Phys. Chem. B* 108: 16344-16347.
10. Martin, J. I., Nogués, J., Liu, K., Vicent, J. L., and Schuller, I. K. 2003. Ordered magnetic nanostructures: fabrication and properties. *Journal of Magnetism and Magnetic Materials* 256: 449-501.
11. Binnig, G., Rohrer, H., and Gerber, Ch. 1986. Atomic force microscopy. *Phys. Rev. Lett.* 56: 930-933.

12. Martin Y., Abraham, D. W., and Wickramasinghe, H. K. 1988. High-resolution capacitance measurement and potentiometry by force microscopy. *Appl. Phys. Lett.* 52: 1103-1105.
13. O'Shea, S. J., Atta, R. M., Murrell, M. P., and Welland, M. E. 1995. Conducting atomic force microscopy study of silicon dioxide breakdown. *J. Vac. Sci. Technol. B* 13: 1945-1952.
14. Ruskell, T. G., Workman, R. K., Chen, D., Sarid, D., Dahl, S., and Gilbert, S. 1996. High resolution Fowler-Nordheim field emission maps of thin silicon oxide layers. *Appl. Phys. Lett.* 68: 93-95.
15. Williams, C.C. 1999. Two-dimensional dopant profiling by scanning capacitance microscopy. *Annual Review of Materials Science* 29: 471-504.
16. Weaver, J. M. R., and Abraham, D. W. 1991. High resolution atomic force microscopy potentiometry. *J. Vac. Sci. Technol. B* 9: 1559-1561.
17. Hoffmann, B., Houbertz, R., and Hartmann, U. 1998. Eddy current microscopy. *Appl. Phys. A* 66: S409-S413.
18. Lantz, M.A., Jarvis, S. P., and Tokumot, H. 2001. High resolution eddy current microscopy. *Appl. Phys. Lett.* 78: 383-385.
19. Martin, Y., and Wickramasinghe, H.K. 1987. Magnetic imaging by force microscopy with 1000 Å resolution. *Appl. Phys. Lett.* 50: 1455-1457.
20. Hartmann, U. 1988. Magnetic force microscopy: some remarks from the micromagnetic point of view. *J. Appl. Phys.* 64: 1531-1564.
21. Bluhm, H., Wadas, A., Wiesendanger, R., Roshko, A., Aust, J. A., and Nam, D. 1997. Imaging of domain-inverted gratings in LiNbO₃ by electrostatic force microscopy. *Appl. Phys. Lett.* 71: 146-148.
22. Runyan, W. R. 1975. *Semiconductor Measurements and Instrumentation*. New York: McGraw Hill.
23. Schroeder, D. K. 1990. *Semiconductor Material and Device Characterization*. New York: Wiley.
24. Morton, S. A., Turton, J., and Greig, D. 1995. A four-point probe to measure the electrical resistivity of alloys under UHV conditions. *Rev. Sci. Instrum.* 66:3917-3920.

25. Sequeira, C. A. C. and Santos, D. M. F. 2007. Four-point probe electrical measurements on p-n-p InP structures. *Brazilian Journal of Physics*. 37:1077-1083.
26. Kinder, R., Huleniyi, L., and Mika, F. 1996. Determination of the depth of shallow implanted p+n junctions by the four-point probe method. *Phys. Status. Solidi A* 157:393-398.
27. Kulkarni, A. K., Tey, K., and Rodrigo, H. 1995. Electrical characterization of CVD diamond thin films grown on silicon substrates. *Thin Solid Films* 270:189-193.
28. Faglia, G., Comini, E., Sberveglieri, G., Rella, R. et al . 1998. Square and collinear four probe array and Hall measurements on metal oxide thin film gas sensors. *Sensors and Actuators B* 53: 69-75.
29. Sim, S. M., Chen, B. J., and Sun, X. W. 2004. In situ resistance measurement during FCVA deposition of ZnO thin films. *Ceramics International* 30: 2019-2022.
30. Wang S., Wang D., and Chung, D. D. L. 2006. Method of sensing impact damage in carbon fiber polymer-matrix composite by electrical resistance measurement. *J. Mater. Sci.* 41: 2281-2289.
31. Mironov, V. S., Kim, J. K., Park, M., Lim, S., and Cho, W. K. 2007. Comparison of electrical conductivity data obtained by four-electrode and four-point probe methods for graphite-based polymer composites. *Polymer Testing* 26: 547-555.
32. Bowler, N. 2006. Theory of four-point alternating current potential drop measurements on a metal half-space. *J. Phys. D: Appl. Phys.* 39:584-589.
33. Hwang, I. S., and Ballinger, R. G. 1992. A multi-frequency AC potential drop technique for the detection of small cracks. *Meas. Sci. Technol.* 3: 62-74.
34. Poehler, T. O., and Liben, W. 1964. Induction measurement of semiconductor and thin-film resistivity. *Proc. IEEE* 52: 731-732.
35. Zimmerman, J. E. 1961. Measurement of electrical resistivity of bulk metals. *Rev. Sci. Instrum.* 32: 402-405.
36. Myers, W. R. 1958. An electrodeless method for the measurement of electrolytic conductivity and magnetic susceptibility. *J. Sci. Instrum.* 35: 173-175.

37. Yosim, S. J., Grantham, L. F., Luchsinger, E. B., and Wike, R. 1963. Electrodeless determination of electrical conductivities of melts at elevated temperatures. *Rev. Sci. Instrum.* 34: 994-996.
38. Bean, C. P., DeBlois, R. W., and Nesbitt, L. B. 1959. Eddy-current method for measuring the resistivity of metals. *J. Appl. Phys.* 30: 1976-1980.
39. Ogawa, T. 1961. Measurement of the electrical conductivity and dielectric constant without contacting electrodes. *J. Appl. Phys.* 32: 583-592.
40. Khotkevich, V. I., and Zabara, M. Y. 1963. A new arrangement of the induction method of measuring electrical conductivity. *Cryogenics* 3: 33-35.
41. Chaberski, A. Z. 1971. Contactless induction method for electric resistivity measurement. *J. Appl. Phys.* 42: 940-947.
42. Hendrickson, J. R., and Philbrook, J. 1979. Resonant torsional apparatus for contactless measurements of electrical conductivity and magnetic susceptibility of solids. *Rev. Sci. Instrum.* 50: 849-855.
43. Delaney, J. A., and Pippard, A. B. 1972. Electrodeless methods for conductivity measurement in metals. *Rep. Prog. Phys.* 35: 677-715.
44. Wejgaard, W., and Tomar, V. S. 1974. Contactless measurement of electrical resistivity by eddy current methods: discussion and a new technique. *Journal of Physics E: Scientific Instruments* 7: 395-399.
45. Rajotte, R. J. 1975. Eddy-current method for measuring the electrical conductivity of metals. *Rev. Sci. Instrum.* 46: 743-745.
46. Crowley, J. D., and Rabson, T. A. 1976. Contactless method of measuring resistivity. *Rev. Sci. Instrum.* 47: 712-715.
47. Flanders, P. J., and Shtrikman, S. 1980. Contactless conductivity measurements with a rotating sample magnetometer. *Rev. Sci. Instrum.* 51: 617-620.
48. Kraftmakher, Y. 2000. Eddy currents: contactless measurement of electrical resistivity. *Am. J. Phys.* 68: 375-379.
49. Pellicer-Porres, J., Lacomba-Perales, R., Ruiz-Fuertes, J., Martínez-García, D., and Andrés, M. V. 2006. Force characterization of eddy currents. *Am. J. Phys.* 74: 267-271.

50. Íñiguez, J., Raposo, V., Flores, A. G., Zazo, M., and Hernández-López, A. 2005. Measurement of the electrical conductivity of metallic tubes by studying magnetic screening at low frequency. *Am. J. Phys.* 73: 206-210.
51. Neighbor, J. E. 1969. Eddy current method for measuring anisotropic resistivity. *J. Appl. Phys.* 40: 3078-3080.
52. Zeller, C., Denenstein, A., and Foley, G. M. T. 1979. Contactless technique for the measurement of electrical resistivity in anisotropic materials. *Rev. Sci. Instrum.* 50: 602-607.
53. Isono, Y., and Kotani, M. A. 1995. Contactless method for measurement of electrical conductivity in a particular direction. *Meas. Sci. Technol.* 6: 1429-1432.
54. Riherd, M. C., and Schreiber, R. 1973. Eddy current measurements on ultrapure molybdenum and rhenium. *J. Appl. Phys.* 44: 4908-4909.
55. Miyamoto, N., and Nishizawa, J. 1967. Contactless measurement of resistivity of slices of semiconductor materials. *Rev. Sci. Instrum.* 38: 360-367.
56. Miller, G. L., Robinson, D. A. H., and Wiley, J. D. 1976. Contactless measurement of semiconductor conductivity by radio frequency-free-carrier power absorption. *Rev. Sci. Instrum.* 47: 799-805.
57. Yablonovitch, E., and Gmitter, T. J. 1992. A contactless minority lifetime probe of heterostructures, surfaces, interfaces and bulk wafers. *Solid State Electronics* 35: 261-267.
58. Wheeler, E. D., Boone, J. L., Drewniak, J. L. 1994. A contactless method for measuring the bulk resistance of II-VI compound semiconductors. *Rev. Sci. Instrum.* 65: 3844-3847.
59. Tsukada, K., and Kiwa, T. 2006. Magnetic property mapping system for analyzing three-dimensional magnetic components. *Rev. Sci. Instrum.* 77: 063703-063703-6.
60. Beda, P. I., and Sapunov, V. M. 2000. Experience in eddy-current testing of mounting holes in aircraft components. *Russian Journal of Nondestructive Testing* 36: 241-245.
61. Thollon, F., Lebrun, B., Burais, N., and Jayet, Y. 1995. Numerical and experimental study of eddy current probes in NDT of structures with deep flaws. *NDT & E International* 28: 97-102.

62. Rodriguez, P., and Raj, B. 1997. Development of in-service inspection techniques for nuclear power plants in India. *The International Journal of Pressure Vessels and Piping* 73: 59-68.
63. Chen, Z., Yusa, N., and Miya, K. 2008. Enhancements of eddy current testing techniques for quantitative nondestructive testing of key structural components of nuclear power plants. *Nuclear Engineering and Design* 238: 1651-1656.
64. Robinson, D. 1998. Identification and sizing of defects in metallic pipes by remote field eddy current inspection. *Tunneling and Underground Space Technology* 13: 17-27.
65. Keshwani, R., and Bhattacharya, S. 2008. Design and optimization of eddy current sensor for instrumented pipeline inspection gauge. *Sensor Review* 28: 321-325.
66. Topp, D., and Jones, B. A. 1994. Operational experience with the ACFM inspection technique for sub-sea weld inspection. *Environmental Engineering* 7: 9-13.
67. Fukutomi, H., Takagi, T., and Nishikawa, M. 2001. Remote field eddy current technique applied to non-magnetic steam generator tubes. *NDT&E International* 34: 17-23.
68. Helifa, B., Oulhadj, A., Benbelghit, A., Lefkaier, I. K., Boubenider, F., and Boutassouna, D. 2006. Detection and measurement of surface cracks in ferromagnetic materials using eddy current testing. *NDT & E International* 39: 384-390.
69. Blitz, J., Oaten, S. R., and Haijan, N. T. 1986. The testing of ferromagnetic metals with eddy-currents. *Nondestructive Testing Communications* 2: 189-200.
70. Blitz, J. 1991. *Electrical and Magnetic Methods of Nondestructive Testing*. London: Chapman & Hall.
71. Gramz, M., and Stepinski, T. 1994. Eddy current imaging, array sensors and flaw reconstruction. *Res. Nondestr. Eval.* 5: 157-174.
72. Kirby, M. W., and Lareau, J. P. 1997. Eddy current imaging of aircraft using real time image signal processing. *NDT&E International* 30: 176-176.
73. McCary, R., Oliver, D., Silverstein, K., and Young, J. 1984. Eddy current imaging. *IEEE Trans. Magn.* 20: 1986-1988.

74. Blodgett, M., and Nagy, P. B. 1998. Anisotropic grain noise in eddy current inspection of noncubic polycrystalline metals. *Appl. Phys. Lett.* 72: 1045-1047.
75. Blodgett, M., Hassan, W., and Nagy, P. B. 2000. Theoretical and experimental investigations of the lateral resolution of eddy current imaging. *Materials Evaluation* 58: 647-654.
76. Jenks, W. G., Sadeghi, S. S. H., Wikswo Jr, J. P. 1997. SQUIDS for nondestructive evaluation. *Journal of Physics D: Applied Physics* 30: 293-323.
77. Dogaru, T., and Smith, S. T. 2001. Giant magnetoresistance-based eddy-current sensor. *IEEE Trans. Magn.* 37: 3832-3838.
78. Roth, B. J., Sepulveda, N. G., and Wikswo, J. P. 1989. Using a magnetometer to image a two-dimensional current distribution. *J. Appl. Phys.* 65: 361-372.
79. Bos, B., Sahlén, S., and Andersson, J. 2003. Automatic scanning with multi-frequency eddy current on multi-layered structures. *Aircraft Engineering and Aerospace Technology* 75: 491-496.
80. Tsukada, K., and Kiwa, T. 2006. Magnetic property mapping system for analyzing three-dimensional magnetic components. *Rev. Sci. Instrum.* 77: 063703-063703-6.
81. Poehler, T. O., and Liben, W. 1964. Induction measurement of semiconductor and thin-film resistivity. *Proc. IEEE* 52: 731-732.
82. Palmer, B. S., Drew, H. D., and Decca, R. S. 2000. Scanning eddy current dynamometer with 100 μm resolution. *Rev. Sci. Instrum.* 71: 3168-3172.
83. Black, R. C., Wellstood, F. C., Dantsker, E., Miklich, A. H. et al. 1994. Eddy current microscopy using a 77-K superconducting sensor. *Appl. Phys. Lett.* 64: 100-102.
84. Karpen, W., Becker, R., and Arnold, W. 1999. Characterization of electric and magnetic material properties with eddy-current measurements. *Nondestructive Testing Evaluation* 15: 93-107.
85. Cleland, A. N., and Roukes, M. L. 1998. A nanometre-scale mechanical electrometer. *Nature* 392: 160-162.

86. Marchand, B., Vacher, F., Gilles-Pascaud, C., Decitre, J .M., and Fermon, C. 2008. High resolution eddy current probes for nondestructive testing. *Review of Progress in Quantitative Nondestructive Evaluation: 34th Annual Review of Progress in Quantitative Nondestructive Evaluation*. Eds. Thompson, D. O., and Chimenti, D. E. 975: 313-320.
87. Stibal, R., Wickert, M. Hiesinger, P., and Jantz, W. 1999. Contactless mapping of mesoscopic resistivity variations in semi-insulating substrates. *Materials Science and Engineering B* 66: 21-25.
88. Green, B.C., Shang, T., Morine, J. C., Liu, H., Schultz, S. M., Oliphant, T. E., and Hawkins, A. R. 2004. Resolution scaling in noncontact scanning impedance imaging. *Rev. Sci. Instrum.* 75: 4610-4614.
89. Kim, M., Kim, J., Kim, H., Kim, S., Yang, J. et al. 2004. Nondestructive high spatial resolution imaging with a 60 GHz near-field scanning millimeter-wave microscope. *Rev. Sci. Instrum.* 75: 684-688.
90. Binnig, G., Rohrer, H., Gerber, Ch., and Weibel, E. 1982. Surface studies by scanning tunneling microscopy. *Phys. Rev. Lett.* 49: 57-61.
91. Binnig, G., and Rohrer, H. 1983. Scanning tunneling microscopy. *Surface Science* 126: 236-244.
92. Welland, M. E., and Koch, R. H. 1986. Spatial location of electron trapping defects on silicon by scanning tunneling microscopy. *Appl. Phys. Lett.* 48: 724-726.
93. Hansma, P. K., and Tersoff, J. 1987. Scanning tunneling microscopy. *J. Appl. Phys.* 61: R1-R24.
94. Frommer, J. 1992. Scanning tunneling microscopy and atomic force microscopy in organic chemistry. *Chem. Int. Ed. Engl.* 31: 1298-1328.
95. Marti, O., and Amrein, M. 1993. *STM and SFM in Biology*. San Diego: Academic.
96. Stroscio, J. A., and Kaiser, W. J. 1993. *Scanning Tunneling Microscopy*. Boston: Academic.
97. Muralt, P., and Pohl, D. W. 1986. Scanning tunneling potentiometry. *Appl. Phys. Lett.* 48: 514-516.
98. Wiesendanger, R., Güntherodt, H.-J., Güntherodt, G., Gambino, R. J., and Ruf, R. 1990. Observation of vacuum tunneling of spin-polarized electrons with the scanning tunneling microscope. *Phys. Rev. Lett.* 65: 247-250.

99. Bell, L. D., and Kaiser, W. J. 1988. Direct investigation of subsurface interface electronic structure by ballistic-electron-emission microscopy. *Phys. Rev. Lett.* 60: 1406-1409.
100. Bell, L. D., and Kaiser, W. J. 1988. Observation of interface band structure by ballistic-electron-emission microscopy. *Phys. Rev. Lett.* 61: 2368-2371.
101. Lee, T., Liu, J., Chen, N., Andres, R. P., Janes, D. B., and Reifenger, R. 2000. Electronic properties of metallic nanoclusters on semiconductor surfaces: Implications for nanoelectronic device applications. *Journal of Nanoparticle Research* 2: 345-362.
102. Xiao, L., Xiao-Be, H., Jun-Ling, L., Li, G., Qing, H. et al. 2005. Four-probe scanning tunnelling microscope with atomic resolution for electrical and electro-optical property measurements of nanosystems. *Chinese Physics* 14: 1536-1543.
103. Nalladega, V., Sathish, S., and Brar, A. S. 2008. Characterization of defects in flexible circuits with ultrasonic atomic force microscopy. *Microelectronics Reliability* 48: 1683-1688.
104. Hartmann, U. 1999. Magnetic force microscopy. *Annu. Rev. Mater. Sci.* 29: 53-87.
105. Nonnenmacher, M., O'Boyle, M. P., and Wickramasinghe, H. K. 1991. Kelvin probe force microscopy. *Appl. Phys. Lett.* 58: 2921-2923.
106. Gu, Y. Q., Ruan, X. L., Han, L., Zhu, D. Z., and Sun, X. Y. 2002. Imaging of thermal conductivity with sub-micrometer resolution using scanning thermal microscopy. *International Journal of Thermophysics* 23: 1115-1124.
107. Betzig, E., Trautman, J. K., Harris, T. D., Weiner, J. S., and Kostelak, R. L. 1991. Breaking the diffraction barrier: optical microscopy on a nanometric scale. *Science* 22: 1468-1470.
108. Stern, J. E., Terris, B. D., Mamin, H. J., and Rugar, D. 1988. Deposition and imaging of localized charge on insulator surfaces using a force microscope. *Appl. Phys. Lett.* 53: 2717-2719.
109. Terris, B. D., Stern, J. E., Rugar, D., and Mamin, H. J. 1989. Contact electrification using force microscopy. *Phys. Rev. Lett.* 63: 2669-2672.

110. Nyffenegger, R. M., Penner, R. M., and Schierle, R. 1997. Electrostatic force microscopy of silver nanocrystals with nanometer-scale resolution. *Appl. Phys. Lett.* 71: 1878-1880.
111. Jeffrey, S., Oral, A., and Pethica, J. B. 2000. Quantitative electrostatic force measurement in AFM. *Applied Surface Science* 157: 280-284.
112. Olbrich, A., Ebersberger, B., and Boit, C. 1998. Conducting atomic force microscopy for nanoscale electrical characterization of thin SiO₂. *Appl. Phys. Lett.* 73: 3114-3116.
113. Oh, J., and Nemanich, R. J. 2002. Current-voltage and imaging of TiSi₂ islands on Si(001) surfaces using conductive-tip atomic force microscopy. *J. Appl. Phys.* 92: 3326-3331.
114. Schneegans, O., Houze, F., Meyer, R., and Boyer, L. 1998. Study of the local electrical properties of metal surfaces using an AFM with a conducting probe. *IEEE Trans. Compon. Packag. Manuf. Technol. Part A* 21: 76-81.
115. Subrahmanyam, R. 1992. Methods for the measurement of two-dimensional doping profiles. *J. Vac. Sci. Technol. B* 10: 358-368.
116. Snow, E. S., Campbell, P. M., and Perkins, F. K. 1997. Nanofabrication with proximal probes. *Proc. IEEE.* 85: 601-611.
117. Tanaka, I., Kamiya, I., Sakaki, H., Qureshi, N., Allen, S. J., and Petroff, P. M. 1999. Imaging and probing electronic properties of self-assembled InAs quantum dots by atomic force microscopy with conductive tip. *Appl. Phys. Lett.* 74: 844-846.
118. Carroll, D. L., Wagner, M., Ruhle, M., and Bonnell, D. A. 1997. Schottky-barrier formation at nanoscale metal-oxide interfaces. *Phys. Rev. B* 55: 9792-9799.
119. Gautier, B., Fares, B., Prudon, G., and Dupuy, J. 2004. Imaging by atomic force microscopy of the electrical properties difference of the facets of oxygen-ion-induced ripple topography in silicon. *Applied Surface Science* 231-232:136-140.
120. De Wolf, P., Brazel, E., and Erickson, A. 2001. Electrical characterization of semiconductor materials and devices using scanning probe microscopy. *Materials Science in Semiconductor Processing.* 4: 71-76.
121. Matey, J. R., and Blanc, J. 1985. Scanning capacitance microscopy. *J. Appl. Phys.* 57: 1437-1444.

122. De Wolf, P., Stephenson, R., Trenkler, T., Clarysse, T., and Hantschel, T, Vandervorst, W. 2000. Status and review of two-dimensional carrier and dopant profiling using scanning probe microscopy. *J. Vac. Sci. Technol. B* 18: 361-368.
123. Trenkler, T., Hantschel, T., Stephenson, R., De Wolf, P. et al. 2000. Evaluating probes for electrical atomic force microscopy. *J. Vac. Sci. Technol. B* 18: 418-427.
124. Álvarez, D., Fouchier, M., Kretz, J., Hartwich, J., Schoemann, S., and Vandervorst, W. 2004. Fabrication and characterization of full diamond tips for scanning spreading-resistance microscopy. *Microelectronic Engineering* 73-74: 910-915.
125. Petersen, C. L., Grey, F., Shiraki, I., and Hasegawa, S. 2000. Microfour-point probe for studying electronic transport through surface states. *Appl. Phys. Lett.* 77: 3782-3784.
126. Petersen, C. L., Hansen, T. M., Bøggild, P., Boisen, A. et al. 2002. Scanning microscopic four-point conductivity probes. *Sensors and Actuators A* 96: 53-58.
127. Bøggild, P., Hansen, T. M., Kuhn, O., Grey, F., Junno, T., and Montelius, L. 2000. Scanning nanoscale multiprobes for conductivity measurements. *Rev. Sci. Instrum.* 71: 2781-2783.
128. Keller, S., Mouaziz, S., Boero, G., and Brugger, J. 2005. Microscopic four-point probe based on SU-8 cantilevers. *Rev. Sci. Instrum.* 76: 125102-125102-4.
129. Ju, Y., Bing-Feng, J., and Saka, M. 2005. Microscopic four-point atomic force microscope probe technique for local electrical conductivity measurement. *Rev. Sci. Instrum.* 76: 086101-086101-3.
130. Yoshimoto, S., Murata, Y., Kubo, K., and Tomita, K. et al. 2007. Four-point probe resistance measurements using PtIr-coated carbon nanotube tips. *Nano Letters* 7: 956-959.
131. Nagase, M., and Yamaguchi, H. 2007. Nanogap electrodes on Si cantilever for local conductance measurement. *Journal of Physics: Conference Series* 61: 856-860.
132. Franke, K., Besold, J., Haessler, W., and Seegebarth, C. 1994. Modification and detection of domains on ferroelectric PZT films by scanning force microscopy. *Surf. Sci. Lett.* 302: L283-L288.

133. Gruverman, A., Auciello, O., Hatano, J., and Tokumoto, H. 1996. Scanning force microscopy as a tool for nanoscale study of ferroelectric domains. *Ferroelectrics*. 184: 11-20.
134. Christman, J. A., Woolcott, Jr, R. R., Kingon, A. I., and Nemanich, R. J. 1998. Piezoelectric measurements with atomic force microscopy. *Appl. Phys. Lett.* 73: 3851-3853.
135. Bdikin, I. K., Shvartsman, V. V., and Kholkin, A. L. 2003. Nanoscale domains and local piezoelectric hysteresis in $\text{Pb}(\text{Zn}_{1/3}\text{Nb}_{2/3})\text{O}_3$ -4.5% PbTiO_3 single crystals. *Appl. Phys. Lett.* 83: 4232-4234.
136. Harnagea, C., Pignolet, A., Alexe, M., Hesse, D., and Gösele, U. 2000. Quantitative ferroelectric characterization of single submicron grains in Bi-layered perovskite thin films. *Applied Physics A: Materials Science & Processing* 70: 261-267.
137. Rugar, D., Mamin, H. J., Guethner, P., Lamber, S. E., and Stern, J. E. 1990. Magnetic force microscopy: General principles and application to longitudinal recording media. *J. Appl. Phys.* 68: 1169-1183.
138. Grütter, P., Mamin, H. J., Rugar, D. 1992. In *Scanning Tunneling Microscopy II*, ed. Wiesendanger, R., and Güntherodt, H. J. 151-207. Heidelberg: Springer.
139. Rice, P., Moreland, J., and Wadas, A. 1994. DC magnetic force microscopy imaging of thin-film recording head. *J. Appl. Phys.* 75: 6878-6880.
140. Svedberg, E. B., Khizroev, S., and Litvinov, D. 2002. Magnetic force microscopy study of perpendicular media: signal-to-noise determination and transition noise analysis. *J. Appl. Phys.* 91: 5365-5370.
141. Takekuma, I., Haseyama, M., Sueoka, K., and Mukasa, K. 2002. Two-dimensional analysis of magnetic microstructures in the DC-demagnetized state and magnetization fluctuations in the transition region using MFM images. *Journal of Magnetism and Magnetic Materials* 239: 359-362.
142. Schmidt, J., Skidmore, G., Foss, S., Dan Dahlberg, E., and Merton, C. 1998. Magnetization reversal processes in perpendicular anisotropy thin films observed with magnetic force microscopy. *Journal of Magnetism and Magnetic Materials* 190: 81-88.

143. Asenjo, A., Jaafar, M., Navas, D., and Vazquez, M. 2006. Quantitative magnetic force microscopy analysis of the magnetization process in nanowire arrays. *J. Appl. Phys.* 100: 023909-023909-6.
144. Bai, J., Takahoshi, H., Ito, H., Saito, H., and Ishio, S. 2004. Dot-by-dot analysis of magnetization reversal in perpendicular patterned CoCrPt medium by using magnetic force microscopy. *J. Appl. Phys.* 96: 1133-1137.
145. Giaever, I. 1960. Energy gap in superconductors measured by electron tunneling. *Phys. Rev. Lett.* 5: 147-148.
146. Stroscio, J. A., and Kaiser, W. J. 1993. *Scanning Tunneling Microscopy*. San Diego: Academic Press.
147. Teague, E. C. 1986. Room temperature gold-vacuum-gold tunneling experiments. *Journal of Research of the National Bureau of Standards* 91: 171-233.
148. Soler, J. M., Baro, A. M., Garcia, N., and Rohrer, H. 1986. Interatomic forces in scanning tunneling microscopy: giant corrugations of the graphite surface. *Phys. Rev. Lett.* 57: 444-447.
149. Dürig, U., Gimzewski, J. K., and Pohl, D. W. 1986. Experimental observation of forces acting during scanning tunneling microscopy. *Phys. Rev. Lett.* 57: 2403-2406.
150. Salmeron, M., Ogletree, D. F., Ocal, C., Wang, H.-C., Neubauer, G., and Kolbe, W. 1991. Tip-surface forces during imaging by scanning tunneling microscopy. *J. Vac. Sci. Technol. B* 9: 1347-1352.
151. Moreland, J., and Rice, P. 1990. High-resolution, tunneling-stabilized magnetic imaging and recording. *Appl. Phys. Lett.* 57: 310-312.
152. Moreland, J., and Rice, P. 1991. Tunneling stabilized magnetic force microscopy with a gold-coated, nickel-film. *J. Appl. Phys.* 70: 520-522.
153. Israelachvili, J. N., and Tabor, D. 1972. The measurement of Van der Waals dispersion forces in the range 1.5 to 130 nm. *Proc. R. Soc. A* 331: 19-38.
154. Teague, E. C., Scire, F. E., Baker, S. M., and Jensen, S. W. 1982. Three-dimensional stylus profilometry. *Wear* 83: 1-12.
155. Bhushan, B. 2004. *Handbook of Nanotechnology*. New York: Springer.

156. Wiesendanger, R. 1994. *Scanning Probe Microscopy and Spectroscopy*. London: Cambridge University Press.
157. Goddenhenrich, T., Lemke, H., Hartmann, U., and Heiden, C. 1992. Force microscope with capacitive displacement detection. *J. Vac. Sci. Technol. A* 8: 383-387.
158. Erlandsson, R., McClelland, G. M., Mate, C. M., and Chiang, S. 1988. Atomic force microscopy using optical interferometry. *J. Vac. Sci. Technol. A* 6: 266-270.
159. Meyer, G., and Amer, N. M. 1988. Novel optical approach to atomic force microscopy. *Appl. Phys. Lett.* 53: 1045-1047.
160. London, F. 1937. The general theory of molecular forces. *Trans. Faraday Soc.* 33: 8-27.
161. Ohnesorge, F., and Binnig, G. 1993. True atomic resolution by atomic force microscopy through repulsive and attractive forces. *Science* 260: 1451-1456.
162. Giessibl, F. J. 2003. Advances in atomic force microscopy. *Reviews of Modern Physics* 75: 949-983.
163. Martin, Y., Williams, C. C., and Wickramasinghe, H. K. 1987. Atomic force microscope-force mapping and profiling on a sub 100-Å scale. *J. Appl. Phys.* 61: 4723-4729.
164. Albrecht, T. R., Grutter, P., Horne, H. K., and Rugar, D. 1991. Frequency modulation detection using high-Q cantilevers for enhanced force microscope sensitivity. *J. Appl. Phys.* 69: 668-673.
165. Kitamura, S., and Iwatsuki, M. 1995. Observation of silicon surfaces using ultrahigh-vacuum noncontact atomic force microscopy. *Jpn. J. Appl. Phys.* 35: L668-L671.
166. Zhong, Q., Inniss, D., Kjoller, K., and Elings, V. B. 1993. Fractured polymer/silica fiber surface studied by tapping mode atomic force microscopy. *Surface Science* 290: L688-L692.
167. Höper, R., Gesang, T., Possart, W., Hennemann, O.-D., and Boseck, S. 1995. Imaging elastic sample properties with an atomic force microscope operating in the tapping mode. *Ultramicroscopy* 60: 17-24.
168. Cappella, B. and Dietler, G. 1999. Force-distance curves by atomic force microscopy. *Surface Science Reports* 34: 5-104.

169. Schönenberger, C., and Alvarado, S. F. 1990. Observation of single charge carriers by force microscopy. *Phys. Rev. Lett.* 65: 3162-3164.
170. Hirsekorn, S., Rabe, U., Boub, A., and Arnold, W. 1999. On the contrast in eddy current microscopy using atomic force microscopes. *Surface and Interface Analysis* 27: 474-481.
171. Landau, L. D. and Lifshitz, E. M. 1960. *Electrodynamics of Continuous Media*. Oxford: Pergamon.
172. Poltz, J. 1983. On eddy currents in thin plates. *Archiv für Elektrotechnik* 66: 225-229.
173. Krakowski, M. 1982. Eddy-current losses in thin circular and rectangular plates. *Archiv für Elektrotechnik* 64: 307-311.
174. Wadas, A. and Hug, H. J. 1992. Models for the stray field from magnetic tips used in magnetic force microscopy. *J. Appl. Phys.* 72: 203-206.
175. Veeco Probes. Santa Barbara, CA.
176. Meaden, G. T. 1965. *Electrical Resistance of Metals*. New York: Plenum.
177. Walters, D. A., Cleveland, J. P., Thomson, N. H., Hansma, P. K. et al. 1996. Short cantilevers for atomic force microscopy. *Rev. Sci. Instrum.* 67: 3583-3590.
178. Sader, J. E. 1995. Parallel beam approximation for V-shaped atomic force cantilevers. *Rev. Sci. Instrum.* 66: 4583-4587.
179. Sader, J. E. 1999. Calibration of rectangular atomic force microscope cantilevers. *Rev. Sci. Instrum.* 70: 3967-3969.
180. Chambers, R. G. and Park, J. G. 1961. Measurement of electrical resistivity by a mutual inductance method. *Br. J. Appl. Phys.* 12: 507-510.
181. Kraftmakher, Y. 1991. Measurement of electrical resistivity via the effective magnetic susceptibility. *Meas. Sci. Technol.* 2: 253-256.
182. Edgar, A. and Quilty, J. W. 1993. A mutual inductance apparatus for measuring magnetic susceptibility and electrical conductivity. *Am. J. Phys.* 61: 943-946.
183. Bleaney, B. I. and Bleaney, B. 1976. *Electricity and Magnetism*. London: Oxford University Press.

184. Jovanović, M. T., Tadić, S., Zec, S., Mišković, Z., and Bobić, I. 2006. The effect of annealing temperatures and cooling rates on microstructure and mechanical properties of investment cast Ti-6Al-4V alloy. *Materials and Design* 27: 192-199.
185. Huang, P., Zhang, G., Wu, Z., Cai, J., and Zhou, Z. 2006. Inspection of defects in conductive multi-layered structures by an eddy current scanning technique: simulation and experiments. *NDT&E International* 39: 578-584.
186. Banerjee, S., Sanyal, M. K., and Datta, A. 1996. A simulation study of multi-atom tips and estimation of resolution in atomic force microscopy. *Applied Surface Science* 99: 255-260.
187. Hutter, J. L., and Bechhoefer, J. 1993. Calibration of atomic-force microscope tips. *Rev. Sci. Instrum.* 64:1868-1873.
188. Goodman, F. O., and Garcia, N. 1991. Roles of the attractive and repulsive forces in atomic-force microscopy. *Physical Review B* 43: 4728-4731.
189. Hutter, J. L., and Bechhoefer. 1993. Manipulation of van der Waals forces to improve image resolution in atomic force microscopy. *J. Appl. Phys.* 73: 4123-4129.
190. Iijima, S. 1991. Helical microtubules of graphitic carbon. 2004. *Nature* 354:56-57.
191. Popov, V. N. Carbon nanotubes: properties and application. *Materials Science and Engineering: R* 43: 61-102.
192. Breuer, O., and Sundararaj, U. 2004. Big returns from small fibers: a review of polymer/carbon nanotube composites. *Polymer Composites* 25: 630-645.
193. Burda, C., Chen, X., Narayanan, R., and El-Sayed, M. A. 2005. Chemistry and properties of nanocrystals of different shapes. *Chem. Rev.* 105: 1025-1102.
194. Kelly, K. L., Corondo, E., Zhao, L. L., and Schatz, G. C. 2003. The optical properties of nanoparticles: the influence of size, shape, and dielectric environment. *J. Phys. Chem. B* 107: 668-677.
195. Michaels, A. M., Nirmal, M., and Brus, L. E. 1999. Surface enhanced Raman spectroscopy of individual Rhodamine 6G molecules on large Ag nanocrystals. *J. Am. Chem. Soc.* 121: 9932-9939.

196. Tominaga, J., Mihalcea, C., Büchel, D., Fukuda, H. et al. 2001. Local plasmon photonic transistor. *Appl. Phys. Lett.* 78: 2417-2419.
197. Courjon, D. 2003. *Near-Field Microscopy and Near-Field Optics*. London: Imperial College Press.
198. Okamoto, H. and Imura, K. 2006. Near-field imaging of optical field wavefunctions in metal nanoparticles. *J. Mater. Chem.* 16: 3920-3928.
199. Murray, P. T., and Shin, E. 2008. Formation of silver nanoparticles by through thin film ablation. *Materials Letters* 62: 4336-4338.
200. Born, M., and Wolf, E. 1999. *Principles of Optics*. Cambridge: Cambridge University Press.
201. Petrashov, V. T. 1984. An experimental study of helicon resonance in metals. *Rep. Prog. Phys.* 47: 47-110.
202. Maxfield, B. W. 1969. Helicon waves in solids. *Am. J. Phys.* 37: 241-269.
203. Houck, J. R., and Bowers, R. 1964. New type of flux meter for the measurement of high magnetic fields at low temperatures. *Rev. Sci. Instrum.* 35: 1170-1172.
204. Bowers, R., Legendy, C., and Rose, F. 1961. Oscillatory galvanomagnetic effect in metallic sodium. *Phys. Rev. Lett.* 7: 339-41.
205. Chambers, R. G. and Jones, B. K. 1962. Measurement of high-field Hall effect by an inductive method. *Proc. R. Soc. A* 270: 417-34.
206. Taylor, M. T., Merrill, J. R., and Bowers, R. 1963. Low-frequency magnetoplasma resonance in metals. *Phys. Rev.* 129: 2525-2529.
207. Pendry, J. B., Holden, A. J., Stewart, W. J., and Youngs, I. 1996. Extremely low frequency plasmons in metallic mesostructures. *Phys. Rev. Lett.* 76: 4773-4776.
208. Johnson, W. L. 2001. Electromagnetic acoustic transducer and methods of determining physical properties of cylindrical bodies using an electromagnetic acoustic transducer. *The Journal of the Acoustical Society of America* 110: 1719-1719.
209. Jafari-Shapoorabadi, R., Konrad, A., and Sinclair, A. N. 2005. The governing electrodynamic equations of electromagnetic acoustic transducers. *J. Appl. Phys.* 97: 10E102-10E102-3.

210. Suchkov, G. M., Katasonov, Yu. A., and Garkavyi, V. V. 2000. Experimental study of sensitivity of electromagnetic-acoustic transducers for flaw detection by nondestructive echo testing using bulk shear waves. *Russian Journal of Nondestructive Testing* 36: 83-86.
211. Suchkov, G. M. 2000. The main advantage of electromagnetic-acoustic testing technique. *Russian Journal of Nondestructive Testing* 36: 760-762.
212. Hsu, D. K., Im, K., and Yang, I. 1999. Applications of electromagnetic acoustic transducers in the NDE of non-conducting composite materials. *KSME International Journal* 13:403-413.
213. Southgate, P. D. 1969. An approximate theory of skin-effect acoustic generation in conductors. *J. Appl. Phys.* 40: 22-29.
214. Rabe, U., and Arnold, W. 1994. Acoustic microscopy by atomic force microscopy. *Appl. Phys. Lett.* 64: 1493-1495.
215. Yamanaka, K., Ogiso, H., and Kolosov, O. 1994. Ultrasonic force microscopy for nanometer resolution subsurface imaging. *Appl. Phys. Lett.* 64: 178-180.
216. Yoshizawa, Y., Oguma, S., and Yamauchi, K. 1988. New Fe-based soft magnetic alloys composed of ultrafine grain structure. *J. Appl. Phys.* 64: 6044-6046.
217. McHenry, M. E., Johnson, F., Okumura, H., Ohkubo, T. et al. 2003. The kinetics of nanocrystallization and microstructural observations in FINEMET, NANOPERM and HITPERM nanocomposite magnetic materials. *Scripta Materialia* 48: 881-887.
218. Herzer, G. 1993. Nanocrystalline soft magnetic materials. *Physica Scripta T* 49A: 307-314.
219. Ślavska-Waniewska, A. and Lachowicz, H. K. 2003. Magnetostriction in soft magnetic nanocrystalline materials. *Scripta Materialia* 48: 889-894.
220. Takata, K. and Tomiyama, F. 2000. Strain imaging of a magnetic material. *Jpn. J. Appl. Phys.* 39: 3090-3092.
221. Gruverman, A., Auciello, O., and Tokumoto, H. 1996. Scanning force microscopy for the study of domain structure in ferroelectric thin films. *J. Vac. Sci. Technol. B* 14: 602-605.

222. Agronin, A. G., Rosenwaks, Y., and Rosenman, G. I. 2003. Piezoelectric coefficient measurements in ferroelectric single crystals using high voltage atomic force microscopy. *Nano Lett.* 3: 169-171.
223. Beirlein, J. D., and Vanherzeele, H. 1989. Potassium titanyl phosphate: properties and new applications. *J. Opt. Soc. Am. B* 6: 622-633.
224. Cheng, L. K., and Beirlein, J. D. 1993. KTP and isomorphs-recent progress in device and material development. *Ferroelectrics* 142: 209-228.
225. Houe, M., and Townsend, P. D. 1995. An introduction to methods of periodic poling for second-harmonic generation. *J. Phys. D* 28: 1747-1763.